The X_2^- Files: Modeling Photodissociation of Molecular Ions in Clusters

by

James R. Faeder

A.B., Harvard College, 1991

A thesis submitted to the

Faculty of the Graduate School of the

University of Colorado in partial fulfillment

of the requirements for the degree of

Doctor of Philosophy

Committee on Chemical Physics

1998

This thesis entitled:
The X_2^- Files: Modeling Photodissociation of Molecular Ions in Clusters
written by James R. Faeder
has been approved for the Committee on Chemical Physics

Robert Parson

W. Carl Lineberger

Date

The final copy of this thesis has been examined by the signatories, and we find that both the content and the form meet acceptable presentation standards of scholarly work in the above mentioned discipline.

Faeder, James R. (Ph.D. Chemical Physics)

The X_2^- Files: Modeling Photodissociation of Molecular Ions in Clusters

Thesis directed by Associate Professor Robert Parson

A model is developed to study the photodissociation dynamics of molecular ions in clusters and condensed phases. The excess charge on the dissociating solute molecule couples strongly to the surrounding solvent, so that the direction and magnitude of charge flow in the excited state becomes critical to the dynamics. An accurate description of the charge flow is given by an effective Hamiltonian for the ground and excited electronic states of the solute that includes the strong solute-solvent coupling. The electronic structure of the isolated solute molecule is determined using high-level ab initio calculations, and the resulting eigenstates are used along with spectroscopic data to parameterize the solute-solvent interactions. The solvent-solvent interactions are handled using empirical potentials. Electronic relaxation of the excited solute molecule occurs via radiationless transitions between the strongly coupled solute electronic states. The complete nonadiabatic dynamics are modeled using classical trajectories that evolve on a single adiabatic electronic potential surface at a time with hopping between surfaces determined by a semiclassical algorithm.

The model is applied to study the photodissociation of dihalide anions within molecular clusters, and detailed comparisons with experiments are given. For both $I_2^-Ar_n$ and $I_2^-(CO_2)_n$ the model gives good agreement with experimental branching ratios for dissociation versus recombination. The role of anomalous charge flow in the excited state, in which the excess charge lo-

calizes on the less solvated atom, is demonstrated in $I_2^-Ar_n$ by the ejection of bare and weakly-solvated I^-. There is an even more dramatic effect in $I_2^-(CO_2)_n$ photodissociation, where the coupling between anomalous charge flow and the solvent funnels trajectories to a narrow region on the potential energy surface where they undergo nonadiabatic relaxation. Simulations of time-resolved photoelectron spectra also give excellent agreement with experiment, and demonstrate that the model correctly describes the time scales for dissociation, recombination, and vibrational relaxation. Preliminary application to $ICl^-(CO_2)_n$ clusters demonstrates the importance of asymmetric solvation for the dissociation dynamics. These and other applications currently in progress demonstrate the many insights into the fundamental chemistry of photodissociation that can be gained with this model.

in memory of my grandmother Estelle.

Acknowledgements

Many people have helped me along my 6 1/2 year journey through graduate school. The project described in this thesis is the result of a group effort. After John Papanikolas did the initial simulations, Paul Maslen, Nikki Delaney, and I have worked to expand his model in the hopes of gaining further insights. This has proved a very difficult task, because whatever sophistication John's simulations lacked were more than made up for by his keen understanding of both the experiments and the underlying physics. Over the years, we in the second generation of modelers have benefited greatly from the sage advice of this old warrior.

This project would never have happened without Paul Maslen. From his whirlwind of ideas emerged the foundations of our model. His expertise in performing electronic structure calculations was also vital, and, for better or for worse, much of his computer code still lurks in the vast underworld of the modeling program. From his opinionated ramblings on current events to his tall tales of mountain adventures, Paul has also been a fun guy to work with. I would like to thank him especially for his thorough reading of this thesis, which has improved both the accuracy and clarity.

Nikki Delaney has also been a major contributor to this project and a good friend. In the past year of working together we have gained more insights than in all my previous years on the project. Our very different backgrounds

and views of the world have accelerated this process of discovery and have sparked many interesting conversations.

Robert Parson has been a great advisor in all the best senses of the word. His breadth and depth of knowledge is tremendous, from chemistry to European history, and I have learned a great deal from him over the years. He has been a patient and encouraging teacher throughout my career. At the same time he has not been afraid to give me the little push I needed to maintain my focus. Robert has also been an excellent editor of my writing, and this thesis owes a great deal to his helpful criticisms and suggestions.

For the problems studied in this thesis, modeling and experiments are intertwined, and we have benefited greatly from our experimental collaborators. Carl Lineberger deserves special thanks not only because of his enthusiasm and support, but also for his foresight and perseverance in studying the systems we model. John Papanikolas has been the ultimate "inside man," because of his intimate knowledge of both the simulations and the experiments. Both Carl and John have such extraordinary insight that in years of modeling it has always been hard to discover something they did not already know, or had at least considered. Many other members of Carl's group have also helped along the way: Vasil Vorsa, Maria Nadal, Sreela Nandi, Paul Campagnola, Doo Wan Boo, and Andrei Sanov all deserve thanks. In the past year our collaboration with Dan Neumark's group at Berkeley has also been both fruitful and enjoyable. I would also like to thank his students Jeff Greenblatt and Martin Zanni, with whom I have shared many interesting conversations on subjects as diverse as photoelectron spectroscopy and vegetables.

I have had many great teachers here at CU, and they also deserve special thanks. David Nesbitt and Chris Greene demystified quantum mechanics

for me. Both my advisor, Robert, and Paul Beale taught excellent statistical mechanics courses. All of my professors at CU have been supportive and helpful to me on a wide range of subjects.

The support staff at JILA also deserve special thanks for making it a more cheerful and professional environment in which to work. The computing staff in particular have been helpful, patient, persistent, and generally fun to be around. Thanks to Chela Kunasz, Anne Hammond, Ralph Mitchell, Joel Frahm, and Alan Dunwell!

In addition to my coworkers and collaborators, I would like to thank my other friends in graduate school: Bill Chapman, Scott Davis, John Farrell, Rudi Horne, Chris Myatt, Roger Sommer, Holger Vömel, Ondrej Votava, Miles Weida, Paul Winter (hang in there, Paul, it's almost over!), and many others.

I would also like to thank my parents, grandparents, and many other family members who have comforted me during this long journey and given me the occasional helpful nudge. I thank my parents in particular for instilling in me a love of learning and a dedication to doing things right that have carried me throughout my education. I also wish to remember my grandmother Estelle, a person whose inquisitive spirit and tireless capacity for reason have always inspired me. It is sad to me that she did not live to see the day when I completed my Ph.D., but, like all the others who have supported me through this 6 1/2 years, I am sure she had no doubt that the day would finally come.

Last, but most important, I would like to thank my fiancé, Sarah Gallagher, who has supported and encouraged me through the long process of completing this work. Our five years together, running parallel with my thesis research, have been a time of learning, exploration, and most of all fun, allowing me to approach my work from feelings of happiness and fulfillment.

Contents

Chapter

Figures

Figure

Tables

Table

Chapter 1

The X_2^- Files

"The truth is out there."

"Trust no one."

These two mantras from the popular television show "The X Files" have inspired the work presented in this thesis. It is not that I feel there is a high-level government conspiracy to thwart our research on the photodissociation dynamics of molecular ions in clusters—although it has at times seemed like there was a low-level conspiracy to deny it funding. Rather, I have drawn inspiration from the idea that fundamental truths lay waiting for discovery in these systems, truths of which experimental studies have given only a tantalizing glimpse. Through the window of molecular simulation, I hoped to develop a complete picture of these simple chemical reactions, which offer to tell us a great deal about how the strong interactions between a solute and its surrounding solvent affect chemistry. The raging paranoia expressed by the second slogan is a reminder that biases from the past often cloud our interpretation of new information, and to find truth we must open ourselves to new interpretations, no matter how crazy they seem at first.

The characterization of photodissociation dynamics in many different solvated environments—clusters, liquids, and solid matrices—is an ongoing

focus of major research. As our experimental knowledge of these systems grows, so too does the need for theoretical insight, and modeling has become a nearly equal partner in the efforts to understand these complex dynamics. The goal of this thesis is to provide a complete model for the photodissociation dynamics of a diatomic ion inside a molecular cluster or other solvated environments.

Figure 1.1 illustrates the photodissociation of a dihalide anion, I_2^-, inside a small cluster of atoms. The curves represent the potential surfaces of the isolated molecule, which serve as an approximate indication of the forces experienced by the dissociating molecule. Following excitation to a repulsive state, the iodine atoms fly apart and begin to encounter the surrounding atoms. In some cases, the momentum for dissociation is too great for the solvent to overcome, and solvated atomic fragments are produced. In other cases, the solvent atoms arrest the dissociating fragments, producing recombination on one of the two lower potential surfaces. The last step in Fig. 1.1 illustrates an important difference between photodissociation dynamics in clusters and in the condensed phases. In clusters, evaporation of the solvent atoms from the cluster dissipates the energy released by the photoexcitation and stabilizes the recombined products. In continuous media, the energy is dissipated through the excitation of low frequency phonon modes, or soundwaves.

The size of the solute-solvent interactions is greatly magnified in ionic systems by the presence of excess charge on the solute. One key feature that differentiates photodissociation dynamics in neutral and charged species is the flow of the excess charge within the solute (also shown in Fig.1.1), which is strongly coupled to the motion of the solvent. In diatomic ions there is a competition between the bonding forces, which tend to spread the charge over the solute molecule, and the charge-solvent interactions, which favor localization

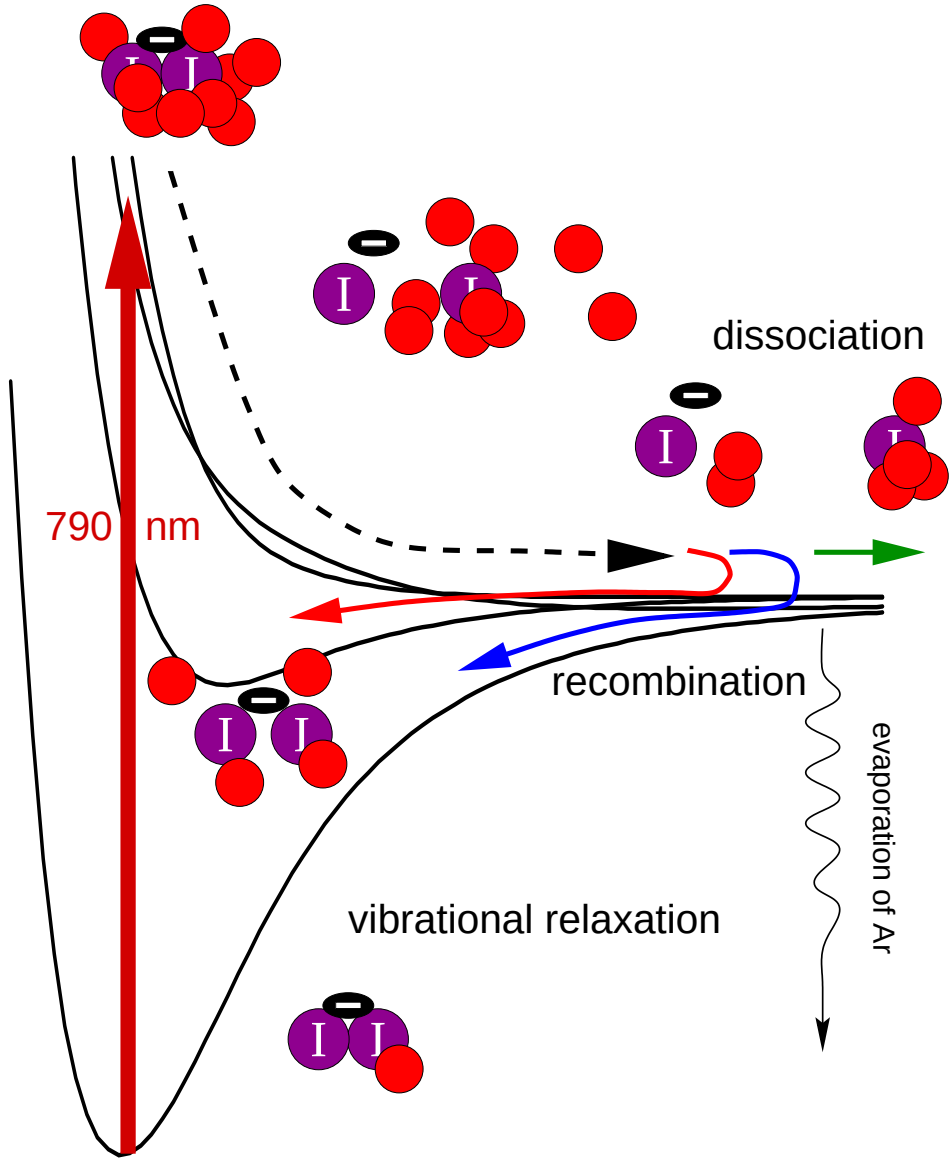

Figure 1.1: Photodissociation of I_2^- inside a small atomic cluster. Evaporation of the solvent atoms or molecules is the key mechanism for dissipating the energy released as the solute dissociates and relaxes.

of the charge onto a single atom. As the solute dissociates, the localization of charge drives the solvent towards the nascent atomic ion. At the same time, this asymmetric reorganization of the solvent begins to exert a strong polarizing force on the solute. An unexpected outcome of this interplay between solute charge localization and solvent reorganization is illustrated in Fig.1.1, where the charge, which is shared equally at the start of dissociation, flows onto the less solvated iodine atom, a consequence of the particular properties of the excited electronic state. In some cases, this *anomalous* charge flow results in the surprising escape of a bare I^- ion from the cluster, just one example of the many complex behaviors exhibited by these systems.

Anomalous charge flow arises when the electronic state of the molecule has a strongly antibonding character, as illustrated in Fig. 1.2. Consider a molecule with two electronic states, $X^- \cdots X$ and $X \cdots X^-$. In the absence of solvent molecules, the bonding interactions give rise to a delocalized charge distribution in both the bonding and antibonding states, $X\cdot\bar{\cdot}\cdot X$. At long bond lengths these two states become degenerate. This degeneracy is lifted by solvating one end of the molecule: the ground state is $SX^- \cdots X$ and the excited state $SX \cdots X^-$, where "S" denotes the solvent. At shorter bond lengths the solvent polarizes the solvent charge distribution to an extent that depends on the strength of the solute-solvent interaction relative to the bonding interaction. The direction of polarization depends on the electronic state. In the ground state the charge flows toward the more solvated end, $SX\cdot\overleftarrow{\cdot}\cdot X$, while in the excited state the charge flows toward the less solvated end, $SX\cdot\overrightarrow{\cdot}\cdot X$, the anomalous charge flow. It can also be said that this excited state has negative polarizability. In real molecules, the magnitude and direction of the excited state polarizabilities depends on the details of the solute electronic structure,

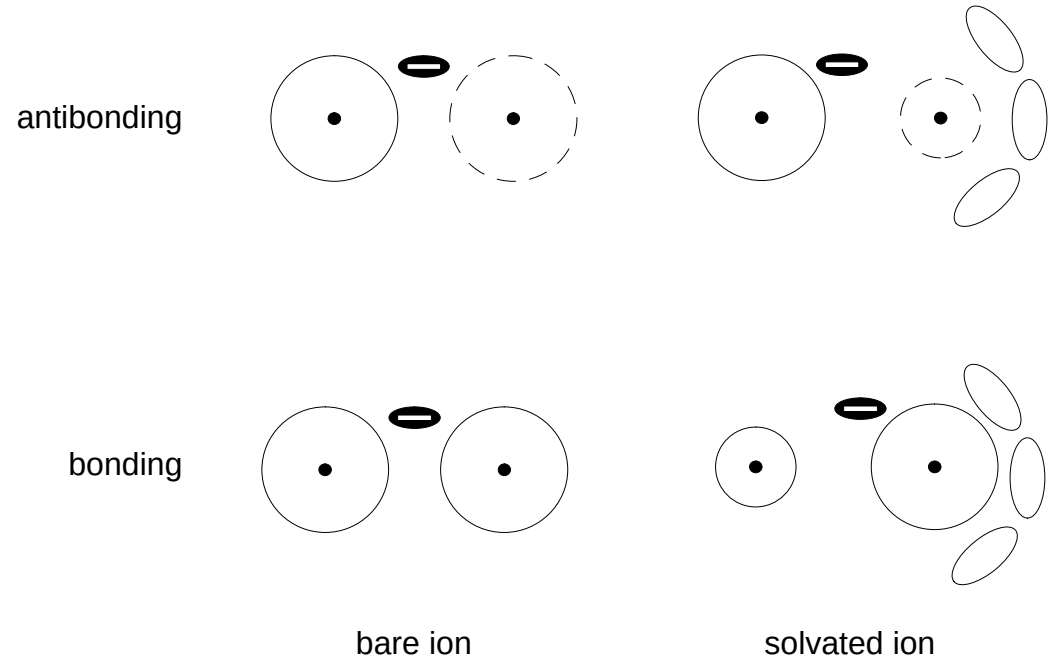

Figure 1.2: Anomalous charge flow in a diatomic molecular ion. In the bare ion the charge is shared equally between the two nuclei in both bonding and antibonding states. When solvation is asymmetric, the charge localizes on the more solvated atom in the ground electronic state, leaving less charge density on this atom in the excited state.

which in the halogens is affected by strong spin-orbit coupling.

This discussion demonstrates the need for a sophisticated model to understand the dynamics of photodissociation of charged species. Because of the strong interactions between solute and solvent, the model must describe how the excited state solute electronic structure is affected by the solvent, which is what gives rise to charge flow. A method for handling the complex curve crossings that precede recombination in the lower states is also required. In clusters, the solute-solvent interactions must be handled at a molecular level, since the dielectric continuum treatment, which has often been used to simplify these interactions in the condensed phase, is inappropriate for the highly inhomogeneous solvent configurations that arise.

The remainder of this chapter provides greater context for the development of the model presented in this thesis. Section 1.1 presents a brief review of the work on I_2 photodissociation, and is followed by a description of the experiments that have characterized dihalide anion photodissociation. Section 1.3 reviews previous attempts to model dihalide anion photodissociation, which have focused on I_2^- and Br_2^-. Finally, Sec. 1.4 presents an overview for the remainder of the thesis, describing the model for photodissociation and its applications to a number of different systems studied by experiment.

1.1 Caging in I_2 Photodissociation

The recombination of photodissociated I_2 in solution was first observed in the early 1930's by Franck and Rabinowitch, who called this process the "cage effect" [1]. Later, Noyes and coworkers carried out systematic studies of the effect of excitation wavelength and solvent viscosity on the recombination rate [2–5]. The first time-resolved measurements of I_2 caging in solution were made by Eisenthal and coworkers using picosecond lasers [6]. In this experiment a pump pulse excites I_2 to the B state, which predissociates, eventually leading to geminate recombination in the ground state. The time scale for recombination was measured by monitoring the absorption of a probe pulse, which was time-delayed from the pump. Following photoexcitation, they observed a transient bleach in the probe absorption over the first 20 ps, followed by a partial recovery of the absorption over 100–200 ps. Although the basic picture of dissociation, caging, and recombination used to interpret these experiments was correct, the idea that the absorption recovery was monitoring the rate of diffusively-controlled recombination was later found to be incorrect.

In 1982, Nesbitt and Hynes [7] showed that time scale for absorption recovery could be accounted for primarily by the slow vibrational relaxation of I_2 in its ground electronic state. The view of the dissociation dynamics that has come to be accepted has been described in the review of Harris et al. [8]. Caging and electronic relaxation to the ground state take place on a rapid time scale of less than 2 ps and are followed by a slow vibrational relaxation spanning a range of 50 ps to several nanoseconds depending on the solvent. The initial misinterpretation of the picosecond experiments made the important point that theoretical modeling is required to make a definitive interpretation of these kinds of experiments.

A new generation of femtosecond experiments on I_2 dissociation is aimed in part at observing coherent vibrational motion of the dissociating molecule. Several experiments have observed coherent recoil of I_2 from the solvent molecules in clusters [9, 10] and rare gas matrices [11, 12], and very recently in gas phase collisions [13]. Perhaps somewhat surprisingly, coherent motion has not been observed in studies of high pressure gases and liquids [14–17]. In all of the systems where it has been observed, coherent motion of I_2 has been confirmed by molecular dynamics modeling [18, 19].

Models of I_2 dissociation in clusters and condensed phases have proliferated and been successful in large part because the molecular interactions can be described by relatively simple pair potentials. The gas phase potential curves of I_2 have been well-characterized by spectroscopy [8]. The use of pair potentials to study atomic and molecular fluids is also well established [20]. The key to the success of simple models, however, has been the ability to treat the electronic structure of I_2, which itself is rather complicated, as separable from the solute-solvent interactions. The underlying reason for this separa-

bility is that the electrostatic nature of the molecule changes very little upon dissociation or electronic excitation—there is no significant flow of charge for example—so that the coupling between the solute and solvent is weak. Another reason for the success of simple models is that the dynamics of primary interest in the experiments, namely vibrational relaxation, occurs on a single adiabatic potential surface, so that the difficult issue of nonadiabatic transitions does not have to be confronted directly.

Despite the relatively weak coupling between I_2 and its surroundings, there are a number of problems in I_2 dynamics for which adiabatic pair potentials are not adequate. One surprising finding was that a single argon atom clustered with I_2 can be sufficient to bring about caging—the "one-atom cage effect" [21, 22]. The origin of this effect has been the subject of ongoing controversy, in which solvent-induced nonadiabatic couplings have been implicated as a likely mechanism [23–25]. In larger clusters, liquids, and matrices, the dynamics on the sub-picosecond time scale following photoexcitation to the B state are strongly affected by nonadiabatic transitions to predissociative states. Modeling these nonadiabatic dynamics requires a method for determining the electronic coupling induced by the solute-solvent interactions. An interaction model for halogen–rare-gas interactions has recently been developed using the diatomics-in-molecules approach [25, 26] and used to simulate nonadiabatic dynamics of I_2 photodissociation in argon clusters [25], liquid xenon [26], and solid rare-gas matrices [27]. In conjunction with the recent femtosecond experiments, these simulations should greatly enhance our understanding of the role solute-solvent coupling plays in the early time dynamics following photoexcitation.

1.2 Experiments on Dihalide Anion Photodissociation

Photodissociation reactions involving charged species involve much stronger interactions between the solvent and solute than those involving neutral species. As we saw in Fig. 1.1 and the discussion that followed, the electronic structure of the dissociating solute is strongly coupled to solvent motion. Electronic relaxation from the initially excited state to a lower state in which recombination can occur involves not only a curve crossing, but also a fundamental change in the character of the solute wave function, which can be brought about through electron transfer or solvent rearrangement. Understanding the process of dissociation and recombination in ionic systems may thus provide key insights on the interplay of solute-solvent interactions affecting far more complicated chemical reactions.

There is also a more practical reason for the recent interest in clusters with ionic chromophores, which is that mass spectrometry may be used to select specific reactant sizes and provide a detailed analysis of the products. Systematically varying the size of the reactant cluster produces a detailed microscopic picture of the effect solvent molecules exert on the reaction under study. It is often said that cluster properties provide a bridge between the behavior of the reactants in the gas phase and in continuous media, and it is true that reaction dynamics in even small clusters may resemble those in condensed phases, a good example of which is the one-atom cage effect alluded to earlier. Reaction dynamics in clusters may also exhibit unique behaviors, which are interesting in their own right and test our understanding of the fundamental interactions between solute and solvent. The ejection of less solvated I^- shown in Fig. 1.1 and discussed more extensively in Chapter 5 provides a

good example.

Photodissociation of the dihalide anion I_2^- is illustrated in Fig. 1.3. Several experiments on caging of $Br_2^-(CO_2)_n$ and $I_2^-(CO_2)_n$ clusters carried out by Lineberger and coworkers [28, 29] posed a simple question: what is the effect of microsolvation on the rate of recombination? This question was addressed by measuring the branching ratios for dissociation and recombination as a function of cluster size from the bare ion up to clusters with as many as several dozen CO_2 molecules, enough to form far more than a complete solvent shell around the anion. The major finding of these studies was that the caged fraction rises very rapidly as a function of cluster size, becoming unity by the completion of the first solvation shell [28, 29], $n = 13$ for Br_2^- and $n = 16$ for I_2^-. This was a surprising result given that between 30 and 90% of I_2 dissociates in solution [8], and is perhaps even more surprising in light of the later finding that as much as 40% of I_2^- dissociates when excited at the same wavelengths in polar solvents [30]. The rapid onset of caging in these clusters has been attributed to the strong electrostatic interactions between the solute anion and the CO_2 molecules, although there is so far no explanation for the difference between the cluster results and those in solution.

Subsequent experiments by the Lineberger group have characterized the photodissociation of I_2^- in clusters with a variety of other solvent molecules [31–35] and of the heteronuclear ICl^- in CO_2 clusters [36]. The results for argon have so far been the best characterized and the most interesting. Besides the rapid onset of caging and the observation of complete caging by the closure of the first solvation shell, two new phenomena were observed: recombination in an excited electronic state and the ejection of minimally solvated I^- ions. Although the products of these two phenomena were evident from the original

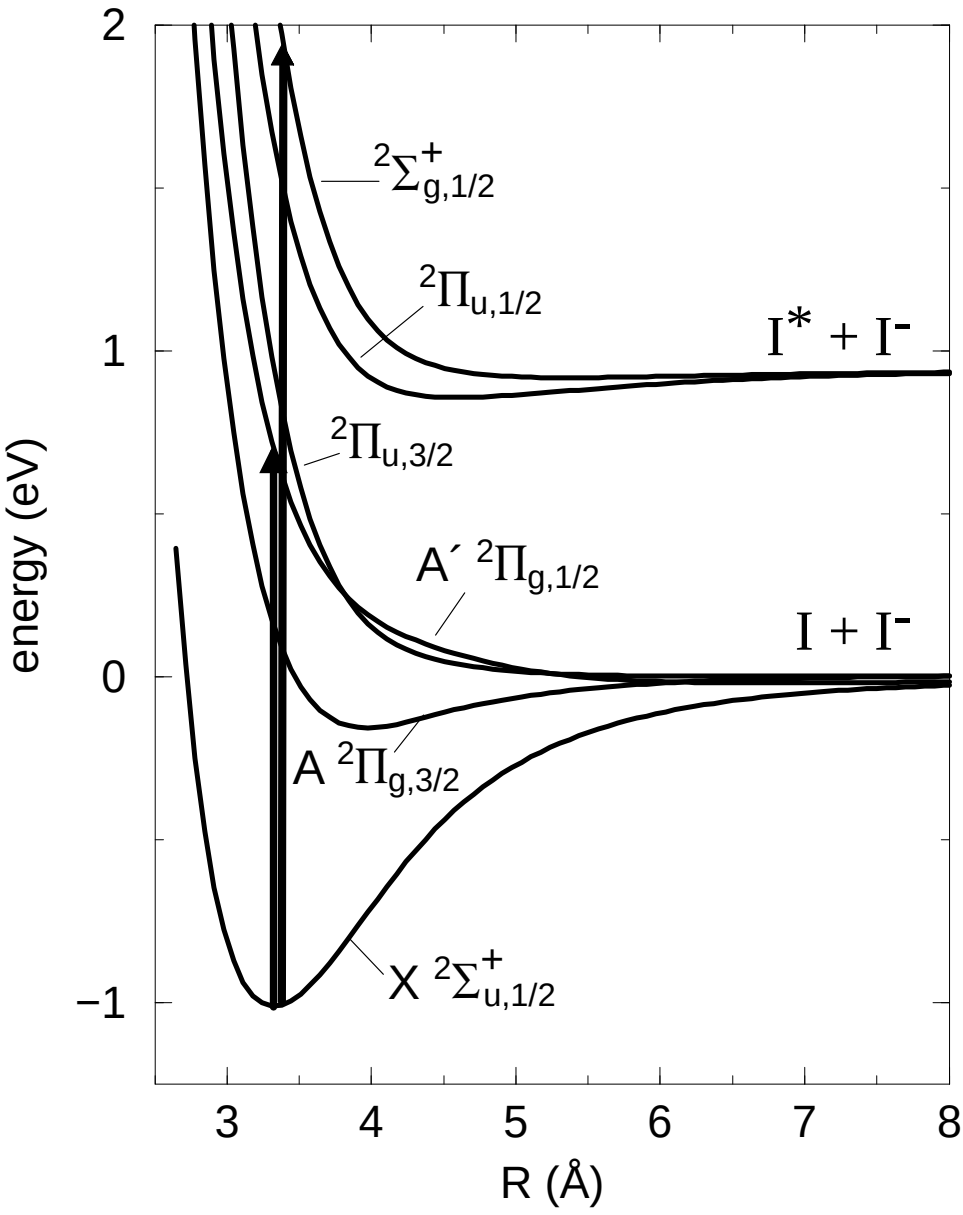

Figure 1.3: Photodissociation of I_2^- on the gas phase potential curves. The shorter arrow illustrates the IR excitation used in most of the photodissociation studies, while the longer arrow indicates the recently studied UV excitation.

experiments, the processes giving rise to them were unambiguously identified afterwards through modeling [27, 37] and time-resolved experiments [38]. The caging fractions in ICl^- photodissocation also revealed an unexpected result: a rapid increase in caging with cluster size suddenly peaked at $n = 5$ and then rapidly decayed to zero [36]. Solvated Cl^- ions are the only product of ICl^- photodissociation for n larger than 10. A possible explanation for this behavior based on simulation results is given in Chapter 8.

Lineberger and coworkers have also carried out time-resolved pump-probe experiments of I_2^- photodissociation in clusters [32, 33, 39–43]. The overall recovery of the probe absorption is much more rapid than for I_2 in solution for all the solvent molecules that have been studied, with the exception of argon. The time scale for complete absorption recovery is about 10 ps for a complete solvent shell of CO_2, OCS, and N_2O, but on the order of 200 ps for argon. An explanation for this difference in terms of the much weaker binding energy of the argon solvent has been given [44] and is discussed in Chapter 6. The most dramatic result of the pump-probe experiments has been the observation of a peak at 2 ps in the absorption recovery, which has been attributed to coherent recombination on the A state (see Fig. 1.3) [41, 42]. This bump appears at similar times in CO_2, OCS [45], and N_2O [35], but is absent in argon [43]. Barbara and coworkers [30, 46–48] have also observed this phenomenon on the same 2 ps interval in solution, and have supported the assignment of recombination in the excited state using UV probe measurements [30]. The fact that the bump disappears in the UV probe absorption suggests that the bump does not arise from probe absorption near the bottom of the ground state well. Despite this additional evidence, the assignment of the bump to coherent recombination in an excited state remains unproven given

the tremendous uncertainties in the spectroscopy of solvated I_2^- at long bond lengths or in excited states. Banin et al. have also observed coherent vibration of I_2^- in its ground electronic state following photodissociation of I_3^- [49–53].

A method for studying photodissociation in ionic clusters using femtosecond photoelectron spectroscopy (FPES) has recently been developed by Neumark and coworkers [38, 54]. This technique uses a probe that detaches the excess electron from the photoexcited cluster. By measuring the kinetic energy of the detached electrons, Neumark and coworkers determine the electron affinity of the transient species, which is sensitive both to chemical bonding interactions within the solute and to interactions between the solute and solvent. FPES experiments on $I_2^-Ar_6$ have characterized the dynamics of direct dissociation, while the spectra from $I_2^-Ar_{20}$ photodissociation directly track the dynamics of electronic and vibrational relaxation. The $I_2^-Ar_{20}$ measurements confirmed the Lineberger group's observation of long-lived recombination in an excited electronic state. The most recent FPES studies on $I_2^-(CO_2)_n$ [55] demonstrate the importance of charge flow in the dissociation of relatively small clusters ($n = 4$), where the results of this thesis (see Chapter 7) imply that the charge localizes onto the less solvated iodine atom, but I^- is prevented from escaping by its strong attraction to the solvent. Evidence for the transient formation of a less solvated I^- ion, which is subsequently captured by the solvent, was seen in the spectral evolution. In $I_2^-(CO_2)_{16}$ the spectra revealed time scales for transient I^- formation following dissociation, and for recombination and vibrational relaxation. In addition there was some evidence for transient recombination on the A state on a 2–4 ps time scale, but a definitive assignment could not be made.

Lineberger and coworkers have also recently studied photodissociation

of I_2^- in the UV [34], where the excited state correlates to $I^- + I^*$, spin-orbit excited iodine (see Fig. 1.3). An interesting result of these experiments is that a relatively small number of solvent molecules, less than a full solvation shell, is able to cage this highly excited state and induce electronic relaxation down to the ground electronic state of I_2^-. This is a large solvent effect, given that the spin-orbit splitting of atomic iodine is about 1 eV. It is also a surprising result considering that collisional deactivation of I^* is very inefficient in the gas phase [56]. The model described in this thesis also predicts this relaxation in CO_2 clusters (which has yet not been experimentally observed) and indicates that state-dependent charge flow is the key to the mechanism [57].

1.3 Simulations of Dihalide Anion Photodissociation

As the problems with interpreting the early I_2 experiments in solution pointed out, understanding experimental studies of photodissociation requires theoretical modeling. This is perhaps even more true for the dihalide anion experiments where the solute-solvent interactions are much stronger and greatly alter the electronic structure of the dissociating molecule. Because of the large differences between the neutral and ionic systems, intuition developed from experiments on I_2 can be misleading, as we will see below. Experience has shown that molecular modeling is one of the best methods available for developing an understanding of previously unexplored dynamics. An accurate model also allows study of the systems in ways that cannot be explored directly by experiments.

The first simulations of dihalide anion photodissociation were performed by Amar and Perera, who examined Br_2^- dissociation in argon and

CO_2 clusters. Until very recently, these were the only studies to examine in detail the processes of dissociation and recombination; most subsequent studies have focused exclusively on the dynamics of vibrational relaxation. Amar and Perera modeled charge flow by assigning a partial charge to each bromine atom that varied as a function of the bond length: as the molecule dissociated the charge on one atom decayed to zero while the charge on the other atom increased to -1. There was an ambiguity in the model in deciding which atom the charge should localize onto. Amar and Perera identified two cases: one in which the charge localized onto the more solvated atom, which in subsequent work [58] has been called "normal" charge switching, and another in which the charge localized on the less solvated atom—which has been called "anomalous" charge switching. They found that the dissociation dynamics and the caging fraction, particular for clusters with only about half a solvation shell, differed greatly for the two charge switching cases. They also found that the dynamics were quite sensitive to the choice of switching function, which was picked somewhat arbitrarily because they had no direct knowledge of the electronic structure of the dissociating molecule. The major limitation of their model was that because the charge switching depended only on the solute bond length, the solvent had no direct effect on the solute electronic structure—it could not polarize the dissociating anion.

Despite the limitations of the model, the early studies by Amar and Perera have made several important contributions to our understanding of photodissociation dynamics. First, they showed the importance of structural caging, in which atoms or molecules at the "cap" positions, i.e. along the solute bond axis, act as a particularly efficient caging mechanism. Second, and more importantly, they identified the important role of charge flow in determining

the dynamics of dissociation and caging. Their suggestions for improving the model for the anion electronic structure by incorporating ab initio calculations and a more sophisticated charge distribution greatly influenced the course of the work reported in this thesis. Finally, they recognized the possible importance of extended nonadiabatic coupling and suggested using a semiclassical model to treat the nonadiabatic dynamics, another essential feature of the model adopted in this thesis. Despite their many insights into the problem of modeling anion photodissociation, Amar and Perera mysteriously gave up on the problem, leaving future modeling to others more closely associated with the experiments.

Picking up where Amar and Perera left off, Papanikolas and coworkers [42, 58, 59] developed a more extensive model for the photodissociation of $I_2^-(CO_2)_n$ clusters. Their major improvement to the previous model was to allow the solute electronic structure to respond directly to the solvent through a two-dimensional charge-switching function. This was motivated in part by their finding that the simple bond-length-dependent charge-switching function used in previous studies prevented the I_2^- from recombining, a result that was clearly unphysical. In the spirit of electron transfer theory, they defined a one-dimensional "solvent coordinate" and used ab initio calculations of I_2^- in a uniform electric field to fit the charge-switching function as a function of the bond length and the solvent coordinate. Because of the complexity of the excited state electronic structure, they decided only to model the ground electronic state in this way and focus on studying the effect of charge flow on vibrational relaxation. Simulations of the excited state dynamics used the ground state charge switching function and were intended only as a means of preparing an initial ensemble at the top of the ground state well for modeling

the subsequent vibrational relaxation. Their findings, supported by subsequent modeling of I_2^- vibrational relaxation by Benjamin et al. in polar liquids [60], were that charge flow leads to very rapid vibrational energy transfer in the upper portion of the ground state well and that the overall rate of vibrational relaxation was very fast, on the order of 1 ps [42, 58]. Given that the overall rate for the absorption recovery was on the order of 10 ps, they suggested that the recombination times in I_2^- were substantially longer than the vibrational relaxation—a reversal of the behavior in the I_2 system, where vibrational relaxation was always the rate-limiting step.

An alternative point of view has been presented by Barbara and coworkers, who have modeled I_2^- vibrational relaxation in solution and the resulting pump-probe spectra [30]. They have suggested that because of the Franck-Condon factors only the lowest few vibrational states make substantial contributions to the absorption recovery, which is thus primarily sensitive to vibrational relaxation at the bottom of the I_2^- well. This explanation requires that the vibrational relaxation is highly nonexponential and proceeds at a much faster rate at high vibrational energies, which is consistent with both the Papanikolas [42, 58] and Benjamin [60] studies. Their model also assumes that the recombination dynamics and initial steps of vibrational relaxation (up to 50% of the total vibrational energy) occur on a time scale of less than 300 fs. The differences in the recombination dynamics proposed for the liquid and cluster studies possibly reflect the differences in dynamics between the two media, likely a result of the much greater density in the liquid. So far, however, there have been no simulations of the dissociation process in the liquid, so there is no additional evidence to suggest that 300 fs represents a plausible time scale for recombination and substantial vibrational relaxation to take place (the cluster

simulations clearly preclude this possibility). In fact the absorption recovery, including the placement of the coherent bump at 2 ps, occurs on similar time scales in both the clusters and liquids. It is therefore quite possible that the photodissociation dynamics are more similar than has been suggested, and this is certainly an area where more extensive modeling would be very useful.

Models of I_2^- in liquids have focused entirely on vibrational relaxation in the ground state. Benjamin and Whitnell studied vibrational relaxation of I_2^- in ethanol and water using molecular dynamics simulations with a fixed charge model [61]. Hynes and coworkers have developed a two-state valence bond model to study the effect of charge flow on the rate of vibrational relaxation [62, 63]. A simplified version of this model was used by Benjamin et al. [60] in molecular dynamics simulations, which found that the highly nonexponential relaxation was a direct result of including the adiabatic charge flow. As in the work of Papanikolas et al., simulations on the excited state were used solely to provide initial conditions for the study of vibrational relaxation. Ladanyi and Parson [64] have also recently studied vibrational relaxation in $I_2^-(CO_2)_n$ clusters using the Papanikolas model with a CO_2 model that allows bending and found that the vibrational relaxation is only weakly affected by the addition of intramolecular flexibility in the solvent.

Although the role of charge flow in dihalide anion vibrational relaxation is now well established, many questions remain unanswered about the role of charge flow in the dynamics of caging and recombination. To date no simulations have demonstrated the coherent excited state recoil that is hypothesized to produce the bump at 2 ps. The rapid onset of caging with cluster size was only partially explained by the work of Amar and Perera. There also remains controversy about the time scales for the caging and recombination

in clusters vs. solution, as well as the unexplained observation of only partial caging in solution. No simulations of ICl^- photodissociation with its unexpectedly low caging fractions have so far been published. Understanding of the UV photodissociation experiments also requires a mechanism for the electronic relaxation of the states dissociating to $I^- + I^*$.

1.4 Thesis Overview

It is clear from the previous simulations that a model to answer these and other unresolved issues in dihalide anion photodissociation must extend previous treatments in the following ways. First, there must be a complete model for the electronic structure of the solute interacting with the solvent in a state-dependent manner. Second—a requirement not explicitly mentioned above—because of the excess charge the electronic polarization of the solvent molecules must be included in the model to give realistic interaction potentials. Some previous models have included the solvent polarization, but none have combined this with an accurate description of the excited state electronic structure. Finally, the model must go beyond an ad hoc treatment of the nonadiabatic or surface-hopping dynamics. The work described in this thesis represents the most comprehensive effort to develop such a model for the dihalide anions.

During the course of this development, Batista and Coker [27] reported the first nonadiabatic simulations of photodissociation in $I_2^-Ar_n$ using a semiempirical model for the electronic structure that, while simpler than the model described here, reproduced the essential dynamics that are also observed in our model. While this was in some ways disappointing, the fact that two in-

dependent approaches produced similar results has increased the confidence in both models. At the same time, their study left open the need to develop new concepts and approaches to understand the complex nonadiabatic dynamics, which has been a major focus of our work.

The remainder of this thesis is organized as follows. Chapters 2–4 discuss the model we have developed to simulate photodissociation of dihalide anions. Chapter 2 describes a general Hamiltonian used to determine the electronic structure of a manifold of solute states in the presence of strong solute-solvent interactions. Chapter 3 then discusses how this Hamiltonian is evaluated for the dihalide anions interacting with CO_2 and argon, and discusses generalizations to other solvent molecules. Chapter 4 describes how the dynamics of photodissociation are computed on the the model potential surfaces using classical trajectories with surface-hopping to approximate the nonadiabatic dynamics. Chapters 5–8 present applications of the model to particular systems of interest—$I_2^-Ar_n$, $I_2^-(CO_2)_n$, and $ICl^-(CO_2)_n$. Chapter 5 describes simulations of $I_2^-Ar_n$ photodissociation, demonstrating the accuracy of the model and providing a definitive assignment of all the observed photofragments. Chapter 6 contains simulations of the time-resolved photoelectrons spectra from $I_2^-Ar_n$ photodissociation, which agree well with experiment and reveal time scales for dissociation, recombination, and vibrational relaxation in these clusters. Chapter 7 describes the first complete simulations of $I_2^-(CO_2)_n$ photodissociation and discusses the role of charge flow in the excited state dynamics. Finally, Chapter 8 presents structures for $ICl^-(CO_2)_n$ clusters and makes a preliminary assessment of their effect on the dissociation dynamics.

The bulk of this thesis describes the potential model and the methods used to calculate the dynamics, which is an accurate reflection of the time

I have spent working on this project. As I hope to show in the application chapters, the model has so far provided many insights into the dynamics of photodissociation. Collectively, however, these chapters represent more of a "proof of concept" for the model rather than a complete picture of the dynamics. Further study and development of the model is an ongoing process and should provide many more insights in the years to come.

References for Chapter 1

[1] J. Franck and E. Rabinowitch, Trans. Faraday Soc. **30**, 120 (1934).

[2] J. Zimmerman and R. M. Noyes, J. Chem. Phys. **21**, 2086 (1950).

[3] F. W. Lampe and R. M. Noyes, J. Amer. Chem. Soc. **76**, 2140 (1954).

[4] D. Booth and R. M. Noyes, J. Amer. Chem. Soc. **82**, 1868 (1960).

[5] L. F. Meadows and R. M. Noyes, J. Amer. Chem. Soc. **82**, 1872 (1960).

[6] T. Chuang, G. Hoffman, and K. Eisenthal, Chem. Phys. Lett. **25**, 201 (1974).

[7] D. J. Nesbitt and J. T. Hynes, J. Chem. Phys. **77**, 2130 (1982).

[8] A. L. Harris, J. K. Brown, and C. B. Harris, Ann. Rev. Phys. Chem. **39**, 341 (1988).

[9] Q. Liu, J.-K. Wang, and A. H. Zewail, Nature **364**, 427 (1993).

[10] J.-K. Wong, Q. Liu, and A. H. Zewail, J. Phys. Chem. **99**, 11309 (1995).

[11] R. Zadoyan, Z. Li, P. Ashjian, C. Martens, and V. Apkarian, Chem. Phys. Lett. **218**, 504 (1994).

[12] R. Zadoyan, Z. Li, C. Martens, and V. Apkarian, J. Chem. Phys. **101**, 6648 (1994).

[13] C. Wan, M. Gupta, J. Baskin, Z. Kim, and A. Zewail, J. Chem. Phys. **106**, 4353 (1997).

[14] Y. Yan, R. Whitnell, K. Wilson, and A. Zewail, Chem. Phys. Lett. **193**, 402 (1992).

[15] C. Lienau, J. Williamson, and A. Zewail, Chem. Phys. Lett. **213**, 289 (1993).

[16] C. Lienau and A. Zewail, Chem. Phys. Lett. **222**, 224 (1994).

[17] Q. Liu, C. Wan, and A. Zewail, J. Chem. Phys. **105**, 5294 (1996).

[18] Q. Liu, J.-K. Wong, and A. H. Zewail, J. Phys. Chem. **99**, 11321 (1995).

[19] Z. Li, R. Zadoyan, V. A. Apkarian, and C. C. Martens, J. Phys. Chem. **99**, 7453 (1995).

[20] M. P. Allen and D. J. Tildesley, *Computer Simulation of Liquids*, Claredon Press, Oxford, 1987.

[21] K. L. Sanger, G. M. McClelland, and D. R. Herschbach, J. Phys. Chem. **85**, 3333 (1981).

[22] J. Valentini and J. Cross, J. Chem. Phys. **77**, 572 (1982).

[23] M. L. Burke and W. Klemperer, J. Chem. Phys. **98**, 1797 (1993).

[24] O. Roncero, N. Halberstadt, and J. A. Beswick, in *Reaction Dynamics in Clusters and Condensed Phases*, edited by J. Jortner, R. D. Levine, and B. Pullman, Kluwer Academic, Dordrecht, 1994.

[25] A. A. Buchachenko and N. F. Stepanov, J. Chem. Phys. **104**, 9913 (1996).

[26] V. S. Batista and D. F. Coker, J. Chem. Phys. **105**, 4033 (1996).

[27] V. S. Batista and D. F. Coker, J. Chem. Phys. **106**, 7102 (1997).

[28] M. Alexander, N. Levinger, M. Johnson, D. Ray, and W. Lineberger, J. Chem. Phys. **88**, 6200 (1988).

[29] J. Papanikolas, J. Gord, N. Levinger, D. Ray, V. Vorsa, and W. Lineberger, J. Phys. Chem. **95**, 8028 (1991).

[30] P. K. Walhout, J. C. Alfano, K. A. M. Thakur, and P. F. Barbara, J. Phys. Chem. **99**, 7568 (1995).

[31] V. Vorsa, P. J. Campagnola, S. Nandi, M. Larsson, and W. C. Lineberger, J. Chem. Phys. **105**, 2298 (1996).

[32] V. Vorsa, *Photodissociation Dynamics of Mass-Selected Anions and Anionic Clusters*, PhD thesis, University of Colorado, 1996.

[33] M. Nadal, *The Study of the Photodissociation and Recombination Dynamics of Mass-Selected Cluster Ions: Solvent Effects on the Structure and Dynamics of the Ionic Chromophore*, PhD thesis, University of Colorado, 1996.

[34] S. Nandi, A. Sanov, N. Delaney, J. Faeder, R. Parson, and W. C. Lineberger, to be submitted.

[35] M. E. Nadal, S. Nandi, D. W. Boo, and W. C. Lineberger, J. Chem. Phys., submitted.

[36] M. E. Nadal, P. D. Kleiber, and W. C. Lineberger, J. Chem. Phys. **105**, 504 (1996).

[37] J. Faeder, N. Delaney, P. Maslen, and R. Parson, Chem. Phys. Lett. **270**, 196 (1997).

[38] B. J. Greenblatt, M. T. Zanni, and D. M. Neumark, Science **276**, 1675 (1997).

[39] D. Ray, N. Levinger, J. Papanikolas, and W. Lineberger, J. Chem. Phys. **91**, 6533 (1989).

[40] J. Papanikolas, V. Vorsa, M. Nadal, P. Campagnola, J. Gord, and W. Lineberger, J. Chem. Phys. **97**, 7002 (1992).

[41] J. Papanikolas, V. Vorsa, M. Nadal, P. Campagnola, H. Buchenau, and W. Lineberger, J. Chem. Phys. **99**, 8733 (1993).

[42] J. M. Papanikolas, *I_2^- Photodissociation and Cage Recombination Dynamics in Size-Selected $I_2^-(CO_2)_n$ Clusters*, PhD thesis, University of Colorado, 1994.

[43] V. Vorsa, S. Nandi, P. J. Campagnola, M. Larsson, and W. C. Lineberger, J. Chem. Phys. **106**, 1402 (1997).

[44] J. Faeder and R. Parson, J. Chem. Phys., in press.

[45] A. Sanov, S. Nandi, and W. C. Lineberger, J. Chem. Phys., in press.

[46] A. E. Johnson, N. E. Levinger, and P. F. Barbara, J. Phys. Chem. **96**, 7841 (1992).

[47] D. A. V. Kliner, J. C. Alfano, and P. F. Barbara, J. Chem. Phys. **98**, 5375 (1993).

[48] J. Alfano, Y. Kimura, P. Walhout, and P. Barbara, Chem. Phys. **175**, 147 (1993).

[49] U. Banin, A. Waldman, and S. Ruhman, J. Chem. Phys. **96**, 2416 (1992).

[50] U. Banin and S. Ruhman, J. Chem. Phys. **98**, 4391 (1993).

[51] U. Banin and S. Ruhman, J. Chem. Phys. **99**, 9318 (1993).

[52] U. Banin, A. Bartana, S. Ruhman, and R. Kosloff, J. Chem. Phys. **101**, 8461 (1994).

[53] U. Banin, R. Kosloff, and S. Ruhman, Chem. Phys. **183**, 289 (1994).

[54] B. J. Greenblatt, M. T. Zanni, and D. M. Neumark, Chem. Phys. Lett. **258**, 523 (1996).

[55] B. J. Greenblatt, M. T. Zanni, and D. M. Neumark, J. Chem. Soc. Faraday Trans., submitted.

[56] D. Husain and R. J. Donovan, Electronically excited halogen atoms, in *Advances in Photochemistry*, edited by J. N. Pitts, Jr, G. S. Hammond, and W. A. Noyes, Jr, volume 8, pp. 1–75, Wiley-Interscience, New York, 1971.

[57] N. Delaney, J. Faeder, and R. Parson, in progress.

[58] J. M. Papanikolas, P. E. Maslen, and R. Parson, J. Chem. Phys. **102**, 2452 (1995).

[59] P. E. Maslen, J. M. Papanikolas, J. Faeder, R. Parson, and S. V. ONeil, J. Chem. Phys. **101**, 5731 (1994).

[60] I. Benjamin, P. F. Barbara, B. J. Gertner, and J. T. Hynes, J. Phys. Chem. **99**, 7557 (1995).

[61] I. Benjamin and R. M. Whitnell, Chem. Phys. Lett. **204**, 45 (1993).

[62] B. J. Gertner, K. Ando, R. Bianco, and J. T. Hynes, Chem. Phys. **183**, 309 (1994).

[63] R. Bianco and J. T. Hynes, J. Chem. Phys. **102**, 7885 (1995).

[64] B. M. Ladanyi and R. Parson, J. Chem. Phys. **107**, 9326 (1997).

Chapter 2

Effective Hamiltonian for Solvated Molecular Ions

Recent experimental studies of the photodissociation of molecular ions in clusters [1–5] and in solution [6–12] have highlighted a central issue in chemical dynamics: the influence of solvation on chemical bonding and reactivity.[1] In these systems, as the solute ion dissociates the excess charge that was originally delocalized over the molecule localizes onto one atom. This intramolecular charge flow is closely coupled to the dynamics of the surrounding medium, since an asymmetric solvent environment favors a compact atomic charge distribution over a diffuse molecular one. The magnitude and direction of the charge flow also depends sensitively on the nature of the solute electronic wave function, as was discussed in Chapter 1. In bonding states the charge flows in the direction of greater solvation, while in antibonding states the charge flows toward the less solvated atom—in other words, the polarizability of antibonding excited states is negative [14–16]. Moreover, a typical open-shell ion contains several near-degenerate valence states which can be transiently populated by nonadiabatic transitions during the course of the dissociation. Classical trajectory simulations of these complex dynamics require an accurate description of both the ground and the excited electronic states of the solvated

[1] This chapter is a modified form of Ref. 13

ion at every time step. An accurate treatment of the excited states also requires that correlation between the solute electrons be included at a high level. Since full ab initio molecular dynamics is only feasible for the smallest clusters, a faster method must be devised. In this chapter an effective Hamiltonian for the solute electronic structure is derived from an ab initio description of the isolated solute wave function and an electrostatic model of the solute-solvent interactions.

A complete description of solvent-solute interactions must incorporate the electronic polarizability of the solvent molecules as well as their static charge distributions. This is critically important for solvents having no permanent moments at all, such as argon. The first theoretical studies to include solvent electronic polarizability were based on a dielectric continuum model of the solvent [17–23]. The most pertinent result of those studies is that the solute-solvent "dispersion" interaction, which arises from intermolecular electron correlation, must be included in order to obtain a qualitatively correct picture of solvation. It is not surprising that the dispersion interaction is important in solvation, for it is roughly proportional to both the solvent and the solute polarizabilities [24], the near-degenerate states of the solute being highly polarizable. Owing to the magnitude of the dispersion interaction, the usual perturbative treatment [25] cannot be applied. Thus, non-perturbative approaches had to be devised [18, 19, 21, 22]. Frequently an adiabatic separation can be made between the fast solvent polarizability and the relatively slow solute electrons [17–19], considerably simplifying the treatment of dispersion.

Early simulations were restricted to adiabatic dynamics on a single potential energy surface [8, 14, 26–28]. More recently, nonadiabatic transitions were included explicitly by Batista and Coker, who studied the photodisso-

ciation of $I_2^- Ar_n$ using a model that includes the solvent electronic polarizability [29]. Their Hamiltonian [29–31] is based on the Diatomics in Ionic Systems model of Last and George [32], in which the semiempirical Diatomics in Molecules Hamiltonian is augmented by an operator representing the solvent polarization energy produced by the solute charge. This treatment takes advantage of the adiabatic separation between solute and solvent electronic motion to obtain a relatively simple description of the solute-solvent dispersion interaction. The nonadiabatic transitions, which are essential for a consistent treatment of the photodissociation and subsequent recombination dynamics, were included using semiclassical surface-hopping methods [33–36]. Simulations using this model successfully reproduced the experimentally observed product distributions for the photodissociation of $I_2^- Ar_n$ clusters [29].

In recent publications [15, 16, 37] we have briefly outlined a different approach to this problem, one based on accurate ab initio solute wave functions rather than empirical models of the solute electronic structure. The ab initio approach offers a superior description of the solute charge distribution, and can be applied to more complex solute molecules for which an empirical parameterization of the charge distribution is not feasible. It represents an extension of the conventional theory of long-range intermolecular forces [38] to account for the strong polarization of the solute charge distribution and the exceptionally large solute-solvent dispersion interaction. The model successfully reproduces experimental product distributions [15, 16] and time-resolved photoelectron spectra [37].

The effective Hamiltonian for the solute derived in this chapter allows one to determine how the electronic states of the isolated solute are perturbed by the polarizable solvent. The approach is explicitly molecular,

but closely parallels treatments based on continuum dielectric models [17–19]. No assumptions are made about the form of the solute wave function; instead, the Hamiltonian is formulated using the distributed multipole analysis (DMA) [39–42], which is particularly well suited for dealing with charge densities that are obtained from ab initio calculations. An important feature of the effective Hamiltonian is its extensive use of the DMA for *transition* charge densities [42, 43]—matrix elements of the distributed multipole operators between two different molecular eigenstates. These transition densities allow the solute charge distribution to polarize in response to the external fields that act on it, and thus enable the model to describe solvent-induced charge localization without adopting a localized representation for the solute basis functions. This is a significant practical advantage since ab initio electronic wave functions are often delocalized.

This chapter is organized as follows. The effective Hamiltonian is derived in Sec. 2.1. The derivation begins with a review of the familiar expression for the induction energy of the solvent, and goes on to show how this expression is modified when a solute having several low-lying excited states is incorporated into the solvent. Section 2.2 discuss the methods used to evaluate the matrix elements of the effective Hamiltonian. Further discussion of the physical approximations made in deriving this Hamiltonian, and of its relationship to previous work, is included in Sec. 2.3. Section 2.4 contains a brief summary.

2.1 Derivation of the Effective Hamiltonian

In this section an effective Hamiltonian is derived for the interaction of the solute electrons with an arbitrary number of polarizable solvent molecules. Here is an overview of the derivation.

Assuming the Born-Oppenheimer separation between the nuclear and electronic coordinates, we can express the electronic Hamiltonian for the solute-solvent system as a function of the nuclear coordinates, using a distributed multipole (DM) expansion of the intermolecular Coulombic interactions. Since this expansion neglects the repulsive interactions that arise when different molecular charge distributions overlap, these interactions are accounted for by adding a short-range term. The only assumption made about this short-range Hamiltonian is that it is unaffected by the solvent electronic polarization. In other words, we assume that the polarization of the solvent charge distribution is small enough so that the repulsive interactions due to charge overlap do not change substantially.

Section 2.1.2 presents a derivation of the induction energy of a polarizable solvent possessing permanent electrostatic moments using the DM notation. Although Stone has previously derived this expression using a perturbative approach [41], this alternative derivation forms a useful foundation for discussing solvent-solute interactions. The induction energy for the solvent is expressed as the expectation value of the Hamiltonian using a wave function that is a product of wave functions for each solvent molecule. Since this Hartree approximation neglects both the intermolecular electron correlation (dispersion) that arises from electronic motion and the exchange-repulsion interaction arising from short-range overlap, we account for these effects with the

short-range terms added to the Hamiltonian. The induction energy is obtained by variationally optimizing the induced multipoles on each solvent molecule, which is equivalent to optimizing the solvent wave function.

This treatment of the solvent electronic polarization is extended in Sec. 2.1.3 to include interaction with the solute electrons. An effective Hamiltonian operator for the solute electrons is determined by variationally optimizing the solvent-induced multipoles as before, but with an additional source term for the solute. This procedure assumes that the solvent electronic polarization responds instantaneously to the fluctuations in the solute charge distribution that arise from motion of the solute electrons. This adiabatic separation has also been referred to as the Born-Oppenheimer limit for the solvent electronic polarization [19], and its validity is discussed later in Sec. 2.3.3. Essentially, it requires that the electronic states of the solute ion be much more closely spaced that those of the solvent, which is usually true for open-shell solute and closed-shell solvent molecules. Though the resulting effective Hamiltonian (Eq. 2.15) operates only on the solute electrons, it depends on all of the nuclear coordinates and on the permanent moments and polarizabilities of the solvent molecules.

2.1.1 Hamiltonian for the Solute-Solvent System

The electrostatic potential arising from a molecular charge distribution may be expanded in a multipole series, the convergence of which may be greatly accelerated by using distributed multipoles instead of a single-center expansion [39, 40, 42]. In particular, the distributed expansion converges for points that lie outside of the charge distribution but inside the molecular radius, where the single-center expansion breaks down. In clusters and condensed

phases molecules usually pack closely, so that accurate representation of the electrostatic interactions in this regime is essential.

In the DM expansion, several sites (usually atoms and bond centers) are chosen within each molecule, and then the multipoles for the entire molecule are partitioned into contributions from each of these sites. At each site the moments are expanded to a given order in real spherical tensor moments [44]. For example, the z component of the dipole moment at site i of molecule A is given by $Q_z^{A_i}$. The single-site multipole expansion can be recovered from the distributed-site expansion by use of multipole translation operators that shift the multipoles from all the distributed sites to a common site [39, 45–47].

The intermolecular electrostatic energy for non-overlapping charge distributions takes the form [41]

$$E^{\text{ele}} = \frac{1}{2} \sum_{A_i, B_j, t, u} Q_t^{A_i} T_{tu}^{A_i B_j} Q_u^{B_j} \tag{2.1}$$

where the sum runs over the sites and multipole orders on each pair of molecules in the system, and the factor of $1/2$ compensates for double counting of the pairs. The elements of the interaction tensor T depend on the intermolecular distances and orientations. The element $T_{tu}^{A_i B_j}$ gives the coordinate dependence of the interaction between the multipole of order t on site i of molecule A and the multipole of order u on site j of molecule B. Although the tensor elements are rather complicated functions for all but the lowest order of multipoles, explicit expressions for them have been tabulated [42, 44, 48] and they may be computed efficiently even for high orders [45–47, 49]. Note that $T^{A_i A_j}$ *is always zero* because it is assumed that Coulomb interactions within a single molecule are accounted for in the intramolecular energy. In what follows, the site in-

dices and the order-component subscripts are suppressed, and the interaction between two molecules becomes simply $Q^A T^{AB} Q^B$.

The intermolecular components of the electronic Hamiltonian for the solute-solvent system may be expanded similarly in terms of distributed multipole *operators* [41, 42]. The classical multipoles used to obtain the interaction energy through Eq. 2.1 are simply the expectation values of these operators with respect to the molecular wave functions. The electronic Hamiltonian for the solute-solvent system then takes the form

$$\begin{aligned} \hat{\mathcal{H}} &= \hat{h}^C + \sum_A \hat{H}^A \\ &\quad + \frac{1}{2} \sum_{A,B} \hat{Q}^A T^{AB} \hat{Q}^B + \sum_A \hat{q}^C T^{CA} \hat{Q}^A \\ &\quad + \hat{h}^{\mathrm{sr}}. \end{aligned} \tag{2.2}$$

The indices A and B run over all molecules in the solvent, while C designates the solute ion. Upper and lower case operators act on the solvent and solute electrons, respectively. $\hat{H}$ and $\hat{h}$ are the electronic Hamiltonians of the isolated molecules, while $\hat{Q}$ and $\hat{q}$ are the DM operators of the solvent and solute. The operator $\hat{h}^{\mathrm{sr}}$ accounts for short-range interactions that arise from the overlap of charge distributions of neighboring molecules. As mentioned above, it is assumed throughout the derivation that $\hat{h}^{\mathrm{sr}}$ is not affected by polarization of the solvent and so is an operator only in the solute electronic space, although it does depend on the nuclear coordinates of both the solute and solvent.

2.1.2 Induction Energy of the Solvent

In order to demonstrate the variational optimization of the multipoles induced in the polarizable solvent, we first consider the Hamiltonian for the solvent alone. This is given by the second and third terms in Eq. 2.2,

$$\begin{aligned} \hat{H}^{\text{solv}} = & \sum_A \hat{H}^A + \frac{1}{2}\sum_{A,B} \hat{Q}^A T^{AB} \hat{Q}^B \\ \equiv & \hat{H}^{\text{self}} + \hat{H}^{\text{ele}} \end{aligned} \tag{2.3}$$

where the short-range interactions have been dropped for simplicity.

It is assumed that the wave function can be written as a Hartree product,

$$|\Psi^{\text{solv}}\rangle = \prod_A |\overline{\psi}^A\rangle. \tag{2.4}$$

The Hartree approximation neglects intermolecular electron correlation, which gives rise to dispersion forces. However, except at short range the dispersion interactions are usually small compared to electrostatic interactions and thus can be accounted with empirical short-range interactions.

The ground state energy and wave function of the solvent in the Hartree approximation are determined by varying the single-molecule wave functions $|\overline{\psi}^A\rangle$ to minimize the expectation value of the solvent Hamiltonian, $\langle\Psi^{\text{solv}}|\hat{H}^{\text{solv}}|\Psi^{\text{solv}}\rangle$. The expectation value of $\hat{H}^{\text{solv}}$ is expressed as a function of the permanent and induced moments on each molecule, and then variationally minimized with respect to the induced moments to obtain the induction energy.

The expectation values of each multipole operator can be written as

the sum of a permanent and an induced moment,

$$\langle \overline{\psi}^A | \hat{Q}^A | \overline{\psi}^A \rangle \equiv Q^A + \delta Q^A \tag{2.5}$$

where the permanent moment Q^A is the expectation value of the operator with respect to the *isolated* molecular wave function, and δQ^A is the corresponding induced moment. The expectation value of $\hat{H}^{\rm ele}$ is then given by

$$\begin{aligned} E^{\rm ele}(\delta Q) &= \frac{1}{2}\sum_{AB}(Q^A + \delta Q^A)T^{AB}(Q^B + \delta Q^B) \\ &= \frac{1}{2}(Q + \delta Q)\cdot T \cdot (Q + \delta Q) \end{aligned} \tag{2.6}$$

where a convenient matrix-vector notation has been introduced in the second line. The components of the vector Q and the row and column indices of the matrix T run over all the solvent molecules.

To account fully for the electronic polarization of the solvent molecules, the work required to produce this polarization must be added. The "self-energy" of each solvent molecule, $\langle \overline{\psi}^A | \hat{H}^A | \overline{\psi}^A \rangle$, may be expanded in powers of the induced moments. The term linear in δQ^A must be zero, since otherwise the isolated molecule would possess induced moments. Assuming that the degree of polarization is small, the expansion is truncated at second order to obtain:

$$E^{\rm self}(\delta Q^A) = E^A + \frac{1}{2}\sum_{ijtu} \delta Q_t^{A_i} [\alpha^{-1}]_{tu}^{A_i A_j} \delta Q_u^{A_j} \tag{2.7}$$

where E^A is the internal energy of the isolated molecule A and $\alpha^{A_i A_j}$ is its polarizability tensor. The self-energy is expressed in a form that allows for dis-

tributed polarizabilities relating multipoles of arbitrary order [41, 50]. If the induced moments are large, hyperpolarizability terms involving higher powers of the induced moments must also be included in the self-energy. Since E^A is just the internal energy of the isolated solvent molecule at the given intramolecular coordinates, it may be set to zero for a rigid molecule. For flexible molecules it is the potential function for the molecule's internal force field.

The total solvent energy is the sum of the electrostatic and self-energy contributions,

$$E^{\text{solv}}(\delta\mathsf{Q}) = E^{\text{intra}} + \frac{1}{2}\delta\mathsf{Q}\cdot\boldsymbol{\alpha}^{-1}\cdot\delta\mathsf{Q} + \frac{1}{2}(\mathsf{Q}+\delta\mathsf{Q})\cdot T\cdot(\mathsf{Q}+\delta\mathsf{Q}) \tag{2.8}$$

where the matrix notation has been extended to include a solvent polarizability matrix $\boldsymbol{\alpha}$. This matrix is block diagonal since it contains no elements connecting different molecules. E^{intra} is the total intramolecular energy of the isolated solvent molecules, which is just the sum of the internal energies E^A.

Since the energy expression is quadratic in the induced moments, minimizing it leads to a linear response equation relating the induced and permanent moments in the solvent,

$$\begin{aligned}\delta\mathsf{Q} &= -\left[\mathsf{T}+\boldsymbol{\alpha}^{-1}\right]^{-1}\cdot\mathsf{T}\cdot\mathsf{Q} \\ &\equiv -\boldsymbol{\chi}\cdot\mathsf{T}\cdot\mathsf{Q}.\end{aligned} \tag{2.9}$$

Here we have introduced the generalized electric susceptibility $\boldsymbol{\chi}$, which is a symmetric tensor. $\boldsymbol{\chi}$ describes the electronic polarization response of the

solvent to the generalized potential V given by

$$\mathsf{V} \equiv \mathsf{T} \cdot \mathsf{Q}. \tag{2.10}$$

The generalized potential contains the electrostatic potential and its derivatives (field, field gradient, etc.) at every site in the solvent.

By eliminating the induced moments δQ from Eq. 2.8 via Eq. 2.9, the minimized solvent energy can be written in terms of the susceptibility and permanent moments,

$$E^{\text{solv}} = E^{\text{intra}} + \frac{1}{2}\mathsf{Q} \cdot \mathsf{T} \cdot \mathsf{Q} - \frac{1}{2}\mathsf{Q} \cdot \mathsf{T} \cdot \boldsymbol{\chi} \cdot \mathsf{T} \cdot \mathsf{Q}. \tag{2.11}$$

The second term in this equation is the electrostatic energy due to interactions between the permanent multipoles, while the third term is the induction energy arising from the induced moments. The solvent energy can also be written in terms of the generalized potential V in the compact form

$$E^{\text{solv}} = E^{\text{intra}} + \frac{1}{2}\mathsf{Q} \cdot \mathsf{V} - \frac{1}{2}\mathsf{V} \cdot \boldsymbol{\chi} \cdot \mathsf{V}. \tag{2.12}$$

From this expression it is clear that the electrostatic and induction energies written in the DM notation are simply a generalization of the standard expressions for these quantities in terms of single-center moments.

2.1.3 Effective Hamiltonian for the Solute-Solvent System

The solvent is now allowed to polarize in response to the *solute*. To obtain an effective Hamiltonian that operates on the solute electrons, we average over the solvent electrons while allowing them to respond instantaneously

to the solute electrons. The resulting expression for $\hat{h}^{\text{eff}}$ in terms of the induced solvent moments is similar to Eq. 2.8,

$$\begin{aligned}\hat{h}^{\text{eff}}(\delta\mathsf{Q}) &= E^{\text{intra}} + \hat{h}^{C} + \hat{h}^{\text{sr}} \\ &\quad + \frac{1}{2}\delta Q \cdot \boldsymbol{\alpha}^{-1} \cdot \delta Q \\ &\quad + \frac{1}{2}(Q + \hat{q} + \delta Q) \cdot T \cdot (Q + \hat{q} + \delta Q) \end{aligned} \tag{2.13}$$

where the rows and columns of the matrix T have been extended to include both solvent and solute. Note that the intramolecular term $\frac{1}{2}\hat{\mathsf{q}} \cdot \mathsf{T} \cdot \hat{\mathsf{q}}$ does not contribute to the Hamiltonian because all the intramolecular elements of T are zero, and that the vector Q has non-zero multipoles only at the solvent sites, while $\hat{\mathsf{q}}$ has non-zero multipoles only at the solute sites.

The induced moments on the solvent molecules are obtained by variational minimization as before. Since the part of Eq. 2.13 that depends on $\delta\mathsf{Q}$ differs from Eq. 2.8 only by the addition of $\hat{\mathsf{q}}$ to the electrostatic term, it is not surprising that the induced moments are given by

$$\delta\mathsf{Q} = -\boldsymbol{\chi} \cdot \mathsf{T} \cdot (\mathsf{Q} + \hat{\mathsf{q}}) \tag{2.14}$$

which differs from the linear response of the solvent alone by the addition of the solute multipole operators as a source term. The induced solvent multipoles are now given by an operator in the solute space, reflecting the fact that the solvent electrons adjust instantaneously to the positions of the solute electrons. Equation 2.14 may be used to eliminate $\delta\mathsf{Q}$ from Eq. 2.13 giving the effective

Hamiltonian for the solute-solvent system

$$\begin{aligned}\hat{h}^{\text{eff}} &= E^{\text{intra}} + \hat{h}^{C} + \hat{h}^{\text{sr}} \\ &\quad + \frac{1}{2}(Q+\hat{q})\cdot T \cdot (Q+\hat{q}) \\ &\quad - \frac{1}{2}\left(\mathsf{Q}+\hat{\mathsf{q}}\right)\cdot \mathsf{T}\cdot \boldsymbol{\chi}\cdot \mathsf{T}\cdot\left(\mathsf{Q}+\hat{\mathsf{q}}\right). \end{aligned} \tag{2.15}$$

Introducing the generalized-potential operator arising from the solute, $\hat{\mathsf{v}} = \mathsf{T}\cdot\hat{\mathsf{q}}$, this can be rewritten as

$$\begin{aligned}\hat{h}^{\text{eff}} &= E^{\text{intra}} + \hat{h}^{C} + \hat{h}^{\text{sr}} \\ &\quad + \frac{1}{2}(Q+\hat{q})\cdot (V+\hat{v}) \\ &\quad - \frac{1}{2}\left(\mathsf{V}+\hat{v}\right)\cdot \boldsymbol{\chi}\cdot\left(\mathsf{V}+\hat{v}\right). \end{aligned} \tag{2.16}$$

Equations 2.15 and 2.16 express the Hamiltonian for the solute-solvent system in terms of operators $\hat{h}$, $\hat{q}$ and $\hat{v}$ that act only on the solute electrons. The Hamiltonian depends parametrically upon the nuclear coordinates of both solute and solvent. As is discussed in more detail later, the two-electron operator $\hat{\mathsf{v}}\cdot\boldsymbol{\chi}\cdot\hat{\mathsf{v}}$ has contributions from both induction and dispersion interactions. We now discuss how the effective Hamiltonian is evaluated by the introduction of a basis for the solute space and an electrostatic model for the solvent.

2.2 Evaluation of the Effective Hamiltonian

2.2.1 Solute Basis

The effective Hamiltonian, $\hat{h}^{\text{eff}}$, may be evaluated in any representation, its eigenvalues depending upon the space spanned by the solute basis but

not upon the choice of basis functions for that space. A natural choice of basis is the set of eigenstates of the isolated solute, in which the diagonal elements of $\hat{h}^C$ are the potential energy surfaces of the isolated solute.

The diagonal elements of $\hat{h}^{\text{eff}}$ modify the isolated solute potential surfaces to take into account the interaction of each of these states with the solvent, while the off-diagonal elements allow the solute to polarize in response to the solvent. In practice it is necessary to truncate the space of solute electronic states when evaluating $\hat{h}^{\text{eff}}$. For open-shell ionic solutes it is often sufficient to include only the valence states, since these enable intramolecular charge-transfer and hence account for the majority of the polarization response. Both bonding and antibonding states must be included in order to correctly describe the molecular polarizability.

In applications to solvated I_2^- [15, 16, 37] the lowest six electronic states were retained, comprising all states that correlate to I^- (^1S) + I (^2P). No information about higher electronic states is known either from experiment or from theory. [51] An additional complication in I_2^- is its large spin-orbit coupling, which leads to a transition from eigenstates that are predominantly Hund's case (a) in character at the equilibrium bond length to states that are case (c) at large bond distances [51]. Since each state in this open-shell system has a twofold spin degeneracy by Kramers' theorem, $\hat{h}^{\text{eff}}$ is represented by a 12×12 matrix. Further details of the model Hamiltonian for I_2^- and ICl^- in clusters are given in Chapter 3.

The eigenvalues of $\hat{h}^{\text{eff}}$ are the multidimensional potential energy surfaces of the entire solute-solvent system. At each step of a molecular dynamics simulation $\hat{h}^{\text{eff}}$ is evaluated and diagonalized to give the energies and forces required to propagate the trajectory to the next step. Details of the tech-

niques used to compute molecular dynamics trajectories and the nonadiabatic dynamics on these potential surfaces are given in Chapter 4.

2.2.2 Coulombic Interactions

Evaluation of $\hat{h}^{\text{eff}}$ requires a set of permanent multipoles and polarizabilities for the solvent and evaluation of the solute DM operators. The electrostatic properties of the solvent can be obtained from a wide variety of sources [25, 42, 52, 53]. For a simple solvent such as argon, only the point polarizability is needed for a reasonably accurate representation. Higher order polarizabilities and hyperpolarizabilities have a negligible effect on the interaction energy, especially given the uncertainties in the short-range interactions. For CO_2, we have found that a five-site distributed charge model [54], combined with single-center parallel and perpendicular polarizabilities, [52] provides an adequate description. Higher order DM [40] and distributed polarizabilities [50] from ab initio calculations also exist for CO_2, but it is not clear that these give a more accurate description of the intermolecular potential [55].

Parameterization of the solute is more involved. The matrix elements of the solute DM operators are evaluated directly from the solute basis functions. For I_2^- we found that a four-site DM expansion up to quadrupole order was sufficient. Although DM's are widely used to represent the charge distribution of a single electronic state, a key feature of our effective Hamiltonian is the use of distributed *transition* multipoles. These off-diagonal DM's are not widely available for ab initio wave functions, and we have obtained them by a minor modification of the interface between Stone's DMA package and the ab initio program MOLPRO [56]. Calculation of the DM operators adds a negligible cost to the ab initio calculations. When the calculations are performed

on a grid of solute geometries—we used 50 points for I_2^-—interpolation can be used to evaluate both the DM matrix elements and the electronic energy at arbitrary solute geometries.

The evaluation of the two-electron operator in the solute induction-dispersion term, $\hat{\mathsf{v}} \cdot \boldsymbol{\chi} \cdot \hat{\mathsf{v}}$, requires further elaboration. The one-electron DM matrix elements q_{ij} are obtained from the ab initio calculation as described above. By inserting the identity, $\sum_k |k\rangle\langle k|$, and restricting the sum to the basis states of the solute, we can write the matrix elements of the two-electron operator in terms of one-electron matrix elements,

$$(\hat{\mathsf{v}} \cdot \boldsymbol{\chi} \cdot \hat{\mathsf{v}})_{ij} = \sum_{k}^{n_{\text{basis}}} \mathsf{v}_{ik} \cdot \boldsymbol{\chi} \cdot \mathsf{v}_{kj}. \tag{2.17}$$

This approximation is consistent with allowing the solute to polarize and fluctuate only in the space defined by the solute basis functions.

Evaluation of the susceptibility tensor $\boldsymbol{\chi}$ is usually the most computationally demanding step in constructing $\hat{h}^{\text{eff}}$. When only a single source term is present, it may be efficient to evaluate the induced moments, $\delta\mathsf{Q} = -\boldsymbol{\chi} \cdot \mathsf{V}$, using an iterative procedure. Because the source term in $\hat{h}^{\text{eff}}$ is an operator, however, a different set of induced moments must be computed for each pair of basis states. In clusters, where the number of polarizable sites is relatively small, it is therefore more efficient to compute $\boldsymbol{\chi}$ directly by inverting the matrix $[\mathsf{T} + \boldsymbol{\alpha}^{-1}]$. This matrix is positive definite until the onset of polarization catastrophe, which occurs when the polarizable sites on different molecules are too closely spaced [57]. Cholesky decomposition [58] is well suited for the computation of $\boldsymbol{\chi}$ because it is highly efficient and fails for matrices that are not positive definite, providing a warning that the linear response approximation

is no longer valid.

2.2.3 Short-range Interactions

The short-range effective Hamiltonian may be split into two components,

$$\hat{h}^{\mathrm{sr}} = \hat{h}^{\mathrm{sr}}_{sS} + E_{SS} \tag{2.18}$$

where s and S denotes the solute and solvent respectively. The solvent-solvent interaction energy, E_{SS}, is assumed to be independent of the solvent wave function, and so is simply a function of the solvent nuclear coordinates. In most potential models used for liquid simulations, the short-range interactions are represented by pairwise atom-atom Lennard-Jones potentials, while the long-range electrostatic interactions are calculated using distributed charges to represent the overall charge distribution. Such models, augmented by the inclusion of solvent polarizability, are easily applied to the effective Hamiltonian. Atom-atom Lennard-Jones potentials have been used to represent the short-range solvent interactions in applications to argon and CO_2 solvents [15, 16, 37].

Determining the short-range solute-solvent interactions is somewhat more complicated. In general, these interactions will depend on the electronic state of the solute. The approach adopted in this work has been to adopt the simplest potential model for the short-range interactions that will fit the available data from experiments. For both of the solvents that have been studied so far, state-independent atom-atom Lennard-Jones parameters have been fit to reproduce the potentials of I and I^- interacting with a single solvent molecule as determined by high-resolution photoelectron spectroscopy [59, 60].

These parameters alone were sufficient for $I_2^-(CO_2)_n$, but it was necessary to introduce an additional state-dependent term to reproduce the anisotropy of the I–Ar interaction, which depends on the orientation of the iodine quadrupole moment [15] (See Chapter 3 for details).

2.2.4 Dynamics on the Model Potential Surfaces

The eigenstates of $\hat{h}^{\text{eff}}$ are obtained at each step in a molecular dynamics simulation by the following process:

(1) Obtain solute basis state energies and distributed multipole operators from splined data evaluated at the current value of the solute internal coordinates. The energies of the solute basis states form the diagonal matrix $\hat{h}^C$.

(2) Compute Coulombic terms in the expression for the effective Hamiltonian, the last two terms of Eq. 2.15, from the distributed solute multipoles, the solvent charge distribution, and the solvent polarizabilities.

(3) Calculate the solvent intramolecular energy, E^{intra}.

(4) Calculate the short-range interactions, $\hat{h}^{\text{sr}}$.

(5) Diagonalize $\hat{h}^{\text{eff}}$ to get eigenvectors and energies for all states.

(6) If necessary, compute the forces on the current adiabatic state by calculating the derivatives of the effective Hamiltonian with respect to the nuclear coordinates $\mathbf{R}$ and using the Hellmann-Feynman theorem,

$$\mathbf{F} = -\nabla_{\mathbf{R}}\langle\psi|\hat{h}^{\text{eff}}|\psi\rangle = -\langle\psi|\nabla_{\mathbf{R}}\hat{h}^{\text{eff}}|\psi\rangle. \tag{2.19}$$

2.3 Discussion

2.3.1 Solvent-solute interaction energy

The electronic energy of the solute-solvent system is the expectation value of $\hat{h}^{\text{eff}}$ with respect to the wave function of the solute,

$$\begin{aligned} E(\psi) &= E^{\text{intra}} + \langle\psi|\hat{h}^C|\psi\rangle + \langle\psi|\hat{h}^{\text{sr}}|\psi\rangle \\ &\quad + \frac{1}{2}\mathsf{Q}\cdot V + \frac{1}{2}\mathsf{Q}\cdot\langle\psi|\hat{v}|\psi\rangle + \frac{1}{2}\langle\psi|\hat{q}|\psi\rangle\cdot V \\ &\quad - \frac{1}{2}\mathsf{V}\cdot\boldsymbol{\chi}\cdot\mathsf{V} - \frac{1}{2}\langle\psi|\hat{\mathsf{v}}|\psi\rangle\cdot\boldsymbol{\chi}\cdot\mathsf{V} - \frac{1}{2}\mathsf{V}\cdot\boldsymbol{\chi}\cdot\langle\psi|\hat{\mathsf{v}}|\psi\rangle \\ &\quad - \frac{1}{2}\langle\psi|\hat{\mathsf{v}}\hat{\mathsf{v}}|\psi\rangle\cdot\boldsymbol{\chi} \end{aligned} \tag{2.20}$$

in which the last line involves the scalar product of the second rank tensors $\hat{\mathsf{v}}\hat{\mathsf{v}}$ and $\boldsymbol{\chi}$. The term $1/2\langle\hat{\mathsf{q}}\rangle\cdot\langle\hat{\mathsf{v}}\rangle$ has been discarded since all intramolecular Coulombic terms are zero. The self-energy $\langle\hat{h}^C\rangle$ of the solute is evaluated exactly, rather than in the usual harmonic approximation (Eq. 2.7), because the higher-order terms are essential for the description of a highly polarizable molecule. All the terms in Eq. 2.20 containing either the solvent multipoles Q or the solvent potential V describe electrostatic and induction interactions. The last term contains both induction and dispersion interactions:

$$\begin{aligned} -\frac{1}{2}\langle\hat{\mathsf{v}}^2\rangle\cdot\boldsymbol{\chi} &= -\frac{1}{2}\langle\hat{\mathsf{v}}\rangle\cdot\boldsymbol{\chi}\cdot\langle\hat{\mathsf{v}}\rangle \qquad \text{induction} \\ &\quad -\frac{1}{2}[\langle\hat{\mathsf{v}}^2\rangle - \langle\hat{\mathsf{v}}\rangle^2]\cdot\boldsymbol{\chi} \qquad \text{dispersion.} \end{aligned} \tag{2.21}$$

The induction term describes the interaction of the solvent polarizability with the *average* potential arising from the charge distribution of the solute, $\langle\hat{\mathsf{v}}\rangle$. The dispersion term arises from the interaction of the solvent polarizability

with the fluctuations about this average, $[\langle\hat{\mathsf{v}}^2\rangle - \langle\hat{\mathsf{v}}\rangle^2]$. These fluctuations are due to motion of the solute electrons and may be exceptionally large when two potential surfaces are nearly degenerate. This is readily seen for the case of H_2^+ stretched almost to bond dissociation, where the charge distribution fluctuates between $H^+ \ldots H$ and $H \ldots H^+$, with a mean charge of 1/2 on each atom. Large fluctuations may occur whenever two Lewis structures are brought into resonance by solvation effects. Omission of the fluctuations leads to spurious localization of the excess solute charge on a single atom, [17] since the induction energy is greatest if all the charge is concentrated at a single point. Because of the large magnitude of the solute fluctuations, it is essential to include them to obtain qualitatively correct results [17–19, 23, 61, 62]. This is in contrast to the much smaller fluctuations arising from the solvent electrons and from the core electrons in the solute, which are usually absorbed in the empirical short-range Hamiltonian.

The dispersion term in the energy expression, Eq. 2.21, arises because the solvent electronic polarization is assumed to respond instantaneously to fluctuations of the valence solute electrons. Only the solute valence electron fluctuations are included because of the restriction of the solute basis to include only valence excitations. If instead the time scales for the electronic motion in the solute and solvent were comparable, it would be more appropriate to use a Hartree-product wave function (Eq. 2.4) for the entire solute-solvent system. The dispersion term would then be absent from the energy expression Eq. 2.20 and the corresponding Schrödinger equation for the solute would be nonlinear [19, 63].

2.3.2 Comparison with other treatments

We can now compare our effective Hamiltonian and energy expression with previous work on similar systems. We do not attempt to review the many approaches that have been taken towards incorporating medium effects into electronic structure calculations, but rather focus on a few studies that address the problem in which we are interested: a small, highly polarizable solute dissociating inside a polarizable solvent or cluster.

One popular approach is to treat the solvent as a dielectric continuum [17–19, 22, 63, 64]. Kim and Hynes [19] have developed a variational expression, based on a multiconfiguration self-consistent field wave function, for the free energy of an interacting solute-solvent system. We consider here only the adiabatic limit (referred to by Kim and Hynes as the "Born-Oppenheimer limit") of this theory, in which the solvent electronic polarization is regarded as fast compared with the electronic degrees of freedom of the solute. In the adiabatic limit an effective Hamiltonian for the solute may be obtained by minimizing the free-energy expression with respect to the solvent electronic polarization. This leads to an effective free energy operator for the solute, G^{BO}, which may be written in terms of our generalized solute potential $\hat{v}$ as

$$\begin{aligned} \hat{G}^{\mathrm{BO}} &= \hat{h}^{C} + G^{\mathrm{or}} \\ &+ \left[1 + 4\pi\chi^{\mathrm{el}}\right]^{-1} \hat{\mathsf{v}} \cdot \mathsf{P}^{\mathrm{or}}(\mathsf{r}) \\ &- \frac{1}{2}\left[4\pi + \chi^{\mathrm{el}^{-1}}\right]^{-1} \hat{\mathsf{v}} \cdot \hat{\mathsf{v}}, \end{aligned} \tag{2.22}$$

where G^{or} is the internal free energy of the solvent including the self-energy and solvent-solvent interactions, χ^{el} is the solvent electronic susceptibility, and

$\mathsf{P}^{\mathrm{or}}(\mathsf{r})$ is the orientational polarization of the solvent. In dielectric continuum models the only solvent multipoles are dipoles, so the generalized solute potential $\hat{v}$ is proportional to the electric field arising from the solute at each point in the solvent. As an aid in comparison with continuum solvent models, the effective Hamiltonian (Eq. 2.15) can be rewritten as

$$\begin{aligned} \hat{h}^{\mathrm{eff}} &= \hat{h}^{C} + E^{\mathrm{solv}} \\ &+ \hat{\mathsf{v}} \cdot \left[1 + \alpha \cdot \mathsf{T}\right]^{-1} \cdot \mathsf{Q} \\ &- \frac{1}{2} \hat{\mathsf{v}} \cdot \left[\mathsf{T} + \alpha^{-1}\right]^{-1} \cdot \hat{\mathsf{v}} \end{aligned} \tag{2.23}$$

using the identity

$$\mathsf{T} \cdot \left[1 + \alpha \cdot \mathsf{T}\right]^{-1} = -\mathsf{T} \cdot \left[\mathsf{T} + \alpha^{-1}\right]^{-1} \cdot \mathsf{T} + \mathsf{T}. \tag{2.24}$$

There is a close correspondence between the free-energy operator and the Hamiltonian, as expected. G^{or} corresponds to the internal energy of the solvent, E^{solv}, χ^{el} corresponds to the solvent polarizability $\boldsymbol{\alpha}$, and $\mathsf{P}^{\mathrm{or}}(\mathsf{r})$ corresponds to the permanent solvent multipoles Q. The free-energy operator and the Hamiltonian exhibit the same dependence on the solvent polarizability, and both involve the *square* of the solute-potential *operator*, rather than the square of its expectation value, reflecting the importance of electronic fluctuations within the solute. It can be shown [64] that the factor 4π in $\hat{G}^{\mathrm{BO}}$ arises from the mutual interaction between induced solvent dipoles, and plays the role of the interaction tensor T in $\hat{h}^{\mathrm{eff}}$.

Most previous treatments of the photodissociation of solvated ions have described the solute charge distribution in terms of an empirical, local-

ized basis. For example, the charge distribution for the basis function $|\mathrm{I}^-\ldots\mathrm{I}\rangle$ is modeled by a single point charge at the I^- nucleus, and the transition multipoles $\langle \mathrm{I}^-\ldots\mathrm{I}|\hat{q}|\mathrm{I}\ldots\mathrm{I}^-\rangle$ are set to zero. From our point of view this model amounts to a monopole approximation to the distributed multipole expansion. Studies of the energetics [20, 65] and ground-state dynamics [9, 14] of I_2^- in clusters and in solution combined this description of the charge distribution with empirical potential energy curves of the isolated solute. Localized basis functions (implied by use of a tight binding Hamiltonian) have also been used by Garcia, Bennemann and coworkers to study the dynamics of ionized Hg_n clusters [66, 67]. However, in their approach, the solute electric field operator is replaced by its expectation value, so that their model corresponds to the "self-consistent" limit in which solute fluctuations are neglected [19, 64], rather than to the adiabatic limit used here.

The earliest dynamical studies [9, 14] were restricted to the ground state potential energy surface of the solute-solvent system. Batista and Coker [29, 31] have gone beyond this restriction to simulate the adiabatic and nonadiabatic photodissociation dynamics of $\mathrm{I}_2\mathrm{Xe}_n$ and $\mathrm{I}_2^-\mathrm{Ar}_n$ on multiple electronic surfaces, using an effective Hamiltonian based on the Diatomics-in-Ionic-Systems (DIIS) model of Last and George [32]. The DIIS model augments a semiempirical Diatomics-in-Molecules Hamiltonian with an operator that represents the strong Coulombic interaction of the ionic solute with the electronic polarizability of the solvent. The resulting effective Hamiltonian operator is essentially the same as our effective Hamiltonian (Eq. 2.15), although the derivation and perspective are very different. Our model differs from theirs primarily in the choice of solute basis functions. Batista and Coker expand the solute wave function in a basis of empirical, localized functions such as the $|\mathrm{I}^-\ldots\mathrm{I}\rangle$ function

described above. The charge distribution corresponding to each basis function is approximated by a single point charge at the I^- nucleus, and off-diagonal matrix elements such as $\langle I^- \ldots I|\hat{v}|I \ldots I^-\rangle$ are set to zero. As a consequence of these approximations the the solute multipole and potential operators, $\hat{q}$ and $\hat{v}$, are diagonal in the localized basis.

These semiempirical, localized-basis approaches capture the dominant features of an ionic charge distribution. However, while empirical solute potential curves may be reasonably accurate, empirical charge distributions are invariably rather crude, especially at shorter bond lengths. For instance, a single point-charge may adequately describe the charge distribution of $|I^- \ldots I\rangle$ near dissociation, but it becomes an increasingly poor approximation at shorter bond lengths. The neglect of matrix elements of the multipole operators that are off-diagonal in the localized basis, which is essentially equivalent to neglect of the overlap between the basis functions, may also be expected to be inaccurate at short internuclear distances. These approximations introduce significant errors into the solvated potential surfaces in the neighborhood of the equilibrium bond length. While it is not easy to predict their effect on the photodissociation dynamics, some of the most interesting properties of solvated ions, such as anomalous charge switching on excited states [15, 16], are sensitive to the details of the solute charge distribution at the equilibrium bond length. In contrast, ab initio wave functions may be used to calculate multipoles to any order, enabling one to build up an accurate representation of the potential arising from the solute charge distribution. High-level ab initio calculations may also be applied to molecules with complicated electronic structure, where a semiempirical valence-bond wave function may not be adequate.

2.3.3 Validity of the adiabatic approximation

The adiabatic approximation is only valid if the solvent fluctuates at a significantly higher frequency than the solute [19]. Ideally the solute energy levels consist of a narrow spectral envelope that is quasi-degenerate with the ground state and well separated from the more highly excited states. Transitions between states within this envelope give rise to low frequency fluctuations that may be treated adiabatically. Since it is not always immediately clear whether the adiabatic separation applies, we now consider the variation of the dispersion energy with the fluctuation frequency of the solute. For simplicity we use a perturbative approach. Although this will not give quantitative results for systems exhibiting large fluctuations, it is sufficient to determine whether the adiabatic approximation may be used.

The solvent's response to a fluctuating field is proportional to its frequency-dependent polarizability, $\alpha(\omega)$. The usual perturbative formula for the dispersion energy [25] between two molecules A and B may be written as

$$\begin{aligned} E^{\text{dispersion}} = & \\ & -\frac{1}{2}{\sum_{i\in A}}' T^{BA}\langle 0|\hat{Q}^A|i\rangle\langle i|\hat{Q}^A|0\rangle T^{AB}\alpha^{BB}\left(\Delta E^A_{0i}\right) \\ & -\frac{1}{2}{\sum_{j\in B}}' T^{AB}\langle 0|\hat{Q}^B|j\rangle\langle j|\hat{Q}^B|0\rangle T^{BA}\alpha^{AA}\left(\Delta E^B_{0j}\right). \end{aligned} \tag{2.25}$$

The first term of this expression contains fluctuations due to molecule A and the frequency-dependent polarizability of molecule B, while in the second term the roles of molecules A and B are reversed. The fluctuations arising from molecule A, $\langle 0|\hat{Q}^A|i\rangle\langle i|\hat{Q}^A|0\rangle$, occur at frequencies ΔE^A_{0i} corresponding to electronic transitions from the ground state to excited states $|i\rangle$. The response

of molecule B is proportional to $\alpha^{BB}(\Delta E^A_{0i})$, its polarizability at the characteristic frequency for fluctuations in the other molecule. At zero frequency $\alpha^{BB}(\omega)$ is equal to the static polarizability. As ω increases, $\alpha^{BB}(\omega)$ increases monotonically until it diverges at the first electronic transition frequency of molecule B. The formula given above is not valid at the resonant frequency, but we are chiefly concerned with the lower frequencies that characterize the solute. At low frequencies, the frequency-dependent polarizabilities may be replaced by static polarizabilities, in which case the above expression reduces to a perturbative approximation to the adiabatic limit. More generally, the adiabatic separation may be used whenever the solvent's frequency-dependent polarizability is approximately equal to its static polarizability over the range of fluctuation frequencies exhibited by the solute.

As an example we consider the solute I_2^-, in the solvents argon, carbon-dioxide, water, ammonia and benzene. The wave function of solvated I_2^- is expanded in a basis consisting of the six lowest states of isolated I_2^-. The solute fluctuates at frequencies corresponding to electronic excitations, and the highest electronic excitation in the six-state model [15] occurs at 3 eV. As the frequency is increased from 0 eV to 3 eV, the polarizabilities of argon [68], carbon dioxide [69], and water [70] increase by 3–4%, while ammonia [70] and benzene [71] show a 6–7% increase. The adiabatic approximation to the dispersion energy will be in error by roughly 3–7%, and this is accurate enough for most purposes. The error introduced by the adiabatic approximation increases rapidly with the frequency of the solute fluctuations. At 5.5 eV the polarizabilities of argon, carbon dioxide and water are 13–19% greater than their static values, and the polarizabilities of ammonia and benzene have increased by 42–46%.

2.4 Summary and Conclusion

We have derived an effective Hamiltonian for the electronic structure of a solute interacting with an assembly of polarizable solvent molecules. The potential surfaces for an envelope of solute electronic states are determined by diagonalizing the effective Hamiltonian matrix in a basis of low-lying electronic states of the isolated solute. Coulombic interactions between the solute and the solvent are assumed to dominate the potential surfaces, which is appropriate for both ionic systems and highly polar systems. Distributed multipoles are used to describe the solute charge density operator and the solvent's permanent charge distribution, while distributed polarizabilities describe the electronic polarization of the solvent. Short range interactions arising from overlap of molecular charge distributions are treated empirically.

The effective Hamiltonian consists of the five terms given in Equation 2.16: E^{intra} describes the solvent internal degrees of freedom, and is taken to be zero for the case of rigid molecules; $\hat{h}^C$, the Hamiltonian of the isolated solute, is a diagonal matrix containing the potential surfaces of the isolated solute basis states; $\hat{h}^{\mathrm{sr}}$ incorporates the short-range forces arising from overlapping molecular charge densities and is fitted to reproduce the known features of the experimental potentials; $\frac{1}{2}(\mathsf{Q}+\hat{\mathsf{q}})\cdot(\mathsf{V}+\hat{\mathsf{v}})$ contains the interactions of the solute and solvent charge densities with the potential created by the permanent multipole moments of the solvent; and $-\frac{1}{2}(\mathsf{V}+\hat{v})\cdot\boldsymbol{\chi}\cdot(\mathsf{V}+\hat{v})$ represents interactions of the solute and solvent charge densities with the electronic polarization of the solvent, which is assumed to respond instantaneously to fluctuations of the valence solute electrons.

The form of the effective Hamiltonian allows a detailed potential

model of the solute-solvent system to be constructed from high-level ab initio calculations of the ground and excited state wave functions of the isolated solute. It is not necessary to assume a particular form (e.g. valence bond) for the solute wave function. Preliminary applications to photodissociation of I_2^- in clusters of argon and carbon dioxide have shown good agreement with experiment and have deepened our understanding of the underlying dynamics [15, 16, 37], as Chapters 5–7 discuss. A major finding of these studies has been that the dynamics on the excited states depends strongly on the direction of charge localization, which undergoes a fundamental shift as the molecule dissociates because of the strong state mixing induced by spin-orbit coupling. These results indicate that a high-level description of the solute wave function is required for an accurate description of the solute-solvent interactions and the resulting dynamics.

References for Chapter 2

[1] J. Papanikolas, J. Gord, N. Levinger, D. Ray, V. Vorsa, and W. Lineberger, J. Phys. Chem. **95**, 8028 (1991).

[2] J. Papanikolas, V. Vorsa, M. Nadal, P. Campagnola, H. Buchenau, and W. Lineberger, J. Chem. Phys. **99**, 8733 (1993).

[3] V. Vorsa, P. J. Campagnola, S. Nandi, M. Larsson, and W. C. Lineberger, J. Chem. Phys. **105**, 2298 (1996).

[4] V. Vorsa, S. Nandi, P. J. Campagnola, M. Larsson, and W. C. Lineberger, J. Chem. Phys. **106**, 1402 (1997).

[5] B. J. Greenblatt, M. T. Zanni, and D. M. Neumark, Science **276**, 1675 (1997).

[6] D. A. V. Kliner, J. C. Alfano, and P. F. Barbara, J. Chem. Phys. **98**, 5375 (1993).

[7] J. Alfano, Y. Kimura, P. Walhout, and P. Barbara, Chem. Phys. **175**, 147 (1993).

[8] P. K. Walhout, J. C. Alfano, K. A. M. Thakur, and P. F. Barbara, J. Phys. Chem. **99**, 7568 (1995).

[9] I. Benjamin, P. F. Barbara, B. J. Gertner, and J. T. Hynes, J. Phys. Chem. **99**, 7557 (1995).

[10] U. Banin, A. Waldman, and S. Ruhman, J. Chem. Phys. **96**, 2416 (1992).

[11] U. Banin and S. Ruhman, J. Chem. Phys. **98**, 4391 (1993).

[12] U. Banin, R. Kosloff, and S. Ruhman, Chem. Phys. **183**, 289 (1994).

[13] P. E. Maslen, J. Faeder, and R. Parson, Mol. Phys., submitted.

[14] J. M. Papanikolas, P. E. Maslen, and R. Parson, J. Chem. Phys. **102**, 2452 (1995).

[15] J. Faeder, N. Delaney, P. Maslen, and R. Parson, Chem. Phys. Lett. **270**, 196 (1997).

[16] N. Delaney, J. Faeder, P. E. Maslen, and R. Parson, J. Phys. Chem. A **101**, 8147 (1997).

[17] J. N. Gehlen, D. Chandler, H. J. Kim, and J. T. Hynes, J. Phys. Chem. **96**, 1748 (1992).

[18] R. A. Marcus, J. Phys. Chem. **96**, 1753 (1992).

[19] H. J. Kim and J. T. Hynes, J. Chem. Phys. **96**, 5088 (1992).

[20] B. J. Gertner, K. Ando, R. Bianco, and J. T. Hynes, Chem. Phys. **183**, 309 (1994).

[21] R. Bianco, J. J. I. Timoneda, and J. T. Hynes, J. Phys. Chem. **98**, 12103 (1994).

[22] R. Bianco and J. T. Hynes, J. Chem. Phys. **102**, 7864 (1995).

[23] R. Bianco and J. T. Hynes, J. Chem. Phys. **102**, 7885 (1995).

[24] P. W. Atkins, *Molecular Quantum Mechanics*, Oxford, New York, 1983.

[25] G. C. Maitland, M. Rigby, E. B. Smith, and W. A. Wakeham, *Intermolecular Forces, Their Origin and Determination*, Clarendon, Oxford, 1981.

[26] L. Perera and F. G. Amar, J. Chem. Phys. **90**, 7354 (1989).

[27] I. Benjamin, U. Banin, and S. Ruhman, J. Chem. Phys. **98**, 8337 (1993).

[28] I. Benjamin and R. M. Whitnell, Chem. Phys. Lett. **204**, 45 (1993).

[29] V. S. Batista and D. F. Coker, J. Chem. Phys. **106**, 7102 (1997).

[30] V. S. Batista and D. F. Coker, J. Chem. Phys. **105**, 4033 (1996).

[31] V. S. Batista and D. F. Coker, J. Chem. Phys. **106**, 6923 (1997).

[32] I. Last and T. F. George, J. Chem. Phys. **86**, 3787 (1987).

[33] J. C. Tully, J. Chem. Phys. **93**, 1061 (1990).

[34] S. Hammes-Schiffer and J. C. Tully, J. Chem. Phys. **101**, 4657 (1994).

[35] D. F. Coker and L. Xiao, J. Chem. Phys. **102**, 496 (1995).

[36] D. F. Coker, Computer simulation methods for nonadiabatic dynamics in condensed systems, in *Computer Simulation in Chemical Physics*, edited by M. P. Allen and D. J. Tildesley, pp. 315–377, Kluwer, Dordrecht, 1993.

[37] J. Faeder and R. Parson, J. Chem. Phys., in press.

[38] A. D. Buckingham, P. W. Fowler, and A. J. Stone, Internat. Rev. Phys. Chem. **5**, 107 (1986).

[39] A. J. Stone, Chem. Phys. Lett. **83**, 233 (1981).

[40] A. J. Stone and M. Alderton, Mol. Phys. **56**, 1047 (1985).

[41] A. J. Stone, Chem. Phys. Lett. **155**, 102 (1989).

[42] A. J. Stone, *The Theory of Intermolecular Forces*, Oxford, New York, 1996.

[43] C. A. Hunter, J. K. M. Sanders, and A. J. Stone, Chem. Phys. **133**, 395 (1989).

[44] S. L. Price, A. J. Stone, and M. Alderton, Mol. Phys. **52**, 987 (1984).

[45] L. Greengard and V. Rokhlin, J. Comput. Phys. **73**, 325 (1987).

[46] L. Greengard, *The Rapid Evaluation of Potential Fields in Particle Systems*, MIT Press, Cambridge, MA, 1988.

[47] C. A. White and M. Head-Gordon, J. Chem. Phys. **101**, 6593 (1994).

[48] A. J. Stone and R. J. A. Tough, Chem. Phys. Lett. **110**, 123 (1984).

[49] C. A. White, B. G. Johnson, P. M. W. Gill, and M. Head-Gordon, Chem. Phys. Lett. **230**, 8 (1994).

[50] A. J. Stone, Mol. Phys. **56**, 1065 (1985).

[51] P. E. Maslen, J. Faeder, and R. Parson, Chem. Phys. Lett. **263**, 63 (1996).

[52] C. G. Gray and K. E. Gubbins, *Theory of Molecular Fluids*, volume 1, Clarendon, Oxford, 1984.

[53] C. E. Dykstra, *Ab Initio calculations of the structures and properties of molecules*, Elsevier, Amsterdam, 1988.

[54] C. S. Murthy, S. F. O'Shea, and I. R. McDonald, Mol. Phys. **50**, 531 (1983).

[55] M. J. Weida and D. J. Nesbitt, J. Chem. Phys. **105**, 10210 (1996).

[56] MOLPRO, a package of ab initio programs by H.-J. Werner and P. J. Knowles, with contributions from J. Almlöf, R. D. Amos, M. J. O. Deegan, S. T. Elbert, C. Hampel, W. Meyer, K. Peterson, R. Pitzer, A. J. Stone, and P. R. Taylor, version 94.3 (1994).

[57] B. T. Thole, Chem. Phys. **59**, 341 (1981).

[58] W. H. Press, S. A. Teukolsky, W. T. Vetterling, and B. P. Flannery, *Numerical Recipes in C: The Art of Scientific Computing*, Cambridge University Press, New York, 2nd edition, 1992.

[59] Y. Zhao, C. C. Arnold, and D. M. Neumark, J. Chem. Soc. Faraday Trans. **89**, 1449 (1993).

[60] Y. Zhao, I. Yourshaw, G. Reiser, C. C. Arnold, and D. M. Neumark, J. Chem. Phys. **101**, 6538 (1994).

[61] D. G. Truhlar, K. Onda, R. A. Eades, and D. A. Dixon, Int. J. Quantum Chem. Symposium **13**, 601 (1979).

[62] J. Schnitker and P. J. Rossky, J. Chem. Phys. **86**, 3462 (1987).

[63] B. T. Thole and P. T. van Duijnen, Theor. Chim. Acta **55**, 307 (1980).

[64] H. J. Kim and J. T. Hynes, J. Chem. Phys. **93**, 5194 (1990).

[65] P. E. Maslen, J. M. Papanikolas, J. Faeder, R. Parson, and S. V. ONeil, J. Chem. Phys. **101**, 5731 (1994).

[66] M. E. Garcia, G. M. Pastor, and K. H. Bennemann, Phys. Rev. B **48**, 8388 (1993).

[67] W. Klaus, M. E. Garcia, and K. H. Bennemann, Z. Phys. D **35**, 43 (1995).

[68] S. K. Ghosh and B. M. Deb, Theor. Chim. Acta **62**, 209 (1983).

[69] R. D. Amos, N. C. Handy, P. J. Knowles, J. E. Rice, et al., J. Phys. Chem. **89**, 2186 (1985).

[70] E.-A. Reinsch, J. Chem. Phys. **83**, 5784 (1985).

[71] S. P. Karna, G. B. Talapatra, and P. N. Prasad, J. Chem. Phys. **95**, 5873 (1991).

Chapter 3

Model Hamiltonian for Dihalide Anions in Clusters

This chapter discusses evaluation of the effective Hamiltonian described in the previous chapter for a dihalide anion in various solvent clusters. The main goal here is to incorporate the experimentally known features of the potentials with an accurate treatment of the electrostatic interactions, which dominate because of the excess solute charge. The solute electronic structure is determined using high-level ab initio calculations. These ab initio potential curves of the isolated solute are corrected to agree with the experimentally known parameters. The corresponding solute wave functions, parameterized in terms of distributed multipole operators, provide the basis for determining the electrostatic interactions between the solute and solvent. The solvent is treated in a more empirical fashion, using distributed charges, point polarizabilities, and pair potentials. The greatest uncertainty lies in the short-range solute-solvent interactions, for which only rough estimates of the binding energies are available. More plentiful data about the interactions of the individual solute atoms and ions with a solvent molecule are fit to give a pairwise representation of these interactions, but there remains a substantial uncertainty in the interactions of the dissociating solute with the solvent. Therefore, the only way to validate these model potentials is by comparison of dynamical simulations

with the results of corresponding experiments, as Chapters 5–8 discuss.

Although this chapter focuses on I_2^- and ICl^- as solute molecules with argon and CO_2 as solvent molecules, the procedures apply to a range of solutes and solvents. The ab initio calculations and empirical spin-orbit corrections used to obtain the electronic structure of I_2^- and ICl^- could be applied directly to other dihalide anions. A similar parameterization could also be performed for polar molecules and ions with a limited space for valence excitations. The only restriction on solvent molecules is that charge transfer or chemical reaction between solute and solvent not be important in the excitation energy range of interest.

The chapter is organized as follows. The first section describes the electronic structure of I_2^- and ICl^- as determined by high-level ab initio calculations [1] and discusses how the properties of the low-lying electronic states affect the photodissociation dynamics. Only the first part of this section, describing the basic solute properties, and the last two parts, describing the solute wave functions and charge distributions, are necessary for a qualitative understanding of the system; the remaining sections discuss details of the calculations and comparison to experiments and previous calculations. The second section discusses the solvent model for argon and CO_2, which includes the solvent charge distribution, solvent electronic polarizabilities, and short-range solvent-solvent interactions. The third section describes methods for parameterizing the short-range solute-solvent interactions, which is possibly the most difficult step in determining the model for the system. Although some general guidelines are discussed, the procedures outlined in this section are the most system-specific. The final section presents some conclusions.

3.1 Electronic Structure of I_2^- and ICl^-

3.1.1 Basic Properties

The dihalide anions, one electron short of a complete valence shell, behave like one-electron molecules, with the position of the hole determining the symmetry of the electronic state. Considering the valence s electrons as occupying a closed subshell, there are 11 valence p electrons that must be placed into 6 valence p orbitals—σ, π, π^*, and σ^*—as shown in the orbital correlation diagram of Fig. 3.1. In the absence of spin-orbit splitting, there are four distinct energy levels arising from a total of 12 molecular states, 2 $^2\Sigma$ and 2 $^2\Pi$, which all dissociate to give a ^2P halogen atom and a ^1S halide anion. These states are referred to as the case (a) states because they are the eigenstates of the solute Hamiltonian, $\hat{h}^C$, when Hund's case (a) electronic angular momentum coupling is a valid approximation, i.e. in the absence of spin-orbit coupling. The potential curves for these case (a) states in I_2^- and ICl^- are shown in Fig. 3.2(a). There is a single asymptote for the homonuclear dihalides and two asymptotes for the heteronuclear dihalides, split by the electron affinity difference of the two halogens. In the homonuclear dihalides there is an additional inversion symmetry that is broken only by the presence of an asymmetric solvent field.

The Hund's case (a) curves illustrate several important points. First, there is a strong attraction in the Σ bonding state, while the remaining curves are repulsive or only slightly attractive. Second, the Σ^* antibonding state lies above the Π^* antibonding state at the equilibrium bond length, R_e, which strongly influences the character of the spin-orbit coupled excited states, as discussed below. Finally, there is a crossing between the Σ^* and Π^* states at intermediate bond lengths, which is due to the interaction between the positive

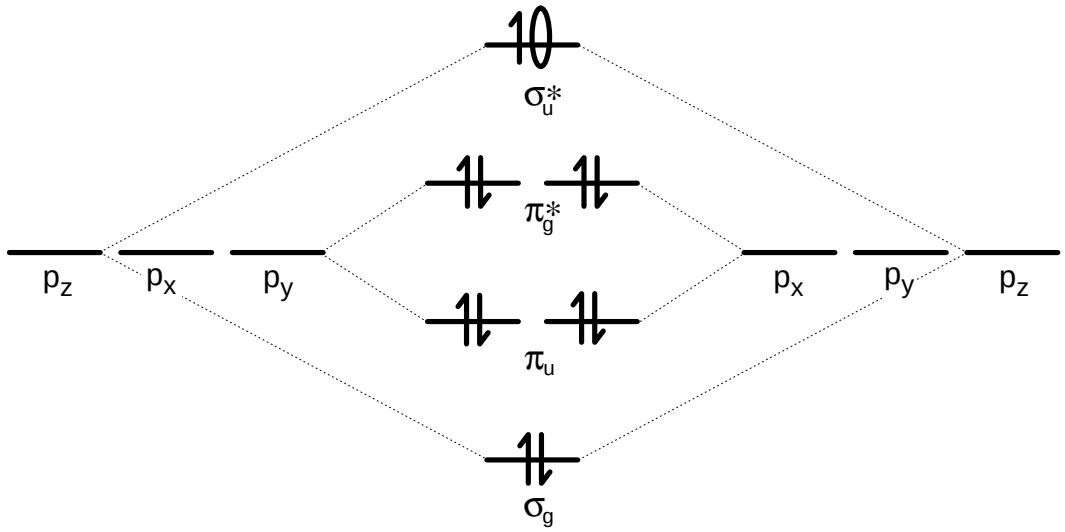

Figure 3.1: Orbital correlation diagram for X_2^- without spin-orbit coupling [Hund's case (a)]. There are six doublet states corresponding to the electron hole occupying one of the six valence orbitals. The symmetry of the total wave function is simply that of the orbital containing the hole.

quadrupole moment of the neutral atom and the negative charge of the ion. This interaction is attractive for the Σ states, and repulsive for the Π states.

In addition to being useful for understanding the electronic structure of these anions, the case (a) states are important for calculations because most ab initio programs do not include spin-orbit coupling. In the calculations described below, the case (a) states are determined using the ab initio program MOLPRO and then used as a basis for computing a semiempirical spin-orbit Hamiltonian. Because this Hamiltonian takes complex values, it is more convenient to evaluate $\hat{h}^{\text{eff}}$ using the case (a) basis states, which are real.

The inclusion of spin-orbit coupling splits the four Hund's case (a) levels into six, and lifts the degeneracy of the atomic $^2P_{3/2}$ and $^2P_{1/2}$ states, giving rise to two asymptotes in I_2^- and four asymptotes in ICl^-, as illustrated in Fig. 3.2(b). An orbital correlation diagram based on the Hund's case (c) atomic states is shown in Fig. 3.3. Although the Hund's case (a) labels are

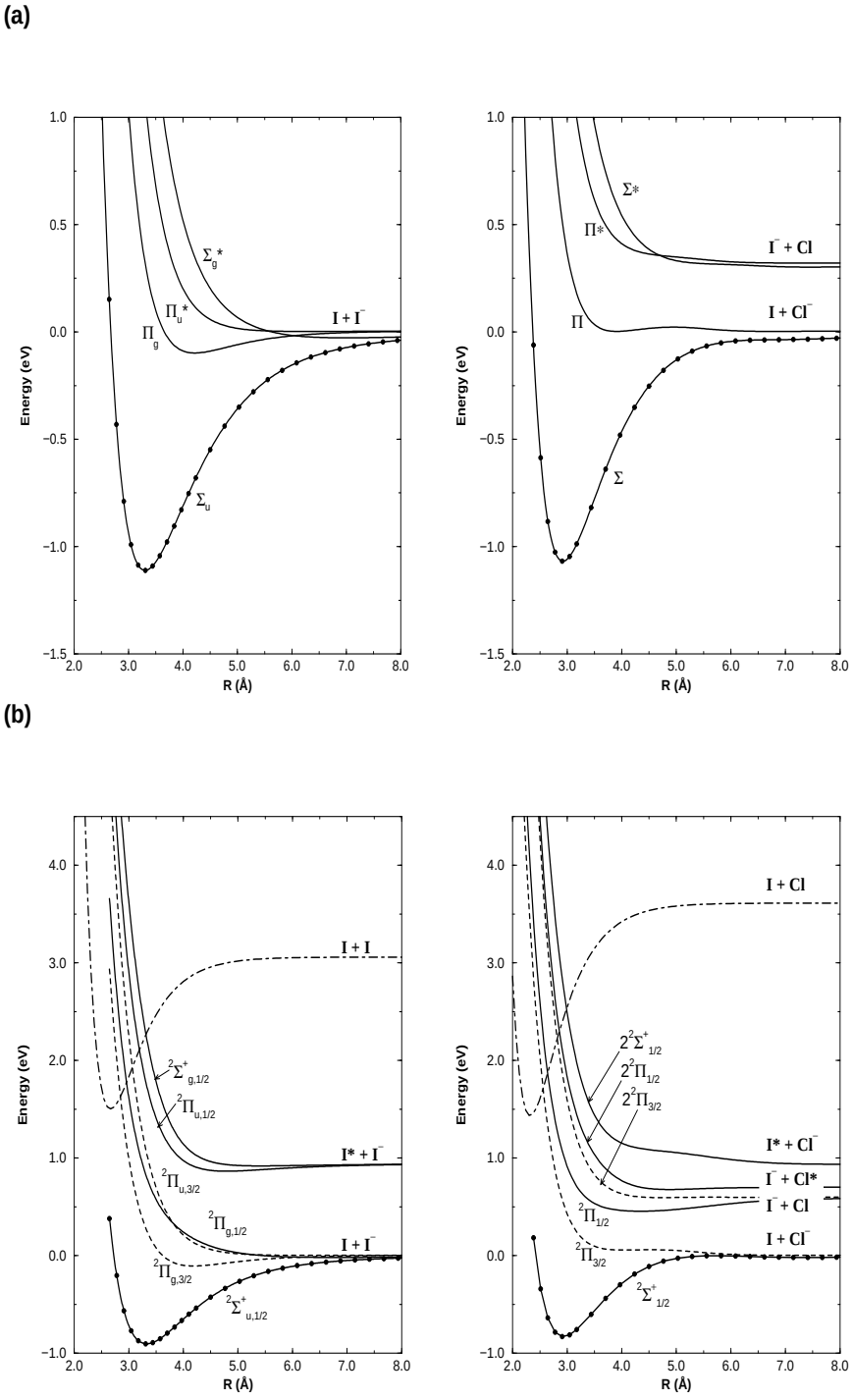

Figure 3.2: Ab initio potential curves for ICl^- and I_2^-. (a) Without spin-orbit. (b) Including spin-orbit coupling. The Hund's case (a) labels used in (b) are approximately valid near R_e, but become inappropriate as the bond dissociates (see Sec. 3.1.7). Parameters for the neutral curves were taken from Ref. 2.

Table 3.1: Electron affinities and spin-orbit splittings of the halogen atoms.

Atom	Electron affinity[a] (eV)	Spin-orbit splitting (eV)
F	3.4012	0.0510[b]
Cl	3.6127	0.1094[c]
Br	3.3636	0.4569[d]
I	3.0591	0.9427[d]

[a] Ref. 3.
[b] Ref. 4.
[c] Ref. 5.
[d] Ref. 6.

still used to describe the curves, only Ω, the projection of the total electronic angular momentum onto the internuclear axis, remains valid. In I_2^- the g and u parity labels also remain valid.

At long bond lengths, the case (c) coupling picture completely describes the states of the system. In the case of atomic iodine $^2P_{3/2}$ and $^2P_{1/2}$ states are split by about 1 eV; other values of the spin-orbit coupling are shown in Table 3.1.

At bond lengths near the equilibrium separation, the bonding interaction is comparable to the spin-orbit coupling, so a hybrid of the case (a) and case (c) pictures governs the states. The case (c) states are a mixture of the case (a) states with the dominant case (a) state determining the approximate symmetry label. The dominant case (a) state comprises at least 90% of the wave function at R_e (see Sec. 3.1.7), so the case (a) labels provide a good description near the equilibrium bond distance. This mixing at R_e is important experimentally, however, because the transitions that have been used to study these systems (see Fig. 3.4) rely on mixing of the Σ^* character into one of the Π states for intensity. The perpendicular $\Sigma \rightarrow \Pi$ transition is too

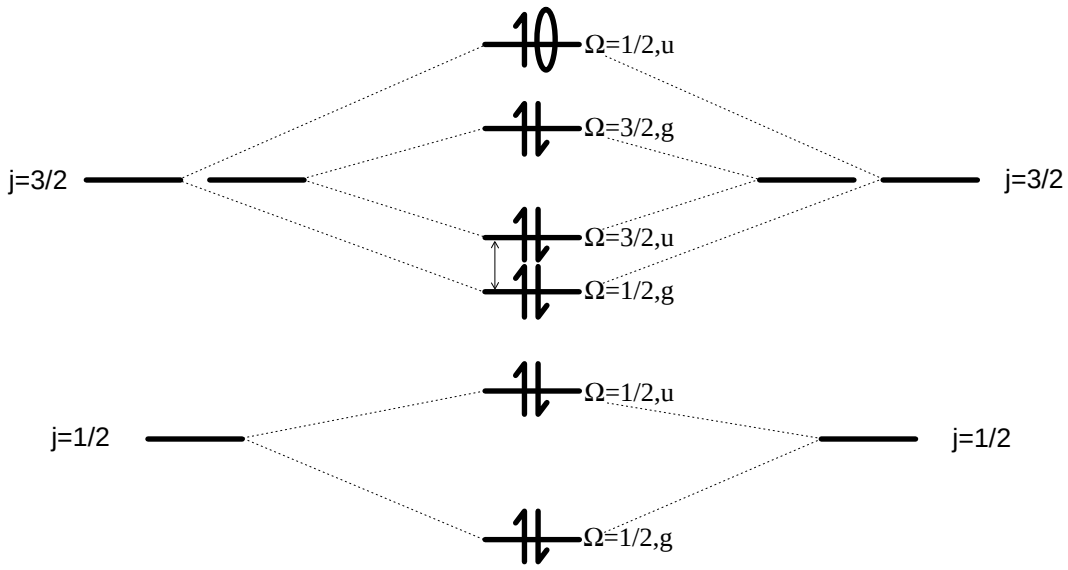

Figure 3.3: Orbital correlation diagram for X_2^- including spin-orbit coupling [Hund's case (c)]. There are six doublet states corresponding to the electron hole occupying one of the six valence orbitals. As the bond coupling increases, the orbitals indicated by the arrow cross because the upper and lower orbitals correlate to bonding and antibonding orbitals respectively.

weak on its own to be used in the experiments, while the parallel $\Sigma \rightarrow \Sigma^*$ transition moment is always large (see Table 3.5). The mixing is also important because the bonding and antibonding character of each state determines the direction of excess charge flow. The fact that the character of the excited state wave function changes dramatically as the molecule dissociates plays a key role in the dynamics, as discussed in subsequent chapters. The importance of the antibonding states for both the transition moments and the charge flow demonstrates the need to include all four of the low-lying case (a) electronic states in the solute Hamiltonian.

The isolated molecule potential curves including spin-orbit coupling that are used in the simulations of I_2^- and ICl^- photodissociation are shown in Fig. 3.4. The curves differ from the ab initio curves in Fig. 3.2 in that they have

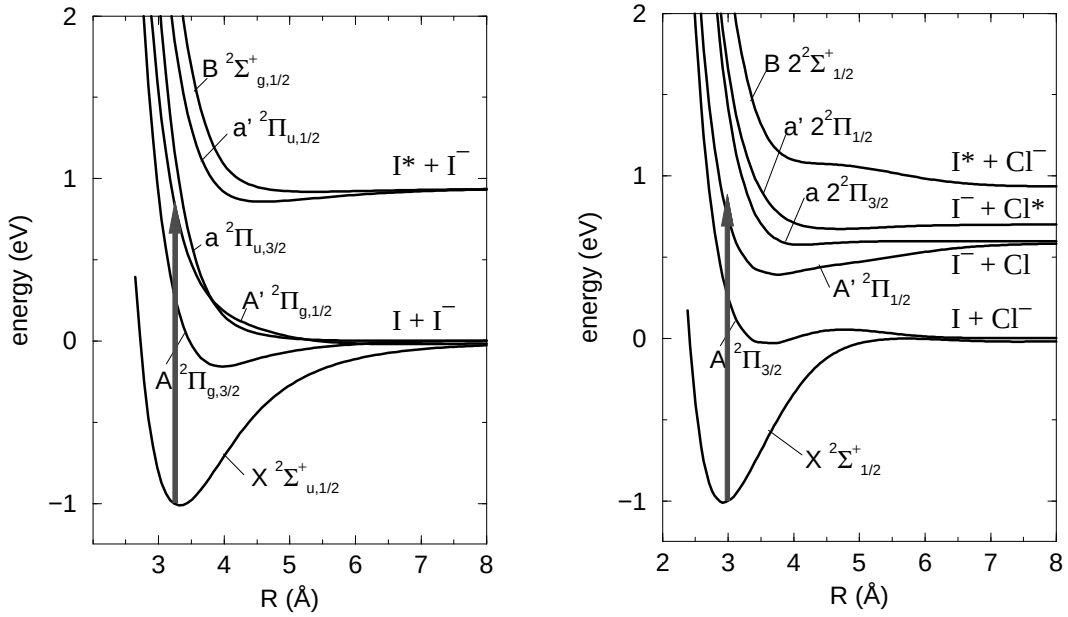

Figure 3.4: Scaled potential curves for I_2^- and ICl^-. The ground state of each molecule has been scaled to match the experimental well depths, while the excited states have been shifted by the same amount to preserve the energy spacings. The transitions used to excite the solute in the photodissociation experiments are indicated by the arrows.

been scaled to reproduce the experimentally known well depth in the ground electronic state, which is 1.01 eV for both I_2^- [7] and ICl^- [8]. Because the energy gaps between the ground and excited states are in good agreement with experiment at R_e (see Sec. 3.1.6), the excited states are scaled by the same amount as the ground state to preserve the spacings between states. Details of the scaling procedure are described in Sec. 3.1.4. Both anions have slight wells in several of their excited states, which are increased by the scaling procedure. In I_2^- the A state well depth of 160 meV at 4.0 Å is deep enough to create permanently trapped metastable species, which are observed experimentally (see Chapter 5). In ICl^- the A state is also slightly bound, but there is also a more substantial well in the A' state on which photodissociation occurs. The role of these features in ICl^- is so far less clear.

3.1.2 Previous Experiments and Calculations

There is relatively little experimental information about the electronic structure of I_2^- and ICl^- in the gas phase. Only the ground state potential of I_2^- has been directly characterized by spectroscopic techniques [7]. The bond dissociation energies of both anions in the ground state have been estimated by other techniques [8–12], although there is considerable variation among the values. Absorption spectra from photodissociation experiments have been reported for the band around 700 nm [8, 13]. The only other gas phase data available are from dissociative electron attachment measurements [14, 15], which yield information about the anion curves near the neutral geometry.

For I_2^- the electronic absorption spectrum and the frequencies of several vibrational transitions have been measured both in crystal matrices and solution [16, 17]. Chen and Wentworth [9] have combined the experimental data for most of the diatomic halogen anions to create semiempirical potential energy curves for all of the states considered here. Recently, they have improved these fits by incorporating newer data [18, 19]. It is important to point out, however, that while these fits combine the available experimental data, there are no direct experimental measurements of most of the spectroscopic quantities that are extracted from these curves. Only the transition energies, the vertical electron affinities, the bond dissociation energy of the ground electronic state, and vibrational frequencies of the ground electronic state have been measured directly. For example, the equilibrium bond length of the ground electronic state was estimated by summing the ionic and covalent radii of iodine [18, 19]. It is also unknown what effect matrices or solutions have on the measurements to which the curves were fit. Zanni et al. have re-

cently used photoelectron spectroscopy to obtain the first direct measurements of the equilibrium bond length and the bond dissociation energy [7]. They have also used a resonance Raman technique to obtain the equilibrium vibrational frequency. Their measurements have shown that the previous values of R_e and D_e were in error by about 5–10%.

Less data is available for ICl^-. The only electronic absorption spectrum other than the single band cited above was measured in solution by Shida et al. [17]. The observed peak positions are nearly identical to those reported for I_2^- in the same work, a result which is inconsistent with the limited gas phase data [8] and the present calculations.

There have also been few ab initio calculations performed on either of these molecules, and none, to our knowledge, include the effects of spin-orbit coupling. The first calculations on both molecules were due to Tasker et al. [20] with a valence bond method using core potentials and a small basis consisting of only s and p functions. This is the only calculation of ICl^- of which we are aware. The excited states were calculated and transition energies were reported, but without the inclusion of spin-orbit coupling it is difficult to assess the meaning of these energies. For example, the $^2\Pi_{3/2}$ and $^2\Pi_{1/2}$ states of these molecules, which are degenerate in the absence of spin-orbit coupling, are split by about 0.5 eV. Bowmaker et al. performed calculations on I_2^- at the SCF level [21]. More recently, Danovich et al. used relativistic core potentials to perform calculations on I_2^- and several other iodo-containing species [22]. They reported results for the ground state, comparable to our results but omitting spin-orbit coupling. While their dissociation energies show fortuitous agreement with experiment, our experience is that inclusion of spin-orbit coupling reduces the calculated dissociation energies by as much as 50%.

Gellene and Sharp have also recently performed calculations of the I_2^- ground state using coupled cluster and density functional methods [23]. Applying a semiempirical correction for the spin-orbit coupling, they obtain good values for the I_2^- well depth using the density functional methods but find too shallow a well using the coupled cluster methods.

We have performed multireference configuration interaction (MRCI) calculations of the ground and excited states of these ions and incorporated the effects of spin-orbit coupling by adding an empirical one-electron operator to the ab initio Hamiltonian. The results represent the most complete theoretical treatment of these ions to date.

3.1.3 Details of the Ab Initio Calculations

The ab initio calculations were performed with the MOLPRO program [24], using the internally contracted multi-reference CISD method developed by Knowles and Werner [25, 26]. The orbitals and reference configurations were obtained from state-averaged complete active space (CASSCF) calculations [27, 28] including the lowest two Σ states, the lowest two Π_x states, and the lowest two Π_y states. The six states arise from the ^2P states of the neutral halogen and the ^1S state of the halogen ion. All six states were assigned equal weight during the orbital optimization.

Effective core potentials were avoided in favor of all-electron basis sets, largely because of doubts about the accuracy of the available core potentials for iodine. The medium-sized polarized basis sets of Sadlej [29, 30] were used in all of the calculations. The suggested additional polarization functions have also been included so that the basis sets are (13s10p4d)/[7s5p2d] and (19s15p12d4f)/[11s9p6d2f] for Cl and I respectively. In order to roughly equal-

ize the error in the CISD electron affinities of Cl and I, the orbital exponents of chlorine's first contracted d function (0.9528 and 0.3580) have been scaled by 0.9195. The resulting exponents are 0.8761 and 0.3292.

To reduce the cost of the CASSCF calculations, the inner orbitals of the dihalides were optimized via a single-reference all-electron SCF calculation, and then frozen during the CASSCF calculation. During the CISD calculation, only the six valence p orbitals were correlated. Including the valence s orbitals in the correlation space had only a small effect, decreasing the well depth for the ground state of I_2^- by 18 meV, or 2%. We opted to exclude the valence s orbitals from the correlation space because basis set superposition error rises very rapidly with the number of correlated electrons, and is especially problematic for weakly-bound homonuclear molecules.

Table 3.2 contains the number of active orbitals in the SCF, CASSCF and CISD calculations. Size consistency errors inherent in the CISD energy were ameliorated by adding an approximate cluster correction due to Pople [24]. The charge distributions of the wave functions were obtained using the distributed multipole analysis (DMA) developed by Stone [31].

Table 3.2: Number of active orbitals belonging to each irreducible representation of the C_{2v} point group for ICl^- and I_2^-.

molecule	method	A_1	B_1	B_2	A_2
ICl^-	SCF	18	8	8	2
	CASSCF	8	4	4	1
	CISD	2	2	2	0
I_2^-	SCF	26	12	12	4
	CASSCF	18	8	8	2
	CISD	2	2	2	0

3.1.4 Empirical Treatment of Spin-Orbit Coupling

The ab initio calculations leave out spin-orbit coupling, which we include by setting up and diagonalizing the effective Hamiltonian operator

$$\hat{h}^C = \hat{h}^a + \hat{h}^{\mathrm{SO}}, \tag{3.1}$$

where $\hat{h}^a$ is the ab initio Hamiltonian and $\hat{h}^{\mathrm{SO}}$ is a semiempirical Hamiltonian described below. Since spin must be considered, the basis set for this Hamiltonian consists of a direct product of the six ab initio spatial wave functions with the doublet spin functions α and β, resulting in 12 basis states. $\hat{h}^a$ is thus represented by a diagonal 12×12 matrix with the ab initio energies in degenerate pairs on the diagonal.

The spin-orbit coupling between these basis states is approximated by the one electron Hamiltonian [32]

$$\hat{h}^{\mathrm{SO}} = \sum_i \frac{\alpha^2}{2} \left(\frac{Z_A}{r_{iA}^3} \hat{\mathbf{l}}_{iA} + \frac{Z_B}{r_{iB}^3} \hat{\mathbf{l}}_{iB} \right) \cdot \hat{\mathbf{s}}_i, \tag{3.2}$$

where $\hat{\mathbf{l}}_{iN}$ is the orbital angular momentum of electron i about nucleus N, etc. In principle, the matrix elements of this operator could be evaluated exactly from the ab initio wave functions and the spin components. Such a procedure would, however, be very unlikely to give the correct asymptotic spin-orbit splittings for the atoms. We chose instead to approximate the Z/r^3 operators with the experimental values for the appropriate atomic spin-orbit coupling

constants, ζ, so that

$$\hat{h}^{\mathrm{SO}} \approx \sum_i \frac{\alpha^2}{2} \left(\zeta_A \hat{\mathbf{l}}_{iA} + \zeta_B \hat{\mathbf{l}}_{iB} \right) \cdot \hat{\mathbf{s}}_i. \tag{3.3}$$

Evaluating this operator involves computing matrix elements of the spin angular momentum operator, which are just the components of the 2×2 Pauli spin matrices, together with matrix elements of the orbital angular momentum operator, which were evaluated exactly using the ab initio wave functions. Because the radial operator Z/r^3 decays rapidly as the electron moves away from the nucleus, matrix elements of the spatial part of the spin-orbit operator connecting atomic orbitals on different nuclei were set to zero. In practice two-center integrals were excluded by setting to zero the two-center contributions to the ab initio one particle density matrices. This procedure gives the exact asymptotic values for the atomic spin-orbit splittings, because the angular integrals attain their correct values at large internuclear separations. As the atoms are brought together the spin-orbit coupling varies *only* because (1) the energy separations between the basis states change, and (2) the atomic angular momenta $\hat{\mathbf{l}}_A$ and $\hat{\mathbf{l}}_B$ change. The radial components ζ_A and ζ_B are held fixed at the atomic values.

The model also requires the nonadiabatic coupling matrix elements with respect to the solute bond length. These couplings are also computed in MOLPRO directly from the ab initio wave functions. They have been computed for ICl^-; however, in the case of the states considered in the I_2^- manifold, all of the couplings vanish by symmetry.

To parameterize the model, the matrix elements of $\hat{h}^C$ are computed at a series of solute geometries. In the case of ICl^- and I_2^-, the lowest six

eigenstates are computed at a total of 50 geometries. Because $\hat{h}^{\mathrm{SO}}$ is complex and the remaining terms in $\hat{h}^{C}$ are real, it is convenient to use the ab initio case (a) eigenstates as the actual basis states for the model. In this representation $\hat{h}^{a}$ is diagonal and its matrix elements are simply the ab initio energies, while $\hat{h}^{\mathrm{SO}}$ has both diagonal and off-diagonal terms. Damped cubic splines are used to interpolate the values of $\hat{h}^{C}$ between the grid points.

We employ a simple scaling procedure to adjust the ground state well to match the best known experimental values. The adjustment is done on the case (a) curves to avoid extra transformations between the case (a) and case (c) states. It can be seen from Tables 3.6 and 3.7 that in the region near R_e, there is little mixing of the ground case (a) Σ state with the excited states. Therefore, scaling the Σ state has little effect on the energies of the excited states. All of the case (a) states are shifted by the same amount in order to preserve the energy spacings between the states, which agree well with the experiments. The amount of the shift is given by

$$\Delta(R) = \left(\frac{c-1}{2}\right)\left(1 - \tanh\left(\frac{R-R_c}{w_c}\right)\right)\left[V^{\Sigma}(R) - V^{\Sigma}(\infty)\right], \qquad (3.4)$$

where the parameters c, R_c, and w_c are chosen to give the correct well depth for the ground state without shifting R_e significantly (< 0.01Å). In the simulations of later chapters, we have not adjusted R_e of the ground state to match the experimental value, although we have compensated for this discrepancy in simulations of the photoelectron spectra.

3.1.5 Simulation of Absorption Spectra

Electronic absorption spectra from the ground electronic and vibrational states are computed from the calculated curves and transition moments using a modified reflection approximation [33] described by Heller [34]. The total absorption cross section at frequency ω from the initial state i to the final state f is given by

$$\sigma_{if}(\omega) = 4\pi^2 \alpha a_0^2 \omega \left| V_f'(q_T) \right|^{-1} \left| \mu_{if}(q_T) \psi_i(q_T) \right|^2 , \tag{3.5}$$

where V_f is the upper state potential, q_T is the classical turning point on the upper state, and μ_{if} and ψ_i are the transition moments and ground state vibrational wave functions respectively. For a given ω and initial state energy E_i, the classical turning point is defined by $\hbar\omega = V_f(q_T) - E_i$. We have approximated the ground vibrational state by a harmonic oscillator of frequency ω_e, determined from the calculated ground state curve, a minor approximation given the small anharmonicities of the ground states (see Sec. 3.1.6). This method is convenient, and, though approximate, should give good results for our application. As a test, we have computed the absorption spectrum of ICl^- using an exact time-dependent quantum method and found deviations much smaller than the expected accuracy of the electronic structure calculations.

3.1.6 Results and Comparison with Previous Work

The calculated ab initio potential curves for the lowest six electronic states of I_2^- and ICl^- are shown in Fig. 3.2. The curves in part (a) of the figure represent the raw data from the ab initio calculation, which does not include spin-orbit coupling. These Hund's case (a) basis states are used to construct

the effective spin-orbit Hamiltonian described in Sec. 3.1.4. All of the states considered here correspond to a hole in a p atomic orbital on either I or Cl. In the bonding region, this correlates to a hole in either a σ^* or π^* antibonding orbital, giving rise to the bonding Σ and Π states respectively, or to a hole in σ or π bonding orbitals, giving rise to the Σ^* and Π^* states. In I_2^- the Hund's case (a) basis states are degenerate at infinite separation, corresponding to $I^- + I\ (^2P)$. In ICl^- the asymptotic energies correspond to $Cl^- + I\ (^2P)$ and $I^- + Cl\ (^2P)$, and they are split by the electron affinity difference between I and Cl. The calculated value of this difference, 0.596 eV, compares well with the experimental value of 0.553 eV [3], though it should be noted that the basis set was adjusted to minimize the discrepancy.

Tables 3.3 and 3.4 present the spectroscopic constants extracted from the potential curves and also a comparison with previous experimental and theoretical results. We have not presented the vertical electron affinities of I_2 or ICl, because the ab initio calculations do not converge well for bond lengths much shorter than R_e. As can be seen from Fig. 3.2, the equilibrium bond length of the neutral is in both cases considerably shorter than that of the ion.

Comparison of calculated and measured bond dissociation energies in the ground state shows that the calculated D_e is in error by about 10–20%. This shortfall is probably due to inadequacies in the one electron basis sets. Teichteil and Pelissier [35] have reported similar problems in obtaining accurate results for D_e in I_2. There is good agreement between the current results without spin-orbit coupling and the best previous calculation [22], but the good agreement between the results neglecting spin-orbit coupling and experiment is fortuitous. Neglecting spin-orbit coupling raises the energy of the asymptote with respect to the well because the mixing is much stronger at long bond lengths where the

Table 3.3: Spectroscopic constants for I_2^-.

State		T_e (eV)	R_e (Å)	D_e (eV)	ω_e (cm^{-1})	$\omega_e x_e$ (cm^{-1})
$^2\Sigma^+_{u,1/2}$	current calc.	0.0	3.33	0.905	99.9	0.35
	current calc. scaled [a]	0.0	3.32	1.013	106.4	0.36
	current calc. case (a)	0.0	3.35	1.111	105.9	0.31
	prev. calc. w/o s.o.c. [b]	0.0	3.23	1.111	112.6	0.35
	semi-empirical [c]	0.0	3.40	1.113	116	0.37
	expt. [d]	0.0	3.205	1.014	110	0.37
$^2\Pi_{g,3/2}$	current calc.	1.16	4.18	0.11	38	
	current calc. scaled	1.17	3.96	0.16	55	
	semi-empirical	1.14	4.06	0.200	46	
$^2\Pi_{g,1/2}$	current calc.	1.71	unbound			
	semi-empirical	1.55	4.71	0.06	23	
$^2\Pi_{u,3/2}$	current calc.	1.96	unbound			
	semi-empirical	1.65	4.67	0.08	27	
$^2\Pi_{u,1/2}$	current calc.	2.66	4.79	0.08	25	
	semi-empirical	2.35	4.33	0.18	40	
$^2\Sigma^+_{g,1/2}$	current calc.	3.14	5.40	0.025	12	
	semi-empirical	3.10	5.24	0.11	24	

[a] See Sec. 3.1.4. Scaling has a minimal effect on all but the lowest two states.
[b] Ref. 22. QCISD using relativistic effective core potentials.
[c] Ref. 19.
[d] Ref. 7.

Table 3.4: Spectroscopic constants for ICl^-.

State		T_e (eV)	R_e (Å)	D_e (eV)	ω_e (cm^{-1})	ω_e (cm^{-1})
$^2\Sigma^+_{1/2}$	current calc.	0.0	2.93	0.831	179.5	0.9
	current calc. scaled [a]	0.0	2.93	1.011	195.8	0.9
	current calc. case (a)	0.0	2.92	1.068	184.1	
	prev. calc. w/o s.o.c. [b]	0.0	3.07	0.73	159	0.9
	expt. [c]	0.0	–	1.01	–	
$^2\Pi_{3/2}$	current calc.	1.36	unbound			
	current calc. scaled	1.37	3.60	0.030	75	
$^2\Pi_{1/2}$	current calc.	1.86	4.36	0.14	33	
	current calc. scaled	1.86	3.73	0.20	68	
$2^2\Pi_{3/2}$	current calc.	2.63	unbound			
	current calc. scaled	2.64	4.11	0.02	45	
$2^2\Pi_{1/2}$	current calc.	2.86	4.88	0.028	31	
	current calc. scaled	2.87	4.68	0.031	28	
$2^2\Sigma^+_{1/2}$	current calc.	3.57	unbound			
	current calc. scaled	3.58	unbound			

[a] See Sec. 3.1.4.

[b] Ref. 20. Valence bond using small basis set and nonrelativistic core potentials.

[c] Ref. 8.

Hund's case (a) states are degenerate. The current calculations overestimate the experimental value of R_e by about 5%. The value reported by Danovich et al. [22] is closer to the experiment, which may be due to their use of effective core potentials, or to our neglect of other relativistic effects.

The excited state curves are all unbound or very weakly bound in comparison with the ground state, as one would expect from simple molecular orbital considerations. Through comparison with the known bond dissociation energies of Xe_2^+, Chen and Wentworth [18, 19] have suggested that all of the excited states of I_2^- are slightly bound. Given the limits of the current calculations, we do not expect these wells to be accurately reproduced, and there are differences between our calculated values and the semiempirical fits.

Simulated absorption spectra for I_2^- and ICl^- are shown in Figs. 3.5 and 3.6. In I_2^- there are two prominent bands at about 750 and 400 nm. The 400 nm band corresponds to a charge transfer transition and is much more intense than the band at 700 nm, which borrows its intensity from the 400 nm band. The weak band at about 1100 nm arises from a perpendicular $\Sigma \rightarrow \Pi$ transition. In ICl^- there are three prominent bands. The charge transfer band at 350 nm is by far the most intense, with the other two bands deriving their intensity through mixing of Σ and Σ^* character. This intensity borrowing is substantially weaker in ICl^-. There are also two very weak perpendicular transitions at about 500 and 900 nm.

Direct comparison of the simulated spectra with experimental data is shown in Table 3.5. For the three optically allowed transitions of I_2^-, the agreement is quite good. Particularly encouraging is the agreement with the positions, widths, and absolute cross sections of the $^2\Pi_{1/2}$ absorption bands observed by gas phase photodissociation [8, 13]. Because the $\Sigma \rightarrow \Pi$ transition

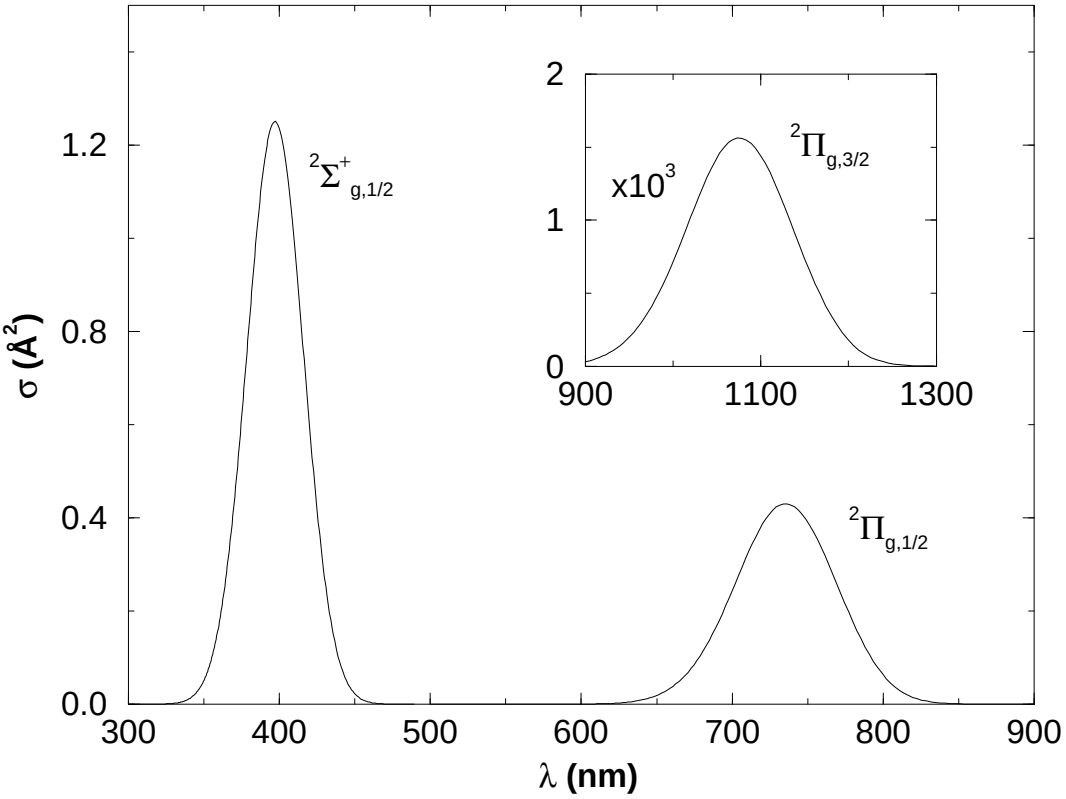

Figure 3.5: Calculated absorption spectrum from the ground state of I_2^-. Inset shows the weak infrared band due to the perpendicular transition to the $^2\Pi_{g,3/2}$ state.

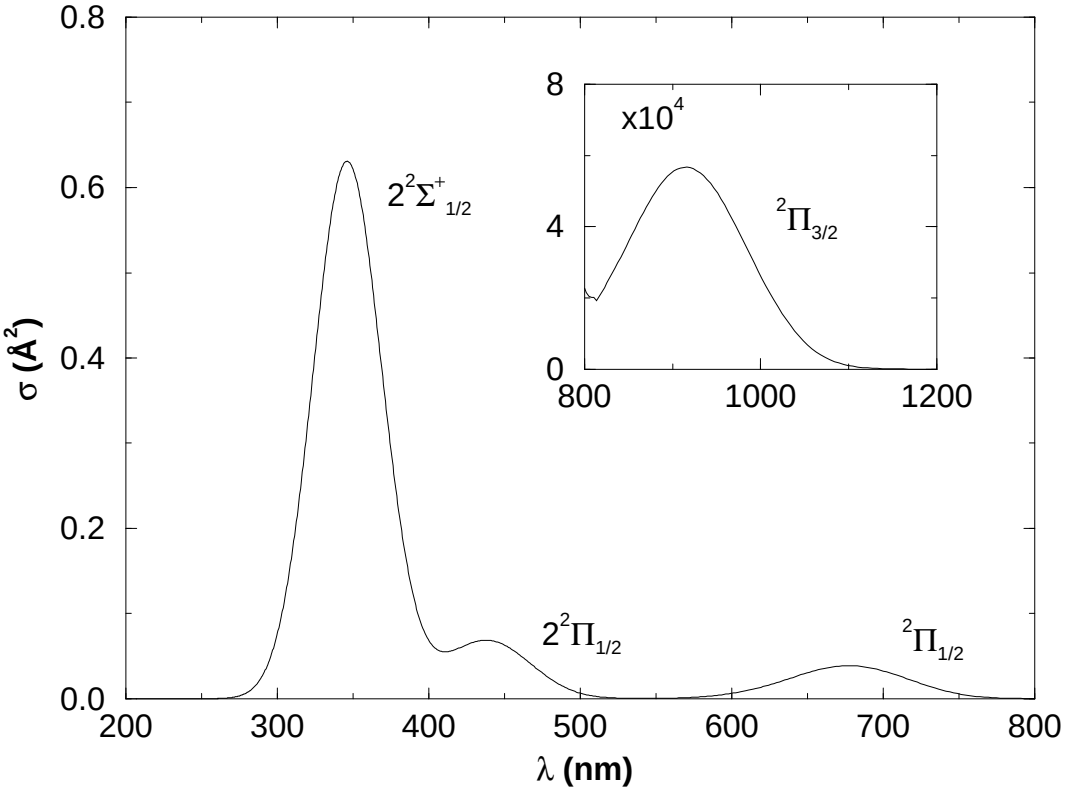

Figure 3.6: Calculated absorption spectrum from the ground state of ICl^-. Inset shows the weak infrared band due to the perpendicular transition to the $^2\Pi_{3/2}$ state.

moment is very small, almost all the oscillator strength of this band is derived from $\Pi \leftrightarrow \Sigma^*$ mixing induced by the spin-orbit coupling. The absolute cross section should thus be sensitive to the extent of this mixing, and the good agreement, to within the reported experimental error, suggests that it is correct at R_e. The case (a) character of the wave functions is shown at several bond lengths in Tables 3.6 and 3.7. The $^2\Pi_{1/2}$ state has 9.8% Σ^* character in I_2^- but only 1.6% Σ^* in ICl^-, which accounts for the six-fold reduction in the intensity of this band relative to the $^2\Sigma^+_{1/2}$ band in going from I_2^- to ICl^-.

There is significant disagreement in the excitation energies to the two excited states of Π_u symmetry in I_2^-. This transition is dipole forbidden, so its appearance at 585 nm (2.12 eV) in the matrix absorption spectra means that the crystal field must be causing significant mixing with states of g symmetry. It is not known whether this mixing shifts the energy of the Π_u state significantly, or whether the state involved is the $\Pi_{u,3/2}$ or the $\Pi_{u,1/2}$. Chen and Wentworth [9, 18] have assigned the 585 nm transition to the $\Pi_{u,1/2}$ state, but if the assignment were changed to $\Pi_{u,3/2}$, the agreement with our calculations would be considerably better. There is evidence from the solution data [17] for an additional absorption band around 480 nm (2.58 eV), which supports this re-assignment.

There is also some disagreement between the calculated absorption spectrum for ICl^- and the spectrum measured in solution [17]. The solution data show almost no shift in the spectra between I_2^- and ICl^-, which disagrees qualitatively with the current calculations. The origin of this discrepancy is unknown, but the good results for I_2^- combined with the good agreement for the $^2\Pi_{1/2}$ absorption of ICl^- measured by photodissociation provide some weight for the validity of the current calculations.

Table 3.5: Calculated absorption spectra from the ground electronic state compared with experimental results.

Excited State			Peak Position (eV)	Peak Position (nm)	σ_{max} (Å^2)	FHWM (eV)	Total intensity (relative units)
I_2^-	$^2\Pi_{g,3/2}$	calc.	1.16	1070	0.0016	0.16	1/280
		matrix [a]	1.08	1150		0.19	1/56
		solution [b]	1.20	1030			
	$^2\Pi_{g,1/2}$	calc.	1.69	736	0.43	0.18	1.0
		matrix	1.55	800		0.22	1.0
		solution	1.68	737			
		direct [c]	1.65	750	0.5	0.18	
	$^2\Sigma^+_{g,1/2}$	calc.	3.12	397	1.3	0.35	5.6
		matrix	3.10	400		0.55	6.1
		solution	3.13	395			
ICl^-	$^2\Pi_{3/2}$	calc.	1.36	914	0.00015	0.24	1/71
		solution	1.20	1030			
	$^2\Pi_{1/2}$	calc.	1.83	676	0.039	0.25	1
		solution	1.68	737			
		direct [d]	1.77	700	0.039	0.23	
	$2^2\Pi_{3/2}$	calc.	2.66	467	0.00097	0.46	1/22
	$2^2\Pi_{1/2}$	calc.	2.83	438	0.068	0.44	3.0
	$2^2\Sigma^+_{1/2}$	calc.	3.59	346	0.63	0.56	36
		solution	3.22	385			

[a] Ref. 16. [b] Ref. 17. [c] Ref. 13. [d] Ref. 8.

Table 3.6: Case (a) composition of the spin-orbit coupled states of I_2^- as a function of the bond length.

		% Basis Function Character			
State	R (Å)	Σ_u	Σ_g^*	Π_g	Π_u^*
$^2\Sigma^+_{u,1/2}$	R_e	95.9	0.0	0.0	4.1
	5.3	77.7	0.0	0.0	22.3
	∞	66.7	0.0	0.0	33.3
$^2\Pi_{g,3/2}$	R_e	0.0	0.0	100.0	0.0
	5.3	0.0	0.0	100.0	0.0
	∞	0.0	0.0	100.0	0.0
$^2\Pi_{g,1/2}$	R_e	0.0	9.8	90.2	0.0
	5.3	0.0	63.4	36.6	0.0
	∞	0.0	66.7	33.3	0.0
$^2\Pi_{u,3/2}$	R_e	0.0	0.0	0.0	100.0
	5.3	0.0	0.0	0.0	100.0
	∞	0.0	0.0	0.0	100.0
$^2\Pi_{u,1/2}$	R_e	4.1	0.0	0.0	95.9
	5.3	22.3	0.0	0.0	77.7
	∞	33.3	0.0	0.0	66.7
$^2\Sigma^+_{g,1/2}$	R_e	0.0	90.2	9.8	0.0
	5.3	0.0	36.6	63.4	0.0
	∞	0.0	33.3	66.7	0.0

Table 3.7: Case (a) composition of the spin-orbit coupled states of ICl^- as a function of the bond length.

		% Basis Function Character			
State	R (Å)	Σ	Σ^*	Π	Π^*
$^2\Sigma^+_{1/2}$	R_e	96.6	0.0	2.8	0.6
	5.3	68.6	3.9	25.7	1.8
	∞	66.7	0.0	33.3	0.0
$^2\Pi_{3/2}$	R_e	0.0	0.0	99.0	1.0
	5.3	0.0	0.0	96.9	3.1
	∞	0.0	0.0	100.0	0.0
$^2\Pi_{1/2}$	R_e	2.4	1.6	94.0	2.1
	5.3	17.0	47.3	24.4	11.4
	∞	0.0	66.7	0.0	33.3
$2^2\Pi_{3/2}$	R_e	0.0	0.0	1.0	99.0
	5.3	0.0	0.0	3.1	96.9
	∞	0.0	0.0	0.0	100.0
$2^2\Pi_{1/2}$	R_e	1.0	3.6	1.1	94.3
	5.3	0.1	28.6	7.6	63.0
	∞	0.0	33.3	0.0	66.7
$2^2\Sigma^+_{1/2}$	R_e	0.1	94.8	2.1	3.0
	5.3	13.7	20.2	42.4	23.8
	∞	33.3	0.0	66.7	0.0

One final point of contention arises from the assignment of the Hund's case (a) labels in dissociative electron attachment experiments [14, 15]. In these experiments, the fragment angular distributions show no evidence of mixing of different Λ states by spin-orbit coupling. This result is consistent with our observation that the Hund's case (a) character becomes dominant as the bond is shortened. In both studies, however, the highest energy peak has been assigned to a state of Π symmetry, in direct contradiction with the current calculations and other assignments based on the absorption spectra [9, 16, 18]. A crossing of the Σ^* and Π^* states cross at bond lengths shorter than R_e could account for this observation, but there is no evidence of such a crossing in the current calculations. Nevertheless, the absorption data and the current calculations strongly support the assignment of the highest electronic state as predominantly Σ in character at R_e.

3.1.7 Mixing of the Case (a) States Due to Spin-Orbit Coupling

The mixing of the case (a) states by spin-orbit coupling has been tabulated for each state of I_2^- and ICl^- at several bond lengths in Tables 3.6 and 3.7. Because Ω is a conserved quantum number, there is no mixing between Σ and Π states at any bond length for the $\Omega = 3/2$ states. The $\Omega = 1/2$ states, however, can be strongly mixed as the bond length increases from R_e. There is a competition between the bonding interactions, which favor the case (a) states, and the atomic spin-orbit coupling, which favors the case (c) states. At R_e of the ground electronic state, the bonding interactions dominate, with the case (a) character accounting for about 90% of the wave function in I_2^- and about 95% ICl^-. For the ground electronic states, which are energetically well-separated from the remaining states, the mixing is especially small. There

is substantially more mixing in I_2^- than ICl^- because the spin-orbit coupling is large for both atoms, and this accounts for the much larger cross section of the experimentally important ground state transition to the $^2\Pi_{1/2}$ state around 700 nm.

Even a small extension of the solute bond can bring about a large change in the character of the solute wave function. The $^2\Pi_{g,1/2}$ state in I_2^- and the $^2\Pi_{1/2}$ state in ICl^- each change from being over 90% Π in character at R_e to predominantly Σ^* at 5.3 Å. The polarizability of an antibonding state is negative, meaning that the electric field and the solute polarization are 180° out of phase. Thus, the polarizability of the excited states is extremely sensitive to the bond length, changing sign in this case between 3 and 5 Å. The other $\Omega = 1/2$ states also undergo substantial changes in character, most notably the $^2\Sigma^+_{g,1/2}$ ($2^2\Sigma^+_{1/2}$ in ICl^-), which is predominantly Π in character at long bond lengths.

The strong solvent electrostatic fields in clusters and condensed phases further mix the solute wave functions, as we will see in future chapters. The mixing of the solute wave functions induced by spin-orbit coupling will be critical for understanding the dynamics of photodissociation.

3.1.8 Solute Charge Distribution

The solute charge distribution is parameterized using the distributed multipole operators discussed in Chapter 2. The matrix elements of these operators are determined for each geometry at which the ab initio wave functions are calculated. When the bonding interactions are strong, the multipoles are distributed over four sites—one on each nucleus and two at equidistant points along the bond axis. At longer bond lengths, the bond sites are gradually

damped using a hyperbolic tangent switching function to reflect the localization of the wave function onto the nuclei. Multipoles through quadrupole must be included at a minimum because the open-shell halogen atoms have a substantial quadrupole moment that interacts strongly with the solvent, as we discuss in more detail below. The quadrupole moments for the valence p orbital in Cl and I from the ab initio calculation are 3.03 and 1.74 atomic units (4.08 and 2.34 Debye Å) respectively.

The absorption spectra discussed in Sec. 3.1.6 above provide the only direct test of the accuracy of the calculated multipole operators. There is apparently good agreement for the magnitudes of the parallel transition moments from the ground electronic state at equilibrium separation. There is also some evidence that the calculated perpendicular transition moments near R_e are too small. Table 3.5 suggests that perpendicular transitions should be several orders of magnitude less intense than the parallel transitions, and yet preliminary measurements of the probe absorption at very early times (< 200 fs) indicate a strong perpendicular component [36].

Aside from these measurements, the only way to determine if the charge distributions of the dissociating molecule are correct is by comparison of simulations to photofragmentation and pump-probe studies of photodissociation in clusters. Obviously, these measurements are sensitive to many factors other than the distribution of solute charge, so it is difficult to test particular components of the model. The overall agreement, however, is quite good, as we will see. There is also a growing body of evidence that the primary feature of the excited state charge distribution, namely anomalous charge switching, is a central component of both the model and the real systems.

3.2 Solvent Model

The solvent can be represented classically by distributed multipoles and polarizabilities. For both cluster solvents we have studied so far, argon and CO_2, we have found that distributed charges and single site polarizabilities are adequate for creating realistic interaction potentials. For argon, the electrostatic model consists of a single dipole polarizability, which is set to the experimental static field value. Five distributed charges are used for the CO_2 model, where the charges are taken from Murthy et al. [37]. These charges reproduce the quadrupole moment of CO_2, and in conjunction with Lennard-Jones sites on the atoms give interaction potentials that reproduce the experimentally observed structures for the dimer and trimer of $(CO_2)_n$ clusters [38]. The polarizability of CO_2 has negligible effect on the solvent-solvent interactions but has a strong interaction with the solute anion. The model includes a single site on CO_2 with different polarizabilities parallel and perpendicular to the bond. The values for all of the parameters used to describe the solvent charge distribution, the solvent-solvent interactions, and the short range solute-solvent interactions described in the next section are shown in Table 3.8.

3.3 Short-Range Solute-Solvent Interactions

The model Hamiltonian has been constructed under the basic assumption that electrostatic terms will dominate both the long-range interactions and the mixing of different solute states. The remaining terms, arising from dispersion and repulsion, provide the shape and energetics of the short-range interaction potentials. In general these terms will depend on the electronic state of the solute, but we expect that if the electrostatic terms are large, as they are

Table 3.8: Potential parameters for $I_2^-Ar_n$, $I_2^-(CO_2)_n$, and $ICl^-(CO_2)_n$.

Ar model		
Polarizability[a]		
$\alpha_{xx} = \alpha_{yy} = \alpha_{zz}$ (Å^3)	1.642	
Dispersion pseudo-charge		
q_{disp} (au)	−20.0	
Induction damping[b]		
R_{damp} (Å)	3.57	
w_{damp} (Å)	0.529	
LJ parameters	σ (Å)	ϵ (meV)
Ar–Ar[c]	3.347	12.2
Ar–I	3.662	15.9
CO_2 model		
Molecular geometry		
$R_{\text{C-O}}$ (Å)	1.16	
Charge distribution[d]	charge (au)	distance from C (Å)
$q_1 = q_5$	0.1216	1.523
$q_2 = q_4$	−0.6418	1.066
q_3	1.0404	0.000
Polarizability[a]		
α_{zz} (Å^3)	4.487	
$\alpha_{xx} = \alpha_{yy}$ (Å^3)	2.127	
Induction damping[b]		
R_{damp} (Å)	2.75	
w_{damp} (Å)	0.529	
LJ parameters	σ (Å)	ϵ (meV)
C–C[d]	2.824	2.256
O–O[d]	3.026	6.477
C–O[d]	2.925	3.823
C–I	3.805	16.33
O–I	3.200	12.56
C–Cl	3.349	10.85
O–Cl	2.700	5.633

[a] Ref. 39.
[b] See Eq. 3.7.
[c] Ref. 40.
[d] Ref. 37.

in ionic systems, the state dependence will be relatively small—too small to extract from the relatively low resolution spectroscopic data available for ionic and open-shelled systems. It is therefore justified, we believe, to use empirical state-independent parameters to describe the short-range interactions, except when the state-dependence is known to be an important effect.

The basic method of handling the short-range interactions places isotropic, pairwise Lennard-Jones (LJ) sites on all the nuclei with parameters fit to match available experimental data,

$$\hat{H}^{\mathrm{sr}} = \sum_{ij}{}' 4\epsilon_{ij} \left(\frac{\sigma_{ij}^{12}}{R_{ij}^{12}} - \frac{\sigma_{ij}^{6}}{R_{ij}^{6}} \right), \tag{3.6}$$

where the indices i and j run over all the atomic sites in the system, and the sum is restricted to include only pairs where the sites reside on different molecules. Note that since the charge on each solute atom depends on the solute wave function, having different short-range interactions for the ionic and neutral atoms requires introducing a state-dependent interaction. It is not obvious, however, that a set of LJ parameters that gives a correct overall potential for the $I^- \cdots CO_2$ interaction will also give the correct interaction for $I \cdots CO_2$, because one would expect the presence of the extra electron to change the effective size of the iodide. Our procedure is to start with the simplest empirical description of the potentials, as given by Eq. 3.6, and modify these as is warranted by the available data. We have found that it is not necessary to change the LJ parameters going from I^- to I in order to get a fit to the experimental interaction potentials. In the case of the $I \cdots Ar$ potentials, however, we have found that an anisotropic and state-dependent dispersion term must be added to reproduce the experimental potential curves, as we also discuss below.

An important limitation of the data available for these systems is that little is known about the interactions of the diatomic solute with the solvent molecules. A rough estimate of the binding energy has been obtained from photofragmentation studies [13, 41], but no spectroscopic data is yet available. Therefore, all of the solute-solvent potentials are fit to the better-known interactions between the solute fragments and the solvent molecules. It is hoped that by fitting potentials to the $I^- \cdots Ar$ and $I \cdots Ar$ interactions, for example, that the potential for $I_2^- \cdots Ar$, where each I atom is approximately halfway between and I and I^- in both size and charge, will be correct. Because we include the electrostatic effects at a high level, we are only relying on the assumption that the short-range solute-solvent interactions are not dramatically altered by the chemical bonding within the solute. There is, unfortunately, no direct way to test the accuracy of the potentials, and we must rely on comparison with the photofragmentation and pump-probe data to determine if our model of these systems is realistic.

A combination of scattering data and photoelectron spectroscopy has been used to determine potentials for neutral and negatively-charged halogen atoms interacting with various solvent molecules [42, 43]. The bond lengths from these fits are accurate to a few percent, while the binding energies are known to about 5%. Given that the binding energies for the solute-solvent pairs are on the order of 10–500 meV, terms that contribute only a few cm^{-1} to the energy have little influence on the fit.

All of the terms used to fit the short-range interactions are pairwise-additive. There is little data for these systems sufficient to resolve the small many-body dispersion terms. The only data on many-body interactions of direct relevance to the model is the study of I^-Ar_n potentials made by Yourshaw

et al. [44]. They found that many-body induction was the major contributor to the many-body interaction—about 15% of the total interaction energy—while many-body exchange and dispersion terms had an effect of at most a few percent. Since our model does treat the many-body induction accurately, inclusion of short-ranged nonadditive effects does not seem warranted.

A well-known problem in many-body polarization models is the singularity that arises when polarizable sites too closely spaced [45]. One solution to this problem to damp the polarization interactions at short bond lengths using a simple radial function,

$$\gamma(R) = \frac{1}{2}\left[\tanh\left(\frac{R - R_{\text{damp}}}{w_{\text{damp}}}\right) + 1\right], \tag{3.7}$$

which is applied to each interaction tensor element connecting each pair of polarizable sites [46]. The parameters R_{damp} and w_{damp} are chosen to have a small effect near equilibrium separations but to turn on damping rapidly when the charge clouds are penetrated. Values of these parameters are shown in Table 3.8.

3.3.1 Argon

Accurate interaction potentials for $\text{I}^- \cdots \text{Ar}$ and $\text{I}(^2P) \cdots \text{Ar}$ are known from a combination of scattering and ZEKE spectroscopy experiments [43]. Fitting the I $(^2P) \cdots$ Ar potential is complicated by the fact that this interaction depends on the orientation of the empty p orbital on the iodine atom. The anisotropy of the $\text{I} \cdots \text{Ar}$ potential is important in the model of I_2^-Ar_n because it is the only mechanism that can significantly mix solute states of different total angular momentum projection Ω. There is an anisotropic

quadrupole induced-dipole interaction, but its magnitude is too small to have an observable effect.

To determine what terms must be added to the potential, let us consider the model Hamiltonian described so far for the interaction of an iodine atom with argon, as shown in Fig. 3.7. Iodine is one electron short of a closed shell, so the three valence states of the atom arise from the electron hole in one of the three p orbitals. There are two Π states with the empty p orbital oriented perpendicular to the I–Ar axis, and one Σ state with the hole along the axis. The model includes the correct atomic spin-orbit coupling that mixes the Σ and Π orbitals to give the ${}^2P_{3/2}$ and ${}^2P_{1/2}$ states, which are split by nearly 1 eV. The LJ sites on the iodine and argon atoms can be fit to give approximately the correct distance dependence of the interaction, but there is only a tiny splitting between the $j = 3/2$ states that arises from the quadrupole on iodine interacting with the dipole polarizability of argon—this interaction is proportional to $1/R^8$. The result is that the two I $({}^2P_{3/2})\cdots$Ar curves are effectively identical and the interaction is isotropic.

The simplest way to induce a splitting between the $\Omega = 3/2$ and $\Omega = 1/2$ states is to add a small negative point charge to the argon atom that interacts only with the quadrupole operators on the solute. To make this a short-range interaction, we change the R-dependence to $1/R^6$. The angular dependence of ion-quadrupole interaction, $\propto P_2(\cos\theta)$, is identical to the known angular dependence of the I $({}^2P)\cdots$Ar interaction, because both arise from a p-shaped charge density interacting with an s-shaped charge density. We use the quadrupole operators from the solute DMA and fit only the magnitude of the pseudo-charge on the argon atoms, which is given in Table 3.8. The negative pseudo-charge results from the fact that the interaction is more

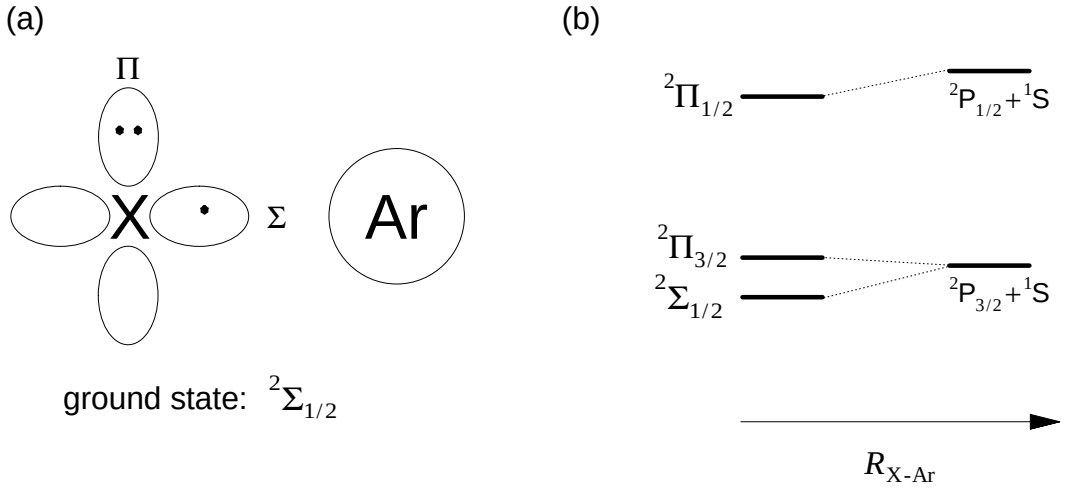

Figure 3.7: Interaction of ^2P halogen atom with argon. (a) shows that the state with a hole in the Σ orbital is lower in energy because the electron density along the X–Ar axis is lower, giving less repulsive overlap. The leading order electrostatic term arises from the quadrupole on X interacting with the induced dipole on Ar, but the magnitude ($\propto 1/R^8$) is < 1 meV. (b) shows the resulting state ordering when spin-orbit coupling is included. The Λ quantum number is not conserved, but the state with more Σ character is lower in energy.

attractive when the hole orbital points toward the argon atom and repulsive when the hole orbital is perpendicular to the I–Ar axis. The addition of this single interaction term to the model gives good agreement with the experimental potential curves as shown in Figure 3.8. The splitting between the $^2\Sigma_{1/2}$ and the $^2\Pi_{3/2}$ states falls off too slowly in the model potential, suggesting that the $1/R^6$ dependence of the anisotropy used in the model fits is too long-ranged, but the magnitude of the disagreement is small.

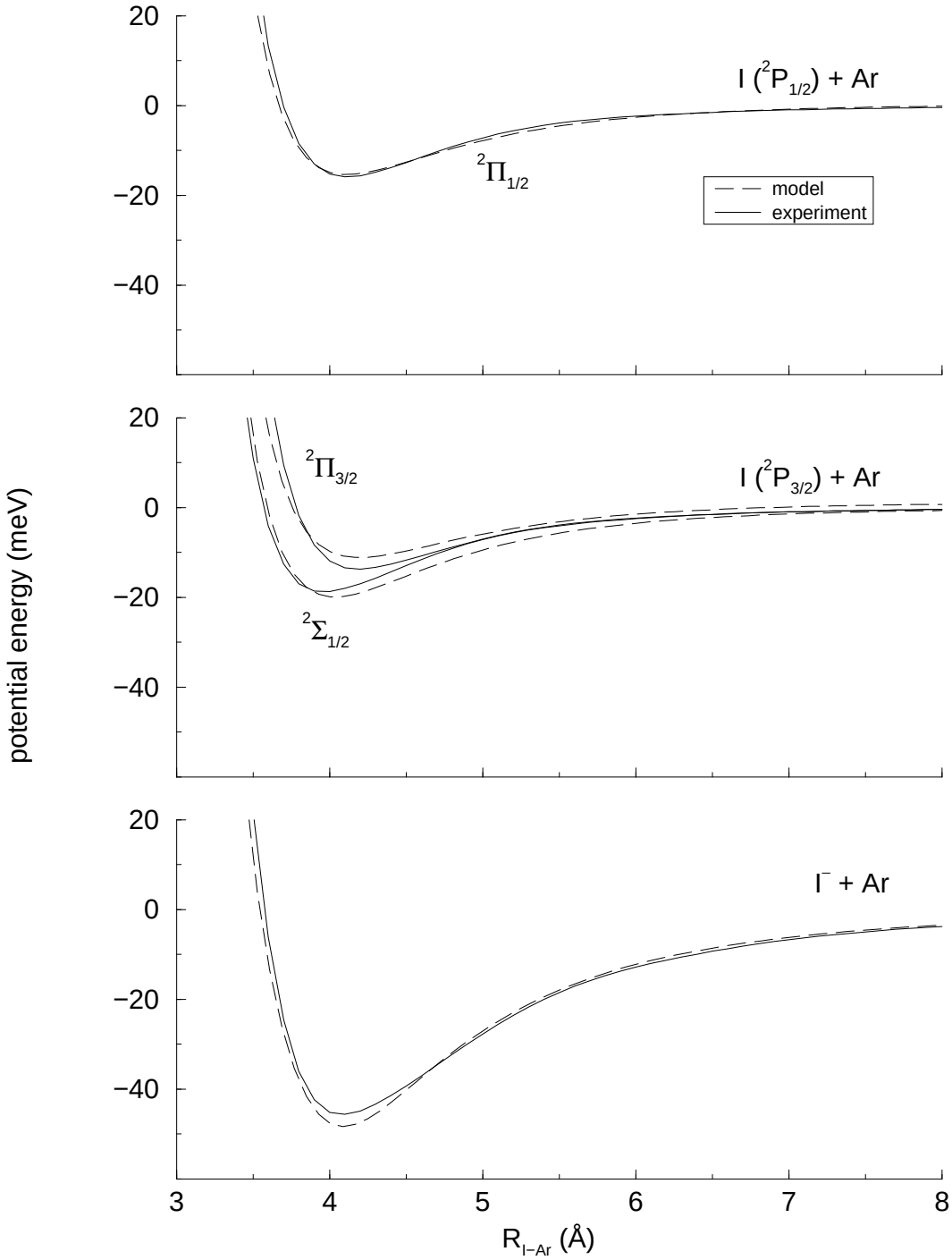

Figure 3.8: Potential curves for I(^2P) interacting with argon. The dashed and solid lines show a comparison between the model and experimental fits. The splitting between the $^2\Sigma_{1/2}$ and the $^2\Pi_{3/2}$ states falls off too slowly in the model potential, suggesting that the $1/R^6$ dependence of the anisotropy used in the model fits is too long-ranged.

3.3.2 CO_2

The $I^- \cdots CO_2$ and $I \cdots CO_2$ interaction potentials for the T-shaped configuration are also known to good accuracy from ZEKE measurements [42]. Much less information is available for the chlorine interaction potentials, so that while the form of the interaction potential is the same as for iodine, the parameters are not as well determined. All of the discussion that follows applies equally to iodine and chlorine except where noted.

The anion is T-shaped because of the strong interaction of the ion with the large CO_2 quadrupole. The electronegative oxygen atoms are repelled strongly by the anion, even forcing CO_2 to bend slightly away from the ion, which has been observed experimentally [47]. In $I^-(CO_2)$ the bending is about 5 degrees, but the bending may be as large as 10° in $Cl^-(CO_2)$ [47]. This suggests that the model should allow the CO_2 to bend, at least in systems where chlorine is present. However, given the lack of potential data, we have chosen to keep CO_2 rigid in our preliminary simulations of $ICl^-(CO_2)_n$. Modeling has indicated that the bending arises mostly from electrostatic effects rather than charge transfer [47], suggesting that it will be possible to extend the current model to include bending in the future. One might expect that for clusters with more than a few CO_2 molecules, the extent of the bending will be reduced by the solvent-solvent interactions, which favor linear CO_2. The photoelectron experiments probe only the T-shaped $I \cdots CO_2$ geometries, which are prepared by detaching an electron from the anion. The linear geometry of the anion is strongly repulsive because of the ion-quadrupole interaction.

It is thought on the basis of the experiments that there are at least stable local minima for the neutral T-shape geometries. The electrostatic in-

teraction between the halogen atom and CO_2 quadrupoles is proportional to $1/R^5$ and is the leading term in the neutral potential. This term contains the correct anisotropy to describe the splitting of the three observed neutral states, which required the additional term in the argon case. The interactions between the quadrupole on the neutral halogen atom and the quadrupole on CO_2 are illustrated in Figure 3.9. The positive halogen quadrupole is parallel to the negative CO_2 quadrupole in the $\Omega = 3/2$ state, resulting in a more attractive interaction than in the $\Omega = 1/2$ state, where the quadrupole-quadrupole interaction is unfavorable. The situation is reversed in the linear geometry.

We have obtained good fits using the four LJ parameters associated with the pairwise atomic interactions in addition to the electrostatic Hamiltonian. The fits to the $I^- \cdots CO_2$ and $I \cdots CO_2$ curves are shown in Figure 3.10 and the LJ parameters for both I and Cl are given in Table 3.8. Since no ZEKE studies of $Cl^- \cdots CO_2$ have been performed, the only experimental information available about the interaction potentials are approximate values of the anion well depth, $D_e = 350$ meV, and the equilibrium geometry, $R_{\text{Cl-C}} = 3.0$ Å [47]. The resulting potential curves for both the anion and neutral interactions are shown in Fig. 3.11. Note that induction damping is not applied to the ICl^- interaction potentials. The difference between the $I^- \cdots CO_2$ interaction potential at R_e with and without damping is about 1% of the binding energy.

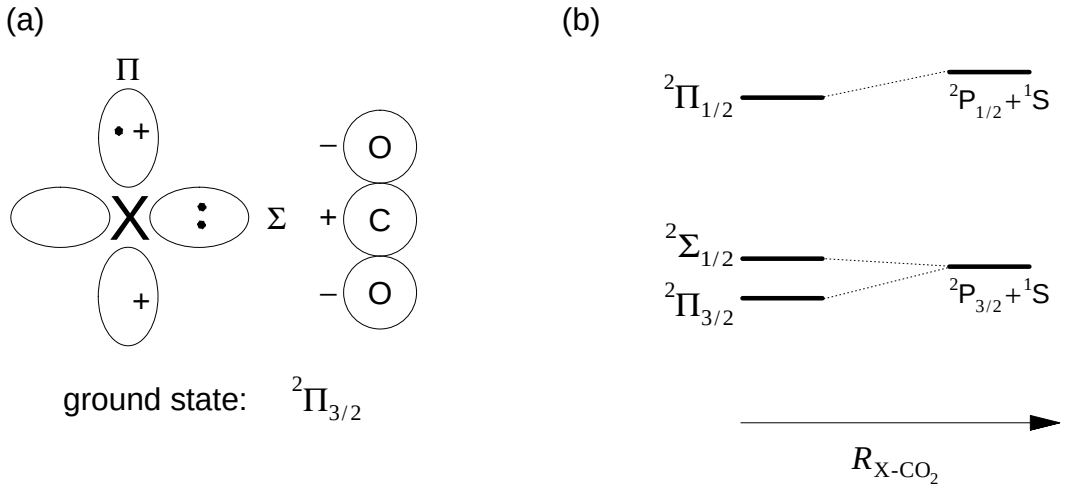

Figure 3.9: Interaction of ^2P halogen atom with CO_2. (a) shows that the state with a hole in the Π orbital is lower in energy because of the resulting positive quadrupole moment, which interacts favorably with the quadrupole on CO_2. In the Σ orientation, the hole interaction with the CO_2 quadrupole is slightly repulsive. (b) shows the resulting state ordering when spin-orbit coupling is included. The ordering of the lower two states is reversed for the linear geometry.

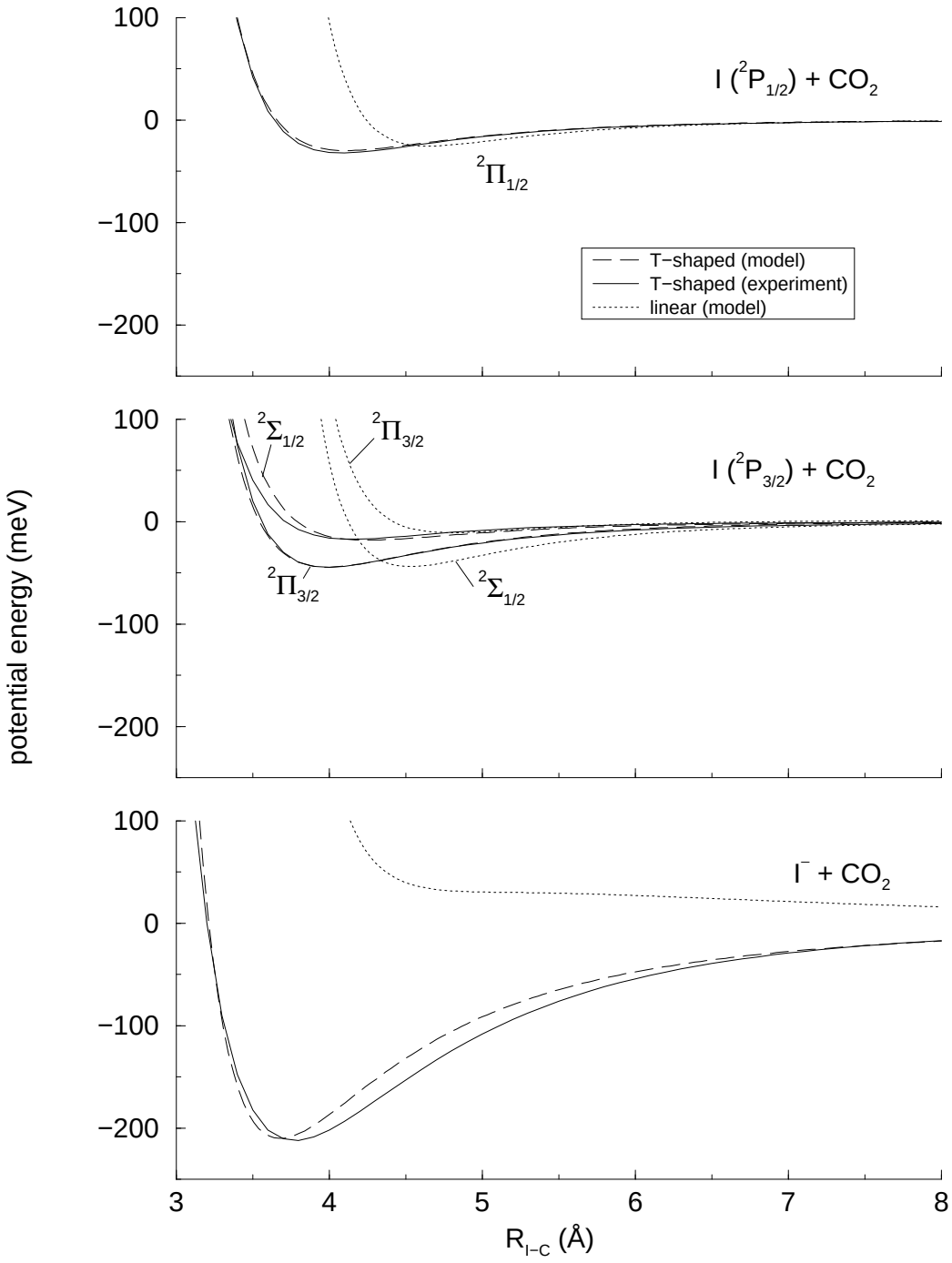

Figure 3.10: Potential curves for I(^2P) interacting with CO_2 in the linear and T-shaped geometries. The dashed and solid lines show a comparison between the model and experimental fits. The interaction for the linear geometry of the anion is strongly repulsive, but there are significant attractive wells for the linear configurations of the neutral states.

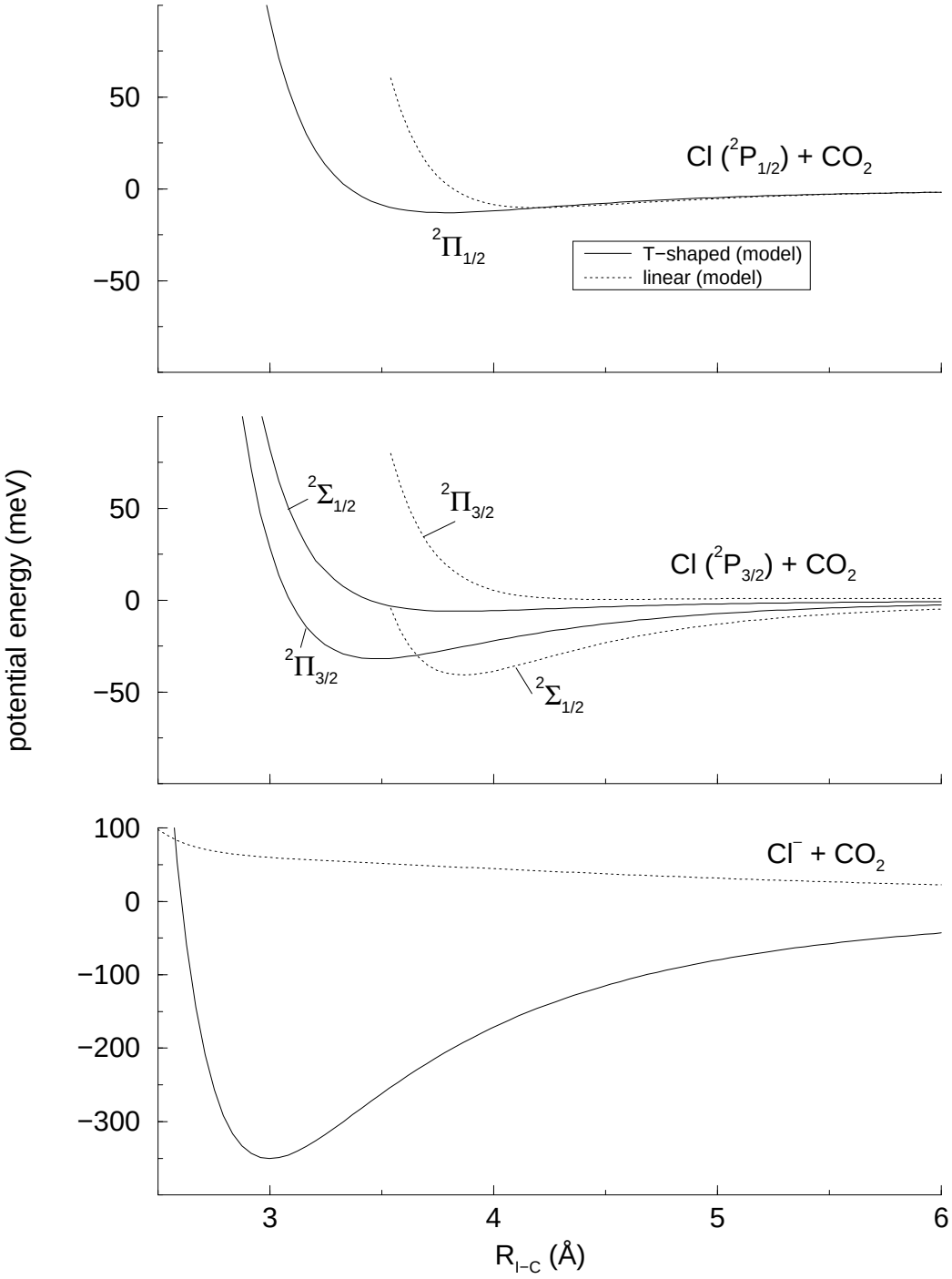

Figure 3.11: Potential curves for Cl(^2P) interacting with CO_2 in the linear and T-shaped geometries. No experimental information is available for the neutral interactions, so these curves represent a "best guess."

3.4 Conclusions

This chapter has described some of the techniques that can be used to parameterize the effective solute-solvent Hamiltonian of Chapter 2. Ab initio calculations augmented by experimental data are used to determine the solute electronic states. The solvent model is given by a combination of the known electrostatic properties of the solvent molecules and simple empirical potentials fit to experimental data. The solute-solvent interactions are determined by the carefully parameterized electrostatic interactions between the solute multipole operators and the solvent electrostatic properties, and by empirical short-range potentials, which are fit to reproduce experimentally determined pair potentials. The method of parameterization is similar to the semiempirical diatomics-in-molecules and diatomics-in-ionic-systems methods discussed briefly in Chapter 2, but with an improved description of the solute wave functions.

The description of how the model parameters are determined has also revealed several properties of the system that strongly influence the dynamics studied in later chapters. Most important is the character of the solute wave function and the changes that occur as the molecule dissociates, creating state-dependent charge flow. The interaction of the solute fragments with the solvent also affects mechanisms for electronic relaxation. In the absence of strong coupling between states of different Ω values, one might not expect the A state (first excited state) to play an important role in the dynamics, but, as discussed in future chapters, it clearly does.

Finally, here are some thoughts on future improvements to the model and methods used to determine model parameters. Clearly, the most direct way

to improve the potentials is to obtain more data for the solute-solvent interactions. Neumark's group has recently measured electron affinities of $I_2^-Ar_n$ and $I_2^-(CO_2)_n$, which give the first direct data about the interaction of the solute anion with individual solvent molecules. A complete photoelectron spectrum of I_2^-Ar or $I_2^-(CO_2)$ is also a possibility. In the future, resonance Raman coupled with photoelectron spectroscopy studies may also help to better characterize the excited states of I_2^- and other dihalide anions. On the computational side, ab initio calculations of the solute with relativistic contributions (including spin-orbit coupling) could be used to test and improve the current solute model. Ab initio methods also hold promise for improving the solute-solvent potentials, particularly for geometries and solvent molecules that have not been studied experimentally. Anisotropic Lennard-Jones parameters [48, 49] or even the more ambitious Gaussian multipoles [50–52] might be used to give a better description of the molecular shapes determined by the short-range interactions. Inclusion of state-dependence in the short-range potentials is also key to improving the models of some non-halogen solutes, such as Mg_2^+, where there are unoccupied valence orbitals. While there are clearly many directions for future improvement, the current model, as described in this and the preceding chapter, already can provide many insights into the systems that have been studied.

References for Chapter 3

[1] P. E. Maslen, J. Faeder, and R. Parson, Chem. Phys. Lett. **263**, 63 (1996).

[2] K. P. Huber and G. Herzberg, *Molecular Spectra and Molecular Structure. IV. Constants of Diatomic Molecules*, Van Nostrand, New York, 1979.

[3] T. M. Miller, Electron affinities, In Lide [53].

[4] S. Bashkin and J. O. Stoner, Jr, *Atomic Energy-Level and Grotrian Diagrams. Volume I. Hydrogen I – Phosphorous XV*, North-Holland, New York, 1978.

[5] S. Bashkin and J. O. Stoner, Jr, *Atomic Energy-Level and Grotrian Diagrams. Volume II. Sulfur I – Titanium XXII*, North-Holland, New York, 1978.

[6] C. E. Moore, *Atomic Energy Levels*, volume 35 of *National Standards Reference Data Series*, National Bureau of Standards, 2nd edition, 1971.

[7] M. T. Zanni, T. R. Taylor, B. J. Greenblatt, B. Soep, and D. M. Neumark, J. Chem. Phys. **107**, 7613 (1997).

[8] M. Nadal, *The Study of the Photodissociation and Recombination Dynamics of Mass-Selected Cluster Ions: Solvent Effects on the Structure and Dynamics of the Ionic Chromophore*, PhD thesis, University of Colorado, 1996.

[9] E. C. M. Chen and W. E. Wentworth, J. Phys. Chem. **89**, 4099 (1985).

[10] D. J. Auerbach, M. M. Hubers, A. P. M. Baede, and J. Los, Chem. Phys. **176**, 107 (1973).

[11] U. Ross, T. Schulze, and H.-J. Meyer, Chem. Phys. Lett. **121**, 174 (1985).

[12] L. Bañares and A. G. Ureña, Chem. Phys. Lett. **176**, 178 (1991).

[13] J. Papanikolas, J. Gord, N. Levinger, D. Ray, V. Vorsa, and W. Lineberger, J. Phys. Chem. **95**, 8028 (1991).

[14] R. Azria, R. Abouaf, and D. Teillet-Billy, J. Phys. B: At. Mol. Opt. Phys. **21**, L213 (1988).

[15] Y. Le Coat, J.-P. Guillotin, and L. Bouby, J. Phys. B: At. Mol. Opt. Phys. **24**, 3285 (1991).

[16] C. J. Delbecq, W. Hayes, and P. H. Yuster, Phys. Rev. **121**, 1043 (1961).

[17] T. Shida, Y. Takahashi, and H. Hatano, Chem. Phys. Lett. **33**, 491 (1975).

[18] J. G. Dojahn, E. C. M. Chen, and W. E. Wentworth, J. Phys. Chem. **100**, 9649 (1996).

[19] E. C. M. Chen, J. G. Dojahn, and W. E. Wentworth, J. Phys. Chem. A **101**, 3088 (1997).

[20] P. W. Tasker, G. G. Balint-Kurti, and R. N. Dixon, Mol. Phys. **32**, 1651 (1976).

[21] G. A. Bowmaker, P. Schwerdtfeger, and L. von Szentpaly, J. Mol. Struct. THEOCHEM **53**, 87 (1989).

[22] D. Danovich, J. Hrušák, and S. Shaik, Chem. Phys. Lett. **233**, 249 (1995).

[23] S. B. Sharp and G. I. Gellene, J. Phys. Chem. **101**, 2192 (1997).

[24] MOLPRO, a package of ab initio programs by H.-J. Werner and P. J. Knowles, with contributions from J. Almlöf, R. D. Amos, M. J. O. Deegan, S. T. Elbert, C. Hampel, W. Meyer, K. Peterson, R. Pitzer, A. J. Stone, and P. R. Taylor, version 94.3 (1994).

[25] H.-J. Werner and P. J. Knowles, J. Chem. Phys. **89**, 5803 (1988).

[26] P. J. Knowles and H.-J. Werner, Chem. Phys. Lett. **145**, 514 (1988).

[27] H.-J. Werner and P. J. Knowles, J. Chem. Phys. **82**, 5053 (1985).

[28] P. J. Knowles and H.-J. Werner, Chem. Phys. Lett. **115**, 259 (1985).

[29] A. J. Sadlej, Theoretica Chimica Acta **79**, 123 (1991).

[30] A. J. Sadlej, Theoretica Chimica Acta **81**, 339 (1992).

[31] A. J. Stone, Chem. Phys. Lett. **83**, 233 (1981).

[32] H. Lefebvre-Brion and R. W. Field, *Perturbations in the Spectra of Diatomic Molecules*, Academic Press, Boston, 1986.

[33] G. Herzberg, *Molecular Spectra and Molecular Structure. I. Spectra of Diatomic Molecules*, Van Nostrand, New York, 2nd edition, 1950.

[34] E. J. Heller, J. Chem. Phys. **68**, 2066 (1978).

[35] C. Teichteil and M. Pelissier, Chem. Phys. **180**, 1 (1994).

[36] A. Sanov and W. C. Lineberger, private communication.

[37] C. S. Murthy, S. F. O'Shea, and I. R. McDonald, Mol. Phys. **50**, 531 (1983).

[38] M. J. Weida and D. J. Nesbitt, J. Chem. Phys. **105**, 10210 (1996).

[39] C. G. Gray and K. E. Gubbins, *Theory of Molecular Fluids*, volume 1, Clarendon, Oxford, 1984.

[40] K. T. Tang and J. P. Toennies, J. Chem. Phys. **80**, 3726 (1984).

[41] V. Vorsa, P. J. Campagnola, S. Nandi, M. Larsson, and W. C. Lineberger, J. Chem. Phys. **105**, 2298 (1996).

[42] Y. Zhao, C. C. Arnold, and D. M. Neumark, J. Chem. Soc. Faraday Trans. **89**, 1449 (1993).

[43] Y. Zhao, I. Yourshaw, G. Reiser, C. C. Arnold, and D. M. Neumark, J. Chem. Phys. **101**, 6538 (1994).

[44] I. Yourshaw, Y. Zhao, and D. M. Neumark, J. Chem. Phys. **105**, 351 (1996).

[45] B. T. Thole, Chem. Phys. **59**, 341 (1981).

[46] A. J. Stone, *The Theory of Intermolecular Forces*, Oxford, New York, 1996.

[47] D. W. Arnold, S. E. Bradforth, E. H. Kim, and D. M. Neumark, J. Chem. Phys. **102**, 3493 (1995).

[48] P. M. Rodger, A. J. Stone, and D. J. Tildesley, Chem. Phys. Lett. **145**, 365 (1988).

[49] P. M. Rodger, A. J. Stone, and D. J. Tildesley, Mol. Phys. **63**, 173 (1988).

[50] R. J. Wheatley, Mol. Phys. **79**, 597 (1993).

[51] R. J. Wheatley and J. B. O. Mitchell, J. Comp. Chem. **15**, 1187 (1994).

[52] R. J. Wheatley, Mol. Phys. **86**, 443 (1995).

[53] D. R. Lide, editor, *CRC Handbook of Chemistry and Physics*, Chemical Rubber, Boca Raton, 73rd edition, 1993.

Chapter 4

Structure and Dynamics Methods

Chapters 2 and 3 described an effective Hamiltonian for the electronic states of a solute embedded in a molecular cluster or solvent. The eigenstates of this Hamiltonian define potential surfaces for each electronic state of the solute as a function of the nuclear positions; these are the Born-Oppenheimer or adiabatic surfaces that govern the nuclear motion when the electrons are assumed to move infinitely quickly. We want to model the dynamics that occur when the solute in its ground electronic state absorbs a photon and is excited to a potential surface on which the solute nuclei are repelled—photodissociation. Because there are many nuclear degrees of freedom in the cluster, the nuclear dynamics on each potential surface must be treated using classical mechanics, i.e. solving Newton's equations of motion for the nuclei under the influence of the Born-Oppenheimer potential surface.

The initial configurations of the cluster prior to photoexcitation are determined by following the molecular dynamics (MD)—the motions of the nuclei—on the ground state potential surface. Trajectories are computed on the ground state surface starting from an arbitrary configuration at a fixed total energy, and are followed until the distribution of energy throughout the cluster reaches equilibrium. After equilibration, cluster configurations are periodically

sampled to construct an ensemble of starting points for photodissociation trajectories. The ensemble is meant to sample the range of initial configurations sampled by an experiment performed under specific conditions, most often at fixed temperature. In characterizing the behavior of clusters at equilibrium, it is also useful to identify local minima of the potential surface [1]. Structural features of these minima often influence the dynamics both before and after photoexcitation.

Following photoexcitation, the solute nuclei fly apart on the repulsive excited state surface. As the solute nears dissociation, its electronic states bunch together, leading to a breakdown of the Born-Oppenheimer picture. The electrons of the solute no longer respond instantly to the motions of the nuclei, so that the true electronic wave function of the solute becomes a mixture of the adiabatic states. An exact treatment of these *nonadiabatic* dynamics would require a quantum-mechanical description of both the electrons and the nuclei, but this is not feasible for systems containing more than a few atoms. Fortunately, there are several approximate methods for treating nonadiabatic dynamics that allow us to retain a classical description of the nuclei. The simulations reported here were performed using a surface-hopping (SH) approach to describe the nonadiabatic dynamics. The nuclei evolve on a single adiabatic state at a time, but this state can change when nonadiabatic coupling with other states occurs. Surface hopping is determined stochastically according to an algorithm in which the probability of occupying each adiabatic state is given by the square of its amplitude in the total nonadiabatic electronic wave function. Because this is an all-or-nothing approach—the trajectory must always be on one surface or another—a large number of trajectories must be computed to determine the correct branching probabilities into each of the coupled states.

This chapter details the methods used to compute optimized geometries, single-state MD trajectories, and nonadiabatic dynamics. Like ancient Gaul, it is divided into 3 parts [2]. The first part presents the coordinates defining the nuclear degrees of freedom and shows how optimized geometries and MD trajectories are computed in this coordinate system. The second part describes the surface-hopping method used to compute nonadiabatic dynamics, making a comparison with other methods and addressing possible pitfalls. The final part details calculation of the forces and nonadiabatic couplings required to compute trajectories and surface-hopping. The methods presented here apply generally to all of the simulations presented in this work. Specific details about the length of trajectories used in equilibration and photodissociation and the procedures for finding minima are presented in the application chapters.

4.1 Adiabatic Dynamics

It is common practice in MD simulations to constrain the intramolecular degrees of freedom when they are not considered vital to the properties of interest. The treatment of molecules as rigid objects is usually justified because the frequencies of the intramolecular vibrations are generally much higher than the frequencies for intermolecular motions. The forces that act between molecules are thus averaged over these internal vibrations and are usually well approximated by fixing each molecule at its equilibrium geometry. Constraining molecules to be rigid has the computational advantage that a much larger time step can be used in integrating the equations of motion since the rapid vibrational oscillations have been removed. On the other hand, there are many cases when it is not desirable to constrain the internal degrees of freedom. It

is obvious that in modeling photodissociation the solute bond must be allowed to break. It is also possible that, when a large amount of energy is put into a cluster on a short time scale through photoexcitation, some of the energy will go to excite internal vibrations of the solvent molecules. Almost all of the simulations performed in this work have used a flexible solute and rigid solvent molecules, and the good agreement of the results with experiment show that this is a reasonable approximation in many cases. In the future, however, it will be important to study the effects of relaxing the internal molecular constraints to determine what role intramolecular vibrations play in dissipating both excess vibrational and electronic energy due to photoexcitation.

Two procedures are in common use for MD of rigid molecules. In the first, each molecule is specified by its center of mass position and its orientation, as defined by three Euler angles [3]. Because the Euler equations of motion contain a singularity that makes numerical integration difficult, these angles are re-expressed as a set of quaternions [3, 4], which gives rise to a singularity-free set of equations [3, 5]. In the second method, referred to here as the method of constraints, the molecular geometry is specified by the Cartesian coordinates of a core group of atoms [6, 7]. Each molecule is held rigid by the application of constraints that hold fixed various bond distances and dihedral angles [3, 7]. The method of constraints is used here because it can treat rigid, flexible, and semi-flexible molecules all on the same footing, depending on which constraints are applied. The number of core atoms depends on the molecular geometry: two core atoms specify a linear molecule, three a planar molecule, and a maximum of four are needed for an arbitrary nonplanar molecule. Constraining all of the core atom distances fixes the molecule as rigid, but individual constraints may be eliminated and replaced by internal

potentials to give the molecule flexibility. The advantage of this approach is that introducing flexibility does not require fundamentally altering the equations of motion, and it is easy to create a computer implementation in which the molecular model can be changed simply through input parameters. Section 4.1.1 describes in more detail the molecular coordinate system in the method of constraints, while Sections 4.1.2 and 4.1.3 present the equations that govern geometry optimization and MD integration in this coordinate system.

4.1.1 Molecular Coordinate System

The description of coordinates used here is based on the method of constraints developed by Ciccotti, Ferrario, and Ryckaert [6, 7], which built on earlier work involving constraint dynamics [8, 9]. They used the Cartesian coordinates of a minimal core of atoms to define rigid subunits within a molecule, and showed that an arbitrary molecule with some degrees of freedom held fixed and others allowed to vary could be described using combinations of rigid subunits and holonomic constraints [4]. They also developed efficient methods for solving the equations of motion in this coordinate system subject to the constraints, showing that for a rigid molecule the method of constraints is about as efficient as using the rigid body equations of motion [6]. The most expensive part of most molecular models is the evaluation of energies and forces (particularly when there are non-additive contributions, as there are in our model), and overhead associated with integrating the additional equations of motion or applying constraints is usually small. What is most important is picking an integration method that yields acceptable accuracy for a maximal step size, so that the number of force evaluations can be limited. The Verlet algorithm [10] and its descendant the velocity Verlet algorithm [11], which we

have used, provide an optimal balance between efficiency and accuracy [3].

The method of constraints specifies three site categories: primary atom, secondary atom, and force center. The primary atoms are the atoms used to define each subunit, and their coordinates are used to integrate the equations of motion. All forces and torques in the system must be converted to forces on the primary atoms. Secondary atoms and force centers are defined with respect to the primary atoms in the subunit to which they belong by a simple linear relation,

$$\mathbf{r}_\alpha = \sum_{i=1}^{n_p} c_{\alpha i} \mathbf{R}_i, \tag{4.1}$$

where $\mathbf{r}_\alpha$ gives the position of the site α, the $\mathbf{R}_i$ are the positions of the primary atoms in the subunit, and n_p is the number of primary atoms in the subunit. As an example, illustrated in Fig. 4.1, we can define linear CO_2 by taking the O atoms as primary atoms and defining the position of the carbon atom as the midpoint of the O–O separation,

$$\mathbf{r}_C = \frac{1}{2}\mathbf{R}_{O_1} + \frac{1}{2}\mathbf{R}_{O_2}. \tag{4.2}$$

Using the chain rule, it is easily seen that the force on the secondary carbon site, $\mathbf{f}_C$ creates an additional force of $\frac{1}{2}\mathbf{f}_C$ on each of the primary oxygen atoms. The forces on secondary sites are transferred to the primary sites by

$$\mathbf{F}_i^s = \sum_\alpha c_{\alpha i} \mathbf{f}_\alpha. \tag{4.3}$$

In the equations of motion for the system, the masses of the secondary atoms also contribute inertial forces, which are discussed in Sec. 4.1.3. This inertial

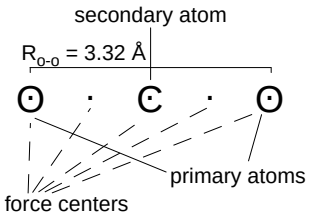

Figure 4.1: Rigid CO_2 model using method of constraints.

force is the only factor that distinguishes the secondary atoms from the force centers.

The complete model for rigid CO_2 has the two primary oxygen atoms, a secondary carbon atom at the bond midpoint, and a bond constraint fixing the O–O distance at r_{O-O},

$$\sigma_{O-O} = |\mathbf{R}_{O_1} - \mathbf{R}_{O_1}|^2 - r_{O-O}^2 = 0. \tag{4.4}$$

Five additional force centers for the point charges and one additional force center for the polarizability along with the pairwise Lennard-Jones interactions associated with the atomic sites complete the potential model described in Chapter 3. Because the polarizability of CO_2 is anisotropic, the polarizable site exerts a torque on the molecule, which is resolved into forces on the primary atoms using the derivatives of the molecular axes with respect to the primary atom positions. Methods for resolving these torques and for determining the forces due to multipole sites of arbitrary order are discussed in Sec. 4.3.4. The required derivatives are straightforward for a linear molecule, but become cumbersome even for nonlinear triatomics. For rigid non-planar molecules with multipoles of dipole and higher order, it is probably simpler to use the torques in the rigid body equations of motion rather than the method of constraints. The advantage of the constraint method comes when one or more internal

degrees of freedom is flexible. Flexible CO_2, for example, can be modeled using three primary atoms with the two C–O bonds held fixed, leaving only the lowest frequency mode, the bend, active. The charges remain fixed at constant points along the C–O bonds as the molecule bends, creating a small dipole for slightly bent configurations. Based on the work of Arnold et al. [12], this dipole may be an important component of the halogen ion–CO_2 interaction for the T-shaped configuration, although we have not yet tested this using our model.

The model for the diatomic solute consists of two primary atoms and 4 force centers for the multipoles located on the nuclei and at equidistant points along the bond. The internal potential of the molecule is built into the effective Hamiltonian described in Chapters 2 and 3. As in the model of CO_2, the primary atomic sites are also associated with pairwise Lennard-Jones potentials that describe the short-range interactions with the solvent atoms. The model for argon consists simply of a single primary atom with associated Lennard-Jones potentials and a force center for the polarizability.

4.1.2 Geometry Optimization

Local minima of potential energy surfaces in clusters often reveal important structural characteristics that affect both static and dynamic properties [1]. We find minimum energy structures using standard optimization techniques augmented by the method of constraints. The optimization methods described here are based on the projection operator method described by Lu, Zhao, and Truhlar [13]. These workers combined projection operators with quasi-Newton optimization algorithms [14], while we have used both quasi-Newton and conjugate gradient techniques [14] to find minima.

Two features must be added to minimization algorithms to ensure that the constraints are obeyed and that the efficiency of the method is maintained. First, the constraints must be projected out of the gradient or force vector, so that infinitesimal displacements along the constrained gradient do not violate the constraints. All of the molecular constraints are holonomic and can be written in the form

$$\sigma_p(\mathbf{R}) = 0, \tag{4.5}$$

where $\mathbf{R}$ is a vector containing the positions of all of the primary atoms in the molecule. The constraint directions, $\hat{t}_p$, are given by

$$\hat{t}_p = \nabla_{\mathbf{R}}\sigma_p(\mathbf{R}) / \left|\nabla_{\mathbf{R}}\sigma_p(\mathbf{R})\right|. \tag{4.6}$$

The projection operator is then defined by

$$\mathsf{P}(\mathbf{R}) \equiv \sum_p \hat{t}_p \otimes \hat{t}_p, \tag{4.7}$$

where $\otimes$ denotes an outer product, $(\mathbf{a} \otimes \mathbf{b})_{ij} = a_i b_j$. The constrained force vector can then be written

$$\mathbf{F}^c = (1 - \mathsf{P}(\mathbf{R})) \cdot \mathbf{F}, \tag{4.8}$$

where $\mathbf{F}$ is the unconstrained force.

The second required component is a method for applying the constraints to a configuration where the constraints are violated by a small amount. These configurations arise even for displacements made using $\mathbf{F}^c$ because the

constraints are in general not linear with respect to the displacements. It is therefore necessary to adjust the molecular configuration following a move so that the constraints are obeyed to within a narrow tolerance. This can be done by making corrections along the direction of the constraint gradients,

$$\mathbf{R}^c = \mathbf{R} - \sum_p \lambda_p \nabla_{\mathbf{R}} \sigma_p(\mathbf{R}), \tag{4.9}$$

where λ_p is a undetermined constant determined by solving the equation

$$\sigma_p(\mathbf{R}^c) = 0 \tag{4.10}$$

for λ_p. Cicotti and Ryckaert [7] have reviewed the methods available for solving the constraint equations, and we focus here on an iterative solution based on the general approach of the SHAKE algorithm used to apply constraints during MD integration [3, 8, 9]. $\mathbf{R}^c$ is determined by iterative application of the constraints. For each constraint, $\mathbf{R}$ is adjusted iteratively using

$$\mathbf{R}^N = \mathbf{R}^{N-1} - \lambda_p^N \nabla_{\mathbf{R}} \sigma_p(\mathbf{R}^{N-1}), \tag{4.11}$$

where $\mathbf{R}^0 = \mathbf{R}$. λ_p^N is determined by Taylor expanding the condition that the constraint be obeyed at $\mathbf{R}^N$,

$$\sigma_p(\mathbf{R}^N) \equiv \sigma_p \left[\mathbf{R}^{N-1} + \lambda_p^N \nabla_{\mathbf{R}} \sigma_p(\mathbf{R}^{N-1})\right] = 0, \tag{4.12}$$

about $\mathbf{R}^{N-1}$ keeping only first order times in λ_p^N. This gives

$$\lambda_p^N = \frac{\sigma_p(\mathbf{R}^{N-1})}{|\nabla_{\mathbf{R}}\sigma_p(\mathbf{R}^{N-1})|^2}. \tag{4.13}$$

The iteration in N is continued until the constraint is obeyed to within a specified tolerance, usually 10^{-6}–10^{-8}, which takes typically only a few steps for simple bond constraints. The loop over constraints is continued until all of the constraints meet the specified tolerance. The procedure requires relatively little computation because the constraints usually apply to only a single molecule at a time, although we have found the method applicable when there are global constraints applying to all molecules simultaneously. In this case the amount of computation scales linearly with the total number of primary atoms in the system; in contrast, the force evaluation scales quadratically with the total number of force centers (primary and secondary).

Two different standard optimization algorithms, conjugate gradient and quasi-Newton, have been adapted to the method of constraints. The conjugate gradient method works by performing a series of line minimizations along approximately conjugate directions determined by a simple update procedure [14]. The conjugacy of directions along which to minimize reduces the interference between successive minimizations and leads to rapid convergence in quadratic regions of the potential [14]. In the modified method we use the constrained gradients, obtained from the projection shown in Eq. 4.8 above, in the update formula. The conjugate gradient obtained from the update procedure is also projected, and each trial configuration along the line minimization is also adjusted to obey the constraints as described in Eqs. 4.11 and 4.13. Schematically, the procedure at step N is given by:

(1) Compute the constrained gradient

$$\mathbf{g}^N = (1 - \mathsf{P}(\mathbf{R}^N)) \cdot \nabla_{\mathbf{R}} E(\mathbf{R}^N). \tag{4.14}$$

(2) Compute the new conjugate direction for line minimization

$$\mathbf{h}^N = \mathbf{g}^N + \gamma^N \mathbf{h}^{N-1}, \tag{4.15}$$

where

$$\gamma^N = \frac{\left(\mathbf{g}^N - \mathbf{g}^{N-1}\right) \cdot \mathbf{g}^N}{\left|\mathbf{g}^{N-1}\right|^2}, \tag{4.16}$$

and project the constraints from this direction to obtain the direction used in line minimization

$$\mathbf{h}_c^N = (1 - \mathsf{P}(\mathbf{R}^N)) \cdot \mathbf{h}^N \tag{4.17}$$

N.B. $\mathbf{h}^N$ rather than $\mathbf{h}_c^N$ is used in the update formula, Eq. 4.15.

(3) Minimize $E(\mathbf{R}^{N+1}(\alpha))$ with respect to α, where

$$\mathbf{R}^{N+1}(\alpha) = \mathbf{R}^N + \alpha \mathbf{h}_c^N - \sum_p \lambda_p \sigma_p (\mathbf{R}^N + \alpha \mathbf{h}_c^N), \tag{4.18}$$

and $\mathbf{R}^{N+1}(\alpha)$ is determined by the method of applying constraints described above.

This cycle is repeated until $\left|\mathbf{g}^N\right|$ falls below a specified tolerance, generally between 10^{-6}–10^{-8}. We have used this constrained CG procedure extensively to find minimum energy structures of various clusters involving

CO_2, and have found it to be efficient. It is faster than simulated annealing techniques using Monte Carlo trajectories previously used by our group [15, 16] and molecular dynamics quenching [17, 18], which we have also tested. A characteristic feature of the CG technique is that gradients of the function are evaluated only at step (1), while most of the function evaluations take place in step (3). (Gradients can be used in the line minimization in step (3), but we have not done so.) This make CG an attractive choice if the gradients are expensive to compute, as, for example, would be the case if the gradients had to be computed by finite differences.

Evaluation of the forces analytically using the model Hamiltonian, however, is only about three times more expensive than evaluation of the energy alone. Therefore, a method that makes use of the gradient in computing each new trial step is likely to outperform CG for these clusters. We have found that the quasi-Newton [14], or variable metric methods, are easy to code and give substantially better performance than the CG method. In these methods an approximate Hessian or inverse Hessian is computed iteratively using gradients at each time step. The approximate Hessian is used at each step to determine the size and direction of the next step. Different update procedures are possible, but for simplicity we use the popular BFGS formula [14]. Here is an outline of the algorithm at step N:

(1) Compute the constrained gradient

$$\mathbf{g}^N = (1 - \mathsf{P}(\mathbf{R}^N)) \cdot \nabla_{\mathbf{R}} E(\mathbf{R}^N). \tag{4.19}$$

(2) Update the approximate inverse Hessian according to

$$\begin{aligned}\mathbf{H}^N &= \mathbf{H}^{N-1} + \frac{\mathbf{dR}\otimes\mathbf{dR}}{\mathbf{dR}\cdot\mathbf{dg}} - \frac{\left(\mathbf{H}^{N-1}\cdot\mathbf{dg}\right)\otimes\left(\mathbf{H}^{N-1}\cdot\mathbf{dg}\right)}{\mathbf{dg}\cdot\mathbf{H}^{N-1}\cdot\mathbf{dg}} \\ &\quad + \left[\mathbf{dg}\cdot\mathbf{H}^{N-1}\cdot\mathbf{dg}\right]\mathbf{u}\otimes\mathbf{u}, \end{aligned} \tag{4.20}$$

where

$$\begin{aligned}\mathbf{dR} &= \mathbf{R}^N - \mathbf{R}^{N-1} \\ \mathbf{dg} &= \mathbf{g}^N - \mathbf{g}^{N-1} \\ \mathbf{u} &= \frac{\mathbf{dR}}{\mathbf{dR}\cdot\mathbf{dg}} - \frac{\mathbf{H}^{N-1}\cdot\mathbf{dg}}{\mathbf{dg}\cdot\mathbf{H}^{N-1}\cdot\mathbf{dg}}. \end{aligned} \tag{4.21}$$

The choice $\mathbf{H}^0 = \mathbf{1}$ results in a positive definite update [14] and is used in this implementation. When $\mathbf{H}^0 = \mathbf{1}$, the initial step follows the direction of steepest descents. At subsequent steps, if the gradient has *increased* along the direction of the previous step, i.e. $\mathbf{dg}\cdot\mathbf{dR} > 0$, the algorithm resets $\mathbf{H}^N$ to $\mathbf{1}$, forcing a steepest descents step to get back on track.

(3) Step the configuration according to

$$\mathbf{R}_u^{N+1} = \mathbf{R}^N - \mathbf{H}^N\cdot\mathbf{g}^N \tag{4.22}$$

to obtain the new unconstrained geometry. In practice it is a good idea to set a limit on the maximum size of the step allowed to prevent the configuration from changing too rapidly.

(4) Apply the constraints to the new geometry,

$$\mathbf{R}^{N+1} = \mathbf{R}_u^{N+1} - \sum_p \lambda_p \sigma_p(\mathbf{R}_u^{N+1}), \tag{4.23}$$

which is determined by applying the constraints iteratively as above.

This cycle is repeated until $\left|\mathbf{g}^N\right|$ falls below a specified tolerance, generally between 10^{-6} and 10^{-8}. This quasi-Newton method is more efficient than CG because the gradient information in incorporated into every step. While both methods in principle achieve linear convergence in the limit that the potential is given by a quadratic form, cluster potential surfaces tend to be highly anharmonic, and the quasi-Newton methods seem to benefit from a more efficient local approach.

4.1.3 Molecular Dynamics

In this section we derive the equations of motion for the primary atoms of each molecule subject to the inertial forces from the secondary atoms and the internal constraints. We then show how these equations are solved numerically using Andersen's velocity Verlet algorithm [11]. The resulting equations are equivalent to those originally derived by Cicotti et al. [6]. The aim here is to provide a more transparent derivation and a set of equations that is closer to the actual numerical implementation.

Let us consider a molecule with n_p primary atoms, n_s secondary atoms, and n_f force centers. The positions of the secondary atoms, $\mathbf{r}_\alpha^s$, and the force centers, $\mathbf{r}_\alpha^f$, are given by

$$\mathbf{r}_\alpha^s = \sum_i^{n_p} c_{\alpha i}^s \mathbf{R}_i \tag{4.24}$$

$$\mathbf{r}_\alpha^f = \sum_i^{n_p} c_{\alpha i}^f \mathbf{R}_i. \tag{4.25}$$

The Lagrangian can now be used to determine the molecular equations of

motion. The kinetic energy is

$$T = \frac{1}{2}\sum_{i}^{n_p} m_i^p \dot{\mathbf{R}}_i \cdot \dot{\mathbf{R}}_i + \frac{1}{2}\sum_{\alpha}^{n_s} m_\alpha^s \dot{\mathbf{r}}_\alpha^s \cdot \dot{\mathbf{r}}_\alpha^s, \tag{4.26}$$

where m_i^p and m_α^s are the masses of the primary and secondary atoms respectively. Substituting the time derivative of Eq. 4.24 into this expression gives

$$\begin{aligned} T &= \frac{1}{2}\sum_{ij}^{n_p}\left(\delta_{ij} m_i^p + \sum_{\alpha}^{n_s} c_{\alpha i}^s m_\alpha^s c_{\alpha j}^s\right)\dot{\mathbf{R}}_i \cdot \dot{\mathbf{R}}_i \\ &\equiv \frac{1}{2}\sum_{ij}^{n_p} \mathsf{M}_{ij}\dot{\mathbf{R}}_i \cdot \dot{\mathbf{R}}_i, \end{aligned} \tag{4.27}$$

where the matrix M is the metric tensor defined in the theory of normal modes [4]. The potential energy, V, is known as a function of the coordinates $\mathbf{R}_i$, $\mathbf{r}_\alpha^s$, and $\mathbf{r}_\alpha^f$, so that the forces with respect to the primary atom coordinates are given by

$$\mathbf{F}_i = -\frac{dV}{d\mathbf{R}_i} = -\frac{\partial V}{\partial \mathbf{R}_i} - \sum_{\alpha}^{n_s} c_{\alpha i}^s \frac{\partial V}{\partial \mathbf{r}_\alpha^s} - \sum_{\alpha}^{n_f} c_{\alpha i}^f \frac{\partial V}{\partial \mathbf{r}_\alpha^f}, \tag{4.28}$$

where the partial derivatives are calculated from the model Hamiltonian using the methods described in Sec. 4.3. Plugging $T - V$ into Lagrange's equations of motion and using the method of undetermined multipliers to obtain the constraint forces [4], we obtain the coupled equations

$$\sum_{ij}^{n_p} \mathsf{M}_{ij}\ddot{\mathbf{R}}_i = \mathbf{F}_i - \sum_{p} \lambda_p \nabla_{\mathbf{R}_i}\sigma_p(\mathbf{R}), \tag{4.29}$$

where the constraints $\sigma_p(\mathbf{R})$ are defined as above in Sec. 4.1.2. Solving this

equation for $\mathbf{R}_i$ gives

$$\ddot{\mathbf{R}}_i = \sum_j^{n_p} (M^{-1})_{ij} \mathbf{F}_j - \sum_p \lambda_p \sum_j^{n_p} (M^{-1})_{ij} \nabla_{\mathbf{R}_j} \sigma_p(\mathbf{R}), \tag{4.30}$$

which, by making the associations

$$\mathcal{F}_i = \sum_j^{n_p} (M^{-1})_{ij} \mathbf{F}_j \tag{4.31}$$

$$\mathcal{R}_i^p = \sum_j^{n_p} (M^{-1})_{ij} \nabla_{\mathbf{R}_j} \sigma_p(\mathbf{R}), \tag{4.32}$$

takes the simple form

$$\ddot{\mathbf{R}}_i = \mathcal{F}_i - \sum_p \lambda_p \mathcal{R}_i^p \tag{4.33}$$

Note that the matrix M only needs to be inverted once during an entire integration because its elements do not depend on the positions of the atoms.

Many different methods may be used to propagate the molecular equations of motion (Eq. 4.33) forward in time. Andersen's velocity version of the Verlet algorithm [11] has been chosen because it maintains acceptable accuracy for relatively large step sizes. Its major advantage over the original Verlet algorithm is that only information from the current time step is required to propagate forward, so the step size may be changed at any point without restarting the integration. This is useful when integrating the nonadiabatic equations of motion simultaneously, as discussed below.

The equations of motion for the positions and velocities are propagated in two separate steps, with the constraints applied at the end of each step using an iterative procedure similar to the one described in Sec. 4.1.2. In

the first step, the new positions are calculated using

$$\mathbf{R}_i(t+h) = \mathbf{R}_i(t) + h\dot{\mathbf{R}}_i + \frac{h}{2}\mathcal{F}_i - \frac{h}{2}\sum_p \lambda_p \mathcal{R}_i^p(t) \tag{4.34}$$

The constraints are applied iteratively. It is convenient to define a separate quantity $\mathbf{q}_i^N$ such that

$$\begin{aligned} \mathbf{q}_i^0 &= \dot{\mathbf{R}}_i(t) + \frac{h}{2}\mathcal{F}_i(t) \\ \mathbf{q}_i^N &= \mathbf{q}_i^{N-1} - \frac{h}{2}\lambda_p^N \mathcal{R}_i^p(t) \qquad (4.35) \\ \mathbf{R}_i^N &= \mathbf{R}_i(t) + h\mathbf{q}_i^N \qquad (4.36) \end{aligned}$$

At each iteration a single constraint is chosen and λ_p^N is determined from the constraint, $\sigma_p(\mathbf{R}^N) = 0$. Plugging Eqs. 4.35 and 4.36 into the constraint and expanding to first order in powers of λ_p^N gives

$$\lambda_p^N = \frac{2\sigma_p(\mathbf{R}^{N-1})}{h^2 \sum_i^{n_p} \mathcal{R}_i^p(t) \cdot \nabla_{\mathbf{R}_i}\sigma_p(\mathbf{R}^{N-1})}. \tag{4.37}$$

Each iteration requires only evaluation of the constraint p and its gradient with respect to the other primary atom positions. The iteration is continued until all of the constraints are satisfied to within a specific tolerance, generally 10^{-6}–10^{-8}.

Once the constrained positions $\mathbf{R}_i(t+h)$ have been determined, the

forces at the new time are calculated and used to propagate the velocities via

$$\begin{aligned}\dot{\mathbf{R}}_i(t+h) &= \dot{\mathbf{R}}_i(t) + \\ &\quad \frac{h}{2}\left[\mathcal{F}_i(t) - \sum_p \lambda_p \mathcal{R}_i^p(t) + \mathcal{F}_i(t+h) - \sum_p {}^v\lambda_p \mathcal{R}_i^p(t+h)\right] \\ &= \mathbf{q}_i^N + \frac{h}{2}\left[\mathcal{F}_i(t+h) - \sum_p {}^v\lambda_p \mathcal{R}_i^p(t+h)\right] \qquad (4.38)\end{aligned}$$

The velocities must be constrained so that they obey the time derivatives of the constraints, $\dot{\sigma}_p\left(\mathbf{R}(t+h), \dot{\mathbf{R}}(t+h)\right)$. This is accomplished by iteration over the constraints

$$\dot{\mathbf{R}}_i^0 = \mathbf{q}_i^N + \frac{h}{2}\mathcal{F}_i(t+h) \qquad (4.39)$$

$$\dot{\mathbf{R}}_i^N = \dot{\mathbf{R}}_i^{N-1} - \frac{h}{2}{}^v\lambda_p^N \mathcal{R}_i^p(t). \qquad (4.40)$$

Requiring the time derivatives of the constraints to obey

$$\dot{\sigma}_p\left(\mathbf{R}(t+h), \dot{\mathbf{R}}(t+h)\right) = 0 \qquad (4.41)$$

and expanding this to first order in ${}^v\lambda_p^N$ gives

$${}^v\lambda_p^N = \frac{2\dot{\sigma}_p\left(\mathbf{R}(t+h), \dot{\mathbf{R}}^{N-1}(t+h)\right)}{h\sum_i^{n_p} \mathcal{R}_i^p(t+h) \cdot \nabla_{\mathbf{R}_i}\dot{\sigma}_p\left(\mathbf{R}(t+h), \dot{\mathbf{R}}^{N-1}(t+h)\right)} \qquad (4.42)$$

The iteration is continued until all of the constraint derivatives fall below the specified tolerance. While this two-step procedure is somewhat more involved than the single-step SHAKE procedure used to apply constraints with the Verlet algorithm, the additional computational expense is negligible. Andersen has

shown that the two-step constraint method, which he calls RATTLE, combined with the velocity Verlet algorithm has the same global error as the Verlet algorithm [11]. The energy conservation is $O(h^2)$, and a simple diagnostic is to check that the standard deviation of the energy over a trajectory scales quadratically with the step size.

4.2 Nonadiabatic Dynamics

Photodissociation in molecular clusters involves dynamics on multiple, highly-coupled potential energy surfaces. A complete description of such a process would require quantum-mechanical treatment of both the nuclear and electronic degrees of freedom in the problem. This is clearly not feasible for systems with more than a few atoms because of the intensive computational demands of quantum methods, which scale exponentially with the number of degrees of freedom. Mixed quantum-classical (MQC) methods, in which the majority of degrees of freedom are described by classical mechanics, scale linearly with number of degrees of freedom and offer an approximate solution to the problem. These methods require that a clear separation can be made between quantum and classical degrees of freedom. In the case of photodissociation in molecular clusters, the separation between quantum and classical degrees of freedom is just the Born-Oppenheimer separation between electronic and nuclear motion: the electronic states of the solute are treated quantum mechanically, while all of the nuclei are treated classically. In what follows, $\mathbf{R}$ will denote the classical coordinates, which are the nuclear positions, and $\mathbf{r}$ will represent the quantum mechanical coordinates, which are the electron positions. The section is divided into three parts. Section 4.2.1 describes various methods

available for treating MQC dynamics, and explains why surface-hopping has been chosen to model photodissociation in clusters. Section 4.2.2 addresses the fundamental problem of treating quantum decoherence that arises in all surface hopping methods and discusses several possible solutions. Finally, Section 4.2.3 presents the details of the surface-hopping algorithm used in the present work.

4.2.1 Mixed Quantum-Classical Methods

Central to all MQC methods is the concept of the classical path, which is the path through configuration space followed by the classical degrees of freedom under the influence of forces determined from both the classical and quantum systems. The quantum-mechanical wave function for the entire system samples a range of classical configurations, so that in order to mimic quantum mechanics many classical paths must be computed starting from a distribution of initial conditions, with the observables determined from ensemble averages over all the paths. The various methods of computing MQC dynamics differ primarily in the way the forces acting on the classical subsystem are determined and in how the paths are averaged in order to compute observables. The use of classical path ideas dates back to Mott [19], who studied the electronic excitation of atoms during collisions using a classical description of the nuclei and wave functions to describe the electrons. The time evolution of the quantum wave function in all classical path treatments is determined by integrating the time-dependent Schrödinger equation along the classical path. The wave function for the quantum subsystem is expanded in some basis of orthonormal functions that may depend parametrically upon the

classical coordinates,

$$\Psi(\mathbf{r}, \mathbf{R}, t) = \sum_i c_i(t)\psi_i(\mathbf{r}; \mathbf{R}). \tag{4.43}$$

The Hamiltonian for the system can be written as an operator on the quantum degrees of freedom

$$\hat{H} = \hat{H}_0(\mathbf{r}; \mathbf{R}) + \hat{T}(\mathbf{R}), \tag{4.44}$$

where $\hat{H}_0(\mathbf{r}; \mathbf{R})$ is the Hamiltonian for fixed nuclei and $\hat{T}(\mathbf{R})$ is the nuclear kinetic energy operator. Putting this wave function and Hamiltonian into the time-dependent Schrödinger equation to determine the time evolution of the coefficients $c_i(t)$ gives

$$i\hbar\dot{c}_i(t) = \sum_j c_j \left(H_{ij} - i\hbar\langle\psi_i|\partial/\partial t|\psi_j\rangle\right). \tag{4.45}$$

The probability of occupying a given quantum state i at time t is given by $|c_i(t)|^2$. Although any representation may be chosen for the electronic basis functions, it is common to choose the eigenstates of $\hat{H}_0$, otherwise known as the adiabatic states, because this is the only representation that can be uniquely defined for a general system. In the adiabatic representation, the equation for the quantum amplitudes reduces to

$$i\hbar\dot{c}_i(t) = c_i E_i - i\hbar \sum_j c_j \dot{\mathbf{R}}(t) \cdot \mathbf{d}_{ij}, \tag{4.46}$$

where E_i is the energy of adiabatic state i, $\dot{\mathbf{R}}(t)$ contains the nuclear velocities, and $\mathbf{d}_{ij}$ is the nonadiabatic coupling vector

$$\mathbf{d}_{ij} = \langle \psi_i | \nabla_{\mathbf{R}} | \psi_j \rangle, \tag{4.47}$$

which enters Eq. 4.45 by application of the chain rule

$$\langle \psi_i | \partial / \partial t | \psi_j \rangle = \dot{\mathbf{R}}(t) \cdot \mathbf{d}_{ij}. \tag{4.48}$$

The matrix elements of the nuclear kinetic energy operator $\hat{T}(\mathbf{R})$ probe second derivatives of the electronic wave function with respect to the nuclear coordinates, and are thus small compared to the $\mathbf{d}_{ij}$ and usually neglected [20–22]. Methods for evaluating the nonadiabatic couplings given by the $\mathbf{d}_{ij}$ are discussed in Sec. 4.3.

The classical path equations of motion, Eq. 4.45 or 4.46, determine how the quantum degrees of freedom respond to the evolution of the classical degrees of freedom. Some method is also needed to determine the forces that act on the classical subsystem as the quantum wave function evolves. Perhaps the simplest force to use is the self-consistent or mean-field force,

$$\mathbf{F}_{\mathrm{MF}} = -\left\langle \Psi(t) | \nabla_{\mathbf{R}} \hat{H}_0(\mathbf{R}) | \Psi(t) \right\rangle, \tag{4.49}$$

which is simply the force averaged over the quantum degrees of freedom. Methods that use this force to determine the classical path are known as self-consistent classical path (SCCP) methods [23]. Trajectories computed using the mean-field force are guaranteed to conserve energy. While SCCP methods have been successfully applied to a wide range of problems [23], they suffer

from several well-known drawbacks [23–26]. Because the SCCP follows an average potential, it cannot reproduce the variety of different paths that arise when the potential surfaces are very different. SCCP methods are thus particularly inappropriate for modeling photodissociation, where dissociation and recombination lead to very different dynamics.

In surface-hopping methods, the primary alternative to SCCP methods, classical trajectories evolve under the forces determined from a single quantum state k,

$$\mathbf{F}_{\mathrm{SH}} = -\left\langle \psi_k | \nabla_{\mathbf{R}} \hat{H}_0(\mathbf{R}) | \psi_k \right\rangle . \tag{4.50}$$

At various points along the trajectory, generally coinciding with regions of strong interstate coupling, hops may take place to different states to reflect the cumulative occupation probabilities determined by the $|c_i(t)|^2$. Unlike the mean-field force, the force on a surface-hopping trajectory responds to changes in the total quantum wave function only at the points where hops can occur. Self-consistency between the quantum wave function and the classical degrees of freedom is thus not realized on an individual trajectory, but is realized for the ensemble of trajectories, which maintains the correct population of quantum states. The main difference between a SH and a SCCP trajectory is thus the length of time a quantum state that is a mixture of the basis states is used to determine the forces; or, in other words, the time scale over which a transition from one basis state to another takes place. In SCCP methods this time scale is infinite: the mixed state is never resolved, which leads to problems when the potentials for the various states differ significantly. In SH methods, the transition from one potential to another is instantaneous, with the difference in

energy made up by some adjustment of the classical velocities. Thus, different SH trajectories may follow divergent trajectories when the states involved have substantially different potentials.

A simple illustration of surface hopping is shown in Fig. 4.2. In this model problem, originally studied by Tully [24], a wavepacket entering on the left in the lower state passes through a region of strong nonadiabatic coupling. At energies below the barrier on the upper state, the part of the wavepacket making the transition to the upper state is reflected back, while the wavepacket on the lower state is accelerated toward the right. The same behavior is exhibited by SH trajectories. After passage through the coupling region, some of the trajectories will be promoted to the upper state and be reflected back, while other will be accelerated on the lower state. In fact, SH methods do an excellent job of reproducing the quantum transmission and reflection probabilities for this problem [24]. In contrast, the SCCP trajectories all follow the path illustrated by the dashed line and are accelerated on the lower surface. This example shows that when a transition is made between two potential surfaces of very different shape, the time scale over which the classical degrees of freedom experience a mixed-state potential is very short. It also illustrates the importance of the choice of basis states in SH methods: if the diabatic states, shown by the dotted lines, were used the SH trajectories would be meaningless. It has been shown [23] that SH methods generally work best when adiabatic potentials are used.

Tully has introduced a general and easily applied SH method called molecular dynamics with quantum transitions (MDQT) [24, 27]. Coker and coworkers have also discussed this method extensively [22, 28] and made numerous applications to multidimensional systems of physical and experimen-

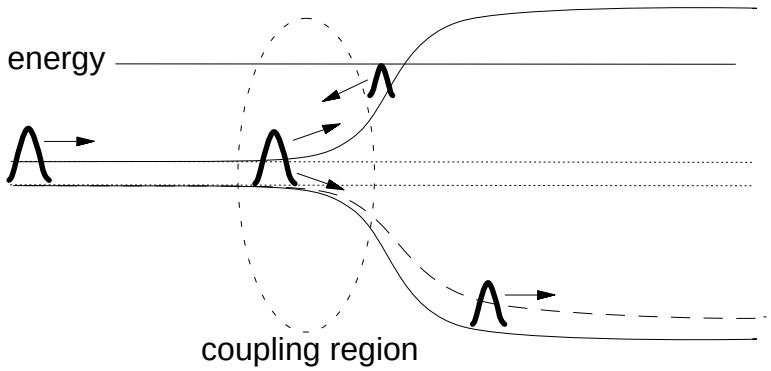

Figure 4.2: Wavepacket dynamics on two coupled potential surfaces. A wavepacket entering on the left in the lower state with energy below the upper state barrier is split into two pieces in the coupling region. The portion that remains on the lower state is accelerated toward the right, while the portion that goes to the upper state is reflected. The reflected wavepacket splits again on its reentry into the coupling region. The dotted lines indicate the diabatic potentials, and the long-dashed line illustrates the mean-field potential.

tal interest [29–37]. Another prescription for carrying out extended surface-hopping dynamics has been given by Kuntz [38], but it has not been widely used. In MDQT, the quantum amplitudes (Eq. 4.46) are integrated throughout the course of a trajectory. At every time step a decision is made whether to switch to a new state using a "fewest switches" algorithm designed to minimize the total number of hops [22, 24]. This algorithm correctly reproduces the probabilities $|c_i(t)|^2$ of occupying each quantum state at any time along a given trajectory. The two major advantages of MDQT over previous SH methods [20, 21] are that regions of strong coupling do not have to be identified in advance and regions of extended coupling may be treated. Both of these properties make MDQT easy to implement in any system, regardless of size, as long as the necessary potential surfaces and couplings can be computed at arbitrary configurations. Because of its simplicity and success, MDQT has become the standard method for computing nonadiabatic dynamics in systems with more

than a few degrees of freedom.

Prehzdo and Rossky [26] have recently incorporated a localized mean force potential in a surface-hopping algorithm to provide smoother hopping among potential curves in regions where the coupling is strong, and have obtained some improvement over MDQT for some one dimensional model problems. Their method represents only a small change from the MDQT procedure, however, because the mean field potential is only used in regions where the coupling is strong and the potential curves differ by a small amount, and it remains to be seen whether this will have an effect on results for larger systems.

One purported advantage of MDQT over earlier SH approaches is the ability to capture certain quantum interference effects. The fact that the quantum amplitudes are not reset at each passage into a new coupling region means that the quantum amplitudes may interfere with each other in subsequent coupling regions, leading to observable interference effects, such as Stueckelberg oscillations [24]. While the MDQT method assumes instantaneous resolution of the mixed state for the purposes of determining the forces acting on a single trajectory, it assumes an infinite time scale for the propagation of the mixed state quantum wave function. Another way of saying this is that the quantum phase coherence is maintained for all time. This inconsistency is present in all SH methods because the time scale for mixed state propagation must be of at least finite duration for transitions to take place. It would perhaps be more consistent, however, to set the quantum state to be the occupied state, i.e. $|\Psi(t)\rangle = |\psi_k\rangle$, following a successful hop, as at least one group has suggested [39, 40]. Then resolution of the mixed state wave function for calculating the forces and for propagating the quantum amplitudes would coincide. This is only a partial solution to the problem, however, because the mixed state is

still propagated indefinitely if no hops occur.

To illustrate possible problems with quantum phase coherence in the MDQT method, we can revisit the model problem illustrated in Fig. 4.2. The wavepacket reflected on the upper potential passes through the coupling region for a second time, creating reflected flux on the lower state as well as the upper state. Because the wavepacket that remained on the lower state during the first passage through the coupling region continued traveling toward the right, there is no interference on the second passage through the coupling region, and the reflection probability in each state is a smooth function of the incident energy. The reflection probabilities calculated using MDQT, however, show rapid oscillations [24]. This spurious interference is caused by propagating the mixed quantum state $|\Psi(t)\rangle$ through both coupling regions. This mixed state should be resolved into a single adiabatic state in situations such as this, where the potential surfaces of the two states differ substantially. In this example, a modified MDQT where the mixed state is resolved following a hop gives the correct results. Other methods for handling the effects of the finite time scale for the resolution of the mixed quantum state, which can be referred to as quantum decoherence, are discussed in the following section.

We have seen that for determination of the forces acting on the classical degrees of freedom, mean-field methods assume an infinite time scale for transitions among different basis states, while SH methods assume an infinitesimal transition time. Pechukas carried out a semiclassical analysis of this problem in a path integral representation [41]. By making a stationary phase approximation he identified the most important path in the classical limit and determined the effective force on the classical degrees of freedom along this path. The effective force for a path starting in state j at time t_1 and ending in

state k at time t_2 is given by

$$\mathbf{F}^p_{jk}(t) = -\mathrm{Re}\left[\frac{\left\langle \tilde{\Psi}_k(t) \middle| \nabla_{\mathbf{R}} \hat{H}_0(\mathbf{R}) \middle| \Psi_j(t) \right\rangle}{\left\langle \tilde{\Psi}_k(t) \middle| \Psi_j(t) \right\rangle}\right], \tag{4.51}$$

where $\Psi_j(t)$ is the total wave function at time t determined by integrating Eq. 4.46 forward from t_1 with $\Psi_j(t_1) = \psi_j$, and $\tilde{\Psi}_k(t)$ is the total wave function at time t determined by integrating Eq. 4.46 *backward* from t_2 with $\tilde{\Psi}_k(t_2) = \psi_k$. This formula gives a smooth evolution of the force over the transition, and thus a trajectory computed using it will conserve energy. There are two main difficulties, however, involving use of the Pechukas force in MQC methods. The first is that the force is nonlocal in time, so that evaluating it requires an iterative procedure, which may be expensive to carry out and is not guaranteed to converge. The second problem lies in choosing the time interval over which the transition takes place. There is no general prescription for choosing this interval, but the results may depend sensitively upon the choice [42–44].

One important application of the Pechukas force is in deriving a scheme for adjusting the classical velocities along a SH trajectory following a hop. It has been shown [20, 21, 25, 28] that for an infinitesimal time interval, the Pechukas formula gives rise to a transition force parallel to the real part of the nonadiabatic coupling vector, $\mathbf{d}_{jk}$. Thus the MDQT trajectories, in which velocities are scaled in the direction of the nonadiabatic coupling vector following a hop, obey the Pechukas force in the limit of an instantaneous transition.

A more rigorous implementation of the Pechukas formula has been used in the stationary phase surface-hopping (SPSH) algorithm of Webster et

al. [45–47], which has been used to simulate the electronic relaxation of an excess electron in bulk water. In order to make the iterative determination of the Pechukas force tractable, they limit transitions to take place over a relatively short time interval Δt, which is chosen to match some characteristic quantum dephasing time for the system of interest. In all of the initial applications of this method [45–47], the mixed quantum state used to determine when transitions take place was also resolved into the occupied state at the end of each Δt interval. Because of the difficulty in calculating the nonlocal force, this interval must be relatively short—on the order of a few classical steps. Subsequent studies have found [42–44] that the overall rates of electronic relaxation are very sensitive to the choice of this decoherence time, and have suggested that the time scales for mixed state propagation and determination of the Pechukas force be separated, with the correct determination of the former time interval being critical to obtaining correct rates of nonadiabatic relaxation. Given that the time scale for the evaluation of the Pechukas force must be short ($\sim$ 1 fs in the solvated electron simulations) and that the velocity rescaling procedure in MDQT is equivalent to applying the Pechukas force for an infinitesimal duration, it is not clear that the additional complexity and expense of the SPSH algorithm yields a significant advantage.

While there are a number of other prescriptions for performing MQC classical dynamics, MDQT stands out because of its simplicity. None of the more sophisticated semiclassical methods [48–51] has been applied to systems with a large number of degrees of freedom, such as are found in the condensed phase or the molecular clusters studied here. Several methods have been recently introduced that make use of classical trajectories but employ a fully quantum mechanical description of the dynamics in nonadiabatic coupling re-

gions [40, 52–55]. These methods have been shown to give accurate results for problems in which the nonadiabatic events are rare and highly localized, but they require considerably more care to implement. MDQT can be carried out easily for any system where the potential surfaces for the states of interest can be calculated. The only additional requirement is the evaluation of the nonadiabatic couplings, which along with the evaluation of the forces, is discussed in Sec. 4.3 below. Integration of the quantum amplitudes (Eq. 4.46), determining when hops occur, and scaling of the velocities following a hop are all described in Sec. 4.2.3 and require minimal computational overhead. A large number of studies have now shown that MDQT can be used to obtain accurate qualitative and often quantitative information about nonadiabatic processes occurring in a wide range of physical systems [23, 29–37, 39, 56–60]. The major source of continuing concern in obtaining accurate results from MDQT trajectories is the length of time the quantum mixed state used to determine surface hopping is allowed to propagate before being resolved. This problem and some possible solutions are discussed in the next section.

4.2.2 Quantum Decoherence

Quantum decoherence arises in complex systems because the electronic wave function is periodically collapsed due to its interaction with the surrounding medium—superposition states are rapidly resolved into eigenstates, squelching interference between parts of the nuclear wave function evolving on different states [42, 44]. This helps to explain why surface-hopping techniques in general work so well in large systems; quantum decoherence assures that the dynamics on all but very short timescales are governed by the forces from a single potential surface.

Two fundamental problems arise when the mixed quantum state used to determine surface hopping is propagated indefinitely. The first is that spurious interference effects may arise from multiple passages through regions of strong nonadiabatic coupling. An example of this effect was given in the previous section. The second problem is that the nonadiabatic transition rates may be incorrect. We saw an example of this problem in the discussion of the SPSH algorithm, where the interval for propagation of the mixed state was too short. Incorrect transition rates also arise when the decoherence time is too long. It is generally believed that extensive averaging over initial conditions will mitigate the effects of spurious quantum interferences, because in systems with a large number of degrees of freedom one expects these coherences to be very sensitive to the initial conditions and thus to wash out easily when the initial conditions are averaged over. We are unaware of any studies that test this expectation. Averaging also does not solve the problem of incorrect transition rates, and some method of determining the decoherence time and resolving the mixed quantum state on this time scale must be devised.

Building on work by Nitzan and coworkers [61, 62], Rossky and coworkers [42–44] have used a frozen Gaussian approximation to the nuclear wave function to estimate decoherence times in multidimensional systems. The starting point of the analysis is a Golden rule expression for the nonadiabatic transition rate from state 1 to state 2,

$$k_{12} = \int_{-\infty}^{\infty} dt \left\langle \sum_n \sum_m \mathbf{d}_n[\mathbf{R}^{(2)}(t)] \cdot \mathbf{v}_n^{(2)}(t)\, \mathbf{d}_m[\mathbf{R}^{(1)}(0)] \cdot \mathbf{v}_m^{(1)}(0)\, J(t) \right\rangle, \quad (4.52)$$

where the angle brackets denote an average over the initial conditions, n and m run over the nuclei, $\mathbf{d}_n[\mathbf{R}^{(2)}(t)]$ is the nonadiabatic coupling between states

1 and 2 evaluated at the nuclear positions given by propagating the initial configuration on state 2 for time t, and $\mathbf{v}_n^{(2)}(t)$ are the velocities obtained from the same propagation. $J(t)$ is the overlap between the nuclear wave functions propagated for time t on the two different potential surfaces,

$$J(t) = \left\langle \chi(\mathbf{R}(0)) \left| e^{iH_2 t/\hbar} e^{-iH_1 t/\hbar} \right| \chi(\mathbf{R}(0)) \right\rangle . \tag{4.53}$$

Eq. 4.52 shows that the transition rate is determined by the product of two correlation functions given by the evolution of the nuclear positions on states 1 and 2. The time scale on which these correlation functions decay to zero is the time scale over which a nonadiabatic transition beginning at $t = 0$ contributes *coherently* to the nonadiabatic transition rate. Transitions beginning at later times affect the rate incoherently. The time scale for the decay of the integrand in Eq. 4.52 is thus the desired decoherence time we wish to obtain.

The first term in the integrand, given by everything except $J(t)$, is the autocorrelation of the nonadiabatic coupling vector projected onto the nuclear velocities, the same quantity that gives rise to state mixing in the classical path expression for the quantum amplitudes, Eq. 4.46. The length of time required for the decay of this autocorrelation function is determined by the size of the coupling region. The effect of this first term is also included in the classical path equations for the quantum amplitudes; the transition rate in both formulations depends on an integration over the nonadiabatic coupling.

The overlap term $J(t)$, however, is unique to the perturbation theory formulation and is the key to understanding the quantum decoherence. Decay of the nuclear overlap places an upper bound on the time scale for the loss of quantum coherence in nonadiabatic transitions, and has been used to define

the characteristic decoherence time [42–44]. The influence of $J(t)$ explains the observation made in the previous section that the time scale for resolution of the mixed state, i.e. loss of coherence, is related to the difference between the two coupled potential surfaces. We see now that decoherence is directly related to the decay of overlap between wavepackets in the classical coordinates propagated on the two potentials.

The loss of quantum coherence signaled by the decay of the nuclear overlap can be quantified by making a Frozen Gaussian approximation to evaluate the nuclear wave functions [42–44]. Inserting these Gaussian functions into the expression for $J(t)$ gives a short time approximation to the overlap, whose decay is given by

$$J(t) \propto \exp\left\{ \sum_n \frac{1}{4a_n\hbar^2} \left[\mathbf{F}_n^1(0) - \mathbf{F}_n^2(0)\right]^2 t^2 \right\}, \tag{4.54}$$

where $\mathbf{F}_n^1(0)$ and $\mathbf{F}_n^2(0)$ are the forces on states 1 and 2 at the time of the transition, and a_n are the widths of the frozen Gaussians, which can be estimated using the thermal de Broglie wavelength,

$$a_n = \frac{1}{\lambda_{\text{th}}^2} = \frac{M_n kT}{2\pi\hbar^2}. \tag{4.55}$$

As discussed by Neria and Nitzan [62], there is some arbitrariness in the choice of these widths, but Eq. 4.54 can be used to give a rough estimate of the decoherence times for a given application. By averaging $J(t)$ over an ensemble of photodissociation trajectories, we have found that for $I_2^-Ar_n$ clusters the decoherence time is on the order of several hundred fs. This time scale is two orders of magnitude longer than the decoherence times for the solvated electron,

which are about 1 fs [42–44]. We thus expect the effect of decoherence on the transition rates to be substantially smaller for our problems.

Now that we have identified the problems posed by quantum decoherence and identified a method for evaluating the decoherence time scale, the question becomes how to patch the MDQT method to make use of this information. In his original description of MDQT [24], Tully suggested a method for quenching the quantum coherences by introducing phenomenological quenching parameters. This can be done by propagating the quantum state using the quantum density matrix, $\rho_{kj} = c_k c_j^*$. The equations for propagating the density matrix in the adiabatic basis are

$$\dot{\rho}_{kj} = \frac{i}{\hbar}\left(E_j - E_k\right)\rho_{kj} + \sum_l \left(\rho_{kl}\dot{\mathbf{R}}\cdot\mathbf{d}_{lj} - \rho_{lj}\dot{\mathbf{R}}\cdot\mathbf{d}_{kl}\right) - \frac{1}{\tau_d}(1-\delta_{kj})\rho_{kj}, \tag{4.56}$$

where the last term introduces damping of the off-diagonal elements, i.e. the coherence, on the characteristic time scale τ_d. The above expression for the overlap decay (Eq. 4.54) can be used to provide an estimate of the appropriate choice for the decoherence parameter τ_d. Bittner and Rossky have implemented a similar procedure and made a systematic study of the effects of varying the decoherence time in both model problems [42] and for simulations of the solvated electron [44]. For the model problems they showed that shortening the decoherence times had the effect of washing out the quantum interference, and had a significant effect on nonadiabatic transition rates and other observables that depend on these rates. For the solvated electron, they have shown that the choice of decoherence time is critical in determining correct excited state lifetimes, and that the very small experimental isotope effect for D_2O is probably

due to a substantially longer decoherence time in D_2O than H_2O [43]. The use of a phenomenological density matrix for determining hopping probabilities in conjunction with perturbation theory estimates of the decoherence times may thus provide a powerful method for solving the problems posed by quantum decoherence.

In the future it will be interesting to apply these methods to the photodissociation problems studied here, in which the decoherence times, the duration of the nonadiabatic coupling and the number of coupling regions are all substantially longer. In the interim, we have chosen a more *ad hoc* approach to handling quantum decoherence effects. Our solution is to reset the quantum amplitudes to specify a pure state after passage through each coupling region, i.e. we set $c_k = 1$ for the occupied state and all other amplitudes to zero. This procedure addresses the problem of spurious quantum interferences resulting from multiple passages through nonadiabatic coupling regions, but does not directly affect the rates of nonadiabatic transitions. As mentioned above, the fact that the quantum decoherence times are several orders of magnitude longer in our systems means that the transition rates are less likely to be strongly affected by quantum decoherence effects. Resetting the quantum amplitudes in between coupling regions has the drawback that in more complex systems the coupling regions are often not well separated, meaning that in practice quantum amplitudes may still be preserved for much longer than the characteristic decoherence time. It is essential not to reset quantum amplitudes when the coupling is strong, because this can cause serious errors in the hopping probabilities, particularly in regions with weakly avoided crossings. Thus the threshold coupling to reset the amplitudes must be chosen large enough that resetting occurs frequently, but small enough to avoid spurious effects.

Although this procedure seems to work in practice, as discussed in Sec. 4.2.3 below, there is obviously some arbitrariness in choosing the threshold coupling.

4.2.3 The Surface-Hopping Algorithm

The algorithm used in this work to compute surface-hopping closely follows the MDQT prescription of Tully [24, 27] with some modifications to account for quantum decoherence. At the beginning of a trajectory the quantum amplitudes are initialized with the amplitude of the initially occupied state set to one and all others set to zero. At each time step, the classical equations of motion are propagated forward one classical time step, Δ. The equations for quantum amplitudes (Eq. 4.46) are then integrated on this interval using an adaptive time step that is much smaller than Δ to ensure convergence of the amplitudes. This second integration adds a negligible cost to the computation of trajectories. Values of the adiabatic energies and the nonadiabatic couplings are obtained along the interval through linear interpolation using the values from the classical trajectory computed at the endpoints of the interval. The classical time step must be small enough that the adiabatic energies are smoothly varying functions on the interval, so that interpolation of their values is accurate. The nonadiabatic couplings may be computed exactly at the interval endpoints, but we have chosen to follow the prescription of Tully and Hammes-Schiffer [27] and compute $[\dot{\mathbf{R}} \cdot \mathbf{d}_{ij}](t + \Delta/2)$ by a symmetrized finite difference, which is discussed in more detail in Sec. 4.3 below. The values at $t - \Delta/2$ are saved and linear interpolation and extrapolation are used to compute values intermediate between t and $t + \Delta$. The overlap of the quantum eigenvectors at successive classical steps is required to meet a threshold (usually 0.9) in order to ensure that narrow regions of strong coupling are not

missed by the integration. The classical stepsize is adaptively reduced when the overlap falls below threshold.

The "fewest switches" algorithm determines surface hopping from the probability flux rather than the amplitudes themselves. The change in probability per unit time of occupying state k is given by [24]

$$\begin{aligned} \dot{\rho}_{kk} &= -\sum_j 2\mathrm{Re}[c_j c_k^*(\mathbf{R}\cdot\mathbf{d}_{kj})] \\ &\equiv \sum_{j\neq k} b_{kj}, \end{aligned} \tag{4.57}$$

so the probability flux out of state k into state j per unit time is $-b_{kj}$. Over a finite time interval Δt, the probability of making a hop from state k to state j is

$$g_{kj} = \frac{-\int_t^{t+\Delta t} b_{kj}(t')dt'}{\rho_{kk}(t)}, \tag{4.58}$$

where $\rho_{kk}(t)$ is the probability of occupying state k at time t. These transition probabilities can be integrated along with the quantum amplitudes at little extra expense. At the end of each classical time step, the transition probabilities are used to determine whether hops take place based on comparison with a random number $0 < \zeta < 1$. A hop can take place to state j only if $g_{kj} > 0$ and $\zeta < g_{kj}$. The number of hops between states is minimized by this first criterion that $g_{kj} > 0$, which means that hops take place only when there is a net flux of probability into the target state. If multiple g_{kj} are greater than zero, hops are determined by considering the target states in succession, subtracting g_{kj} from ζ for each state to which no hop occurs. If no hop is made to any state, integration of the trajectory continues on the current state k.

When the "fewest switches" algorithm determines that a hop should occur, the velocities must be adjusted to conserve energy in the new state. Hops generally occur between states when the energy gap is very small, so while it is reassuring to maintain energy conservation, it is not clear that velocity scaling is crucial in systems with a large number of molecules. Nevertheless, the MDQT procedure calls for scaling the velocities by applying an instantaneous force in the direction $\mathrm{Re}[\mathbf{d}_{kj}]$. Scaling the velocities subject to a set of arbitrary constraints on the velocities in the system requires determining a single scale factor γ, where the velocities for each atom i are changed according to

$$\mathbf{v}_i^{\mathrm{new}}(\gamma) = \mathbf{v}_i^{\mathrm{old}} + \frac{\gamma}{m_i}\mathrm{Re}[\mathbf{d}_{kj}^{(i)}]. \tag{4.59}$$

The molecular constraints are applied to $\mathbf{v}^{\mathrm{new}}(\gamma)$ using the method described in Sec. 4.1.3 above. In order to conserve the total energy, the change in the kinetic energy due to scaling must satisfy

$$\Delta E_{\mathrm{kin}}(\gamma) = -\Delta E_{\mathrm{pot}}, \tag{4.60}$$

where ΔE_{pot} is the difference in potential energy between states k and j. $\Delta E_{\mathrm{kin}}(\gamma)$ is a quadratic function of γ with positive curvature, so to determine the new velocities it is necessary only to find the root of Eq. 4.60 with the smaller absolute value. The smaller root is chosen in order to minimize the changes made to the velocities by the scaling. When the target state is higher in energy than the current state, i.e. ΔE_{pot} is greater than zero, Eq. 4.60 may not have any real roots, in which case the hop is rejected and the current state is not changed. The MDQT procedure also specifies that the component

of the velocity in the direction of the nonadiabatic coupling be reversed [27], which is equivalent to finding the unique nonzero root of $\Delta E_{\mathrm{kin}}(\gamma) = 0$. This velocity reversal occurs because the trajectory is said to be reflected off the barrier to the target state in the direction of the Pechukas force, which for an instantaneous transition coincides with $\mathrm{Re}[\mathbf{d}_{kj}^{(i)}]$. In practice, tests on photodissociation in $I_2^- Ar_n$ clusters seem to indicate that performing the reversal has little effect on the branching ratios [56] but does have the undesirable effect of introducing instantaneous dephasing of the solute vibrations. This effect has also been noted by Müller and Stock [23], who have suggested dropping this procedure from the MDQT algorithm.

The implementation of surface hopping in this work collapses the quantum amplitudes onto a single state periodically during the course of a trajectory to mitigate the effects of spurious quantum coherence. Amplitudes are only reset if all of the nonadiabatic couplings fall below a certain threshold value (10^{-5} atomic units was used in this work). In this work the amplitude resetting was attempted only at 100 fs intervals along each trajectory. This procedure does not damp coherence that arises in extended coupling regions, but prevents coherence from arising for separate passages through strong coupling regions.

4.3 Forces and Nonadiabatic Couplings

Computing MD trajectories and surface-hopping requires determination of forces on the adiabatic potentials and nonadiabatic couplings between the potential surfaces. Calculating these quantities is generally the most time-consuming part of any simulation (other than analysis of the results), and

therefore requires careful consideration. This section is divided into four subsections: Sec. 4.3.1 discusses the general formulas for evaluating these forces and nonadiabatic couplings; Sec. 4.3.2 presents a finite difference method for calculating nonadiabatic couplings [27]; Sec.4.3.3 discusses phase matching of complex eigenvectors, which is required for the current problem because of the Kramers degeneracy resulting from unpaired electron spins; and finally Sec. 4.3.4 gives formulas for evaluating the derivatives of the model Hamiltonian described in Chapter 2 and discusses how these derivatives are converted into forces on the primary atoms.

4.3.1 General Formulas

If we assume that the adiabatic states, ψ_k are defined in terms of an orthonormal set of functions, ϕ_n, such that

$$|\psi_k\rangle = \sum_n \Gamma_{nk}|\phi_n\rangle, \tag{4.61}$$

then the Hellmann-Feynman [63] theorem gives the forces on state k

$$\mathbf{F}_k = -\nabla_{\mathbf{R}}\langle\psi_k|\hat{H}|\psi_k\rangle = -\langle\psi_k|\nabla_{\mathbf{R}}\hat{H}|\psi_k\rangle. \tag{4.62}$$

The important point here is that calculating the forces requires only derivatives of the Hamiltonian and not the derivatives of the eigenfunctions, which are more complicated to compute. The nonadiabatic couplings are given by an off-diagonal version of this relation [21, 64, 65]

$$\mathbf{d}_{jk} = \frac{\langle\psi_j|\nabla_{\mathbf{R}}H|\psi_k\rangle}{E_k - E_j} + \sum_{nn'} \Gamma^*_{nk}\Gamma_{n'j}\langle\phi_n|\nabla_{\mathbf{R}}\phi_{n'}\rangle, \tag{4.63}$$

which involves derivatives of the basis functions, but not of the coefficients that define the adiabatic states. This is useful because obtaining the derivatives of the eigenvector coefficients is a much more involved process than obtaining the eigenvectors themselves, which is done using canned matrix diagonalization routines. Computing the nonadiabatic couplings requires evaluation of the derivatives of the basis functions with respect to the classical coordinates,

$$\mathbf{D}_{nn'} = \langle \phi_n | \nabla_{\mathbf{R}} \phi_{n'} \rangle. \tag{4.64}$$

Often these derivatives can be neglected if the basis functions are independent or slowly varying functions of the classical coordinates. In the case of the low-lying electronic states of I_2^-, all of these couplings vanish for symmetry reasons. For the electronic wave functions of other molecules expressed in a basis of isolated molecule wave functions, this may not be the case. The electronic wave functions of the isolated molecule, the ϕ_n, are themselves made up of linear combinations of primitive basis functions with the coefficients given by an electronic structure calculation. This can be either an ab initio calculation or a semiempirical method such as diatomics-in-molecules. The isolated molecule wave functions are expressed as

$$\phi_n(\mathbf{r};\mathbf{R}) = \sum_s \alpha_s(\mathbf{R}) f_s(\mathbf{r};\mathbf{R}), \tag{4.65}$$

where the $f_s(\mathbf{r};\mathbf{R})$ are the primitive basis functions, which could be atomic oribitals in the case of an ab initio or DIM calculation. The matrix elements involving the derivatives of the basis functions ϕ_n can then be written as a sum

of two components

$$\mathbf{D}_{nn'} = \sum_{ss'} (\alpha_{ns} \nabla_{\mathbf{R}} \alpha_{n's'} \langle f_s | f_{s'} \rangle + \alpha_{ns} \alpha_{n's'} \langle f_s | \nabla_{\mathbf{R}} | f_{s'} \rangle) \tag{4.66}$$

The first term involves derivatives of the eigenvector coefficients of the primitive basis functions, while the second term involves derivatives of the primitive basis functions themselves. Usually the primitive basis functions attached to a molecule depend only on the internal coordinates of that molecule, in which case it is a straightforward matter to evaluate the first term using a simple finite difference method. Such a scheme is implemented in the ab initio program MOLPRO for example, and we have used it to calculated the nonadiabatic coupling in bare ICl^-, as described in Chapter 3. The second term is usually neglected from dynamical calculations, because it is known to give rise to spurious couplings [65, 66].

4.3.2 Finite Difference Nonadiabatic Couplings

The full nonadiabatic coupling vector is required by the MDQT method only when hops occur; at other times the couplings required to integrate the quantum amplitudes (Eq. 4.45) can be computed by a simple finite difference scheme [27]. In this scheme, the couplings are evaluated using a central difference at the midpoint of the classical integration step, following the determination of the classical coordinates and the adiabatic eigenvectors

at $t+\Delta$. We require the matrix elements of the time derivatives

$$\begin{aligned}\dot{\mathbf{R}}\cdot\mathbf{d}_{jk}(t+\Delta/2) &= \langle\psi_j|\partial/\partial t|\psi_k\rangle(t+\frac{\Delta}{2}) \\ &= \sum_{nn'}\Big(\Gamma^*_{nj}(t+\Delta/2)\dot{\Gamma}_{n'k}(t+\Delta/2)\delta_{nn'} \\ &\quad +\Gamma^*_{nj}(t+\Delta/2)\left[\dot{\mathbf{R}}\cdot\mathbf{D}_{nn'}(t+\Delta/2)\right]\Gamma_{n'k}(t+\Delta/2)\Big).\end{aligned} \tag{4.67}$$

It is convenient to express this formula in a matrix notation as

$$\begin{aligned}\dot{\mathbf{R}}\cdot\mathbf{d}(t+\Delta/2) &= \mathbf{\Gamma}^\dagger(t+\Delta/2)\cdot\dot{\mathbf{\Gamma}}(t+\Delta/2) \\ &\quad +\mathbf{\Gamma}^\dagger(t+\Delta/2)\cdot\left[\dot{\mathbf{R}}\cdot\mathbf{D}_{nn'}(t+\Delta/2)\right]\cdot\mathbf{\Gamma}(t+\Delta/2).\end{aligned} \tag{4.68}$$

This expression can be evaluated by making several central difference approximations at $t+\Delta/2$

$$\begin{aligned}\mathbf{\Gamma}(t+\Delta/2) &= \frac{\mathbf{\Gamma}(t+\Delta)+\mathbf{\Gamma}(t)}{2} \\ \dot{\mathbf{\Gamma}}(t+\Delta/2) &= \frac{\mathbf{\Gamma}(t+\Delta)-\mathbf{\Gamma}(t)}{\Delta} \\ \dot{\mathbf{R}}(t+\Delta/2) &= \frac{\mathbf{R}(t+\Delta)-\mathbf{R}(t)}{\Delta} \\ \mathbf{D}(t+\Delta/2) &= \frac{\mathbf{D}(t+\Delta)+\mathbf{D}(t)}{2}.\end{aligned} \tag{4.69}$$

The first term in Eq. 4.68, when evaluated using these central difference approximations, is identical to the finite difference scheme used by Hammes-Schiffer and Tully [27]. As mentioned above, linear interpolation and extrapolation are used to determine the values of the couplings required for integration of the

quantum amplitudes using a time step smaller than Δ. The accuracy of the finite difference approximation to the coupling is controlled by requiring that the overlap of the eigenstates at adjacent time intervals exceed some threshold value, i.e.

$$\langle \psi_k(t) | \psi_k(t+\Delta) \rangle > \text{tol}, \tag{4.70}$$

where tol in our simulations is taken to be 0.9. When the overlap of any of the eigenstates falls below threshold, the size of the classical time step is reduced until this criterion is satisfied.

4.3.3 Phase Matching of Eigenvectors

In the open-shelled molecules studied in this work the presence of unpaired electron gives rise to state degeneracies that are not lifted by any electrostatic interactions with the solvent. Numerical determination of these degenerate eigenstates results in an arbitrary phase being associated with each of the degenerate eigenvectors. If this phase is not preserved in calculations at neighboring geometries, the nonadiabatic coupling calculated from these states will oscillate wildly, making numerical integration of the quantum amplitudes impossible. Several ad hoc methods of handling this problem have been suggested [31, 54, 66], and a more rigorous approach has also been recently developed by Krylov et al. [39, 60]. Unfortunately, the details of this latter method remain unpublished. We have adopted instead the procedure of Maslen et al. [66], which is discussed here in detail. The eigenvectors determined by this method of phase matching have been tested numerically by comparing values of the nonadiabatic couplings computed analytically using

Eq. 4.63 with couplings computed using finite differences. The good agreement for the couplings computed using these two different methods shows that the phase matching scheme adopted here is adequate for computing nonadiabatic dynamics on these potential surfaces.

Maslen's phase matching prescription requires that the nonadiabatic couplings vanish for each member of the degenerate manifold

$$\langle \psi_j | \partial/\partial t | \psi_k \rangle = 0, \quad \forall j,k \in K, \tag{4.71}$$

where K denotes the indices of the manifold members. This requirement can be written in matrix notation as

$$\mathbf{\Gamma}_K^\dagger(t)\dot{\mathbf{\Gamma}}_K(t) + \mathbf{\Gamma}_K^\dagger(t)\left(\dot{\mathbf{R}}\cdot\mathbf{D}\right)\mathbf{\Gamma}_K(t) = 0, \tag{4.72}$$

where $\mathbf{\Gamma}_K(t)$ is a matrix whose columns contains the manifold eigenvectors. Using a finite difference approximation to the time derivative

$$\dot{\mathbf{\Gamma}}_K(t) \approx \frac{\mathbf{\Gamma}_K(t+\Delta) - \mathbf{\Gamma}_K(t)}{\Delta} \tag{4.73}$$

this equation can be manipulated to give

$$\mathbf{\Gamma}_K(t+\Delta) = [\mathbf{1} - \delta\mathbf{R}\cdot\mathbf{D}]\,\mathbf{\Gamma}_K(t), \tag{4.74}$$

where $\delta\mathbf{R} = \mathbf{R}(t+\Delta) - \mathbf{R}(t)$. Now if $\mathbf{\Gamma}'_K(t+\Delta)$ contains the eigenvectors obtained from numerical diagonalization of the Hamiltonian, the phase matched eigenvectors at the new time are related to these unmatched eigenvectors by

the unitary transformation

$$\mathbf{\Gamma}'_K(t+\Delta) = \mathbf{\Gamma}_K(t+\Delta)\mathbf{U}. \tag{4.75}$$

Putting this into the phase matching requirement given by Eq. 4.74 gives the desired transformation matrix

$$\mathbf{U} = \mathbf{\Gamma}_K^{\dagger}(t)\left[\mathbf{1} + \delta\mathbf{R}\cdot\mathbf{D}\right]\mathbf{\Gamma}'_K(t+\Delta). \tag{4.76}$$

$\mathbf{U}$ is only unitary in the limit of an infinitesimal time step, so to maintain the orthonormality of the phase matched eigenvectors, $\mathbf{U}$ is transformed using symmetric orthogonalization,

$$\mathbf{U}_{\text{new}} = \mathbf{S}^{-1/2}\mathbf{U}, \tag{4.77}$$

where

$$\mathbf{S} = \mathbf{U}\mathbf{U}^{\dagger}. \tag{4.78}$$

A central difference approximation is used for the basis function derivatives

$$\mathbf{D} \approx \frac{\mathbf{D}(t+\Delta) + \mathbf{D}(t)}{2}. \tag{4.79}$$

This procedure for determining the phase matched eigenvectors has minimal computational overhead and has been shown to maintain phase continuity, as demonstrated by the accuracy of the nonadiabatic couplings determined using the finite difference formulas of the previous section.

4.3.4 Derivatives of the Model Hamiltonian

In Chapter 2 we presented an effective Hamiltonian for clusters including the electronic states of the solute and the interactions among solute and solvent molecules. We now discuss the computation of the analytic derivatives of this Hamiltonian that are needed to determine the forces and nonadiabatic couplings. The discussion includes only the derivatives of the electrostatic terms, since derivatives of the remaining pairwise terms are standard quantities in MD simulations and have been discussed extensively elsewhere [3, 67]. The derivatives of the electrostatic terms are expressed in Stone's notation [68, 69] as forces and torques acting on the individual multipole sites. The procedures for converting these forces and torques into forces on the primary atoms, as required by our method of computing the molecular dynamics, are described following discussion of the basic derivatives.

The effective Hamiltonian for the electrostatic and induction-dispersion interaction of the solute and solvent can be expanded into five terms,

$$\begin{aligned}\hat{h}^{\mathrm{ele}} &= \frac{1}{2}\mathsf{Q}\cdot\mathsf{T}\cdot\mathsf{Q}+\hat{\mathsf{q}}\cdot\mathsf{T}\cdot\mathsf{Q} \\ &\quad -\frac{1}{2}\mathsf{Q}\cdot\mathsf{T}\cdot\boldsymbol{\chi}\cdot\mathsf{T}\cdot\mathsf{Q}-\hat{\mathsf{q}}\cdot\mathsf{T}\cdot\boldsymbol{\chi}\cdot\mathsf{T}\cdot\mathsf{Q}-\frac{1}{2}\hat{\mathsf{q}}\cdot\mathsf{T}\cdot\boldsymbol{\chi}\cdot\mathsf{T}\cdot\hat{\mathsf{q}},\end{aligned} \tag{4.80}$$

where the first two terms contain the interactions among the permanent multipoles and the last three terms contain the interactions of the permanent multipoles with the induced moments. It is convenient to discuss the derivatives arising from each of these interactions separately because of the large number of terms that arise. The derivatives are computed in terms of the generalized

coordinate X_i, which represents the Cartesian and angular coordinates of each of the multipole sites in the system.

The forces due to the first term in Eq. 4.80, the interactions of the permanent solvent multipoles, are given by

$$\begin{aligned} F_i^{(1)} &= -\frac{1}{2}\frac{\partial}{\partial X_i}\left(\mathsf{Q}\cdot\mathsf{T}\cdot\mathsf{Q}\right) \\ &= -\frac{1}{2}\mathsf{Q}\cdot\frac{\partial\mathsf{T}}{\partial X_i}\cdot\mathsf{Q}, \end{aligned} \tag{4.81}$$

where we have assumed for simplicity that the multipoles contained in Q do not depend on any of the coordinates X_i. Because this term does not depend on the electronic state of the solute, it contributes the same to all of the adiabatic forces and does not contribute to the nonadiabatic couplings. Computation of the forces from this equation and the similar but more complicated expressions presented below may be performed very efficiently. The tensor T contains only pairwise interactions so that there are at most 12 nonzero derivatives of each element T_{ab}, because each multipole site is defined by three position and three orientation coordinates. In fact, since $\mathbf{F}_a = -\mathbf{F}_b$, there are at most 9 unique derivatives. As we will see below, computation of these derivatives involves simple terms already required for the evaluation of the energy, and calculation of the adiabatic energies and forces is only about three times as expensive as calculation of the energies alone.

Terms involving the solute multipole operators $\hat{\mathsf{q}}$ depend on the solute electronic state. The matrix elements of the derivatives of the second term in Eq. 4.80, the interactions of the solute multipole operators with the permanent

solvent multipoles, are given by

$$\begin{aligned}(d_{jk}^{(2)})_i &= \left\langle \phi_j \left| \frac{\partial}{\partial X_i}\hat{\mathsf{q}} \cdot \mathsf{T} \cdot \mathsf{Q} \right| \phi_k \right\rangle \\ &= \mathsf{q}_{jk} \cdot \frac{\partial \mathsf{T}}{\partial X_i} \cdot \mathsf{Q} + \frac{\partial R_c}{\partial X_i}\left(\frac{\partial \mathsf{q}_{jk}}{\partial R_c} \cdot \mathsf{T} \cdot \mathsf{Q}\right), \end{aligned} \tag{4.82}$$

where $(d_{jk}^{(2)})_i$ refers to the matrix elements of the Hamiltonian derivatives rather than the nonadiabatic couplings, which are computed from these derivatives using Eq. 4.63. q_{jk} represents the matrix elements of the multipole operators, $\langle \phi_j | \hat{\mathsf{q}} | \phi_k \rangle$. Derivatives of these operators with respect to the internal solute coordinate R_c are nonzero, and are determined, as are the multipole operators themselves, by cubic spline interpolation. It is in fact rare during the course of a trajectory that all of the derivative matrix elements are evaluated in this way—only when the full nonadiabatic coupling vector is required to adjust the classical velocities following a hop. The remainder of the time only the force on a given adiabatic state ψ is required, for which only the expectation value of the multipole operators, $\langle \hat{\mathsf{q}} \rangle_\psi$, are necessary. The adiabatic force is given by

$$(F_\psi^{(2)})_i = \langle \hat{\mathsf{q}} \rangle_\psi \cdot \frac{\partial \mathsf{T}}{\partial X_i} \cdot \mathsf{Q} + \frac{\partial R_c}{\partial X_i}\left(\frac{\partial \langle \hat{\mathsf{q}} \rangle_\psi}{\partial R_c} \cdot \mathsf{T} \cdot \mathsf{Q}\right). \tag{4.83}$$

Because only the expectation value of $\hat{\mathsf{q}}$ is needed, computation of the forces arising from the quantum wave function is only marginally more expensive than calculation of the purely classical forces.

The terms involving the induced moments can be evaluated by making

use of the relation

$$\begin{aligned}\frac{\partial \boldsymbol{\chi}}{\partial X_i} &= \frac{\partial \left[\mathsf{T} + \boldsymbol{\alpha}^{-1}\right]^{-1}}{\partial X_i} \\ &= -\left[\mathsf{T} + \boldsymbol{\alpha}^{-1}\right]^{-1} \cdot \frac{\partial \mathsf{T}}{\partial X_i} \cdot \left[\mathsf{T} + \boldsymbol{\alpha}^{-1}\right]^{-1} \\ &= -\boldsymbol{\chi} \cdot \frac{\partial \mathsf{T}}{\partial X_i} \cdot \boldsymbol{\chi}. \end{aligned} \tag{4.84}$$

The forces due to the third term in Eq. 4.80, the interactions of the permanent solvent multipoles with the induced multipoles, are given by

$$\begin{aligned} F_i^{(3)} &= \frac{1}{2}\frac{\partial}{\partial X_i}\left(\mathsf{Q} \cdot \mathsf{T} \cdot \boldsymbol{\chi} \cdot \mathsf{T} \cdot \mathsf{Q}\right) \\ &= -\mathsf{Q} \cdot \frac{\partial \mathsf{T}}{\partial X_i} \cdot \boldsymbol{\Delta}_Q - \frac{1}{2}\boldsymbol{\Delta}_Q \cdot \frac{\partial \mathsf{T}}{\partial X_i} \cdot \boldsymbol{\Delta}_Q, \end{aligned} \tag{4.85}$$

which has been simplified by identifying the induced moments, $\boldsymbol{\Delta}_Q \equiv -\boldsymbol{\chi} \cdot \mathsf{T} \cdot \mathsf{Q}$. The matrix elements of the derivatives of the fourth term in Eq. 4.80, the cross term between the solute and solvent multipoles interacting with the induced moments are

$$\begin{aligned} (d_{jk}^{(4)})_i &= \left\langle \phi_j \left| \frac{\partial}{\partial X_i}\left(-\hat{\mathsf{q}} \cdot \mathsf{T} \cdot \boldsymbol{\chi} \cdot \mathsf{T} \cdot \mathsf{Q}\right) \right| \phi_k \right\rangle \\ &= \frac{\partial R_c}{\partial X_i}\left(\frac{\partial \mathsf{q}_{jk}}{\partial R_c} \cdot \mathsf{T} \cdot \boldsymbol{\Delta}_Q\right) + \mathsf{q}_{jk} \cdot \frac{\partial \mathsf{T}}{\partial X_i} \cdot \boldsymbol{\Delta}_Q \\ &\quad + \boldsymbol{\Delta}_{jk} \cdot \frac{\partial \mathsf{T}}{\partial X_i} \cdot \boldsymbol{\Delta}_Q + \boldsymbol{\Delta}_{jk} \cdot \frac{\partial \mathsf{T}}{\partial X_i} \cdot \mathsf{Q}, \end{aligned} \tag{4.86}$$

where $\boldsymbol{\Delta}_{jk} \equiv -\boldsymbol{\chi} \cdot \mathsf{T} \cdot \mathsf{q}_{jk}$ are the induced moments due to the solute multipole matrix elements. It is also useful to express the forces arising from this term

on the adiabatic state ψ,

$$\begin{aligned}(F_\psi^{(4)})_i &= -\frac{\partial R_c}{\partial X_i}\left(\frac{\partial \langle\hat{\mathsf{q}}\rangle_\psi}{\partial R_c}\cdot\mathsf{T}\cdot\boldsymbol{\Delta}_Q\right) - \langle\hat{\mathsf{q}}\rangle_\psi\cdot\frac{\partial\mathsf{T}}{\partial X_i}\cdot\boldsymbol{\Delta}_Q \\ &\quad -\boldsymbol{\Delta}_\psi\cdot\frac{\partial\mathsf{T}}{\partial X_i}\cdot\boldsymbol{\Delta}_Q - \boldsymbol{\Delta}_\psi\cdot\frac{\partial\mathsf{T}}{\partial X_i}\cdot\mathsf{Q}, \end{aligned} \tag{4.87}$$

where $\boldsymbol{\Delta}_\psi \equiv -\boldsymbol{\chi}\cdot\mathsf{T}\cdot\langle\mathsf{q}\rangle_\psi$. The fifth and final term in Eq. 4.80, which arises from the interaction of the solute multipoles with the induced moments, is a two electron operator and is thus somewhat more complicated to evaluate. This operator is determined in terms of one electron operators by inserting the identity operator, $\hat{1} = \sum_n |\phi_n\rangle\langle\phi_n|$, which is approximated by restricting the sum to the basis set used in the calculation of the adiabatic states. The derivative matrix elements are then given by

$$\begin{aligned}(d_{jk}^{(5)})_i &= \left\langle \phi_j \left| \frac{\partial}{\partial X_i}\left(-\frac{1}{2}\hat{\mathsf{q}}\cdot\mathsf{T}\cdot\boldsymbol{\chi}\cdot\mathsf{T}\cdot\hat{\mathsf{q}}\right)\right| \phi_k\right\rangle \\ &= \frac{1}{2}\sum_n\left\{\frac{\partial R_c}{\partial X_i}\left(\frac{\partial\mathsf{q}_{jn}}{\partial R_c}\cdot\mathsf{T}\cdot\boldsymbol{\Delta}_{nk} + \frac{\partial\mathsf{q}_{nk}}{\partial R_c}\cdot\mathsf{T}\cdot\boldsymbol{\Delta}_{jn}\right)\right. \\ &\quad +\mathsf{q}_{jn}\cdot\frac{\partial\mathsf{T}}{\partial X_i}\cdot\boldsymbol{\Delta}_{nk} + \mathsf{q}_{nk}\cdot\frac{\partial\mathsf{T}}{\partial X_i}\cdot\boldsymbol{\Delta}_{jn} \\ &\quad \left.+\boldsymbol{\Delta}_{jn}\cdot\frac{\partial\mathsf{T}}{\partial X_i}\cdot\boldsymbol{\Delta}_{nk}\right\}. \end{aligned} \tag{4.88}$$

The adiabatic forces arising from this term simplify to

$$\begin{aligned}(F_\psi^{(5)})_i &= -\sum_n\left\{\frac{\partial R_c}{\partial X_i}\mathrm{Re}\left(\frac{\partial\mathsf{q}_{\psi n}}{\partial R_c}\cdot\mathsf{T}\cdot\boldsymbol{\Delta}_{n\psi}\right) + \mathrm{Re}\left(\mathsf{q}_{\psi n}\cdot\mathsf{T}\cdot\boldsymbol{\Delta}_{n\psi}\right)\right. \\ &\quad \left.+\frac{1}{2}\boldsymbol{\Delta}_{\psi n}\cdot\frac{\partial\mathsf{T}}{\partial X_i}\cdot\boldsymbol{\Delta}_{n\psi}\right\}, \end{aligned} \tag{4.89}$$

where $\mathsf{q}_{\psi n} = \langle\psi|\hat{\mathsf{q}}|\phi_n\rangle$ and $\boldsymbol{\Delta}_{n\psi} =\equiv -\boldsymbol{\chi}\cdot\mathsf{T}\cdot\mathsf{q}_{n\psi}$. This completes the formulas required to compute the derivatives and forces for the effective Hamiltonian

model. While the equations are a bit cumbersome to look at, they have been coded in an efficient computer program and, as mentioned above, are only about 3 times more expensive to compute than the adiabatic energies alone. We have tested all of the forces and nonadiabatic couplings computed analytically using the above formulas against finite difference approximations to the same quantities to ensure that the coding has been done correctly. The correctness of the forces is also verified by the fact that energy is conserved to high precision along MD trajectories and that the errors in the total energy scale quadratically with the step size when using the velocity Verlet algorithm [3, 11].

We now discuss evaluation of the derivatives of the interaction tensor matrix elements required to compute the forces. The tensor matrix elements derived by Stone and coworkers [68] are expressed in terms of 16 basic variables involving the multipole site positions and the axes used to define the multipoles. The interaction between two multipole sites a and b on molecules A and B is illustrated in Fig. 4.3. The fundamental quantities that occur in the tensor formulas are R_{ab}, the separation vector between sites a and b, and the multipole axes, $\mathbf{w}_a = \mathbf{x}_a, \mathbf{y}_a, \mathbf{z}_a$ and $\mathbf{w}_b = \mathbf{x}_b, \mathbf{y}_b, \mathbf{z}_b$. The axes defining the multipoles on each site may in general differ from the molecular axes, but they are taken to be the same in this work. The 16 variables that occur in the interaction tensor formulas are R_{ab}, $\mathbf{w}_a \cdot \mathbf{R}_{ab}$, $\mathbf{w}_b \cdot \mathbf{R}_{ab}$, and $\mathbf{w}_a \cdot \mathbf{w}_b$. So, for example, the tensor element between the z component of the dipole moment on site a and a charge on site b is given by

$$T^{ab}_{10,00} = \frac{-(\mathbf{z}_a \cdot \mathbf{R}_{ab})}{R^3_{ab}}. \tag{4.90}$$

In Stone's formulation the derivatives of these tensor elements are converted

to forces and torques acting on the molecular center of mass by making use of the chain rule and the derivatives of the 16 basic variables with respect the the center of mass position and orientation [68, 70]. This method assumes that the molecules are rigid, and the approach must be modified to apply to the nonrigid molecules, particularly the solute, considered by our method. We do this by converting the derivatives of the tensor elements with respect to the 16 fundamental variables to forces and torques acting on the multipole sites. These forces and torques are then converted to forces on the primary atoms following an additional application of the chain rule to determine the derivatives of the multipole positions and orientations with respect to the primary atom positions. As mentioned in Sec. 4.1.1, this process is straightforward for linear molecules but cumbersome for larger molecules, and a general procedure for determining these derivatives has not to our knowledge been worked out.

The forces and torques acting on the multipole sites for any given interaction pair can be determined from the derivatives of the fundamental variables with respect to the multipole positions and orientations. The derivatives with respect to the positions are [68, 70]

$$\begin{aligned}
&\nabla_{\mathbf{R}_a}(\mathbf{R}_{ab}) = \frac{\mathbf{R}_{ab}}{R_{ab}} && \nabla_{\mathbf{R}_b}(\mathbf{R}_{ab}) = -\frac{\mathbf{R}_{ab}}{R_{ab}} \\
&\nabla_{\mathbf{R}_a}(\mathbf{w}_a \cdot \mathbf{R}_{ab}) = \mathbf{w}_a && \nabla_{\mathbf{R}_b}(\mathbf{w}_a \cdot \mathbf{R}_{ab}) = -\mathbf{w}_a \\
&\nabla_{\mathbf{R}_a}(\mathbf{w}_b \cdot \mathbf{R}_{ab}) = \mathbf{w}_b && \nabla_{\mathbf{R}_b}(\mathbf{w}_b \cdot \mathbf{R}_{ab}) = -\mathbf{w}_b \\
&\nabla_{\mathbf{R}_a}(\mathbf{w}_a \cdot \mathbf{w}_b) = 0 && \nabla_{\mathbf{R}_b}(\mathbf{w}_a \cdot \mathbf{w}_b) = 0.
\end{aligned} \tag{4.91}$$

Application of the chain rule to derivatives of the expressions for the T_{ab} given by Stone and coworkers [68, 69] using these equations gives the desired forces acting on the multipole sites. For example, the force acting on site a due to

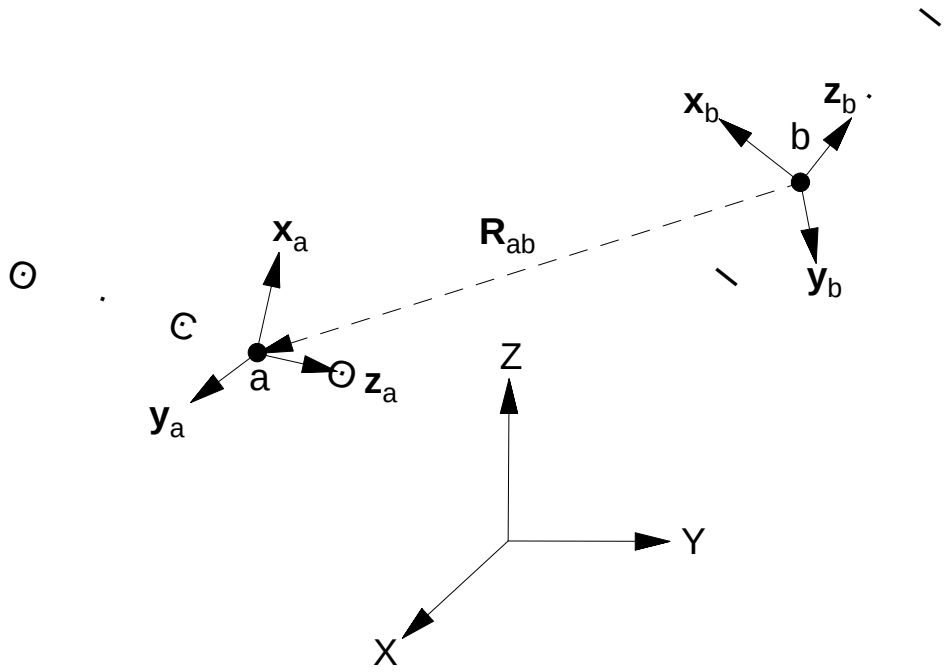

Figure 4.3: Vectors describing the interaction of two multipole sites on different molecules. Vectors denoted by a capital letter are fixed in the space frame, while lowercase vectors are body-fixed.

the dipole-charge interaction listed above is given by

$$\nabla_{\mathbf{R}_a} T^{ab}_{10,00} = -\frac{3(\mathbf{w}_a \cdot \mathbf{R}_{ab})\mathbf{R}_{ab}}{R^5_{ab}} + \frac{\mathbf{w}_a}{R^3_{ab}}. \tag{4.92}$$

The torques about the space-fixed axes are given by the derivatives of the body-fixed multipole axes with respect to rotations about the space-fixed axes. The derivatives of a vector fixed in body-fixed frame with respect to rotations of the body are given by

$$\nabla_{\mathbf{\Omega}} = -\mathbf{v}_{\mathrm{BF}} \times . \tag{4.93}$$

Using this relation and the fact that the site separation vector $\mathbf{R}_{ab}$ is independent of the body-fixed frames, the formulas necessary to compute the torques

are

$$\begin{aligned}
&\nabla_{\boldsymbol{\Omega_a}}(\mathbf{R}_{ab}) = 0 && \nabla_{\boldsymbol{\Omega_b}}(\mathbf{R}_{ab}) = 0 \\
&\nabla_{\boldsymbol{\Omega_a}}(\mathbf{w}_a \cdot \mathbf{R}_{ab}) = \mathbf{w}_a \times \mathbf{R}_{ab} && \nabla_{\boldsymbol{\Omega_b}}(\mathbf{w}_a \cdot \mathbf{R}_{ab}) = 0 \\
&\nabla_{\boldsymbol{\Omega_a}}(\mathbf{w}_b \cdot \mathbf{R}_{ab}) = 0 && \nabla_{\boldsymbol{\Omega_b}}(\mathbf{w}_a \cdot \mathbf{R}_{ab}) = \mathbf{w}_b \times \mathbf{R}_{ab} \\
&\nabla_{\boldsymbol{\Omega_a}}(\mathbf{w}_a \cdot \mathbf{w}_b) = \mathbf{w}_a \times \mathbf{w}_b && \nabla_{\boldsymbol{\Omega_b}}(\mathbf{w}_a \cdot \mathbf{w}_b) = -\mathbf{w}_a \times \mathbf{w}_b.
\end{aligned} \tag{4.94}$$

The torque acting on site a due to the dipole-charge interaction listed above is

$$\nabla_{\boldsymbol{\Omega}_a} T^{ab}_{10,00} = -\frac{\mathbf{w}_a \times \mathbf{R}_{ab}}{R^3_{ab}}. \tag{4.95}$$

There is no torque on a site containing only a charge.

The conversion of these torques to forces on the primary atoms requires an additional application of the chain rule

$$(\nabla_{\mathbf{R}} E)_{\text{torque}} = \nabla_{\mathbf{R}} \boldsymbol{\Omega} \cdot \nabla_{\boldsymbol{\Omega}} E. \tag{4.96}$$

To determine the forces on the primary atoms due to the torques it is necessary to calculate the derivatives of orientation of the body-fixed axes with respect to the primary atom positions. For a linear molecule, i.e. a molecule with just two primary atoms whose positions are $\mathbf{R}_1$ and $\mathbf{R}_2$, the necessary derivatives are

$$\nabla_{\mathbf{R}_1} \boldsymbol{\Omega} = -\nabla_{\mathbf{R}_2} \boldsymbol{\Omega} = -\frac{1}{R^2_{12}} \mathbf{R}_{12} \times, \tag{4.97}$$

where $\mathbf{R}_{12} = \mathbf{R}_1 - \mathbf{R}_2$. Thus the torques on the multipole sites of a given linear

molecule are converted to forces on the primary atoms by

$$\mathbf{F}_1^{\text{torque}} = -\mathbf{F}_2^{\text{torque}} = \sum_a -\frac{1}{R_{12}^2}\mathbf{R}_{12} \times \tau_a. \tag{4.98}$$

It should be straightforward, if tedious, to obtain the necessary derivatives for torque conversion in a nonrigid polyatomic molecule. All that is required is a precise (and preferably closed-form) expression for the body-fixed axes in terms of the primary atom positions. The required derivatives may then be computed analytically or numerically. While the resulting derivative formulas are likely to be cumbersome, numerical evaluation is not likely to slow down calculation of the trajectories because the work required will scale linearly with the number of atoms.

References for Chapter 4

[1] R. S. Berry, Structure and dynamics of clusters: An introduction, in *The Chemical Physics of Atomic and Molecular Clusters*, edited by G. Scoles, Proceedings of the International School of Physics "Enrico Fermi", North-Holland, New York, 1990.

[2] J. Caesar, *De bello Gallico*, Allyn and Bacon, Boston, 1897, translated by Francis W. Kelsey.

[3] M. P. Allen and D. J. Tildesley, *Computer Simulation of Liquids*, Claredon Press, Oxford, 1987.

[4] H. Goldstein, *Classical Mechanics*, Addison-Wesley, Reading, MA, 2nd edition, 1980.

[5] D. J. Evans, Mol. Phys. **34**, 317 (1977).

[6] G. Ciccotti, M. Ferrario, and J.-P. Ryckaert, Mol. Phys. **47**, 1253 (1982).

[7] G. Ciccotti and J.-P. Ryckaert, Comput. Phys. Rep. **4**, 345 (1986).

[8] J.-P. Ryckaert, G. Ciccotti, and H. J. C. Berendsen, J. Comput. Phys. **23**, 327 (1977).

[9] W. F. van Gunsteren and H. J. C. Berendsen, Mol. Phys. **34**, 1311 (1977).

[10] L. Verlet, Phys. Rev. **159**, 98 (1967).

[11] H. C. Andersen, J. Comput. Phys. **52**, 24 (1982).

[12] D. W. Arnold, S. E. Bradforth, E. H. Kim, and D. M. Neumark, J. Chem. Phys. **102**, 3493 (1995).

[13] D. Lu, M. Zhao, and D. G. Truhlar, J. Comp. Chem. **12**, 377 (1991).

[14] W. H. Press, S. A. Teukolsky, W. T. Vetterling, and B. P. Flannery, *Numerical Recipes in C: The Art of Scientific Computing*, Cambridge University Press, New York, 2nd edition, 1992.

[15] J. Papanikolas, J. Gord, N. Levinger, D. Ray, V. Vorsa, and W. Lineberger, J. Phys. Chem. **95**, 8028 (1991).

[16] J. M. Papanikolas, P. E. Maslen, and R. Parson, J. Chem. Phys. **102**, 2452 (1995).

[17] L. Perera and F. G. Amar, J. Chem. Phys. **90**, 7354 (1989).

[18] F. G. Amar and L. Perera, Z. Phys. D **20**, 173 (1991).

[19] N. F. Mott, Proc. Cambridge Philos. Soc. **27**, 553 (1931).

[20] J. C. Tully and R. K. Preston, J. Chem. Phys. **55**, 562 (1971).

[21] J. C. Tully, Nonadiabatic processes in molecular collisions, in *Dynamics of Molecular Collisions*, edited by W. H. Miller, volume Part B, Plenum, New York, 1976.

[22] D. F. Coker, Computer simulation methods for nonadiabatic dynamics in condensed systems, in *Computer Simulation in Chemical Physics*, edited by M. P. Allen and D. J. Tildesley, pp. 315–377, Kluwer, Dordrecht, 1993.

[23] U. Müller and G. Stock, J. Chem. Phys. **107**, 6230 (1997).

[24] J. C. Tully, J. Chem. Phys. **93**, 1061 (1990).

[25] J. C. Tully, Int. J. Quantum Chem. Quantum Chem. Symposium **25**, 299 (1991).

[26] O. Prezhdo and P. Rossky, J. Chem. Phys. **107**, 5863 (1997).

[27] S. Hammes-Schiffer and J. C. Tully, J. Chem. Phys. **101**, 4657 (1994).

[28] D. F. Coker and L. Xiao, J. Chem. Phys. **102**, 496 (1995).

[29] B. Space and D. Coker, J. Chem. Phys. **94**, 1976 (1991).

[30] B. Space and D. Coker, J. Chem. Phys. **96**, 652 (1992).

[31] L. Xiao and D. Coker, J. Chem. Phys. **100**, 8646 (1994).

[32] L. Xiao and D. Coker, J. Chem. Phys. **102**, 1107 (1995).

[33] H. Mei and D. Coker, J. Chem. Phys. **104**, 4755 (1996).

[34] H. Mei, L. Xiao, and D. Coker, J. Chem. Phys. **105**, 3938 (1996).

[35] V. S. Batista and D. F. Coker, J. Chem. Phys. **105**, 4033 (1996).

[36] V. S. Batista and D. F. Coker, J. Chem. Phys. **106**, 7102 (1997).

[37] V. S. Batista and D. F. Coker, J. Chem. Phys. **106**, 6923 (1997).

[38] P. Kuntz, J. Chem. Phys. **95**, 141 (1991).

[39] A. I. Krylov, R. B. Gerber, and R. D. Coalson, J. Chem. Phys. **105**, 4626 (1996).

[40] P. Jungwirth and R. Gerber, J. Chem. Phys. **104**, 5803 (1996).

[41] P. Pechukas, Phys. Rev. **181**, 174 (1969).

[42] E. R. Bittner and P. J. Rossky, J. Chem. Phys. **103**, 8130 (1995).

[43] B. J. Schwartz, E. R. Bittner, O. V. Prezhdo, and P. J. Rossky, J. Chem. Phys. **104**, 5942 (1996).

[44] E. Bittner and P. Rossky, J. Chem. Phys. **107**, 8611 (1997).

[45] F. Webster, P. Rossky, and R. Friesner, Comput. Phys. Comm. **63**, 494 (1991).

[46] F. Webster, J. Schnitker, M. Friedrichs, R. Friesner, and P. Rossky, Phys. Rev. Lett. **66**, 3172 (1991).

[47] F. Webster, E. T. Wang, P. J. Rossky, and R. A. Friesner, J. Chem. Phys. **100**, 4835 (1994).

[48] W. Miller and T. George, J. Chem. Phys. **56**, 5637 (1972).

[49] M. Herman, J. Chem. Phys. **103**, 8081 (1995).

[50] X. Sun and W. Miller, J. Chem. Phys. **106**, 6346 (1997).

[51] V. S. Batista and W. H. Miller, J. Chem. Phys. **108**, 498 (1998).

[52] T. Martinez, M. Ben-Nun, and G. Ashkenazi, J. Chem. Phys. **104**, 2847 (1996).

[53] T. J. Martinez, M. Ben-Nun, and R. D. Levine, J. Phys. Chem. **100**, 7884 (1996).

[54] T. J. Martinez, Chem. Phys. Lett. **272**, 139 (1997).

[55] T. J. Martinez and R. D. Levine, J. Chem. Soc. Faraday Trans. **93**, 940 (1997).

[56] J. Faeder, N. Delaney, P. Maslen, and R. Parson, Chem. Phys. Lett. **270**, 196 (1997).

[57] N. Delaney, J. Faeder, P. E. Maslen, and R. Parson, J. Phys. Chem. A **101**, 8147 (1997).

[58] J. Faeder and R. Parson, J. Chem. Phys., in press.

[59] M. Topaler, M. Hack, T. Allison, Y.-P. Liu, S. Mielke, D. Schwenke, and D. Truhlar, J. Chem. Phys. **106**, 8699 (1997).

[60] A. Krylov and R. Gerber, J. Chem. Phys. **106**, 6574 (1997).

[61] E. Neria, A. Nitzan, R. N. Barnett, and U. Landman, Phys. Rev. Lett. **67**, 1011 (1991).

[62] E. Neria and A. Nitzan, J. Chem. Phys. **99**, 1109 (1993).

[63] W. Pauli, *General Principles of Quantum Mechanics*, pp. 86–87, Springer-Verlag, New York, 1980, translated by P. Achuthan and K. Venkatesan.

[64] R. K. Preston and J. C. Tully, J. Chem. Phys. **54**, 4297 (1971).

[65] J. C. Tully, J. Chem. Phys. **59**, 5122 (1973).

[66] P. E. Maslen, J. M. Papanikolas, J. Faeder, R. Parson, and S. V. ONeil, J. Chem. Phys. **101**, 5731 (1994).

[67] D. C. Rappaport, *The Art of Molecular Dynamics Simulation*, Cambridge University Press, New York, 1995.

[68] S. L. Price, A. J. Stone, and M. Alderton, Mol. Phys. **52**, 987 (1984).

[69] A. J. Stone, *The Theory of Intermolecular Forces*, Oxford, New York, 1996.

[70] P. L. A. Popelier and A. J. Stone, Mol. Phys. **82**, 411 (1994).

Chapter 5

Dynamics of $I_2^-Ar_n$ Photodissociation

In a recent experiment, Lineberger and coworkers [1–3] have studied the photodissociation of I_2^- molecular anions embedded in size-selected clusters containing 1 to 27 argon atoms.[1] As had previously been found for I_2^- clustered with CO_2 [5], the presence of the solvent argon atoms around the I_2^- solute can force the I atoms to recombine after dissociation, a process known as caging. The relative abundance of recombined products increases smoothly but rapidly with the number n of argon atoms in the precursor cluster, from zero for $n \leq 10$ to 100% for $n \geq 16$.

When the recombined products are analyzed according to their mass, they fall into two classes. In the first, all or nearly all of the argon atoms have been lost, indicating that I_2^- has relaxed to the neighborhood of its vibrational ground state with the excess energy being removed by evaporation of argon atoms. In the second, referred to as "metastable," a much larger number of argon atoms remains bound to the solute. Vorsa et al. [1] infer that in these products ground-state I_2^- has not been formed, and suggest two possibilities for the metastable species: a solvent separated pair in which I and I^- are separated by one or more argon atoms, or a trapped excited state in

[1] This chapter is a modified form of Ref. 4

which the I atoms have recombined into the weakly bound $^2\Pi_{g,3/2}$ state (see Fig. 5.1). Provided that evaporation is able to cool such species to low vibrational states in the excited electronic state, they are expected to be relatively stable since collision-induced electronic transitions will be highly improbable when the molecule is near its equilibrium geometry. Further evidence for this interpretation is found in recent femtosecond time-resolved photodetachment experiments by Neumark and coworkers [6]. The transient photodetachment spectrum of the photodissociation products displays a shift that can be attributed to the formation of I_2^- in an excited electronic state.

In the smaller precursor clusters, where caging is incomplete, Vorsa et al. [1] find a bimodal distribution in the *dissociated* products as well. At n=13, for example, the I^- based products fall into two distinct groups, one having 0–3 argon atoms and the other having 5–7 argon atoms. The average number of remaining argon atoms in the second group scales linearly with the precursor cluster size, but the average number in the first group is independent of cluster size.

In this chapter nonadiabatic MD simulations are used to elucidate the mechanisms that give rise to the various product channels observed in the experiment. Photodissociation of molecular cluster ions presents a major challenge for such simulations, since the polarized solvent strongly perturbs the electronic structure of the solute. We treat these perturbations by means of an effective Hamiltonian, constructed by evaluating the solvent-solute interaction in the representation defined by ab initio electronic states of the isolated solute. At each step of the simulation this Hamiltonian is diagonalized, providing the the energies, forces, and nonadiabatic transition probabilities required to propagate the trajectories. The results of our simulation reproduce the observed

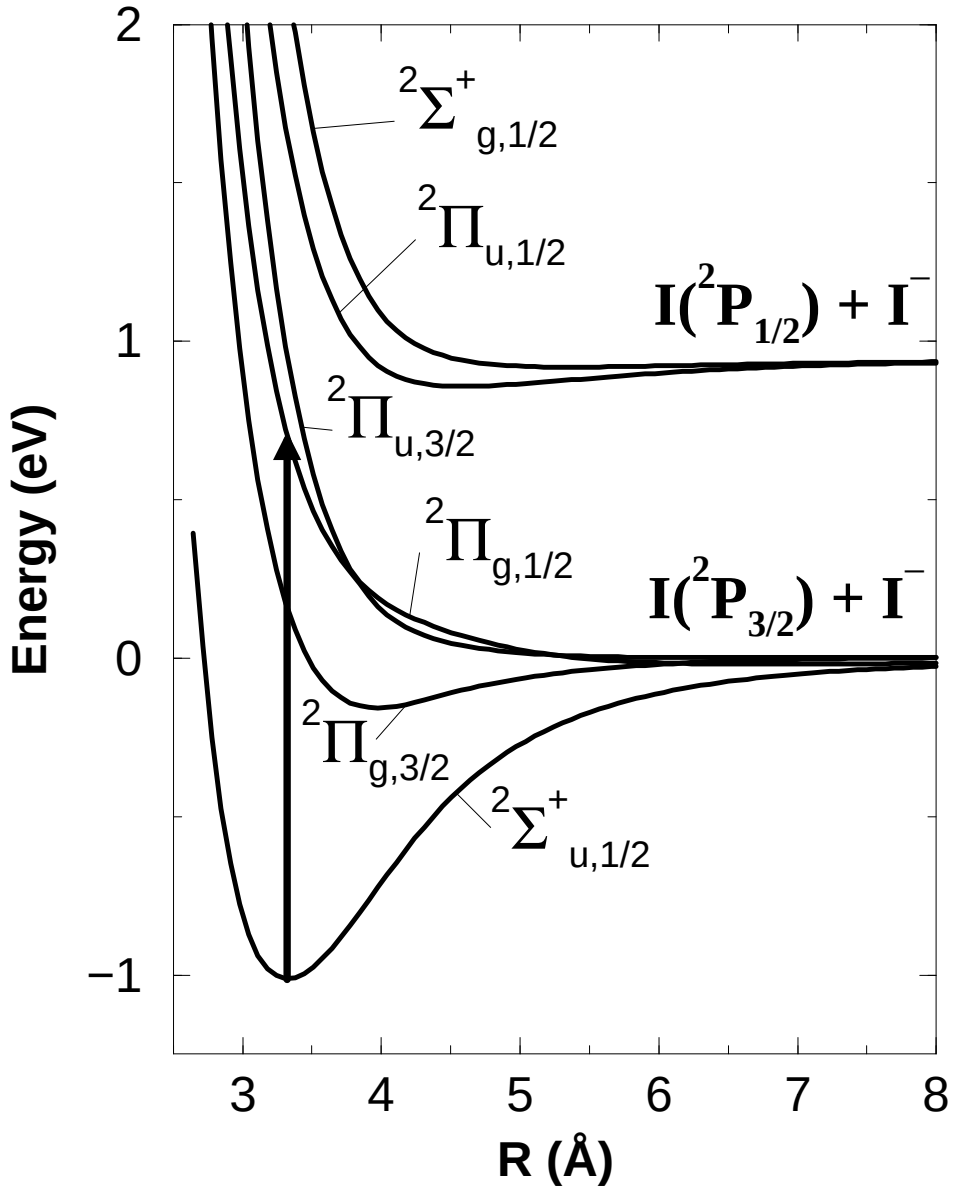

Figure 5.1: Scaled ab initio gas phase potential curves for I_2^-. The arrow shows the 790 nm photexcitation to the $^2\Pi_{g,1/2}$ state modeled in the current simulations.

trends in the experimental dissociation probabilities and branching ratios. For the recombined photofragments, we find no evidence for solvent-separated pairs but we do find significant recombination into the excited state. For dissociated fragments, we find that the low-mass product channel arises from ejection of an I^- ion from the cluster. This peculiar dissociation mechanism is driven by "anomalous charge switching" [7] in the $^2\Pi_{g,1/2}$ excited state. The parallel polarizability of I_2^- in this state is negative, so that charge flows towards the less solvated atom.

5.1 Methods

As described in Chapters 2 and 3, the solute is treated as a diatomic molecule whose electronic states are perturbed by the interaction with the solvent, assuming that there is no charge transfer to the solvent. Since the solute electronic states become nearly degenerate as the molecule dissociates, they can be strongly mixed by even a relatively weak perturbation. This mixing is accounted for by constructing a Hamiltonian using as a basis the lowest six electronic states of the bare I_2^- ion, obtained from a recent ab initio calculation [8]. Within this basis the matrix elements of the solute-solvent interaction, which couple the states of the isolated molecule, are computed. The interaction between the charge distribution of the I_2^- ion and the induced moments on the polarizable argon atoms is responsible for most of the coupling in this system. By diagonalizing this Hamiltonian and taking its derivatives, the energies, forces, and nonadiabatic couplings required for a full treatment of the dissociation dynamics on the multiple electronic potential energy surfaces are obtained. The eigenstates also allow computation of solute properties, such

as the charge distribution and the transition moments, which are vital for understanding the dynamics and for making comparisons between the model and experiment.

5.1.1 Model Hamiltonian

For convenience, the model Hamiltonian of Chapter 2 is presented here in a notation that is somewhat simplified by the absence of permanent solvent multipoles. We write the Hamiltonian of the solute-solvent system

$$\hat{H} = \hat{h}^C + \sum_A \hat{h}^A + \hat{H}^{\rm ind} + \hat{H}^{\rm sr}, \tag{5.1}$$

where $\hat{h}^C$ and the $\hat{h}^A$ are the Hamiltonians of the solute and solvent respectively, $\hat{H}^{\rm ind}$ describes the induction and low frequency dispersion interactions between the charge distribution of the solute and the polarizable solvent, and $\hat{H}^{\rm sr}$ represents the short-range solute-solvent and solvent-solvent interactions arising from dispersion and repulsion. Since the solvent is confined to its ground electronic state, the $\hat{h}^A$ terms are constants and are left out of the calculations.

The lowest six electronic states of the isolated solute form the basis for evaluating $\hat{H}$. $\hat{h^C}$ is clearly diagonal in this representation, and the I_2^- potential curves which define it are shown in Fig. 5.1. Although the two electronic states that dissociate to give spin-orbit excited iodine do not participate directly in the photodissociation dynamics investigated here, their presence in the basis is important for an accurate description of the $^2\Pi_{g,1/2}$ wave function, which undergoes a fundamental shift in character as the molecule dissociates [8]. The depth of the ground $^2\Sigma^+_{u,1/2}$ state well has been scaled from the *ab initio* value of 0.905 eV to bring it into agreement with the most recent experimental value of

1.01 eV [6]. The equilibrium bond length R_e of the scaled ground state is 3.32 Å. The excited states have also been scaled by holding the energy difference with the ground state fixed at the *ab initio* value. R_e and D_e of the scaled $^2\Pi_{g,3/2}$ are 3.96 Å and 158 meV. Each of the states shown has a two-fold spin degeneracy, bringing the total number of basis states to 12. While interactions with the solvent do not lift this degeneracy, the full Hamiltonian does not factorize in a way that makes it possible to reduce its dimension [7].

The properties of the solute electronic wave functions are represented in the form of distributed multipole operators [9, 10]. Moments up through the quadrupole are included on each of four expansion sites, one on each iodine atom and two along the bond (these bond sites are removed as the molecule dissociates). The diagonal elements of the distributed multipole operators provide an accurate representation of the charge distribution in each electronic state. In a polar solvent, for example, diagonal matrix elements of the solute-solvent interaction Hamiltonian would arise from the charge distribution of each electronic basis state interacting with the charge distribution of the solvent. The off-diagonal distributed multipole operators represent *transition charge densities* and give rise to coupling between the electronic basis states in the presence of an electric field, thus allowing the solute molecule to polarize in response to the solvent. Because all of the low-lying states of I_2^- are included in the model, the off-diagonal distributed multipoles should provide a reasonably accurate representation of the solute polarizability.

The lowest order interactions between I_2^- and the argon cluster arise from electronic polarization of the solvent. This is a collective, many-body effect involving distortion of the charge clouds on both solute and solvent molecules. We assume that the time scale for polarization fluctuations in the

solvent is much shorter than that for charge flow in the solute [11–13]. This limit should be valid here since the electronic excitation energy of argon is much larger than the energy gaps between the first few excited states of I_2^-. Following Stone's compact notation for the multipole moments and interaction tensors [10, 14], the induction Hamiltonian may be written as [15]

$$\hat{H}^{\text{ind}} = -\frac{1}{2}\hat{\mu}^A \cdot (\alpha^{AA})^{-1} \cdot \left[1 + \alpha^{AA} \cdot T^{AA}\right]^{-1} \cdot \hat{\mu}^A \tag{5.2}$$

$$\hat{\mu}^A \equiv -\alpha^{AA} T^{AC} \hat{q}^C \tag{5.3}$$

where $\hat{q}^C$ is the solute distributed multipole operator, α is the solvent polarizability tensor, T^{AA} is the interaction tensor between solvent atoms, and T^{AC} is the interaction tensor between solvent atoms and the solute distributed multipole sites. $\hat{\mu}^A$ represents the multipoles induced on solvent molecules by the distributed multipole moments $\hat{q}^C$ on the solute. Since we include only the dipole polarizability of argon (11.07 au [16]), the $\hat{\mu}^A$ are simply the first order induced dipole moments on the solvent atoms. The inverse term in brackets in Eq. 5.2 implicitly takes into account the mutual interaction of the polarized solvent molecules. Constructing it is equivalent to solving the familiar equilibrium linear response equation [10] for the induced dipoles, and computing the quantity $\left[1 + \alpha^{AA} \cdot T^{AA}\right]^{-1} \cdot \hat{\mu}^A$ is equivalent to iterating the induced solvent dipoles to self-consistency. If the induced dipole operators were replaced by classical variables, Eq. 5.2 would be simply the classical induction energy of the solute electrons in the field of the polarized solvent.

The short-range interactions are described by pairwise-additive po-

tentials. The Ar-Ar interactions are modeled by an isotropic Lennard-Jones potential with R_e and D_e fit to match experimental values [17]. Values for all of the interaction parameters discussed here are given in Chapter 3. Fitting the Ar-I potential is complicated by the fact that this interaction depends on the orientation of the empty p orbital on the iodine atom. This anisotropy is physically important because it enables the argon solvent atoms to reorient the p orbital hole on the I atoms, and thus to change the molecular Ω quantum number. Without inclusion of this anisotropy, no excited state recombination is observed in the model. The anisotropy is modeled by adding a $1/R^6$ short-range interaction term having the same angular and state dependence as an ion-quadrupole interaction; this is equivalent to expanding the angular dependence of the potential in Legendre polynomials and retaining the first nonvanishing anisotropic term, proportional to $P_2(\cos\theta)$. This term, together with an isotropic Lennard-Jones potential, enables us to obtain a good fit to the experimental potential curves for both the I-Ar and the I^--Ar interactions, determined from photodetachment spectra [18].

The model Hamiltonian enables us to compute the six-state multidimensional potential surface of arbitrary-sized $I_2^-(Ar)_n$ clusters. In order to carry out molecular dynamics and surface hopping, we must be able to compute derivatives of the Hamiltonian matrix elements with respect to all of the nuclear coordinates, which is discussed in Chapter 4. Computation of these derivatives is greatly simplified by the use of Stone's notation and formulae for the electrostatic interaction tensors and their derivatives [10, 14].

5.1.2 Structure, dynamics, and surface hopping

Molecular dynamics trajectories are computed on the model potential surfaces using the velocity version of the Verlet algorithm [19] as described in Chapter 4. The ensembles used to study the photoexcitation dynamics were composed of 41 configurations obtained following an initial equilibration of 10–20 ps by sampling a 400 ps trajectory at an interval of 10 ps. A timestep of 10 fs was found to give adequate energy conservation during the equilibration period. The photoexcitation process was simulated by placing the the solute in the $^2\Pi_{g,1/2}$ state after adjusting the I_2^- bond length so that the initial energy gap between the ground and excited states matched the 790 nm photon energy. The maximum bond length adjustment required was about 0.04 Å, so this procedure had little effect on the initial configurations except to scale the total kinetic energy release on the excited state to approximately the experimental value. Ensembles were prepared at two temperatures, roughly 40 and 50 K, for the cluster range $n = 6, 8-17, 20$. These temperatures, chosen to match the 40 K estimate of the cluster temperature in the experiments [1], roughly straddle the solid-liquid phase transition region. The underlying cluster structure was also investigated by performing conjugate gradient optimizations [20] on the equilibrated ensembles.

To simulate the nonadiabatic dynamics during the photodissociation, we follow the recent surface-hopping method of Tully [21]. In this method the quantum state amplitudes are integrated along a trajectory using the time-dependent Schrödinger equation

$$i\hbar\dot{c}_i = \sum_j c_j(E_i\delta_{ij} - i\hbar\dot{\mathbf{R}}(t)\cdot\mathbf{d}_{ij}), \tag{5.4}$$

where c_i is the quantum amplitude for state i, E_i is the energy of adiabatic state i, $\dot{\mathbf{R}}(t)$ is a vector containing all of the nuclear velocities, and $\mathbf{d}_{ij}$ is the nonadiabatic coupling vector between states i and j. At each time step the probability of hopping to another state is computed, and the occurrence of a hop is determined probabilistically using Tully's "least switches" algorithm [21]. This algorithm minimizes the total number of hops along a given trajectory while ensuring that the fraction of the total ensemble in a given quantum state will approach the probabilities given by the integration of Eq. 5.4.

When a hop occurs, the velocities are scaled to preserve energy conservation, and the hop is rejected if this scaling cannot be performed. Reference 22 describes an additional "velocity reversal" procedure, in which the velocities in the direction of the nonadiabatic coupling are reversed following a rejected hop. For reasons discussed in Chapter 4, this procedure was not used in simulation results presented here, and we have found that including this scaling does not affect the final product distributions.

Simply integrating Eq. 5.4 along an entire trajectory has been shown to give incorrect transition probabilities arising from spurious coherence effects [21, 23], which are discussed in more detail in Chapter 4. Following the analysis suggested by Schwartz et al., we have estimated the quantum decoherence times for this system to be 100–200 fs in the coupling regions. The current results have been obtained from trajectories in which the quantum amplitudes are reset at an interval of 100 fs. We have found that increasing this interval and/or resetting the amplitudes only in regions of weak coupling have no significant effect on the product distributions.

Following photoexcitation, trajectories were run with a fixed classical timestep of 2 fs, while the quantum amplitudes were integrated using an adap-

tive Runge-Kutta method [20] with a much smaller time step. The quantities $E_i(t)$ and $\dot{\mathbf{R}}(t) \cdot \mathbf{d}(t)_{ij}$ were computed at the intermediate steps of the adaptive integration by the interpolation and extrapolation methods [22] described in Chapter 4. In regions of strong nonadiabatic coupling the classical timestep was also made shorter to ensure accurate calculation of the transition amplitudes. The trajectories were continued until the nuclear configurations met one of two product criteria: dissociative products, where the I-I distance surpassed the cutoff distance of 30 Å, or recombined products, where I_2^- had undergone more than 10 vibrational oscillations in a particular potential well. The time to product formation ranged from 5 to 50 ps. The product criteria were carefully tested and we believe the branching ratios for the model have been accurately determined. The product mass distributions are also reasonably accurate, but should be shifted to lower solvent mass due to the relatively short trajectory lengths and the long times required to evaporate the final argon atoms.

5.2 Results

Figure 5.2 shows the binding energy of each argon atom added to the cluster for the lowest energy structures of $I_2^-Ar_n$, along with the particularly stable structures obtained for n = 6, 13, and 20. The optimized structures show that the argon shell is built up by formation of six-membered rings. The first ring forms around the I_2^- waist, the second around one end of the solute. A single argon atom caps the end, completing the half-shell configuration shown in the middle of Fig. 5.2. The filling of the third ring with cap completes the solvation shell around I_2^- at n = 20. Although two more atoms may crowd the cap positions in n =21 and 22, these structures are somewhat strained.

Each completion of a ring or filling of a cap site produces a structure of greater relative stability. The most stable structures at $n = 6$, 13, and 20 correspond exactly to the noted peaks in the experimental mass spectrum [1], suggesting that the model potential captures the essential structural features of these clusters.

The dissociative trajectories produce two distinct classes of I^-Ar_m products for the precursor cluster range $11 \leq n \leq 14$. The low-mass products, $m \leq 2$, result from direct ejection of I^- from the cluster. This process is depicted in Fig. 5.3(a). The initial configuration, with solvent atoms bound primarily to one end of the cluster, is typical of clusters in this size range and illustrates what we call "asymmetric solvation." The I_2^- dissociates rapidly passing 10 Å separation in the first picosecond of the trajectory, during which the charge localizes on the less solvated I atom. The initially solvated atom is arrested quickly by the solvent. I^- is slowed by its attraction to the solvent but escapes dragging a single argon atom. During the I^- escape there is no opportunity for charge transfer because the energies of the states with different charge character remain well-separated. The formation of the low-mass I^- product is also accompanied by the production of a large neutral cluster, $I{\cdot}Ar_9$.

Figure 5.3(b) shows a trajectory which dissociates to form highly solvated I^-. The initial solvent configuration is more symmetric around I_2^- than in Fig. 5.3(a), and the solvent atoms are in a better position to catch the escaping I^-. By 1 ps solvation of the two I atoms is roughly equal, and further solvation of I^- produces electronic relaxation to a normal charge switching state by about 2 ps. Charge transfer to atom 2 is precluded because of the large I-I separation (>10Å) at these times. The rapid transfer of the solvent facilitates the escape of the neutral I atom, which is notably faster than the

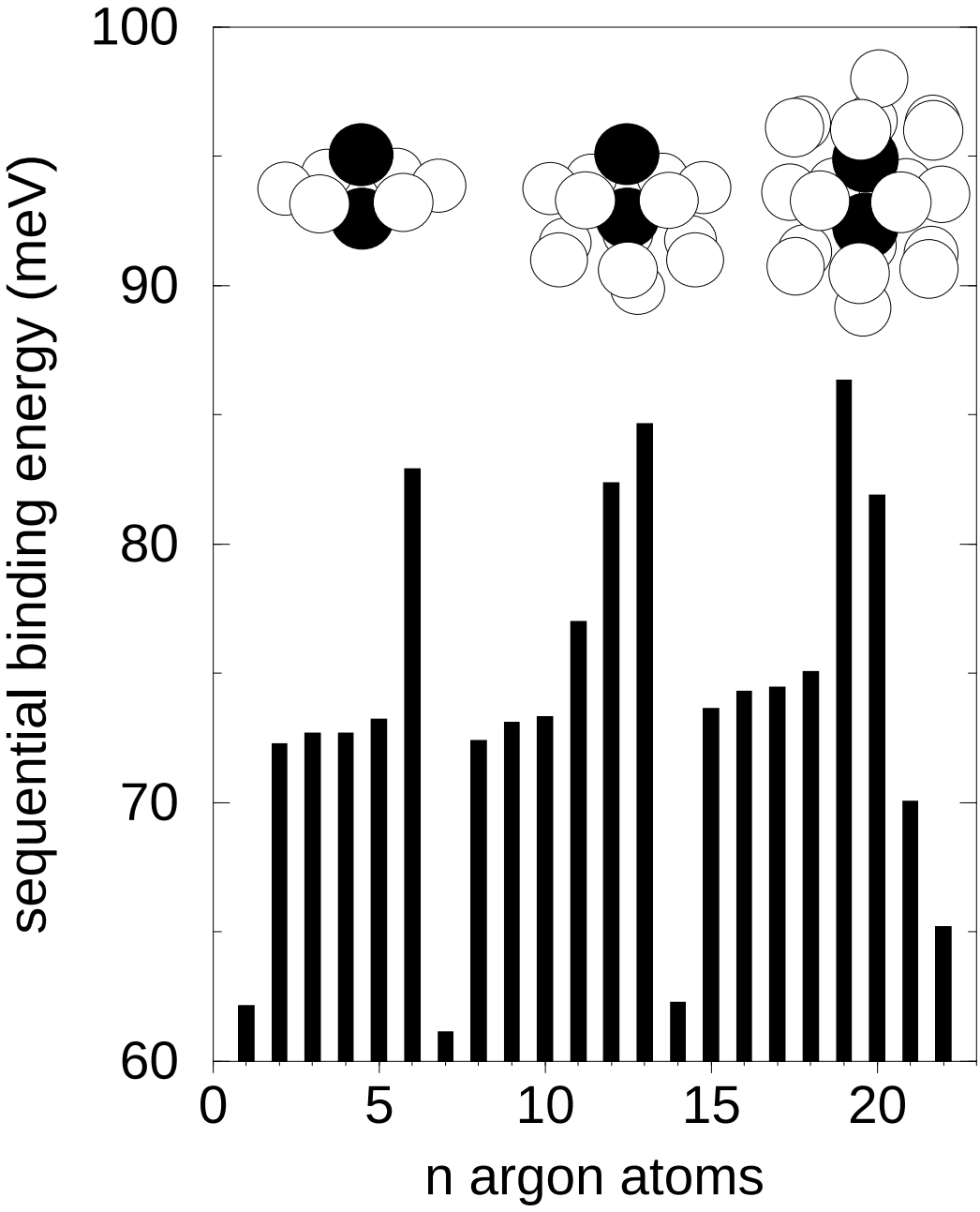

Figure 5.2: Sequential binding energies of argon to I_2^- obtained from the lowest energy structures. The energy for adding the nth argon atom is plotted, and the structures of "magic number" clusters for $n = 6$, 13, and 20 are shown.

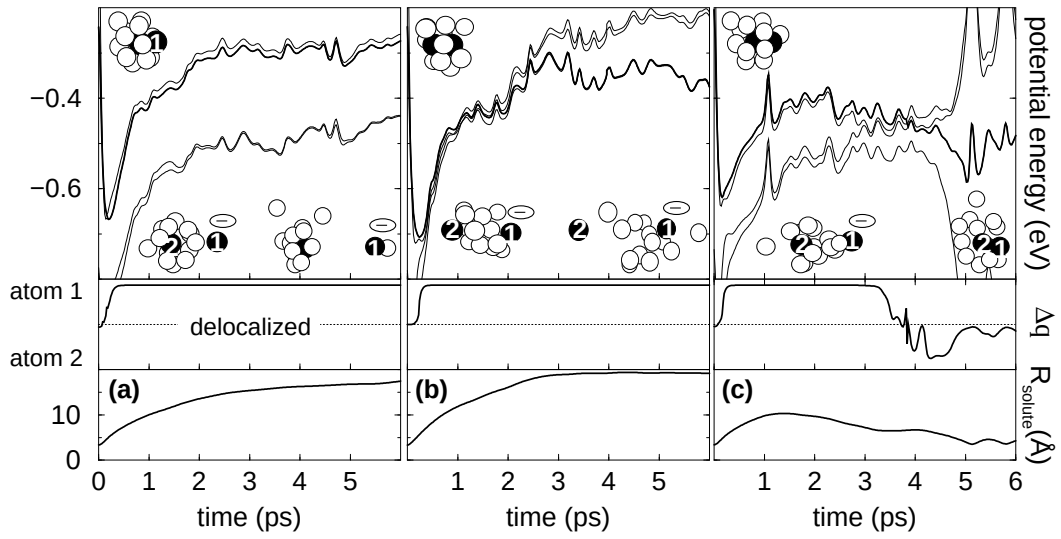

Figure 5.3: Photodissociation of $I_2^-Ar_{13}$. The adiabatic energies, the location of the charge (Δq), and the I-I distance are plotted as a function of time. The heavier line in the top panel shows the energy of the currently occupied state. Snapshots of the configurations showing the localization of the charge are shown at $t = 0$, 1, and 5 ps. (a) shows a dissociative trajectory which forms I^-Ar_1 and $I{\cdot}Ar_9$ as a direct result of the anomalous charge switching. (b) shows a dissociative trajectory which forms I^-Ar_7 and I following solvent transfer from atom 2 to atom 1 during the first few ps. (c) shows a trajectory which recombines in the excited electronic state ultimately forming $I_2^-Ar_5$. Near 4 ps a charge transfer takes place returning the I_2^- to a normal charge switching state where it recombines and the charge delocalizes.

escape of I^- in Fig. 5.3(a). The neutral escapes faster because of its weaker attraction to the remaining cluster, leaving behind I^-Ar_7.

The distinct dissociative channels produce a bimodal distribution of I^-Ar_m products similar to that observed in the experiments. Figure 5.4 shows the product distribution for the $I_2^-Ar_{12}$ precursor. The two modes are present for all precursors in the range $n = 11$–14 but merge for $n \leq 10$. As in the experiment, the center of the high-mass distribution increases with cluster size, while the low-mass distribution remains centered around $m = 0$ or 1.

Figure 5.3(c) shows a trajectory which recombines in the excited $^2\Pi_{g,3/2}$ state. The initial solvent asymmetry is intermediate between the trajectories shown in Fig. 5.3(a) and 5.3(b). The solvent arrests the escape of I^- by about 2 ps, but the solvent interactions are not strong enough to induce electronic relaxation until the solute internuclear separation has returned to about 6 Å. Electronic relaxation occurs via transfer of the charge to atom 2 at around 4 ps. During the subsequent recombination in the excited electronic state, the charge again becomes delocalized. Trajectories which recombine in the ground electronic state are qualitatively similar to the one shown in Fig. 5.3(c).

Roughly half of the trajectories which produce I_2^--based products recombine in the ground electronic state, and the other half recombine in the excited $^2\Pi_{g,3/2}$ state. We do not observe any I_2^--based products where solvent atoms separate the two iodine atoms. Recombination on the $^2\Pi_{g,3/2}$ state appears to produce excited-state I_2^- products with very high efficiency, despite the shallow well depth of this state. Very few trajectories that pass R_e of I_2^- during recombination in the excited state subsequently dissociate to form other products. No dissociation is observed when recombination proceeds past R_e in the ground electronic state.

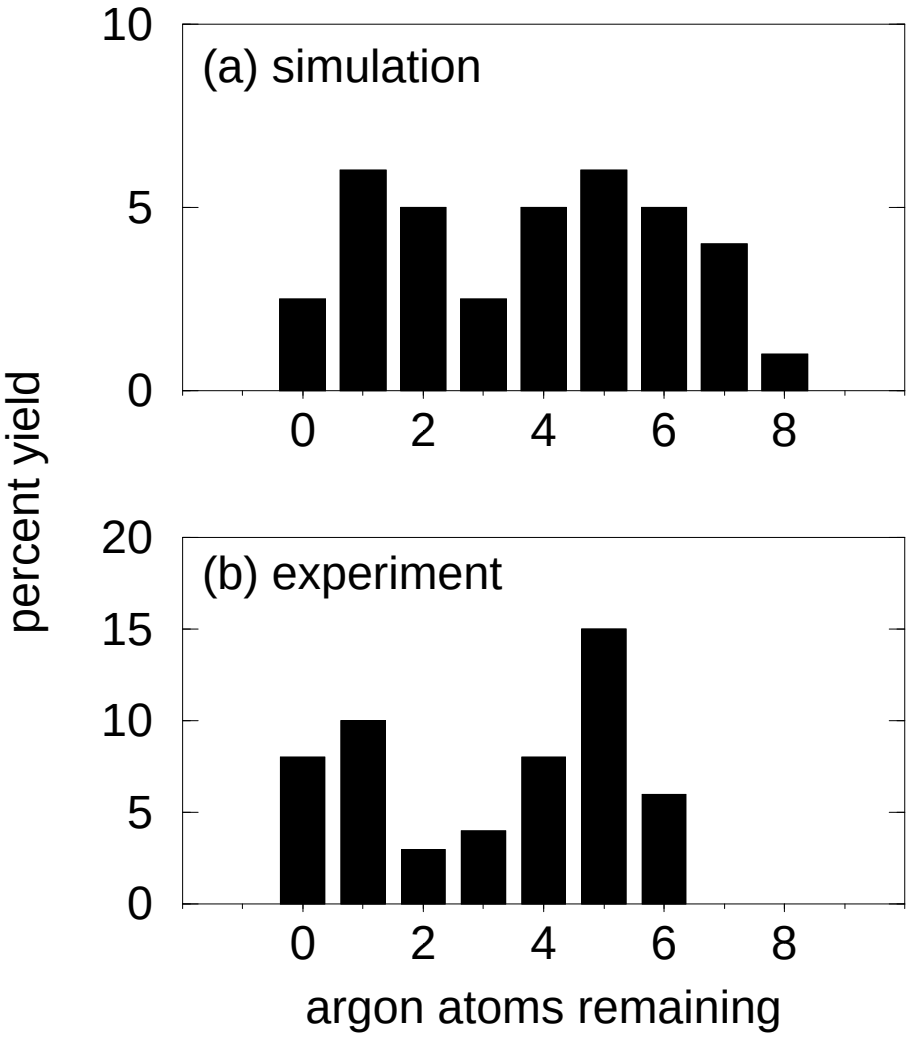

Figure 5.4: I^-Ar_m product distributions from the $I_2^-Ar_{12}$ precursor. For this cluster size the simulation gives 39% dissociation compared to 54% in the experiment. The simulated distribution is expected to shift to slightly lower mass as the trajectories are extended in time.

The branching between recombination in the ground and excited states produces a bimodal product distribution of I_2^--based photofragments. This separation in the product masses arises from the approximately 850 meV difference in the binding energy of the two electronic states on which recombination occurs. Recombination in the excited state releases far less energy and therefore evaporates significantly fewer argon atoms. The trajectories have not all been run for long enough to resolve accurate photofragment distributions for the recombined products, but the large separation in the product channels shows up even at short times.

Figure 5.5 shows the overall branching ratios for photofragmentation from ensembles with an initial temperature of 50 K and demonstrates the generally good agreement between the model and experimental results. The error bars shown in Fig. 5.5 represent the statistical sampling error which arises from the relatively small size of the ensembles. We have generated much larger ensembles for selected cluster sizes and verified that the branching ratios are converged to within the estimated error limits. The simulations reproduce particularly well the rapid closing of the dissociative channel between $n = 10$ and $n = 16$. However, the dissociative branching depends strongly on the temperature of the initial ensemble, so it is premature to make much of the quantitative agreement. This surprising temperature dependence might be associated with what appears to be a solid-liquid phase transition in the 35–50 K range. The simulation results also agree well with the experimental finding of roughly equal amounts of low- and high-mass I_2^--based products. The branching between these two products, which we attribute to ground and excited state recombination respectively, deviates somewhat from the experimental results at intermediate cluster sizes but approaches the same limit in the larger

clusters.

5.3 Discussion

The ejection of I^- during dissociation is the most surprising finding of this study, and the mechanism by which this process occurs provides the key to understanding fundamental aspects of the photodissociation dynamics. The explanation for I^- ejection lies in the electronic properties of the $^2\Pi_{g,1/2}$ state on which dissociation takes place: the component of the polarizability parallel to the molecular axis is negative, so that *charge tends to flow towards the less favorably solvated atom* [7, 24]. This behavior, which we have called "anomalous charge switching," may be understood by considering the eigenfunctions of a particle in a slightly asymmetric double well, or the bonding and antibonding states of a heteronuclear diatomic molecule. In each example, the ground state wave function localizes on the lower-energy well or atom, so by orthogonality the excited state wave function must be polarized in the opposite direction.

Anomalous charge switching arises in our problem because the $^2\Pi_{g,1/2}$ state dissociates to $I{\cdot}Ar_m + I^-$ instead of the normal charge-switching asymptote, $I^-Ar_m + I^*$. The asymptotic behavior is determined by spin-orbit coupling, so if a lighter halide such as chlorine were substituted for iodine, the asymptote would become $Cl^-{\cdot}Ar_m + Cl^*$, and the charge would switch normally.

Anomalous charge switching is evident in the trajectories depicted in Fig. 5.3. In Fig. 5.3(a) I^- is produced when the solute remains in the anomalously switching state throughout the trajectory. Charge localization

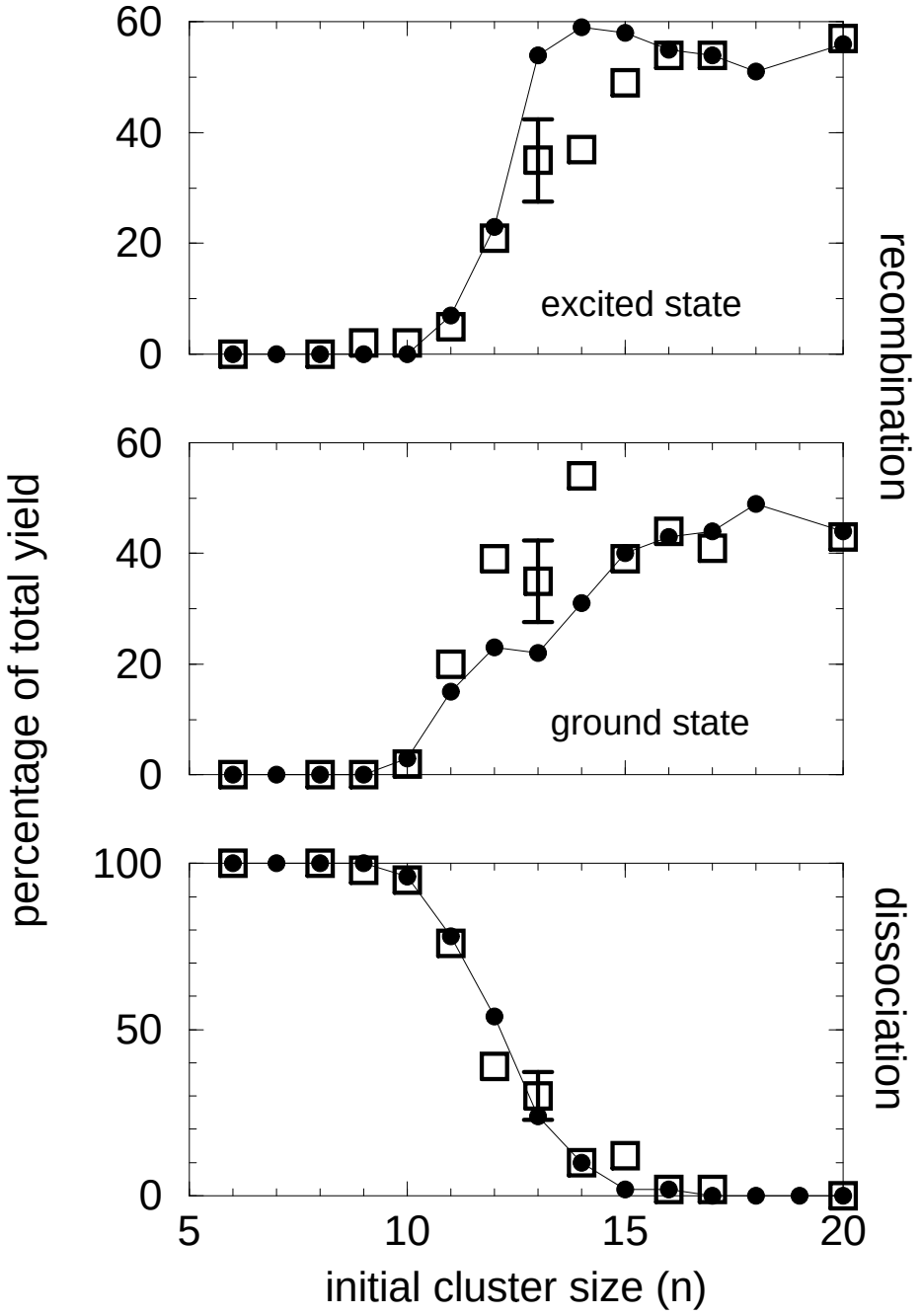

Figure 5.5: Branching ratios for the products of $I_2^-Ar_n$ photdissociation at 790 nm. The filled circles are the experimental data and the squares show the simulation results. One σ error bars based on the statistical sampling are shown for $n = 13$. These ranges are representative of the errors at other sizes since all of the ensembles contained 41 trajectories.

on the less solvated I atom in Fig. 5.3(b) leads to solvent transfer at about 2 ps, allowing the escape of the neutral I atom. In Fig. 5.3(c) the charge resides on the less solvated atom until the solvent induces a charge-transfer near 4 ps which returns the solute to a normal charge switching state where it recombines.

The first two trajectories demonstrate that low-mass I^- products can arise from the same low temperature precursors as the high-mass products. This finding contrasts with the proposal of Vorsa et al. [1] that the low-mass products arise from high-energy isomers in which the I_2^- is bound to the surface of an argon cluster. We have found by simulating the proposed high-energy isomers that the ion dissolves rapidly into the argon clusters on the timescale of about 50 ps, and thus such species are unlikely to survive the 50–100 μs trip from cluster formation to photolysis. Vorsa et al. based their proposal on the supposition that the low- and high-mass product channels are separated in energy by about 300 meV and thus are unlikely to arise from precursors similar in energy. The trajectory in Fig. 5.3(a) illustrates, however, the unexpected result that anomalous charge switching leads to the formation of a highly solvated neutral product which lowers the overall energy of the low-mass channel.

Anomalous charge switching also plays a role in the rapid onset of caging and the closing of the dissociative channels for $10 \leq n \leq 16$. The asymmetric solvation of the initial clusters in this range combined with the flow of charge onto the less solvated atom results in an ion rather than a neutral atom trying to escape from the cluster. The ion–induced-dipole forces thus tend to pull the clusters back together where electronic relaxation and recombination into the lower state potential wells are likely to occur. A simple

energetic argument may explain the onset of recombination around $n = 9$ or 10. In both simulation and experiment, the binding energy of a single Ar atom is estimated to be about 70 meV; combining this with the photon energy of 790 nm, the I_2^- binding energy of 1.01 eV, and a nominal initial cluster temperature of 40 K, we estimate that at least eight argon atoms must be evaporated in order to reduce the energy of I_2^- below the dissociation limit. The closing of the dissociation channel well before the completion of the first solvent shell may result from the fact that for $n > 13$ additional argon atoms are forced to solvate the other iodine, creating a more symmetric solvent distribution and placing the argon atoms in a better position to catch the escaping ion.

One final issue is what determines the state in which the recombination takes place. Both experiment and simulation show approximately equal branching between the two recombination channels, with a slight propensity for the excited state. Since at long bond lengths the two states differ only in the alignment of the empty p orbital on the iodine atom with respect to the molecular axis, this result suggests that the initial alignment of this orbital has been mostly lost by the time the atoms recombine. A small number of I-Ar collisions suffices to reorient the p orbital hole quite efficiently. This result is not surprising since depolarization cross sections in the $^2P_{3/2}$ states of heavy atoms are known to be very large [25–27]. The slight propensity for the excited state may result from the simple fact that it is initially closer in energy to the photoexcited state and thus nonadiabatic transitions will more likely.

5.4 Conclusions

Nonadiabatic molecular dynamics simulations have been used to interpret the results of the cluster photofragmentation experiments of Lineberger and coworkers. The two major classes of dissociated products correspond to ejection either of neutral I atoms or of charged I^- ions from the precursor cluster, the latter process being driven by the anomalous charge flow in the excited electronic state. The two major classes of I_2^--based products correspond to recombination into either the ground state or the excited $^2\Pi_{3/2}$ state. This latter conclusion is in accord with those reached by Neumark and coworkers [6] on the basis of time-resolved photodetachment spectra of the photoproducts. The approximately equal branching between ground and excited state recombination suggests that the during the photodissociation/recombination process the orientation of the electron cloud on the I atom is largely randomized by collision with the Ar atoms.

While this research was being prepared for publication, we received a preprint in which Batista and Coker [28] simulate the same system with nonadiabatic molecular dynamics applied to a semiempirical diatomics-in-molecules Hamiltonian. While this Hamiltonian is constructed differently from ours, it appears to contain the same essential physics. There are some differences in detail between their results and ours but the overall trends are in agreement; they also conclude that the high-mass recombined products arise from excited state recombination. The fact that such similar results are obtained from these two substantially different models suggest that both capture the essential features of the problem.

A major finding of this study is that anomalous charge switching in

the excited state leads to ejection of a negative ion from the cluster. This mechanism would appear to be peculiar to small clusters, since in large clusters or in the condensed phase an electronic transition to a normal charge-switching state will occur before the ion can escape. However, anomalous charge switching itself may be important for large systems as well as small, particularly for processes that are determined by short time dynamics. We intend to pursue these issues in future publications.

References for Chapter 5

[1] V. Vorsa, P. J. Campagnola, S. Nandi, M. Larsson, and W. C. Lineberger, J. Chem. Phys. **105**, 2298 (1996).

[2] V. Vorsa, S. Nandi, P. J. Campagnola, M. Larsson, and W. C. Lineberger, J. Chem. Phys. **106**, 1402 (1997).

[3] V. Vorsa, *Photodissociation Dynamics of Mass-Selected Anions and Anionic Clusters*, PhD thesis, University of Colorado, 1996.

[4] J. Faeder, N. Delaney, P. Maslen, and R. Parson, Chem. Phys. Lett. **270**, 196 (1997).

[5] J. Papanikolas, J. Gord, N. Levinger, D. Ray, V. Vorsa, and W. Lineberger, J. Phys. Chem. **95**, 8028 (1991).

[6] B. J. Greenblatt, M. T. Zanni, and D. M. Neumark, Science **276**, 1675 (1997).

[7] P. E. Maslen, J. M. Papanikolas, J. Faeder, R. Parson, and S. V. ONeil, J. Chem. Phys. **101**, 5731 (1994).

[8] P. E. Maslen, J. Faeder, and R. Parson, Chem. Phys. Lett. **263**, 63 (1996).

[9] A. J. Stone, Chem. Phys. Lett. **83**, 233 (1981).

[10] A. J. Stone, *The Theory of Intermolecular Forces*, Oxford, New York, 1996.

[11] J. N. Gehlen, D. Chandler, H. J. Kim, and J. T. Hynes, J. Phys. Chem. **96**, 1748 (1992).

[12] R. A. Marcus, J. Phys. Chem. **96**, 1753 (1992).

[13] H. J. Kim and J. T. Hynes, J. Chem. Phys. **96**, 5088 (1992).

[14] S. L. Price, A. J. Stone, and M. Alderton, Mol. Phys. **52**, 987 (1984).

[15] P. E. Maslen, J. Faeder, and R. Parson, Mol. Phys., submitted.

[16] D. R. Lide, editor, *CRC Handbook of Chemistry and Physics*, Chemical Rubber, Boca Raton, 73rd edition, 1993.

[17] K. T. Tang and J. P. Toennies, J. Chem. Phys. **80**, 3726 (1984).

[18] Y. Zhao, I. Yourshaw, G. Reiser, C. C. Arnold, and D. M. Neumark, J. Chem. Phys. **101**, 6538 (1994).

[19] H. C. Andersen, J. Comput. Phys. **52**, 24 (1982).

[20] W. H. Press, S. A. Teukolsky, W. T. Vetterling, and B. P. Flannery, *Numerical Recipes in C: The Art of Scientific Computing*, Cambridge University Press, New York, 2nd edition, 1992.

[21] J. C. Tully, J. Chem. Phys. **93**, 1061 (1990).

[22] S. Hammes-Schiffer and J. C. Tully, J. Chem. Phys. **101**, 4657 (1994).

[23] B. J. Schwartz, E. R. Bittner, O. V. Prezhdo, and P. J. Rossky, J. Chem. Phys. **104**, 5942 (1996).

[24] J. M. Papanikolas, P. E. Maslen, and R. Parson, J. Chem. Phys. **102**, 2452 (1995).

[25] A. Gallagher, Phys. Rev. **157**, 68 (1967).

[26] E. A. Yukov, Sov. J. Quant. Electr. **3**, 117 (1973).

[27] W. P. Hess, *Laser photodissociation studies of I^* quantum yields and dynamics*, PhD thesis, University of Colorado, 1988.

[28] V. S. Batista and D. F. Coker, J. Chem. Phys. **106**, 7102 (1997).

Chapter 6

Time-resolved Photoelectron Spectra of $I_2^-Ar_n$ Photodissociation

As discussed in Chapter 1, dihalide anion photodissociation in clusters has been studied extensively both experimentally [1–9] and theoretically [10–15], but several key aspects of the dynamics remain poorly understood.[1] Little is known about the dynamics that take place on the excited state following photoexcitation or about what motions of the solute and solvent are necessary to bring about electronic relaxation and product formation. Full theoretical modeling of these photodissociation reactions is difficult because it requires both a knowledge of the electronic structure of a manifold of states strongly coupled to the many solvent degrees of freedom and a method of computing the complex dynamics on these surfaces. Several groups have recently developed semiempirical Hamiltonians for dihalides [17–19] and dihalide anions [13, 14] interacting with rare gas atoms. The work of Batista and Coker [13, 17, 18] has demonstrated the important role of nonadiabatic dynamics on the multiple potential surfaces in these systems following photoexcitation. Nonadiabatic molecular dynamics simulations of I_2^- photodissociation in argon clusters from Coker's group [13] and confirmed by our group [14] have achieved good agreement with the experimental photoproduct distribu-

[1] This chapter is a modified form of Ref. 16

tions [7]. These simulations, described in Chapter 5, helped to determine that two previously ambiguous product channels in the experimental mass spectra correspond to recombination of I_2^- in an electronically excited state [13] and direct ejection of I^- on a single adiabatic potential surface [14]. To obtain a complete picture of the dynamics following I_2^- photodissociation, however, we need a direct link between the simulations and time-resolved measurements.

Neumark and co-workers [20] have recently measured the transient photoelectron spectrum of $I_2^-Ar_6$ and $I_2^-Ar_{20}$. In their experiment, shown in Fig. 6.1, a 780 nm laser pulse with a width of about 100 fs excites I_2^- to the dissociative A' state, and a subsequent UV pulse detaches an electron, leaving neutral I_2 in a low-lying electronic state. The kinetic energy spectrum of the detached electrons measures the electron affinity of the transient species, serving as a probe of the anion electronic state and its interactions with the local solvent environment. Using this technique, Neumark and co-workers were able to identify the time required for complete dissociation in $I_2^-Ar_6$ and for the recombination of I_2^- into both the X and A states in $I_2^-Ar_{20}$ [20].

This chapter describes calculations of the time-dependent photoelectron spectrum of $I_2^-Ar_6$ and $I_2^-Ar_{20}$. Good agreement is found with the experimental spectra and the model is used to explore the underlying mechanisms of dissociation, recombination, and relaxation.

6.1 Methods

The effective Hamiltonian model used to compute the potential surfaces of the $I_2^-Ar_n$ has been discussed extensively in Chapters 2 and 3, and a briefer description was given in the preceding chapter. To review, the Hamil-

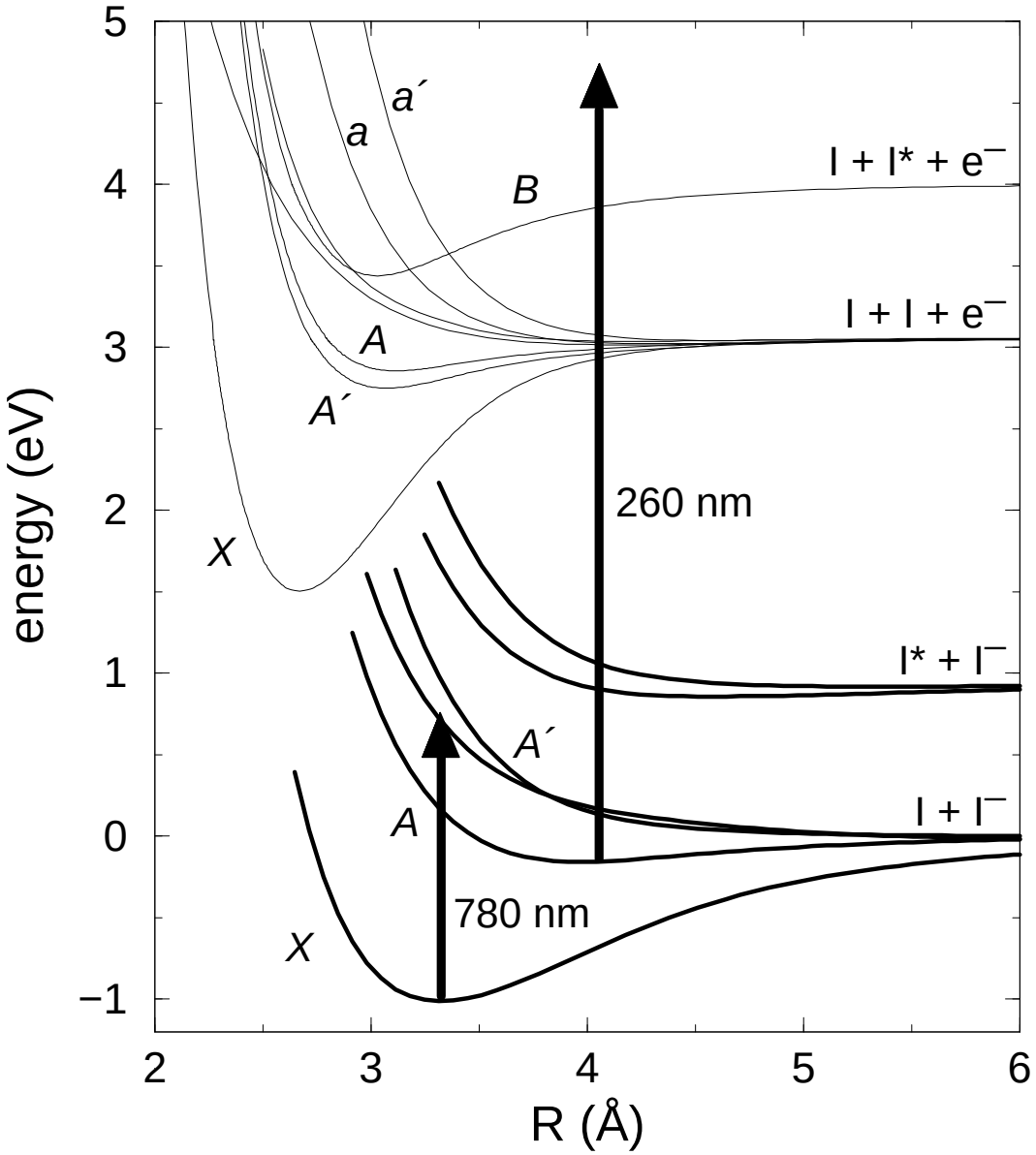

Figure 6.1: Femtosecond photoelectron spectroscopy of $I_2^-Ar_n$ photodissociation. A 780 nm pump laser pulse excites I_2^- to the repulsive A' state. The 260 nm probe pulse detaches the excess electron, leaving I_2 in one of its many low-lying electronic states. The probe pulse shown detaches the electron following cluster-induced electronic relaxation of I_2^- to the A state.

tonian is constructed in the space defined by the lowest six electronic states of bare I_2^-, which are strongly coupled by the argon solvent. The energies and wave functions of these I_2^- states were determined using an ab initio calculation with a semiempirical correction for the spin-orbit coupling [21]. The potential curves used in the model (Fig. 6.1) were obtained by scaling the ab initio curves to reproduce the experimental equilibrium bond distance and well depth for the X state [20, 22] while preserving the ab initio energy spacings. The main solute-solvent interaction arises from the induction of electrostatic moments on the argon atoms by the charge distribution of I_2^-. The operator that describes this interaction is computed from the ab initio wave functions and the experimental polarizability of argon [14, 23]. The diagonal terms of the operator represent the interaction of the charge distribution of a particular I_2^- state with the polarizable solvent atoms, while the off-diagonal terms contain the coupling between the I_2^- states induced by the solvent. The presence of these terms allows the solvent to polarize the charge distribution on I_2^-, an effect that becomes strong as I_2^- dissociates and the basis states become degenerate.

The electrostatic induction potential dominates both the energetics and the couplings in the system. It is therefore practical to handle the remaining interactions, which arise from dispersion and repulsion, empirically with pairwise Lennard-Jones potentials between the atomic sites. The parameters for the Ar$\cdots$Ar interaction are chosen to match the experimental values of R_e and D_e for Ar_2 [24]. The I$\cdots$Ar parameters are adjusted so that the potentials reproduce the experimental values of R_e and D_e for $I^-\cdots$Ar and the three lowest states of I$\cdots$Ar [25]. An additional anisotropic $1/R^6$ interaction term is also required to reproduce the state-dependence of the open-shelled I$\cdots$Ar interaction [14, 25]. Using this procedure ensures that all of the pairwise in-

teractions in the system agree with experimentally determined potentials. The dominant three-body terms in the potential come from the electrostatic induction operator described above.

Simulation of the photoelectron spectrum also requires a model potential for the neutral clusters that result from detaching the electron from I_2^-, leaving I_2 in one of its many low-lying electronic states. In this work we have assumed that the internal potential energy of I_2 is given by the appropriate gas phase potential curve, and the interaction energy is given by the pairwise $I\cdots Ar$ Lennard-Jones potentials used to describe the dispersion and repulsion parts of the $I_2^-\cdots Ar$ interaction [14]. This approximation neglects the state-dependent anisotropic components of the $I\cdots Ar$ interaction [14], but we are not computing dynamics on the I_2Ar_n potential surfaces and the experimental energy resolution is on the order of 100 meV. The electron affinities of I^-Ar_n clusters calculated using the model potentials agree with the experimental values [26] to within about 10%. The simulation includes only the lowest ten states of I_2 [27–30], which degrades the accuracy of the simulated spectra below about 0.7 eV in the electron kinetic energy. Three of these states are not known experimentally, but are inferred from an ab initio calculation [31] to be degenerate with either the known a or a' states [30].

Using the model Hamiltonian and its derivatives, we simulate photodissociation by running molecular dynamics trajectories augmented by Tully's method [32, 33] for computing hops between the coupled potential surfaces. We mitigate the effects of spurious quantum coherence [34, 35] by resetting the quantum amplitudes periodically in regions where the nonadiabatic coupling is weak [14]. The trajectory results give good agreement with the experimentally observed photoproduct distributions and, as we saw in Chapter 5,

provided mechanisms for all four of the experimentally observed product channels, two of which were ambiguous from the experiments [7]. The simulations of the photoelectron spectra described below were performed using a single trajectory for bare I_2^-, 21 trajectories started from an ensemble equilibrated to 40 K for $I_2^-Ar_6$, and 81 trajectories started from an ensemble at 50 K for $I_2^-Ar_{20}$. In all three cases, increasing the number of trajectories and raising or lowering the initial temperature has little effect on the simulated spectra.

The time-dependent photoelectron signal at energy E with pump-probe delay Δ is calculated from a quasi-classical Golden Rule expression,

$$\sigma(E,\Delta) \propto \left\langle \int_{-\infty}^{\infty} dt \exp[-\gamma_{\rm pp}(t-\Delta)^2] \times \right.$$
$$\left. \sum_f \left|\mu_{if}\left(\mathbf{R}(t)\right)\right|^2 \exp\left\{-\gamma_{\rm d}(E)\left[h\nu - E - \left(V_{I_2}^f\left(\mathbf{R}(t)\right) - V_{I_2^-}^i\left(\mathbf{R}(t)\right)\right)\right]^2\right\}\right\rangle,$$

where the brackets denote an average over all trajectories, $\mathbf{R}(t)$ is the nuclear configuration at time t, μ_{if} is the transition dipole for detachment of an electron from state i of I_2^- to state f of I_2, $V_{I_2^-}^i$ and $V_{I_2}^f$ are the energies of those states, and $h\nu$ is the probe laser energy. This expression is similar in form to the one used by Batista and Coker to simulate the pump-probe signal from I_2 in rare gases matrices [18]. The parameters $\gamma_{\rm d}(E)$ and $\gamma_{\rm pp}$ come from the electron detector width and a convolution of the pump and probe laser widths. Because the coordinate dependence of the transition dipoles is unknown, we hold them constant. Simple one-electron selection rules from molecular orbital theory govern which transitions are allowed [9, 36]; however, the large spin-orbit coupling of iodine mixes the electronic configurations to such a high degree [21, 31] that these selection rules are valid only for transitions involving the X states

of I_2 or I_2^-, which are mixed the least because of their large energetic separations from other states. The dipoles for the one-electron forbidden transitions from the excited states of I_2^- to the X state of I_2 are therefore set to zero, while transition dipoles to all other states of I_2 are set to one. We have also scaled the relative magnitudes of transitions out of the X state of I_2^- in order to reproduce the relative intensities of the two bands in the $I_2^-Ar_{20}$ spectra that arise from detachment out of the X state. Transition dipoles to the I_2 X state and to the I_2 excited states are set to twelve and two respectively.

6.2 Results and Discussion

As a test of the simulation method, we have calculated the time-dependent photoelectron spectrum of bare I_2^-, which has been measured in Neumark's group [9]. The experiments probe the rapid dissociation that takes place upon photoexcitation to the repulsive A' state. The experimental and simulated spectra shown in Fig. 6.2 demonstrate the good agreement we obtain. In both simulations and experiment, a broad band peaked near 1.9 eV at $t = 0$ shifts rapidly in about 200 fs over to the spectrum of I^- as the I_2^- dissociates. The spectra evolve only slightly after 200 fs, suggesting that dissociation is essentially complete by then: the I–I separation is 5.4 Å at 200 fs in the simulation. The band shapes at early times are sensitive to the convoluted laser pulse width, which at 200 fs is broad compared to the dynamics being probed. The transient signal at high electron kinetic energy (>2.0 eV) is also sensitive to the inclusion of the entire manifold of I_2 product states. The previous simulation of the experiment [9] failed to reproduce the high energy transients, probably because it included only the X, A, and A' states of I_2.

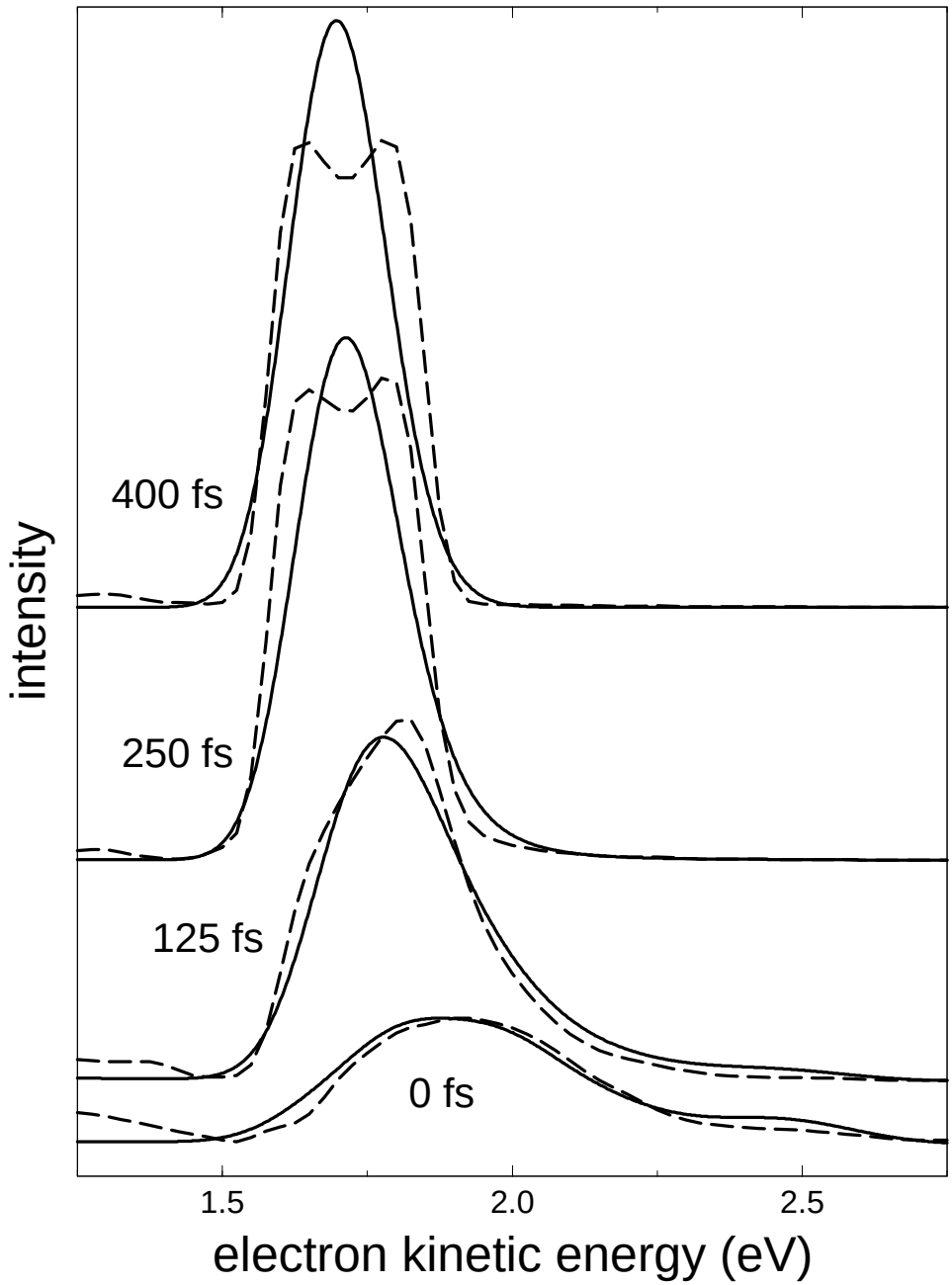

Figure 6.2: Time-dependent photoelectron spectra of I_2^- at various pump-probe delay times. Solid lines are simulation results and dashed lines are experimental results from Ref.9. The full width half maximum convoluted pulse width and detector width are 250 fs and 0.150 eV. The bimodal peaks in the experimental spectra seen at 250 and 400 fs are due to the large solid angle seen by the magnetic bottle photoelectron spectrometer, coupled with an anisotropic electron distribution of the $I^- \rightarrow I$ transition.

$I_2^-Ar_6$ also dissociates rapidly upon photoexcitation, but the argon solvent atoms cause significant shifts in the observed spectra. As shown in Fig. 6.3(a), the experimental and simulated spectra agree well, although there are greater discrepancies at early times than seen in the bare ion spectra. Fig. 6.3(b) shows typical cluster configurations during the dissociation along with the localization of the negative charge, and Fig. 6.3(c) shows the evolution of main peak position. As in the bare ion, the peak shifts rapidly during the first 200 fs toward lower electron kinetic energy as the I_2^- bond dissociates. In the simulations, the argon atoms cluster about the waist of I_2^- having little effect on the dissociating ion. By 300 fs the I–I separation is 6.4 Å, but the argon atoms have moved only slightly. Because the argon cluster remains largely intact, it exerts a shift of just over 100 meV in the peak position, corresponding to the shift observed in cold $I^-(Ar)_{4-5}$ clusters. By itself, this might suggest that $I^-(Ar)_{4-5}$ clusters are somehow formed as an intermediate in the dissociation, followed by rapid evaporation of argon atoms [20]. In our simulation, however, dissociation is direct, with the argon atoms barely moving on the time scale of the peak shift. As the dissociation continues, only 1–2 argon atoms on average catch the escaping ion, and the peak rapidly moves to higher electron kinetic energy, nearly attaining its asymptotic value by 1 ps. There is a slight drift after 1 ps due to the gradual evaporation of argon from clusters in which more than 1 argon atom catch I^-.

The time-dependent photoelectron spectra of $I_2^-Ar_{20}$ probe the dynamics of dissociation and recombination processes that evolve over multiple time scales and potential surfaces. In both experiment and simulation, no dissociated products are observed for this cluster size, and recombination may occur in either the X or A states of I_2^-. In addition to probing the early dynamics of

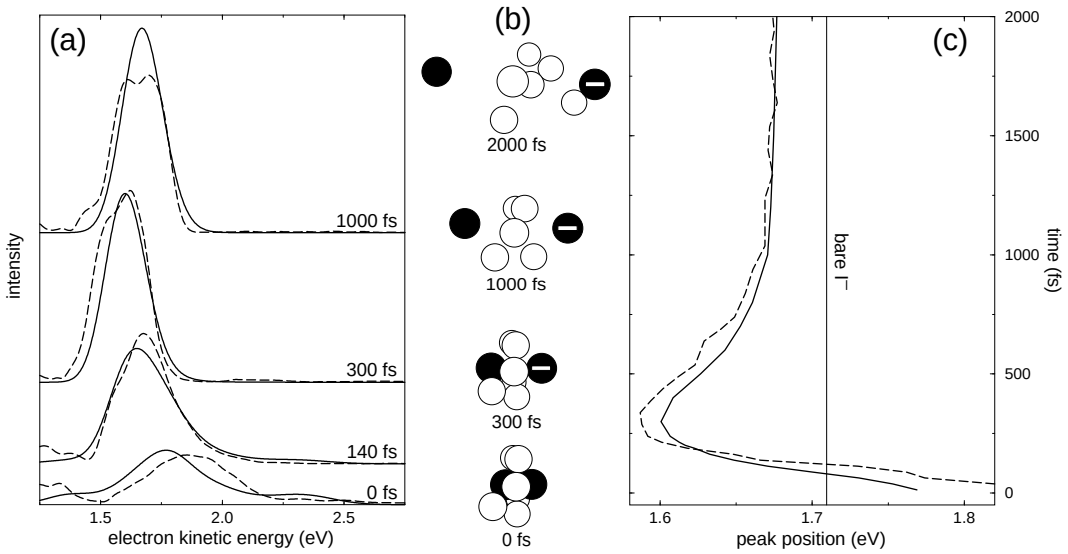

Figure 6.3: Time-dependent photoelectron spectra of $I_2^- Ar_6$ with trajectory snapshots. Spectra at several pump-probe delay times are shown in (a), where solid lines are simulation results and dashed lines are experimental results from Ref. 20. The full width half maximum convoluted pulse width and detector width are 205 fs and 0.150 eV. The snapshots in (b) illustrate a typical trajectory with argon atoms in white and iodine atoms in black. The minus sign on the right iodine atom at $t \geq$300 fs indicates charge localization on the initially less solvated iodine [see Ref. 14]. The position of the main peak in the spectrum is plotted in (c) showing the large shift induced by the argon atoms at 300 fs.

dissociation, the photoelectron spectra reveal the time scales for recombination into these states and the subsequent time required for vibrational and solvent relaxation. Fig. 6.4(a) shows the evolution of the main spectral peak. Up to 1 ps, the motion of the peak is similar to $I_2^-Ar_6$, but the magnitude of the shift is much larger due to the greater number of solvent atoms. Unlike in $I_2^-Ar_6$, the shift toward higher electron kinetic energy between 0.4 and 1.0 ps is due to heating and evaporation of the argon atoms as the dissociating iodine atoms collide with the solvent cage. The simulations indicate that about 3–4 argon atoms are evaporated from the cluster during the initial dissociation event. By 1 ps a substantial fraction of the trajectories have begun to recombine, and between 1 and 5 ps the main peak shifts toward lower energy and diminishes in intensity as two major new features appear in the spectrum at lower and higher energies [see Fig. 6.4(b)]. The simulations show that the new features are due to recombination in the X state, which opens up photoelectron transitions to the X state of I_2. There is good agreement between the experiment and simulation for both the shapes and positions of these new bands. The appearance and growth of the bands provide an estimate of the time required for electronic relaxation and recombination to occur in the X state of I_2^-—about 5–10 ps. Most of the trajectories in the simulation that recombine in the X state do so between 3 and 5 ps, and all have recombined by 15 ps.

Subsequent evolution of the high energy band arises from vibrational relaxation in the X state I_2^-, which occurs rapidly in the first 10–20 ps after recombination, but stretches out over several hundred picoseconds in both the experiment and simulation. This band narrows and shifts to lower energy as I_2^- relaxes in the X state well, increasing the energetic gap for photodetachment to the X state of I_2 from the inner turning point in the I_2^- well. Figure 6.5(a)

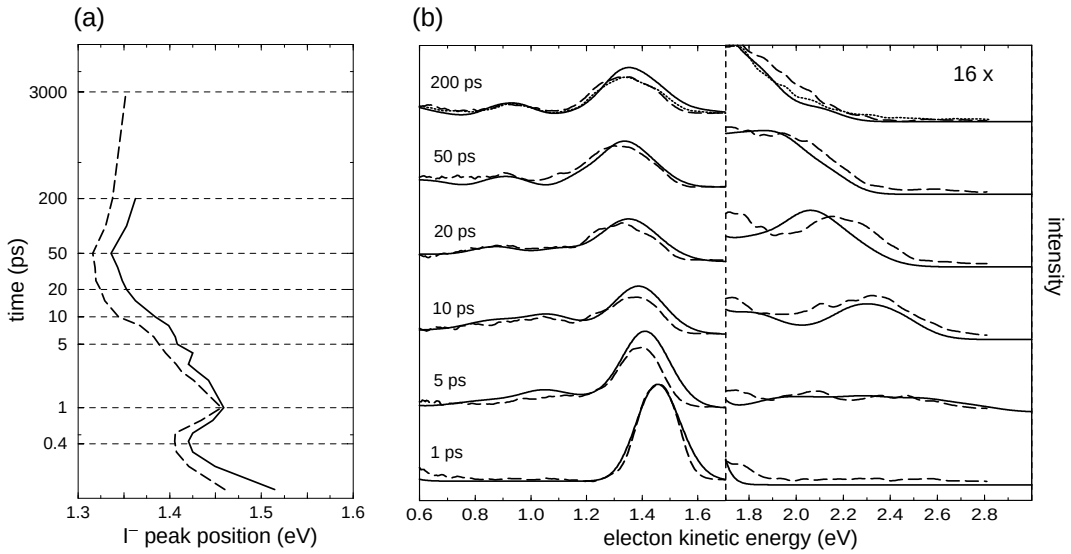

Figure 6.4: Time-dependent photoelectron spectra of $I_2^-Ar_{20}$. Solid lines are simulation results and dashed lines are experimental results from Ref. 20. The position of the main peak is shown in (a) as a function of the pump-probe delay time. Full spectra at a series of delay times are shown in (b) where the right panel shows the high energy tail due to detachment from the X state of I_2^-. The dotted lines show the experimental spectrum at 3 ns. The full width half maximum convoluted pulse width and detector resolution width are 250 fs and 0.150 eV.

displays the ensemble average of the I_2^- total internal energy following electronic relaxation to the X state along with the average number of argon atoms remaining in the cluster. During the first 20 ps, about 80% of the initial vibrational energy is transferred into the solvent, which undergoes rapid evaporation to dissipate the energy. The rate of evaporation decreases dramatically below about $n = 5$, so that the solvent can no longer dissipate excess energy quickly, and thus the rate of vibrational relaxation also slows. Vibrational relaxation is not complete in either the experiment or simulation even by 200 ps. This result reflects the dynamics of evaporation from the small clusters near the bottom of the well rather than the characteristic ability of the argon solvent to absorb energy from the excited solute. In a pump-probe experiment on $I_2^-Ar_{20}$ Vorsa et al. [8] have reported a time constant of 130 ps for the absorption recovery, which probably also reflects this slow vibrational relaxation at the bottom of the X state well.

The experimental and simulated spectra at high energies track each other, although not as closely at longer times, probably indicating that the rates of vibrational relaxation do not match exactly. The experimental spectra reflect a somewhat slower rate of vibrational relaxation than the simulations, which may be expected given that the simulations overestimate the $I^- \cdots Ar$ interaction by about 10% (see Fig. 3.8). In the simulations I_2^- can impart somewhat more vibrational energy to the solvent before the solvent atoms lose their ability to absorb the energy effectively. The experimental spectrum at 3 ns, shown by the dotted line in Fig. 6.4(b), demonstrates that upon further vibrational relaxation the experimental spectrum more closely resembles the simulated spectrum at 200 ps. The observed differences in the spectra at 200 ps correspond to differences in the vibrational energy of 2–3 vibrational quanta,

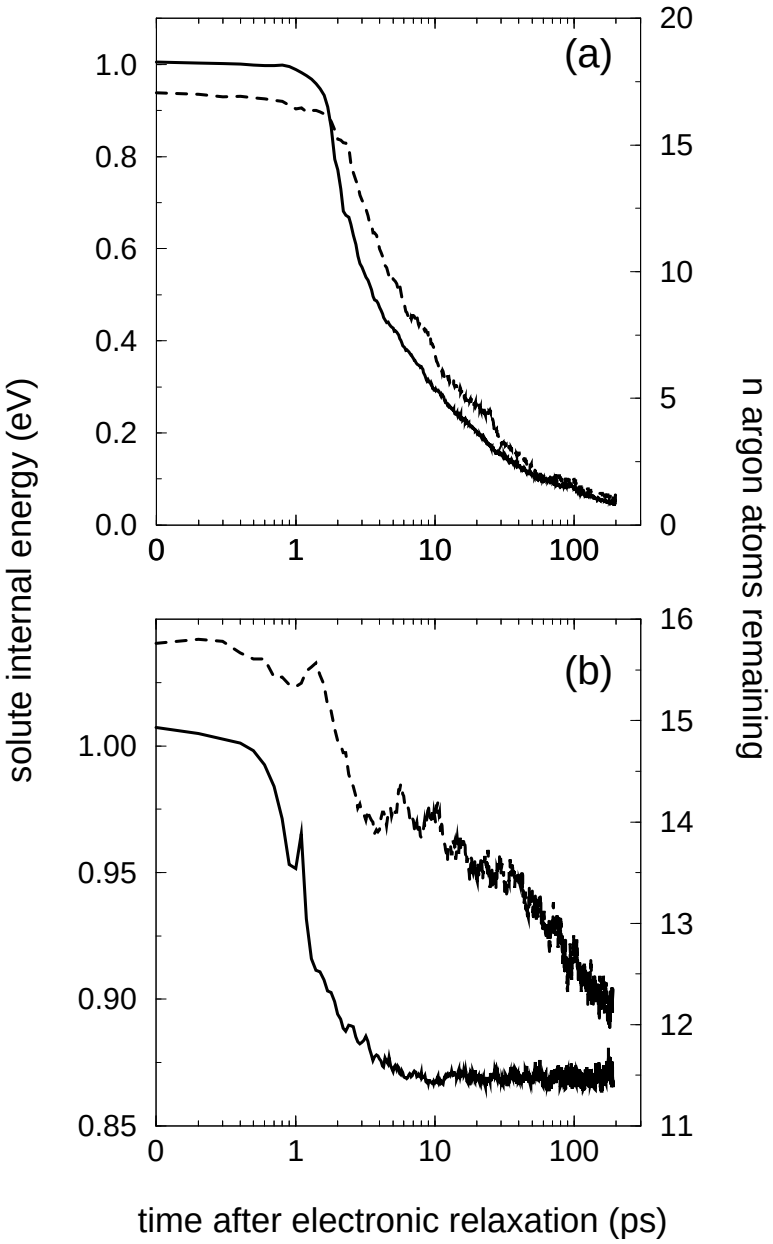

Figure 6.5: Vibrational relaxation and solvent evaporation in $I_2^- Ar_{20}$ following electronic relaxation to the (a) the ground X state and (b) the excited A state. The solute internal energy, referenced to the bottom of the X state well, is shown by the solid line, and the number of solvent atoms remaining in the cluster, defined as inside a radius of 6.0 Å from either iodine atom, is indicated by the dashed line.

or about 40 meV.

The evolution of the main spectral peak, plotted in Fig. 6.4(a), follows the recombination and subsequent vibrational relaxation of I_2^- in the excited A state. This band loses intensity after 1 ps as about 40% of the ensemble recombines in the X state, where the photoelectron transitions are shifted to higher and lower energies. The position of the peak shifts to lower energy as the remainder of the ensemble recombines in the A state. The shape and position of the I^- band are not sensitive to the vibrational energy of the much shallower A state well, so the vibrational relaxation is not reflected in the spectra. The simulations reveal, however, that it takes only a few ps following recombination in the A state for I_2^- to lose nearly all of its vibrational energy, as shown in Fig. 6.5(b). The peak continues to shift to lower energy out to about 50 ps, after which there is a slight shift to higher energy. Some of the shift out to 50 ps probably arises from overlap with bands from X state detachment, which continues to change on this time scale. By simulating the bands separately, however, we determined that some of the shift occurs even in the absence of overlap, because the recombination time in the A state is twice as long on average as in the X state, with recombination in some trajectories taking as long as 40 ps. The shift in the peak does not reach its maximal value until all of the trajectories that recombine in the A state have done so. The slow shift to higher energy after 50 ps reflects the continuing evaporation of argon atoms [see Fig. 6.5(b)], dissipating the remaining excess energy of the clusters. The main band at long times is much broader than the experimental energy resolution, resulting from detachment to all of the different low-lying states of I_2. These states significantly affect the shape of the spectrum at both short and long times.

6.3 Conclusions

The $I_2^-Ar_6$ simulations provide a clearer picture of the dissociation than experiments alone were able to provide. Dissociation occurs directly, and the transient shifts in the photoelectron spectra reflect the breaking of the I_2^- bond, followed by the escape of I^- from the neutral solvent cluster. In $I_2^-Ar_{20}$ the dissociated atoms recombine, and the simulations confirm the interpretation of the experimental shifts as arising from recombination in both the X and A states of I_2^-, followed by vibrational relaxation. The agreement between the model and experiment for the time scales of these processes suggests that the simulations accurately depict the course of a chemical reaction evolving over several different electronic potential surfaces with strong coupling to a solvent. The discussion presented here also demonstrates the importance of modeling in conjunction with the interpretation of experimental results for these systems. Nonadiabatic molecular dynamics simulations coupled with semiempirical Hamiltonian models should continue to provide a useful tool for examining the dynamics of many reactions involving the excited states of charged species in clusters and the condensed phase.

References for Chapter 6

[1] M. L. Alexander, M. A. Johnson, N. E. Levinger, and W. C. Lineberger, Phys. Rev. Lett. **57**, 976 (1986).

[2] M. Alexander, N. Levinger, M. Johnson, D. Ray, and W. Lineberger, J. Chem. Phys. **88**, 6200 (1988).

[3] D. Ray, N. Levinger, J. Papanikolas, and W. Lineberger, J. Chem. Phys. **91**, 6533 (1989).

[4] J. Papanikolas, J. Gord, N. Levinger, D. Ray, V. Vorsa, and W. Lineberger, J. Phys. Chem. **95**, 8028 (1991).

[5] J. Papanikolas, V. Vorsa, M. Nadal, P. Campagnola, H. Buchenau, and W. Lineberger, J. Chem. Phys. **99**, 8733 (1993).

[6] M. E. Nadal, P. D. Kleiber, and W. C. Lineberger, J. Chem. Phys. **105**, 504 (1996).

[7] V. Vorsa, P. J. Campagnola, S. Nandi, M. Larsson, and W. C. Lineberger, J. Chem. Phys. **105**, 2298 (1996).

[8] V. Vorsa, S. Nandi, P. J. Campagnola, M. Larsson, and W. C. Lineberger, J. Chem. Phys. **106**, 1402 (1997).

[9] B. J. Greenblatt, M. T. Zanni, and D. M. Neumark, Chem. Phys. Lett. **258**, 523 (1996).

[10] L. Perera and F. G. Amar, J. Chem. Phys. **90**, 7354 (1989).

[11] P. E. Maslen, J. M. Papanikolas, J. Faeder, R. Parson, and S. V. ONeil, J. Chem. Phys. **101**, 5731 (1994).

[12] J. M. Papanikolas, P. E. Maslen, and R. Parson, J. Chem. Phys. **102**, 2452 (1995).

[13] V. S. Batista and D. F. Coker, J. Chem. Phys. **106**, 7102 (1997).

[14] J. Faeder, N. Delaney, P. Maslen, and R. Parson, Chem. Phys. Lett. **270**, 196 (1997).

[15] N. Delaney, J. Faeder, P. E. Maslen, and R. Parson, J. Phys. Chem. A **101**, 8147 (1997).

[16] J. Faeder and R. Parson, J. Chem. Phys., in press.

[17] V. S. Batista and D. F. Coker, J. Chem. Phys. **105**, 4033 (1996).

[18] V. S. Batista and D. F. Coker, J. Chem. Phys. **106**, 6923 (1997).

[19] A. A. Buchachenko and N. F. Stepanov, J. Chem. Phys. **104**, 9913 (1996).

[20] B. J. Greenblatt, M. T. Zanni, and D. M. Neumark, Science **276**, 1675 (1997).

[21] P. E. Maslen, J. Faeder, and R. Parson, Chem. Phys. Lett. **263**, 63 (1996).

[22] M. T. Zanni, T. R. Taylor, B. J. Greenblatt, B. Soep, and D. M. Neumark, J. Chem. Phys. **107**, 7613 (1997).

[23] C. G. Gray and K. E. Gubbins, *Theory of Molecular Fluids*, volume 1, Clarendon, Oxford, 1984.

[24] K. T. Tang and J. P. Toennies, J. Chem. Phys. **80**, 3726 (1984).

[25] Y. Zhao, I. Yourshaw, G. Reiser, C. C. Arnold, and D. M. Neumark, J. Chem. Phys. **101**, 6538 (1994).

[26] I. Yourshaw, Y. Zhao, and D. M. Neumark, J. Chem. Phys. **105**, 351 (1996).

[27] D. R. T. Appadoo, R. J. Le Roy, P. F. Bernath, S. Gerstenkorn, P. Luc, J. Vergès, J. Sinzelle, J. Chevillard, and Y. D'Aignaux, J. Chem. Phys. **104**, 903 (1996), and references therein.

[28] J. Tellinghuisen, J. Chem. Phys. **82**, 4012 (1985).

[29] K. S. Viswanathan and J. Tellinghuisen, J. Mol. Spec. **101**, 285 (1983).

[30] S. Churassy, F. Martin, R. Bacis, J. Vergès, and R. W. Field, J. Chem. Phys. **75**, 4863 (1981).

[31] C. Teichteil and M. Pelissier, Chem. Phys. **180**, 1 (1994).

[32] J. C. Tully, J. Chem. Phys. **93**, 1061 (1990).

[33] S. Hammes-Schiffer and J. C. Tully, J. Chem. Phys. **101**, 4657 (1994).

[34] E. R. Bittner and P. J. Rossky, J. Chem. Phys. **103**, 8130 (1995).

[35] B. J. Schwartz, E. R. Bittner, O. V. Prezhdo, and P. J. Rossky, J. Chem. Phys. **104**, 5942 (1996).

[36] R. S. Mulliken, J. Chem. Phys. **55**, 288 (1971).

Chapter 7

Dynamics of $I_2^-(CO_2)_n$ Photodissociation

This chapter discusses simulations of photodissociation in $I_2^-(CO_2)_n$ clusters.[1] These are the first simulations of the excited state dynamics that have been performed utilizing a realistic description of the excited state electronic structure. The solute-solvent interactions in these clusters are about three times stronger than they were in the argon clusters discussed in the last two chapters. This large increase in the coupling between the solute and solvent has a profound effect on the dynamics following photoexcitation, particularly for clusters with less than a complete solvation shell. It is no longer possible to eject weakly solvated I^- from the cluster, so all dissociative products involve electronic relaxation. The strong solute-solvent interactions also destabilize the A state well (see Fig. 7.1, so that only transient recombination in this state is observed.

The most interesting consequence of increasing the solute-solvent coupling is the much stronger interplay that develops between the state-dependent charge flow and motion of the solvent. Figure 7.2 illustrates the state-dependence of charge flow for a simple two-state model borrowed from the theory of electron transfer in solutions [2–4]. The diabatic potential curves

[1] This chapter is a modified form of Ref. 1

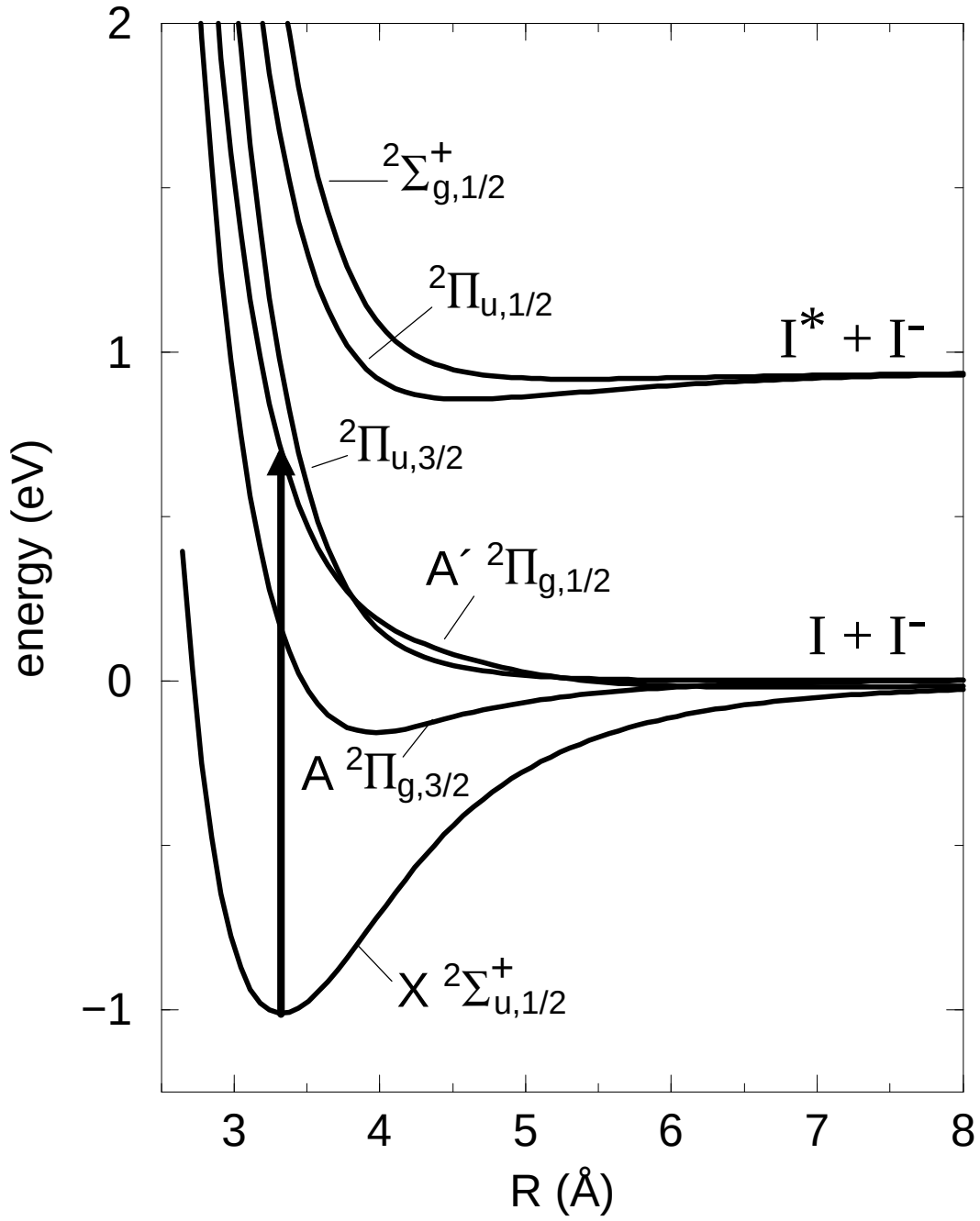

Figure 7.1: Scaled ab initio gas phase potential curves for I_2^-. The arrow shows the 790 nm photoexcitation to the $A'\ ^2\Pi_{g,1/2}$ state modeled in the current simulations.

are two intersecting parabolas whose minima represent solvated iodide and neutral iodine. When the solute bondlength is near its equilibrium value, the electronic coupling is strong and the adiabatic curves are well separated energetically, as represented by the dashed curves. As the solvent moves along the lower adiabatic curve, the charge follows the solvent from one side of the solute to the other. However, the charge moves in just the opposite way on the upper adiabatic state. A vertical excitation, as shown in the figure, changes the solute electronic state, moving the charge from I_A to I_B; however, the solvent still surrounds I_A. The solvent moves towards the charge in an effort to re-establish equilibrium. But, as the solvent coordinate crosses zero, and the solvent favors I_B, the electronic state changes character and the charge returns to I_A. The solvent must change direction once again to pursue the charge. This oscillation, which we have termed "anomalous charge switching" [5–7], persists as long as the solute remains in the excited state. As we saw in Chapter 1, anomalous charge switching is a direct consequence of the antibonding character of the A' state; in general we expect antibonding states to polarize in the opposite direction compared to the normal, bonding states. The solid lines in Fig. 7.2 represent a longer solute bondlength, where the electronic coupling is weaker and transitions between states can occur when the solvent coordinate is near zero.

The major focus of this chapter is to demonstrate that this simple model accurately reflects the potential surfaces on which photodissociation and recombination take place in $I_2^-(CO_2)_n$ clusters. Two-dimensional descriptions of the dynamics involving a solvent coordinate have been used in previous studies of the I_2^- vibrational relaxation in both clusters [5, 8] and liquids [9], but this is the first use of such a picture to examine dynamics on the excited

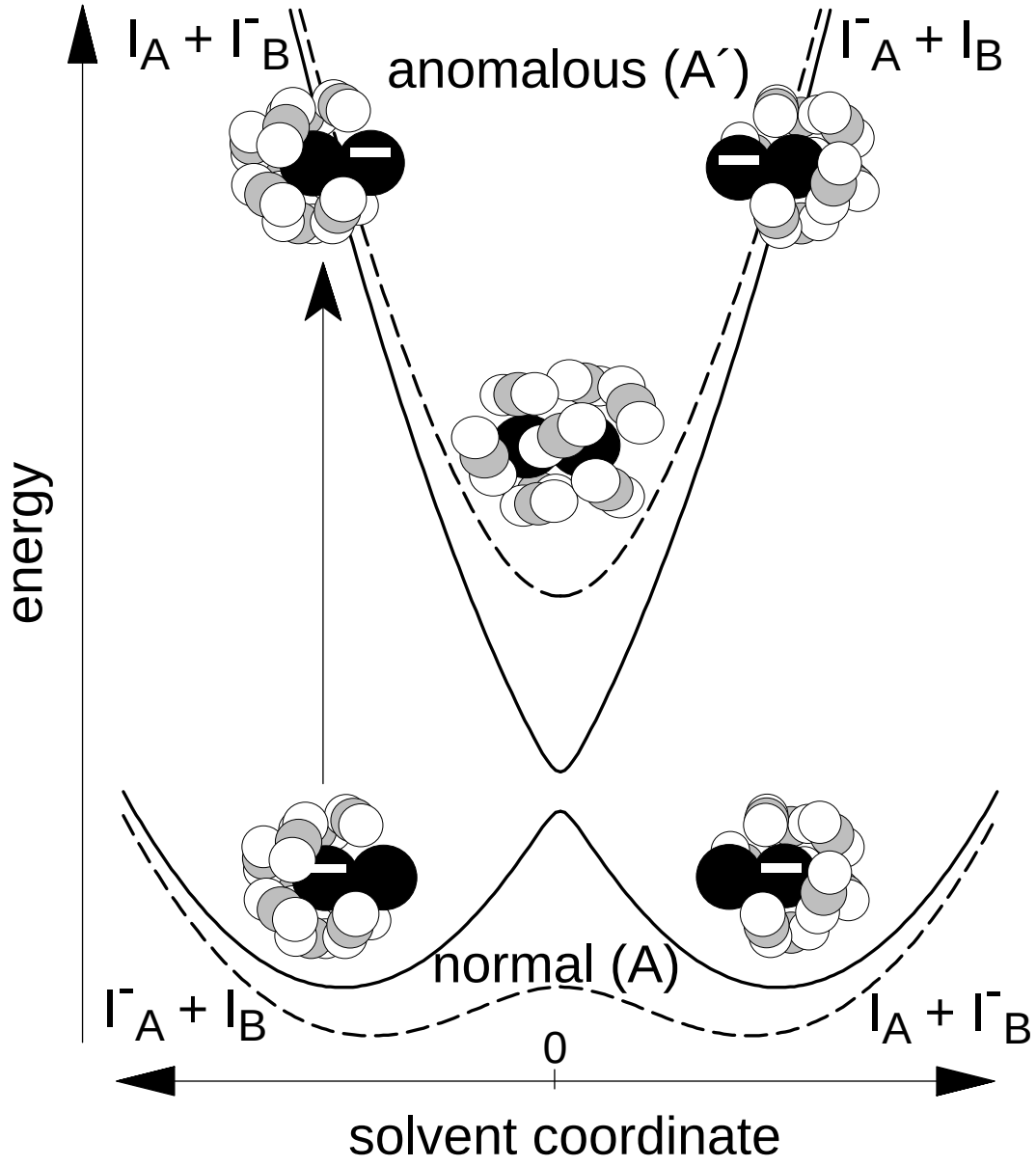

Figure 7.2: Schematic potential energy surfaces of solvated I_2^-. Dashed lines represent a cross-section at small I–I separations, where the bond coupling is strong compared with the solute-solvent interactions. The solid curves represent the weak coupling limit, which arises at longer bondlengths ($R_{\text{solute}} > 5$ Å). Anomalous charge switching in the upper curves is illustrated by the cartoons.

states.

7.1 Methods

The interaction potential between the solute I_2^- and the solvent CO_2 molecules is given by the model Hamiltonian in Chapters 2 and 3. This model includes state-dependent electrostatic and induction interactions between the solute and solvent based on ab initio calculations of the solute wave functions [10] and experimental data for the solvent charge distribution [11] and polarizability [12]. State independent atom-atom Lennard-Jones potentials account for the remaining dispersion and repulsion interactions and are fit to reproduce the known I^-—CO_2 and I—CO_2 potential curves [13]. The CO_2—CO_2 interaction potential is taken from Murthy, et al. [11]. The model captures the sensitive dependence of the solute charge distribution on the solute electronic state, the solute bondlength, and the positions and orientations of the solvent molecules.

The methods for determining cluster structures, preparing initial ensembles, and computing the nonadiabatic dynamics following photodissociation were described in Chapter 4. Nuclear motion on a single potential surface is computed using the velocity version of the Verlet algorithm [14], while hopping between electronic states of the solute is computed using Tully's method [15, 16] with some minor modifications.

For each cluster size studied, 41 trajectories were computed from starting configurations obtained by sampling a single 400 ps trajectory with an average temperature of 80 K. This temperature was chosen to lie on the upper end of the solid-liquid phase transition region in the clusters, based on our

previous experience that such temperatures gave reasonable agreement with experimental results [7]. The products are determined by integrating the trajectories until the nuclear configurations meets either of two criteria: the I–I distance exceeds 20 Å, or I_2^- undergoes more than 100 oscillations in a particular potential well. The dissociation and recombination times vary from a few picoseconds to over 100 ps in some cases where I_2^- is trapped in an excited electronic state before recombining. The time scale for evaporation of CO_2 molecules from the clusters following photodissociation appears to be much longer than the 50–100 ps over which the trajectories are integrated, and thus we do not calculate the final product mass distributions, which are measured experimentally at 5–10 μs [17, 18].

7.2 Results and Discussion

Figure 7.3(a) shows three cluster structures obtained from 80 K ensembles. The average binding energy per CO_2 at 80 K is fairly constant at about 200 meV for $10 \leq n \leq 18$, while for smaller cluster sizes it dips to about 190 meV. These values are consistent with the upper bound of 250 meV estimated from experiment that includes the kinetic energy released upon evaporation [17]. The clusters develop a pronounced asymmetry in the range $7 \leq n \leq 13$, which is illustrated by the middle structure at $n = 10$. More symmetric solvent configurations are shown at $n = 5$, where the solvent tends to clump about the waist of I_2^-, and $n = 16$, the size at which the first solvation shell is thought to close in the experiment [17]. The structures and energetics we observe in our 80 K ensembles are in good agreement with earlier studies using optimized geometries [5, 19, 20].

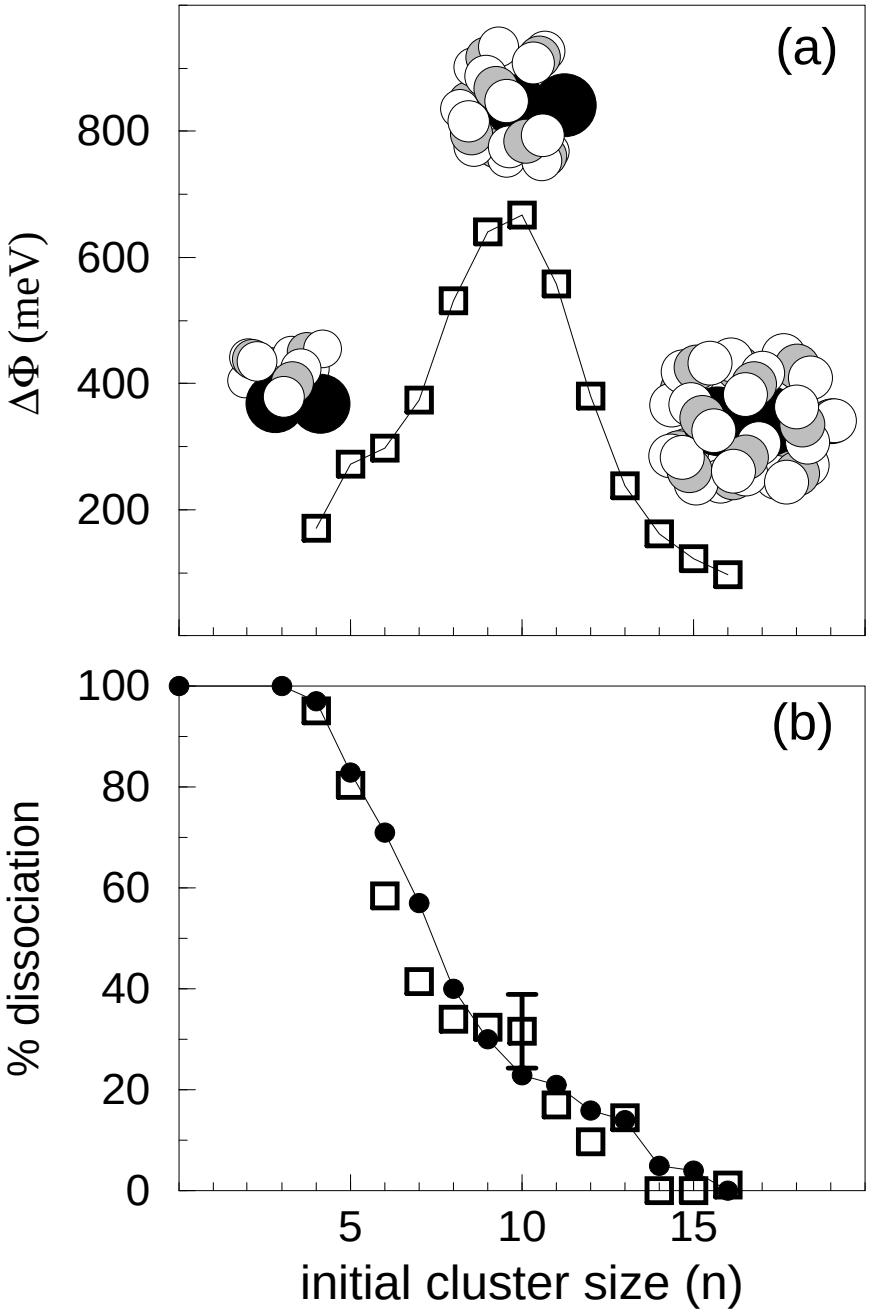

Figure 7.3: (a) Ensemble average of the magnitude of the solvent coordinate as a function of cluster size. Typical structures for $n = 5, 10, 16$ are shown. (b) Branching ratio for the products of $I_2^-(CO_2)_n$ photodissociation at 790 nm. The filled circles are the experimental data and the squares show the simulation results. The 1σ error bar shown for $n = 10$ is based on the statistical sampling and is representative of the error bars at other cluster sizes.

To quantify the degree of solvent asymmetry, we define a solvent coordinate, $\Delta\Phi$, as the change in energy when a charge of $-e$ is moved from I_A to I_B for a fixed nuclear configuration. The average magnitude of $\Delta\Phi$ in the 80 K ensembles peaks at $n = 10$ and is a factor of 5 smaller for $n = 16$, as shown in Fig. 7.3(a). Large values of $\Delta\Phi$ exert a strong force to localize the charge on the favored atom, so that in the most asymmetric configurations, 60% of the excess charge in ground state I_2^- resides on the favored end of the molecule. Large initial solvent asymmetries also strongly influence the dynamics following photodissociation, as we discuss below.

Figure 7.3(b) compares the product branching ratios calculated from the model with the experimental results of Vorsa et al. [18, 21]. The 1σ error bar shown results from sampling a relatively small number of trajectories—41 for each cluster size. The discrepancies between simulation and experiment are within the uncertainties for all but a few cluster sizes, and thus the model accurately reproduces the rapid onset of caging with increasing cluster size observed in the experiments [17, 18]. Also in agreement with experiment are the results that all of the dissociated products arise from ejection of neutral I atoms leaving behind solvated I^-, while all of the recombined products are based on I_2^- in its ground electronic state. In contrast, for argon clusters experiment [18] and simulation [7, 22] found additional product channels corresponding to ejection of I^- ions and to recombination of I_2^- in the A state (see Chapter 5).

In Fig. 7.4 we plot the trajectories for $n = 9$ and 16 in two dimensions: the solute bondlength, and $\Delta\Phi$. The three panels shown for each cluster size partition the trajectories based on electronic state. All trajectories begin in the A' state, shown in the top panel, at $R_{\text{solute}} = 3.3$ Å. Upon reaching the coupling regions marked with ovals, trajectories make transitions to the lower-lying A

and X states, shown on the left and right respectively. Transitions between these two lower states can also occur in the regions outlined with rectangles. For simplicity, we do not show the dynamics on the $^2\Pi_{u,3/2}$ state; it is accessible from the A' state and exhibits anomalous charge switching.

A main feature of the dynamics on the A' state is the narrow range of solvent coordinates observed in the coupling regions. One might expect that as R_{solute} increases the charge and solvent would tend to localize on a single iodine atom. But the A' surface has anomalous character; so that, as depicted in Fig. 7.2, solvent asymmetry creates charge flow toward the less solvated atom, which in turn pulls the solvent back towards more symmetric configurations. Anomalous charge switching thus creates a steep valley on the A' potential surface, funneling trajectories into symmetric solvent configurations. The $n = 16$ trajectories begin with a fairly narrow range of solvent asymmetries that tightens somewhat upon dissociation. The funnel shape is more striking for $n = 9$, where there is a much broader range of initial solvent coordinates. For large initial $\Delta\Phi$, the charge jumps to the escaping atom which slows down and pulls solvent molecules away from the other atom until the solvent configuration becomes nearly symmetric.

Anomalous charge switching also prevents dissociation on the A' state, because the attraction of the CO_2 to I^- is so strong that the negative ion cannot escape. The A' funnel thus has a well in the dissociation coordinate that traps the trajectories in a region where the R_{solute} is about 5–7 Å. The maximal extension of the solute bond in the A' state is somewhat larger on average for $n = 9$ than $n = 16$, but dissociation cannot occur in either case or for any of the cluster sizes studied. In contrast, much larger separations and even I^- ejection were observed in simulations of comparable cluster sizes in $I_2^-Ar_n$ [7, 22].

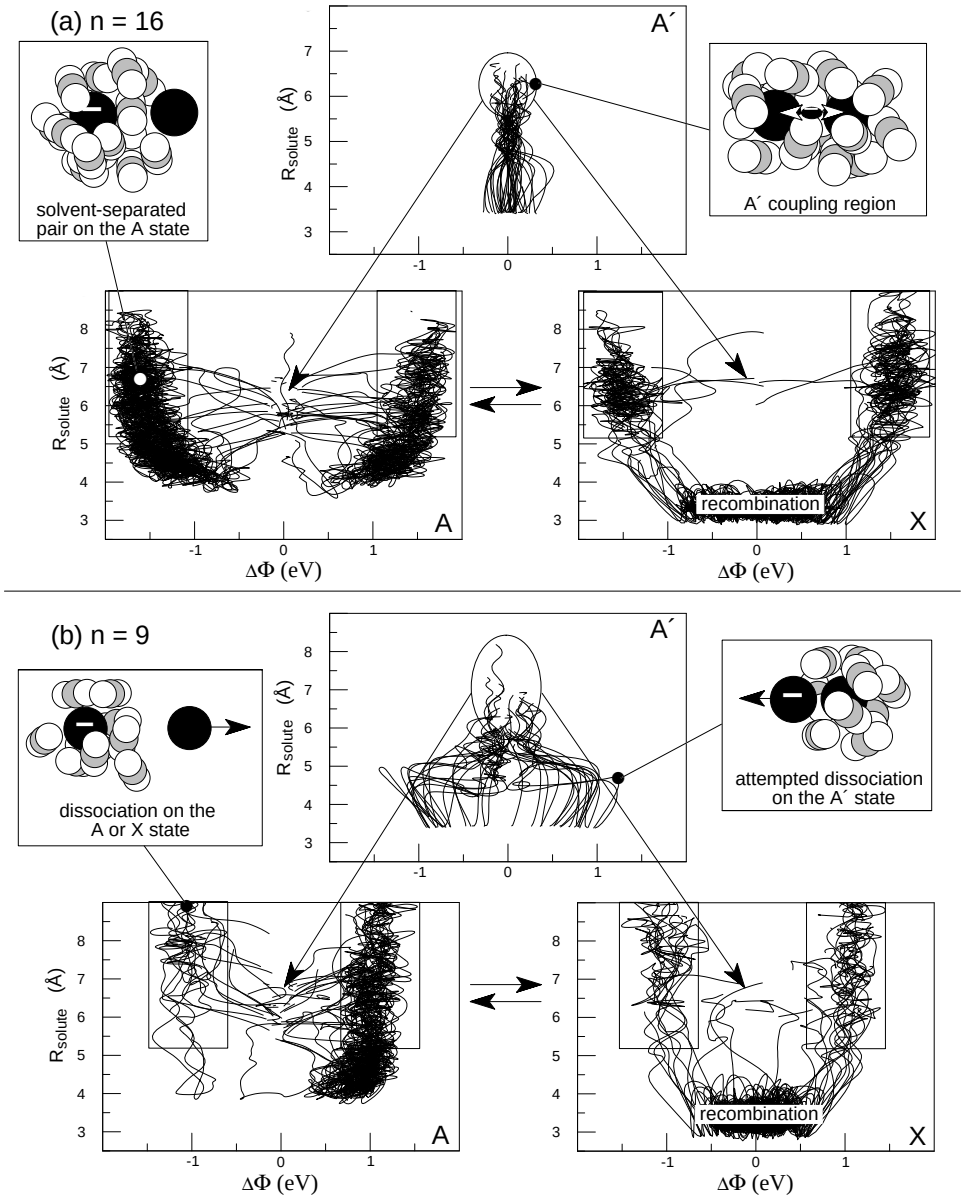

Figure 7.4: Dynamics of an ensemble of 41 trajectories projected onto the solute bondlength and the solvent coordinate for $n = 16$ (a) and $n = 9$ (b). Trajectories begin in the A' state at R_{solute}=3.3 Å and undergo transitions to the lower states in the regions indicated with ovals. $A \leftrightarrow X$ coupling regions are marked with rectangles. The apparent favoring of the right side of the A state in (b) is due to the few trajectories that remain trapped for a long time. (This figure was painstakingly prepared by N. Delaney.)

Following the concerted dynamics in the A' state, electronic relaxation to the X and A states generally takes place less than one picosecond after photoexcitation. The effect of returning to a normal charge switching state is dramatic: charge localizes completely onto one solute atom and the solvent races to the ion, increasing the magnitude of $\Delta\Phi$ to 1 eV or more within 200-500 fs. Meanwhile, R_{solute} hardly changes. The disparity in response time of the solvent and the solute often results in a solvent-separated pair with CO_2 molecules tightly clustered to I^- and the I atom residing on the surface. These pairs, which were not observed in simulations of $I_2^-Ar_n$ clusters [7, 22], eventually either dissociate, via thermal evaporation of I, or recombine on the X state.

Trajectories are often trapped for extended periods in the A state prior to recombination or dissociation, as shown in Fig. 7.4. A state trapping is observed rarely in small clusters, but is common in cluster sizes $n \geq 7$. Both the frequency and length of trapping increase with cluster size. Residence times of 5–25 ps are typical, but product formation can require as long as 50–100 ps. We also observe transient recombination of I_2^-, that is, some trajectories pass within $R_{\text{solute}} = 4$ Å the equilibrium bondlength, on the A state. However, the excited state I_2^- bond is weak compared to the $I^- \cdot CO_2$ solvation energy and the bond is broken before appreciable vibrational relaxation can occur. Nevertheless, both of these metastable cluster configurations contribute to the long lifetimes on the A state.

Formation of recombined products following trapping on the A state requires a coordinated sequence of events. The A state and the X state differ by the alignment of the empty p orbital on iodine. For $R_{\text{solute}} > 5$ Å the alignment of that orbital is readily altered by collisions with solvent molecules [7, 23],

causing electronic transitions back and forth between these two states. To get recombination on the ground state, the solute bondlength must increase for the orbital to be realigned; simultaneously, neutral iodine must break into the first solvation shell, displacing CO_2.

On the ground state, the covalent bond is roughly an order of magnitude stronger than on the A state and is comparable in size to the total solute-solvent interaction. Once a trajectory reaches 5–6 Å on the X state, the strong bond force draws I_2^- back together; the solute rapidly recombines and the magnitude of the solvent coordinate never exceeds 0.5 eV thereafter. Trajectories that hop from the A' state to the X state at short bondlengths recombine directly in roughly 1–3 ps, without forming the solvent-separated pair.

There are two pathways for I_2^- dissociation. During trapping on the A state, neutral iodine is the most weakly bound species in the cluster and therefore readily evaporates. This is the dominant dissociation mechanism for $n \geq 9$. In the smaller clusters, dissociation is generally more direct, with R_{solute} increasing monotonically following the transition from the A' state. Direct dissociation arises because there are fewer solvent molecules to hold the solute atoms together.

7.3 Conclusions

In summary, photoexcitation of I_2^- with a 790 nm photon places the solute on the A' electronic surface, which like the anomalous curves in Fig. 7.2, funnels the trajectories into highly symmetric solvent configurations as I_2^- dissociates. Following electronic relaxation, the A and X surfaces, like the normal

charge switching curves in Fig. 7.2, pull the trajectories towards highly asymmetric solvent configurations. The electronic coupling on the A state is small, and the strong solute-solvent interactions destabilize the weak I_2^- bond, allowing formation of long-lived solvent-separated pairs. Eventually, trajectories in the A state either dissociate or hop to the X state, where the much larger electronic coupling creates a strong pull towards permanent recombination, which occurs rapidly if $R_{\text{solute}} \leq 5$–6 Å. The strong ground state I_2^- bond also leads to direct recombination within a few picoseconds for a significant fraction of trajectories.

The results presented here emphasize that the isolated I_2^- potential curves can be misleading when interpreting the dynamics of photodissociation and recombination in CO_2 clusters. When CO_2 is present, for example, the A' state is not dissociative and also I_2^- cannot recombine permanently in the A state. Previous analyses of pump-probe experiments in these clusters [24–26] have used the isolated curves to locate the Franck-Condon regions for probe absorption. Our results suggest that coupling to the solvent will shift these regions significantly, possibly leading to new interpretations of the experimental signals and the dynamics—particularly the coherent feature observed at 2 ps. Finally, while it is the large solvent asymmetry of the cluster environment that produces the interesting dynamics we report here, we anticipate that these effects may be an amplification of phenomena which occur in the liquid phase as a result of solvent fluctuations. This possibility warrants further study.

References for Chapter 7

[1] N. Delaney, J. Faeder, P. E. Maslen, and R. Parson, J. Phys. Chem. A **101**, 8147 (1997).

[2] R. A. Marcus, Ann. Rev. Phys. Chem. **15**, 155 (1964).

[3] M. D. Newton and N. Sutin, Ann. Rev. Phys. Chem. **35**, 437 (1984).

[4] G. C. Schatz and M. A. Ratner, *Quantum Mechanics in Chemistry*, chapter 10, Prentice Hall, Englewood Cliffs, 1993.

[5] J. M. Papanikolas, P. E. Maslen, and R. Parson, J. Chem. Phys. **102**, 2452 (1995).

[6] P. E. Maslen, J. M. Papanikolas, J. Faeder, R. Parson, and S. V. ONeil, J. Chem. Phys. **101**, 5731 (1994).

[7] J. Faeder, N. Delaney, P. Maslen, and R. Parson, Chem. Phys. Lett. **270**, 196 (1997).

[8] B. M. Ladanyi and R. Parson, J. Chem. Phys. **107**, 9326 (1997).

[9] I. Benjamin, P. F. Barbara, B. J. Gertner, and J. T. Hynes, J. Phys. Chem. **99**, 7557 (1995).

[10] P. E. Maslen, J. Faeder, and R. Parson, Chem. Phys. Lett. **263**, 63 (1996).

[11] C. S. Murthy, S. F. O'Shea, and I. R. McDonald, Mol. Phys. **50**, 531 (1983).

[12] C. G. Gray and K. E. Gubbins, *Theory of Molecular Fluids*, volume 1, Clarendon, Oxford, 1984.

[13] Y. Zhao, C. C. Arnold, and D. M. Neumark, J. Chem. Soc. Faraday Trans. **89**, 1449 (1993).

[14] H. C. Andersen, J. Comput. Phys. **52**, 24 (1982).

[15] J. C. Tully, J. Chem. Phys. **93**, 1061 (1990).

[16] S. Hammes-Schiffer and J. C. Tully, J. Chem. Phys. **101**, 4657 (1994).

[17] J. Papanikolas, J. Gord, N. Levinger, D. Ray, V. Vorsa, and W. Lineberger, J. Phys. Chem. **95**, 8028 (1991).

[18] V. Vorsa, P. J. Campagnola, S. Nandi, M. Larsson, and W. C. Lineberger, J. Chem. Phys. **105**, 2298 (1996).

[19] J. M. Papanikolas, *I_2^- Photodissociation and Cage Recombination Dynamics in Size-Selected $I_2^-(CO_2)_n$ Clusters*, PhD thesis, University of Colorado, 1994.

[20] F. G. Amar and L. Perera, Z. Phys. D **20**, 173 (1991).

[21] V. Vorsa, *Photodissociation Dynamics of Mass-Selected Anions and Anionic Clusters*, PhD thesis, University of Colorado, 1996.

[22] V. S. Batista and D. F. Coker, J. Chem. Phys. **106**, 7102 (1997).

[23] A. I. Krylov, R. B. Gerber, and R. D. Coalson, J. Chem. Phys. **105**, 4626 (1996).

[24] J. Papanikolas, V. Vorsa, M. Nadal, P. Campagnola, H. Buchenau, and W. Lineberger, J. Chem. Phys. **99**, 8733 (1993).

[25] V. Vorsa, S. Nandi, P. J. Campagnola, M. Larsson, and W. C. Lineberger, J. Chem. Phys. **106**, 1402 (1997).

[26] P. K. Walhout, J. C. Alfano, K. A. M. Thakur, and P. F. Barbara, J. Phys. Chem. **99**, 7568 (1995).

Chapter 8

Dynamics of $ICl^-(CO_2)_n$ Photodissociation

Chapter 1 briefly mentioned the surprising results of $ICl^-(CO_2)_n$ photodissociation, where only uncaged, Cl^--based fragments are formed for $n > 10$. In I_2^-, as we have seen, once the solvent cage reaches a certain size, roughly corresponding to a complete shell around the solute, only recombined products are observed. It appears that in ICl^- the forces favoring localization of the charge onto a single atom are strong enough to break the solute chemical bond, or at least prevent it from reforming.

Figure 8.1 illustrates the photodissociation of ICl^- on the bare ion potential curves that were described in Chapter 3. Nadal et al. [1] have measured the photofragmentation of products from bare ICl^- and $ICl^-(CO_2)_n$ clusters following excitation with a red photon, as depicted by the arrow in the figure. Excitation of the bare ion to the A' ($^2\Pi_{1/2}$) state leads to the formation of I^- and Cl. At 644 nm, only I^- products are observed in the experiment; at 740 nm, however, there appears to be some overlap with the perpendicular transition to the A ($^2\Pi_{3/2}$) state, and a small amount of Cl^- (6%) is formed [2]. Because the amount of excitation to the A state is very small in both the bare ion and the clusters, we will neglect it for the remainder of the discussion in this chapter.

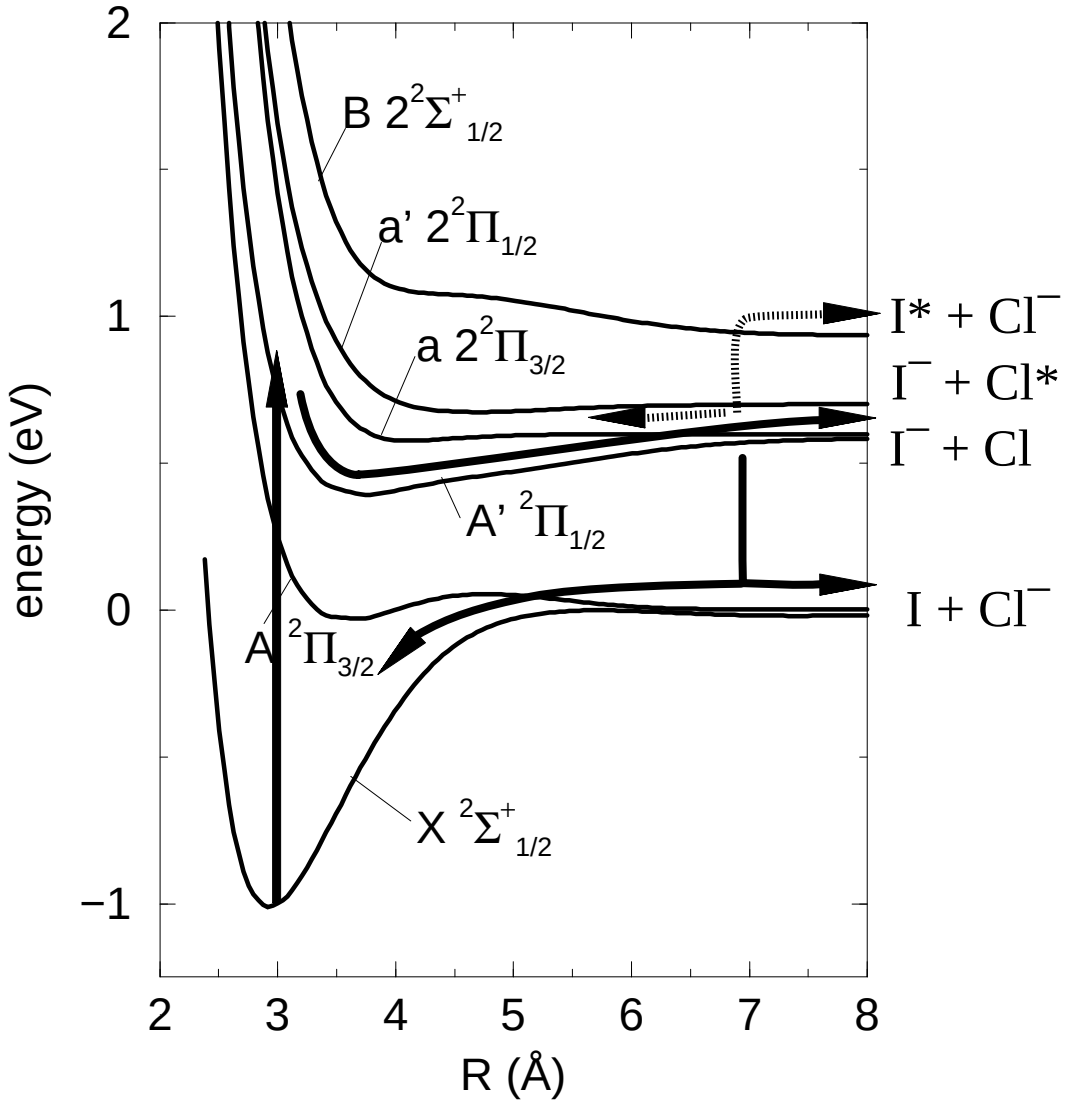

Figure 8.1: Bare ICl^- curves illustrating photoexcitation and avenues for product formation. Direct dissociation in the A' state produces I^--based fragments. The solvent may bring about transitions to the ground electronic state where recombination or dissociation can occur. The dashed arrows indicate other possible pathways observed in the simulations involving recombination in the A' state and dissociation to form Cl^- + I^*.

The product branching ratios for photodissociation of $ICl^-(CO_2)_n$ at 644 nm are shown in Fig. 8.2. The solvent effects on ICl^- photodissociation are much larger than those observed in I_2^-, particularly for small clusters. The formation of caged products from I_2^- photoexcitation is first observed at $n = 6$ [3], while recombined products are observed from dissociation of $ICl^-(CO_2)_1$ at 644 nm—a "one-molecule" cage effect. When ICl^- is solvated by two or more CO_2 molecules, a third product channel opens in which solvated Cl^- is formed. The fraction of I^--based fragments formed drops dramatically with the addition of the first several solvent molecules, reaching zero by $n = 4$. At 740 nm (not shown) the dropoff is even steeper—only 8% of the fragments from $ICl^-(CO_2)_2$ are I^--based. The yield of ICl^--based products, i.e. the caging fraction, peaks at about 75% for $n = 5$, but then gives way to Cl^- product formation, which reaches nearly 100% by $n = 10$.

Two fundamental questions arise from these results: First, why is caging so efficient for small cluster sizes? And second, why does dissociation dominate at the larger cluster sizes? To answer these questions requires an understanding of the mechanisms by which the products are formed, and in particular which electronic states are involved and how the solvent couples them to bring about nonadiabatic transitions. This chapter reports preliminary results of an ongoing attempt to answer these questions and to explore the interplay between charge flow and solvent dynamics in a heteronuclear solute molecule.

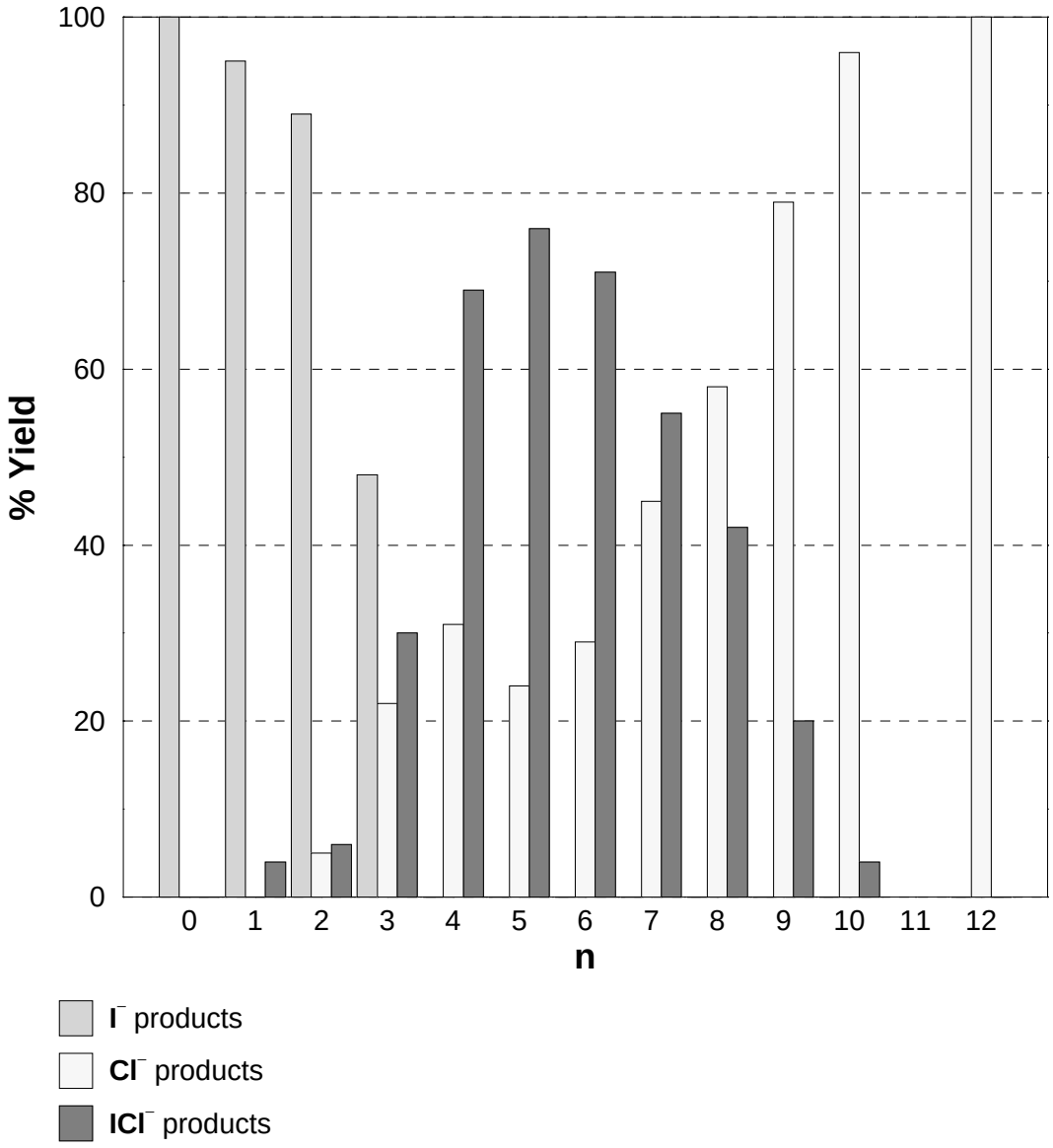

Figure 8.2: Experimentally observed product branching ratios from photodissociation of $ICl^-(CO_2)_n$ at 644 nm from Refs. 1, 2.

8.1 Cluster Structure

As we have seen in Chapters 5–8, the cluster configuration at the instant of photoexcitation strongly influences the subsequent dynamics, especially for the clusters with less than a complete solvation shell. In I_2^- clusters the first several solvent molecules pack around the waist of the anion, leading to very efficient dissociation. Amar and Perera [4] noted the particular importance that a solvent molecule at the "cap" position, i.e. along the solute bond axis, has in producing caging and recombination. They associated onset of caging in Br_2^- clusters with the appearance of minimum energy structures with capping solvent molecules. Our simulations of I_2^- in both argon and CO_2 clusters support this role of a structure in influencing the onset of caging, although other factors, such as the charge flow and the long-range interactions with the solvent, are clearly also important in determining whether or not caging occurs.

Structural effects on caging are even more important in ICl^- than in I_2^- because the solute asymmetry results in tighter binding around the chlorine end of the molecule. The size disparity between I^- and Cl^- and tighter binding of CO_2 to Cl^- were illustrated in Chapter 3. The Cl–C bond distance in $Cl^-\cdot CO_2$ is 3.0 Å, compared with a 3.65 Å I–C separation in $I^-\cdot CO_2$. The binding energies for a single CO_2 molecule in the two clusters are 350 meV and 212 meV respectively. The solvent molecules therefore cluster preferentially around the chlorine end of the molecule, acting as an effective cage even when only a few solvent molecules are present.

The effect of an asymmetric solvent structure around ICl^- may be exaggerated by the kinematics of photodissociation. Because of the mass disparity between I and Cl, the Cl atom receives about 75% of the kinetic energy

released. Furthermore, the masses of Cl (35 amu) and CO_2 (44 amu) are closely matched, so that collisions with the CO_2 solvent are very efficient at removing kinetic energy from the dissociating Cl atoms.

We have characterized the structural features of $ICl^-(CO_2)_n$ clusters in the ground electronic state using a combination of optimized configurations and equilibrated ensembles prepared by running molecular dynamics (MD) trajectories. The ensembles have been constructed and the minimum energy configurations determined by a three-step procedure. First, an ensemble of 40 configurations is generated at an approximate temperature of 120 K by sampling a 200 ps MD trajectory at 5 ps intervals. This temperature is chosen to be high enough that the solvent molecules are fluid and a wide of solvent configurations is sampled, but low enough that evaporation of monomers does not occur. The correct total energy at which to run the trajectory is determined by running shorter trajectories of 5–50 ps duration at several different total energies. Based on these trial runs, the total energy is then set by appropriate scaling of the atomic velocities. A second ensemble with a target temperature of 50 K is generated by cooling each member of the 120 K ensemble over a period of 10 ps. The cooling is accomplished by scaling the velocities at each time step by a small amount to remove kinetic energy. The total amount of kinetic energy removed is simply $Nk\Delta T$, where N is the number of cluster degrees of freedom ($5n$), k is the Boltzmann constant, and ΔT is the total desired temperature change. The lower temperature is chosen so that the clusters are effectively frozen, with the molecules making only small excursions about local minima. The final step is to determine these local minima by the Newton-Raphson optimization method described in Chapter 3.

The lowest energy structures determined by this simulated annealing

process are shown in Fig. 8.3. Binding sites on the Cl end of the molecule are strongly favored over those on the I end. As in the $I_2^-(CO_2)_n$ clusters, the CO_2 molecules always orient themselves perpendicular to the surface of the solute anion in order to maintain a favorable interaction with the negative quadrupole moment. The CO_2 molecules pack tightly around the Cl end of the molecule until all of the sites near Cl are filled—between 6 and 7 solvent molecules. The energy gained for the addition of each CO_2 molecule is plotted in Fig. 8.4. The binding energy for each monomer added to the Cl end of the molecule ranges from 260 to 290 meV. The binding energy at $n = 7$ is somewhat lower, reflecting the additional crowding that must take place to fit a seventh molecule around the Cl half of ICl^-. For $n > 7$, the monomers occupy sites on the I end of the anion, where the binding energy is about 30% lower. As the solvent shell fills, the binding energies increase somewhat because of the favorable solvent-solvent interactions. The structure at $n = 14$ indicates the solvent shell should close at either $n = 14$ or $n = 15$, but simulations at larger cluster sizes will be necessary to locate the closing more precisely.

The solvent asymmetry can be quantified using the solvent coordinate defined in Chapter 7. This solvent coordinate, $\Delta\Phi$, is the energy required to move a charge of $-e$ from the Cl end to the I end for a fixed nuclear configuration. Positive values favor charge on the Cl end, while negative values, which are not observed in either the ground state ensembles or optimized structures, favor charge on the I end. Values of the solvent coordinate for the minimum energy structures and average values for the high and low temperature ensembles are plotted as a function of cluster size in Fig. 8.5. The solvent coordinate increases approximately linearly through about $n = 6$, peaking at $n = 7$ for the minimum structures and low temperature ensemble and at $n = 6$ for the high

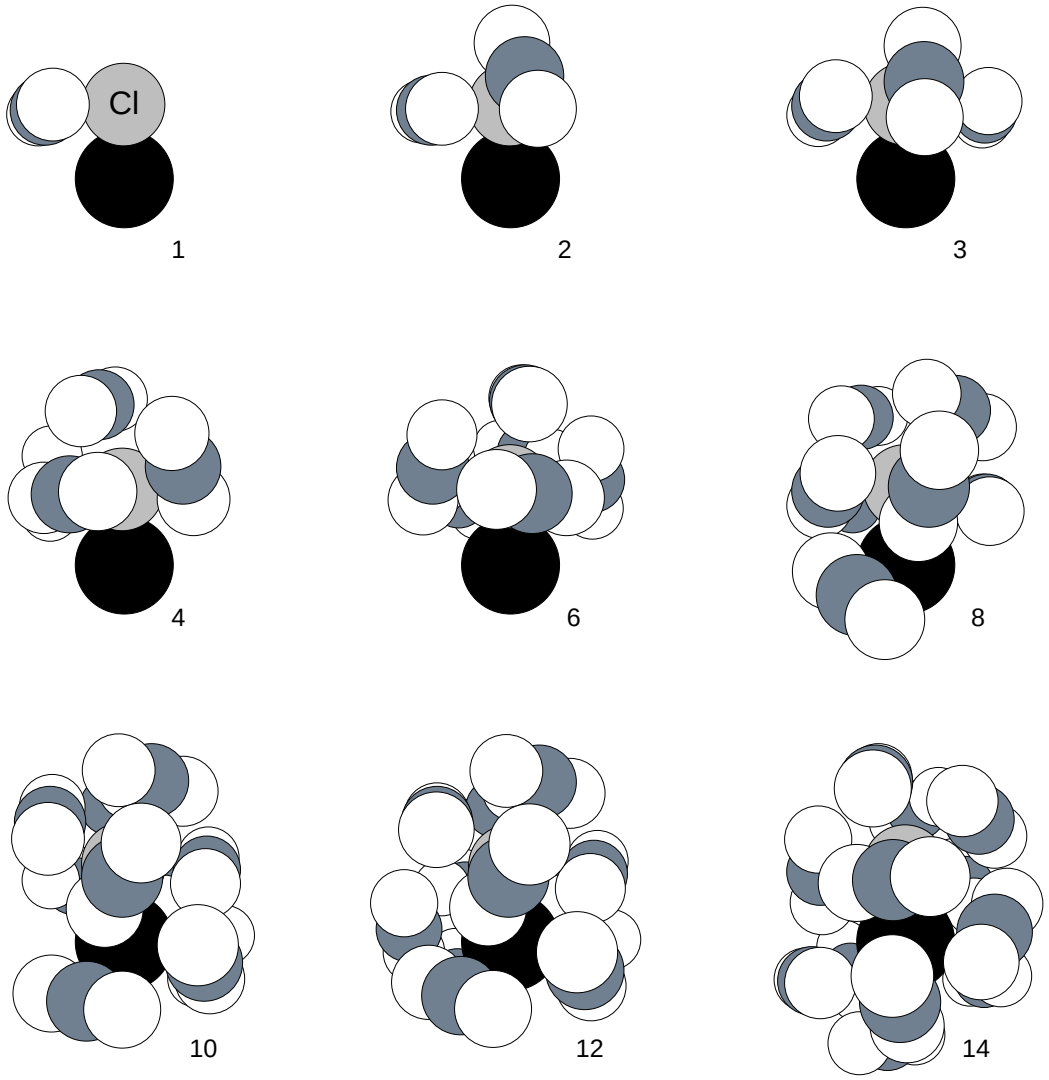

Figure 8.3: Minimum energy structures of $ICl^-(CO_2)_n$, n =1–14. A CO_2 molecule first occupies a site on the ICl^- bond axis at $n = 4$. In the structures for $n = 2$ and 3 the CO_2 molecules are not in a position to block the escape of Cl as ICl^- dissociates.

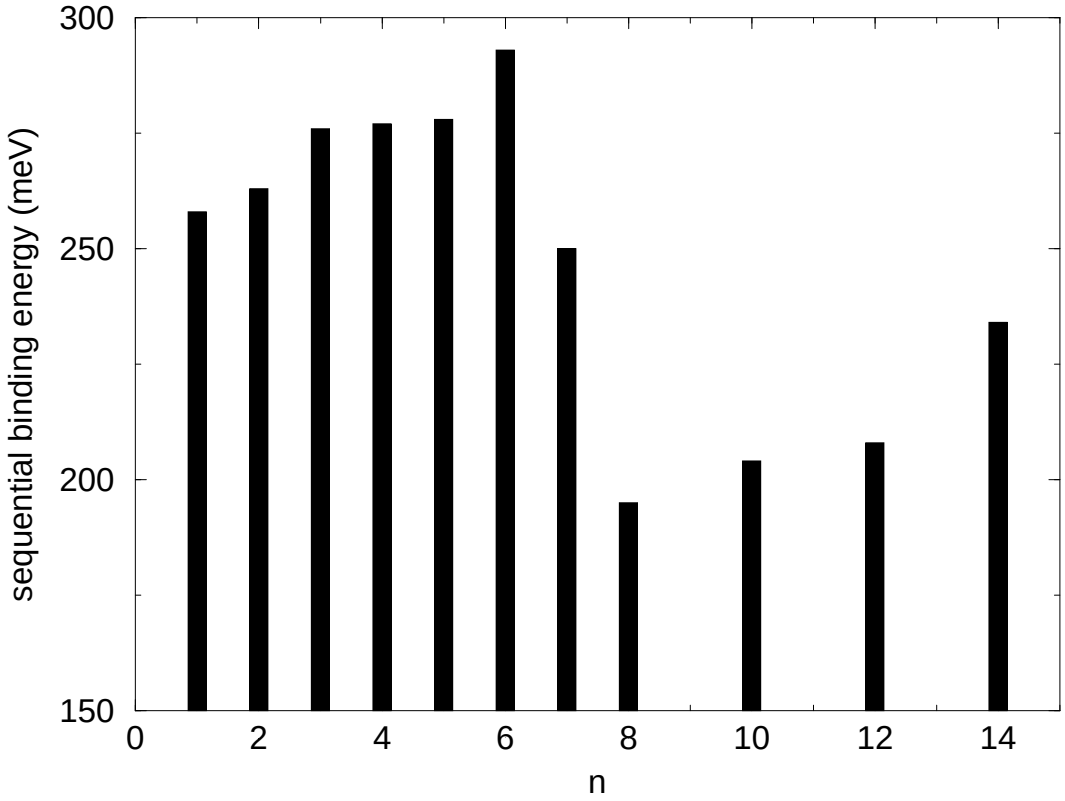

Figure 8.4: Sequential binding energies for minimum energy structures of $ICl^-(CO_2)_n$. This quantity is defined as the amount of energy released by adding the last monomer to the cluster, i.e. PE_n - PE_{n-1}, where PE is the potential energy of the cluster. This quantity is always negative, so the absolute value is plotted here.

temperature ensemble. The magnitude of the asymmetry falls as monomers fill sites around the I end of the anion, but still remains large for the nearly complete solvent shell at $n = 14$—around 800 meV. By comparison, the initial solvent asymmetry in $I_2^-(CO_2)_{16}$ is about 100 meV, while the peak asymmetry, seen in $I_2^-(CO_2)_{10}$, is only about 700 meV. The peak asymmetries in the ICl^- clusters are thus more than double what was seen in I_2^-. The reason for the much larger asymmetries observed in ICl^- is that the solvent molecules pack much closer to the Cl atom than the I atom because of the smaller ionic radius. The large values of the solvent coordinate simply confirm the well-known fact that smaller charge distributions are better solvated than larger ones.

The persistence of the solvent asymmetry as the clusters are heated demonstrates that temperature has little effect on the basic structural properties of the clusters. Temperature has a significant but relatively small effect on $\Delta\Phi$ for the most asymmetric clusters. As these asymmetric clusters are heated, solvent molecules on the Cl end occasionally migrate onto the I end of the anion. The mobility of the solvent molecules is limited as the solvation shell fills, so that temperature has less effect on the solvent asymmetry at larger n.

Properties of the ensembles and the minima are summarized in Tables 8.1–8.3. The data confirm the earlier statement that for a broad range of temperatures heating the clusters has relatively little influence on the basic structural properties. The much smaller number of distinct minima that are found for the n =1–7 clusters suggests that the cage around the Cl is much less flexible than the cage around I. The Mulliken charge on the chlorine atom, q_{Cl}, indicates that ICl^- polarizes significantly in response to the solvent asymmetry. q_{Cl} is -0.61 in bare ICl^-, while it attains a maximum value of about -0.74 at $n = 6$ and 7, the most asymmetric cluster sizes. The degree of polarization is

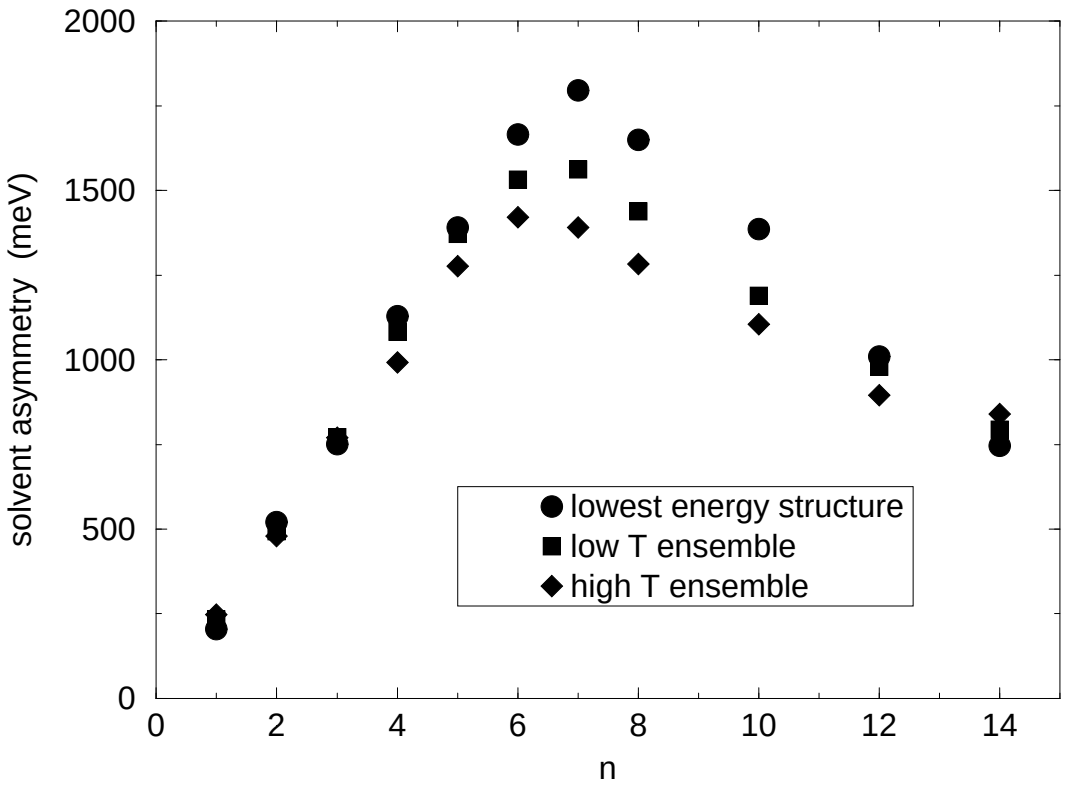

Figure 8.5: Solvent asymmetry as a function of cluster size for $ICl^{-}(CO_2)_n$. The solvent always favors charge at the Cl end of the molecule.

Table 8.1: Average properties of the lower temperature $ICl^-(CO_2)_n$ ensembles with standard deviations in parentheses.

n	T (K)	PE[a] (meV)	$\Delta\Phi$ (meV)	q_{Cl} (au)
1	68(31)	-241(6)	234(43)	-0.63(1)
2	52(17)	-492(7)	494(62)	-0.65(1)
3	60(15)	-742(10)	772(66)	-0.68(1)
4	57(13)	-999(12)	1082(78)	-0.70(2)
5	61(14)	-1269(15)	1372(85)	-0.72(2)
6	69(14)	-1545(18)	1531(104)	-0.74(2)
7	73(16)	-1745(23)	1562(104)	-0.74(2)
8	67(12)	-1919(19)	1438(176)	-0.72(3)
10	65(13)	-2272(29)	1189(148)	-0.70(2)
12	67(9)	-2666(23)	979(187)	-0.68(2)
14	57(9)	-3104(26)	794(157)	-0.66(1)

[a] Cluster potential energy not including ICl^- bond energy (1.010 eV).

comparable to that observed in I_2^- for the most asymmetric cluster sizes, but in ICl^- the polarization remains sizeable even for clusters with a nearly complete solvent shell.

The properties of the minimum energy structures and the ensembles have several consequences for the photodissociation dynamics. The pronounced asymmetry of the small small cluster sizes is the major reason for the early onset of caging. A minimum energy structure with CO_2 in the cap position first appears at $n = 4$, and, as we discuss below, this capping is the primary reason for the large increase in caging at this cluster size in simulations of the photodissociation dynamics. Structural features alone do not determine caging. Even though the I atom receives about 25% of the kinetic energy release, no solvent molecules stand in the way of I escaping in clusters with less than half a solvent shell. Long-range interactions between the solvent molecules and the escaping I atom, enhanced by residual charge or charge flow onto I, are

Table 8.2: Average properties of the higher temperature $ICl^-(CO_2)_n$ ensembles with standard deviations in parentheses.

n	T (K)	PE[a] (meV)	$\Delta\Phi$ (meV)	q_{Cl} (au)
1	139(48)	-226(11)	248(60)	-0.63(2)
2	111(34)	-457(14)	479(94)	-0.65(2)
3	124(35)	-694(23)	770(89)	-0.67(2)
4	121(28)	-934(23)	992(142)	-0.69(2)
5	128(31)	-1190(34)	1276(136)	-0.71(2)
6	125(24)	-1435(31)	1420(132)	-0.73(2)
7	118(25)	-1603(38)	1391(137)	-0.73(2)
8	120(25)	-1769(45)	1282(172)	-0.71(3)
10	122(25)	-2093(54)	1104(181)	-0.69(3)
12	122(14)	-2446(37)	895(203)	-0.67(3)
14	111(18)	-2845(54)	839(209)	-0.67(2)

[a] Cluster potential energy not including ICl^- bond energy (1.010 eV).

Table 8.3: Properties of lowest energy $ICl^-(CO_2)_n$ clusters.

n	PE_n (meV)[a]	$PE_n - PE_{n-1}$ (meV)[b]	PE_n/n (meV)[c]	$\Delta\Phi$ (meV)	# local minima
1	−258	−258	−258	204	1
2	−522	−263	−261	520	2
3	−798	−276	−266	751	3
4	−1075	−277	−269	1129	4
5	−1353	−278	−271	1391	4
6	−1646	−293	−274	1665	3
7	−1896	−250	−271	1796	5
8	−2091	−195	−261	1649	18
10	−2499	−204	−250	1385	35
12	−2916	−208	−243	1010	38
14	−3384	−234	−242	746	37

[a] Cluster potential energy not including ICl^- bond energy (1.010 eV).
[b] Sequential binding energy, i.e. energy gained by adding last CO_2.
[c] Average potential energy per CO_2.

responsible for preventing I escape. A major difference between I_2^- and ICl^- is the much larger magnitude of the solvent asymmetry prevalent in all of the ICl^- structures. For all but the smallest clusters, the solvent asymmetry in the ground state structures is larger than the asymptotic splittings among the bare ion states, so that the B state asymptote, I^* and Cl^-, actually becomes lower than the A' state asymptote of I^- and Cl. When the solvent asymmetry is large enough, this reordering of the states causes the charge in the dissociating molecule to localize on the Cl atom, producing I^* and Cl^-. As we will see below, this profoundly affects the mechanisms by which products are formed.

8.2 Solvent Effects on the Electronic Absorption Spectrum

Nadal et al. [1] have measured the effect of clustering on the ICl^- electronic absorption in the red region of the spectrum. In $ICl^-(CO_2)_4$, the only cluster size studied, they found a small red shift of approximately 10 nm in the $A' \leftarrow X$ absorption band near 700 nm. This is equivalent to a differential shift in the energies of the two states of about 25 meV, which is very small considering that the total solvation energy for this cluster size is about 1 eV. The maximum absolute cross section for the solvated ion, $5 \pm 2 \times 10^{-18}\text{cm}^2$, is the same as the cross section for the bare ion to within the experimental error.

The small effect of solvation on the $A' \leftarrow X$ absorption band suggests that the electronic structure of the anion is not severely perturbed near the equilibrium ICl^- bond distance. An important corollary is that for this excitation energy, charge transfer to the solvent is probably not an important effect. Although CO_2^- is unstable [5], DeLuca and coworkers [6] have determined that $(CO_2)_n$ clusters, where n =2–13, may have electron affinities as

large as 2.2 eV. Because the electron affinity of ICl is about 2.5 eV [1], it is conceivable that photoexcitation could produce charge transfer. One reason that charge transfer is probably not observed, particularly near the equilibrium bond distance (R_e), is that the solvent configuration heavily favors the localized charge distribution on ICl^-. For these solvent configurations, states in which the charge is delocalized on a set of CO_2 molecules or even localized on a single CO_2 molecule are probably stabilized by the solvent much less than the ICl^- states, and are therefore far away in energy.

A second implication of the small red shift observed in the absorption spectrum is that there is only a small change in the charge distribution between the ground and excited states at R_e. If there were a substantial flow of charge onto the I atom from photoexcitation, one would expect a substantial blue shift in the transition energy because the excited state would be less favorably solvated. This suggests that at R_e that charge distribution still favors the Cl end of the anion.

We have calculated the absorption spectrum of $ICl^-(CO_2)_4$ using a semiclassical method similar to the one described in Chapter 3. For each configuration in an ensemble, the solvent nuclei are held fixed and the solute electronic spectrum is calculated using the modified reflection approximation described by Heller [7]. The absorption cross section at frequency ω from the initial state i to the final state f is given by

$$\sigma_{if}(\omega) = 4\pi^2 \alpha a_0^2 \omega \left| V_f'(q_T) \right|^{-1} \left| \mu_{if}(q_T) \psi_i(q_T) \right|^2 , \tag{8.1}$$

where V_f is the upper state potential, q_T is the classical turning point on the upper state, and μ_{if} and ψ_i are the transition moments and ground state

vibrational wave functions respectively. The ground state wave function is approximated by a harmonic oscillator wave function. The total spectrum of the cluster is then computed as an average over the spectra for each configuration in the ensemble.

The simulated $n = 4$ spectrum shown in Fig. 8.6 was calculated by averaging over the lower temperature ensemble described in the previous section. The spectra calculated from the higher temperature ensemble and the lowest energy structure are nearly identical. As in the experiment, the $A' \leftarrow X$ band near 700 nm undergoes a small red shift, although the magnitude of the shift is about 35 nm, or 90 meV, in contrast to the 25 meV experiment shift. The absolute cross sections agree to within the experimental error. The UV $B \leftarrow X$ band undergoes a small blue shift and diminishes somewhat in intensity, while the $a' \leftarrow X$ near 450 nm disappears altogether in the cluster. This suggests that an experimental measurement of this band in the bare ion and the cluster would provide an excellent test of the electronic structure model.

Although there is some disagreement in the magnitude of the $A' \leftarrow X$ band red shift, the simulated spectra support the conclusion that solvation does not radically alter the anion electronic structure. In the simulation, the charge distributions are nearly identical in the X and A' states of the cluster, lending credibility to the inference from the experimental spectra that there is little charge transfer character to the transition. The charge distribution of the A' state in the bare ion favors iodine, but in the cluster, where the Cl end is more favorably solvated at the ground state equilibrium configuration, the A' state polarizes to favor the Cl atom. This tilting of the initial charge distribution in the excited state towards Cl strongly affects the dynamics of photodissociation, as we discuss below.

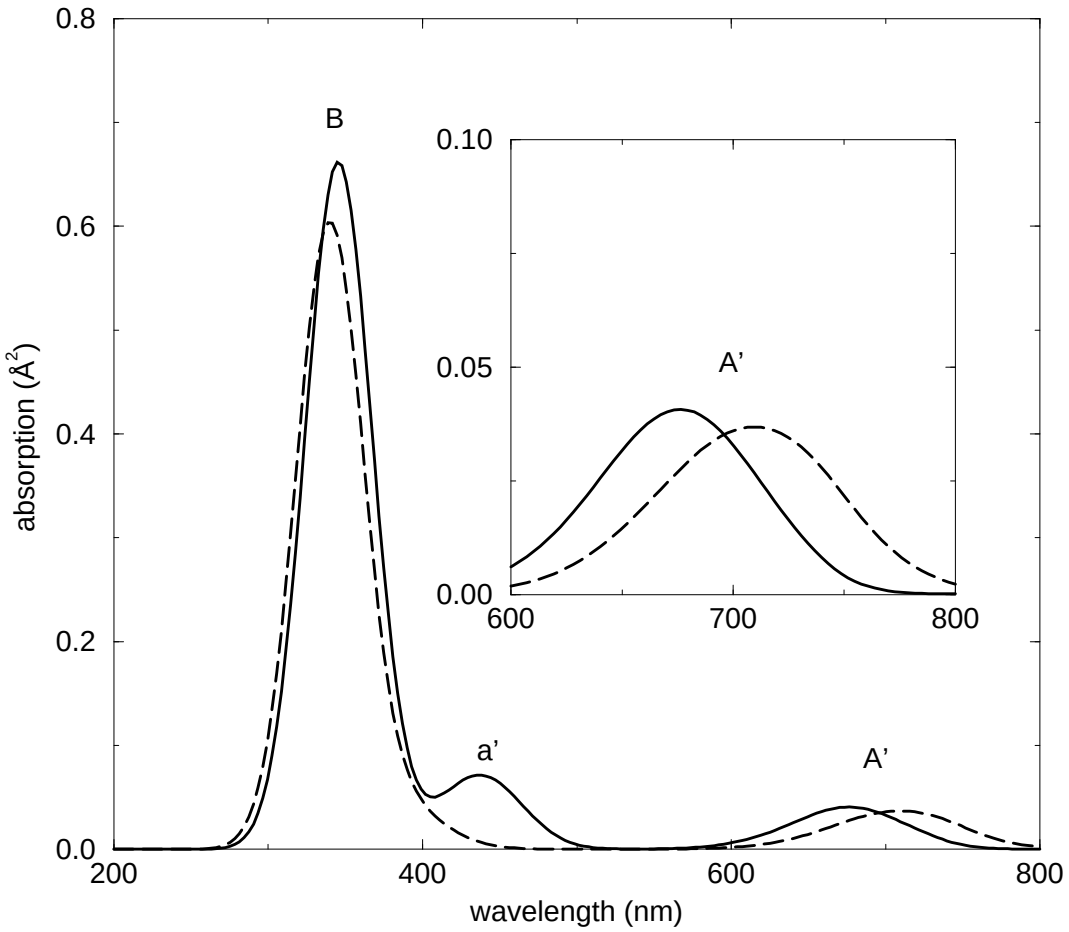

Figure 8.6: Simulated absorption spectra for ICl^- (solid line) and $ICl^-(CO_2)_4$ (dashed line) from the ground state. The absolute absorption cross section is shown as a function of the wavelength for the three parallel transitions. The perpendicular transitions are several orders of magnitude smaller in intensity.

The magnitudes of the spectral shifts, however, cannot be interpreted solely in terms of the charge transfer character of the transitions. While the charge distributions in the X and A' states are similar, the solute-solvent interactions are on average about 60 meV stronger in the A' state, which must be due to slight differences in the distributed multipole charge distribution that are not reflected by the Mulliken populations. The remainder of the 90 meV red shift observed in the simulations is due to changes in the internal solute energy, or "self energy" [8, 9], the expectation value of the isolated solute Hamiltonian ($\hat{h}_C$ in the notation of Chapter 2). The self energy always increases upon solvation because the polarized ground state wave function includes some contributions from the bare ion excited states. The self energy of the excited states may increase or decrease depending on which states are mixed in by polarization. In $ICl^-(CO_2)_4$ the self energy of the A' state is about 10 meV larger than in the bare ion, but the internal energy of the ground state increases by about 40 meV, so the self energy contributes about 30 meV to the observed red shift.

This effect is even more pronounced in the B state, where only a small blue shift is observed despite the fact that the charge distribution changes dramatically upon excitation. The B state solute-solvent interactions are about 340 meV less favorable than in the ground state because a large portion of the charge is shifted onto the I atom. At the same time, however, the internal energy of the B state drops by about 240 meV upon solvation, so the total blue shift is only about 50 meV. This interplay between the solvation energy and the self energy makes it difficult to interpret observed shifts simply in terms of charge transfer character. Detailed knowledge of the solute electronic states is required to separate the contributions from charge transfer and solute

polarization.

8.3 Photodissociation Dynamics

In order to investigate the dynamics of photodissociation in these clusters, surface hopping trajectories were run from the photoexcited state using the methods described in Chapter 4. For each cluster size studied, $n = 2$–4, 8, and 10, 20 trajectories were run from starting configurations selected from the lower temperature ensembles described above. This is a relatively small number of trajectories, so the goal of this preliminary investigation was to provide a survey of the outcomes and mechanisms rather than to make close numerical comparisons with the experimental results. The average starting temperature of the ensembles was 50–60 K, which is lower than the temperatures used to study photodissociation of $I_2^-(CO_2)_n$ clusters. This temperature was chosen because the ensembles were already available from the structural study; there is no reliable experimental estimate of the ICl^- cluster temperature. To start each trajectory, the I–Cl bond length was adjusted to match the 644 nm experimental photoexcitation energy gap. Since this excitation energy lies well within the $A' \leftarrow X$ band, the adjustment required was small, less than 0.1 Å. Trajectories were run for 50 ps or until the I–Cl bond length exceeded 60 Å. A 2 fs step size was used in the integration of the trajectories, which resulted in errors in the energy conservation of the order of 1 part in 10^3.

Table 8.4 shows the simulated photofragment distributions for each of the cluster sizes studied. Four classes of charged products were observed: I^--based fragments, Cl^--based fragments, recombined ICl^--based fragments, and solvent-separated ICl^--based fragments. Products are considered dissoci-

Table 8.4: Product distribution from simulation of $ICl^-(CO_2)_n$ photodissociation at 644 nm.

	Percentage by product channel			
n	I^--based	$(ICl^-)^*$-based	Cl^--based	$I^* \cdots Cl^-$-based
2	80	20	0	0
3	5	20	75	0
4	0	50	50	0
5	0	85	15	0
8	0	5	40	55
10	0	15	40	45

ated when the I–Cl bond length exceeds 15 Å by the end of the trajectory. Recombination was assumed if the I–Cl bond length was less than 4.2 Å and solvent separation was assumed if the I–Cl bond length exceeded 6 Å. There is thus a clear distinction between the products which are recombined and those which are solvent-separated.

Nonadiabatic relaxation to the ground electronic state of ICl^- is observed in only one of the 120 trajectories run for all the cluster sizes. The dynamics observed for the 50 ps trajectories is almost uniformly adiabatic, although a wide range of products results because the solvent strongly mixes the bare ion electronic states.

The production of I^--based fragments and Cl atoms is observed only in the two smallest cluster sizes studied. At $n = 2$ it is the dominant product channel. This product corresponds to direct dissociation on an adiabatic state with similar character to that of the bare ion A' state, where the charge localizes onto the I atom. At 50 ps all of the solvent molecules remain clustered to the I^-, but sufficient internal energy remains in the fragment to evaporate 1 or 2 monomers. This agrees with the experimental results, shown in Fig. 8.7,

where on average 1 solvent molecule is evaporated from the I^- product from $ICl^-(CO_2)_2$. As in the experiment, this channel disappears rapidly between $n = 2$ and 4.

The recombined ICl^--based fragments, which are denoted $(ICl^-)^*$ in Table 8.4, result from recombination in the approximately 200 meV well on the A' state. This channel follows the same basic trend observed in the experiment for the ICl^--based products: a small amount is observed for $n = 2$, followed by a rapid rise to a maximum around $n = 5$, and a sharp decline at larger cluster sizes out to $n = 12$, where the product disappears. The excited $(ICl^-)^*$ fragments observed in the simulations, however, have enough internal energy to evaporate at most a few monomers, even at the largest cluster sizes, while the experimental fragments exhibit a monotonic increase in the number of monomers lost in the range over which they are observed, peaking at nearly 7 for $n = 10$. It is therefore likely that the experimental ICl^- fragments eventually undergo electronic relaxation to the ground state, which releases a large amount of energy that goes into solvent evaporation. At this time there is no experimental information about the time scale on which this electronic relaxation occurs. The mechanisms by which $(ICl^-)^*$ might undergo nonadiabatic relaxation are discussed below.

In the simulations the formation of Cl^--based products is nearly always accompanied by the formation of spin-orbit excited I^*. Cl^- formation becomes the dominant dissociation channel at $n = 3$, which is one cluster size sooner than in the experiments. As in the experiments, its distribution with cluster size is bimodal, with a minimum around $n = 5$, where caging of ICl^- is strongest. At the larger cluster sizes, increased production of Cl^- is accompanied by the appearance of solvent-separated pairs, denoted $Cl^- \cdots I^*$, in

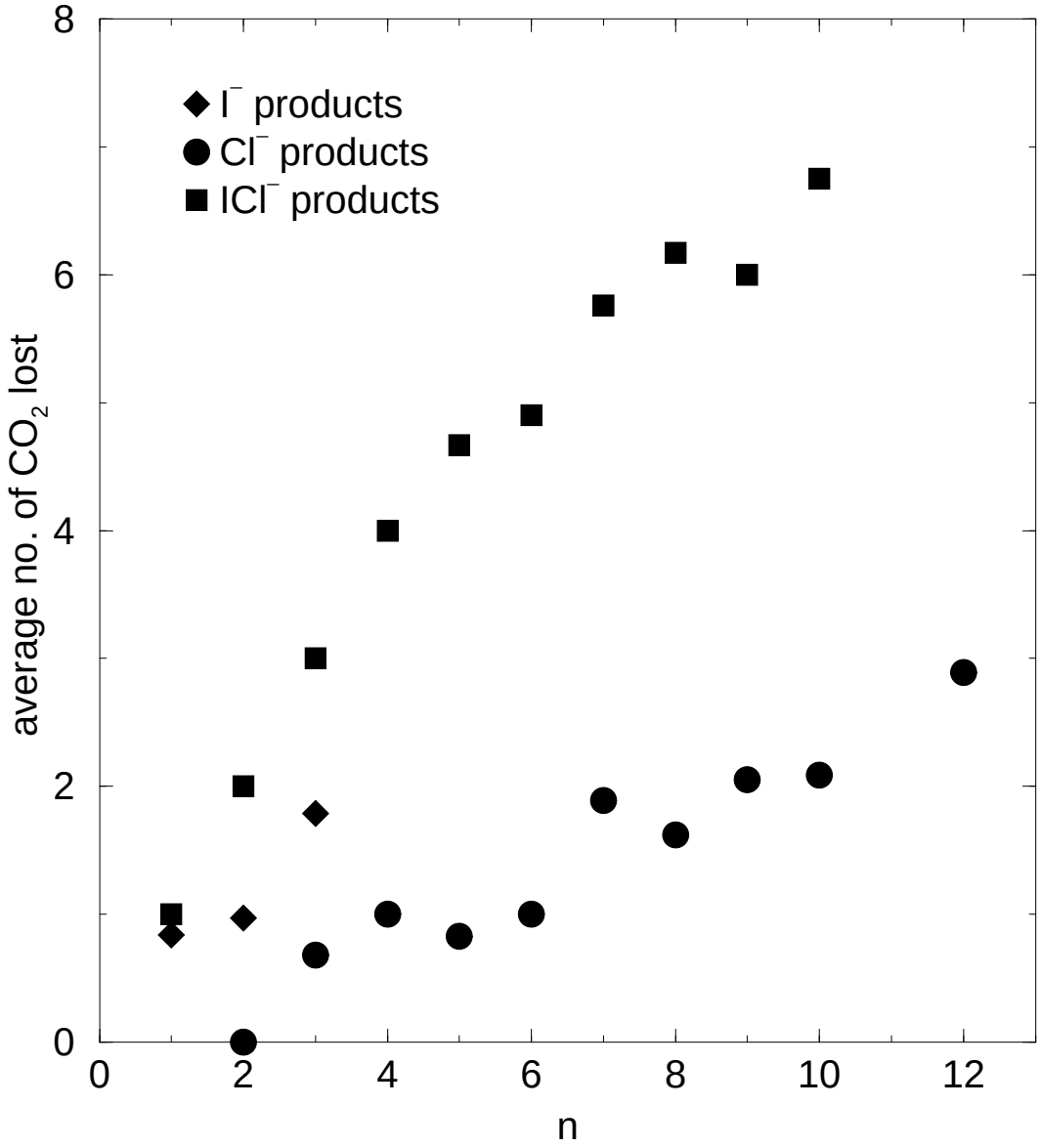

Figure 8.7: Average number of solvent molecules lost for each experimental product channel following photodissociation of $ICl^-(CO_2)_n$ at 644 nm from Ref. 2. Each channel spans a range of 2–3 solvent molecules. Experimental products are detected at 5-10 μs after photoexcitation.

which CO_2 molecules strongly solvate the Cl^- ion while the I^* remains loosely bound to the outside of the cluster. At $n = 8$ and 10, where these solvent-separated pairs are observed, direct dissociation never takes place. Following initial caging of ICl^- by the solvent, Cl^- is formed when the solvent molecules pinch between the I and Cl, localizing the charge on Cl and forming I^*. Dissociation then occurs by evaporation of the I^* from the outside of the solvated Cl^- fragment. The solvent-separated $Cl^- \cdots I^*$ fragments are thus likely to yield Cl^--based fragments but have not yet done so by 50 ps, when the trajectories are stopped.

The small number of monomers lost from the Cl^--based fragments at all the cluster sizes at which they are observed agrees well with the experimental results shown in Fig. 8.7. For $n = 4$ all of the Cl^--based fragments produced at 50 ps are solvated by four monomers, but sufficient internal energy remains in all of the fragments to evaporate an additional solvent molecule. This determination is made by comparing the total internal energy of the fragment (subtracting the center-of-mass kinetic energy) with the binding energies shown in Tables 8.5 and 8.6, which are included here for reference.

Analysis of the preliminary results suggests a new mechanism for product formation in $ICl^-(CO_2)_n$ photodissociation and provides explanations of several unusual trends in the size dependence of the photofragments..

8.3.1 High caging efficiency

The asymmetric solvent structure around ICl^- is expected to strongly enhance caging at the smaller cluster sizes. Because the ICl^--based fragments produced in the simulations are in an excited state, it is not clear what effect the large amount of energy released by electronic relaxation will have on the

Table 8.5: Properties of lowest energy $Cl^-(CO_2)_n$ clusters.

n	Potential Energy (meV)	Seq. Binding Energy (meV)	Avg. Binding Energy (meV)
1	−350	−350	−350
2	−709	−359	−355
3	−1083	−374	−361
4	−1440	−357	−360
5	−1792	−352	−358
6	−2134	−342	−356
7	−2476	−342	−354
8*	−2825	−349	−353
9	−2994	−169	−333

* First solvation shell complete.

Table 8.6: Properties of lowest energy $I^-(CO_2)_n$ clusters.

n	Potential Energy (meV)	Seq. Binding Energy (meV)	Avg. Binding Energy (meV)
1	−214	−214	−214
2	−463	−249	−232
3	−740	−277	−247
4	−1000	−260	−250
5	−1257	−257	−251
6	−1524	−267	−254
7	−1786	−262	−255
8	−2067	−281	−258
9	−2324	−257	−258
10	−2618	−294	−262
11	−2872	−254	−261
12*	−3179	−307	−265

* First solvation shell complete.

observed caging efficiencies. Nevertheless, caging in the excited state is probably the precursor to the formation of caged ground state products, and several basic mechanisms for this caging can be identified.

At the smallest cluster sizes, $n = 2$ and 3, the small amount of caging results primarily from strong long-range interactions with the solvent and between the solute atoms. Structural caging, where a solvent molecule physically blocks the dissociation of the solute atoms, is not observed in these cluster sizes. The solvent molecules initially occupy sites around the Cl end of the molecule, but off the I–Cl bond axis. As the solute dissociates, charge localizes onto the I atom, and the solvent molecules that are initially near the Cl atom are pulled back towards the nascent ion. Usually, the Cl atom escapes, but on occasion it is recaptured by a nearby CO_2 molecule that is being pulled toward I^-, as shown in Fig. 8.8. Although this is not a dominant mechanism for product formation at any cluster size, this long range recombination, where the solvent molecules act as a rope that pulls the dissociating molecule back together, is occasionally observed in larger clusters as well.

Structural caging is the dominant caging mechanism for $n \geq 4$. The presence of a capping molecule in $ICl^-(CO_2)_n$ clusters is the critical factor in determining whether a particular trajectory initially dissociates or recombines. (Trajectories that initially recombine may later dissociate for other reasons discussed below.) To measure the correlation between capping and caging, we characterized all of the initial configurations for the $n = 4$ trajectories as capped or uncapped by visual inspection of the structure. 8 structures were initially capped and 12 uncapped. As shown in Fig. 8.9, the capped trajectories reach a maximum initial bond length of under 4 Å in the first 200 fs after photoexcitation, while in the same period the uncapped trajectories reach about

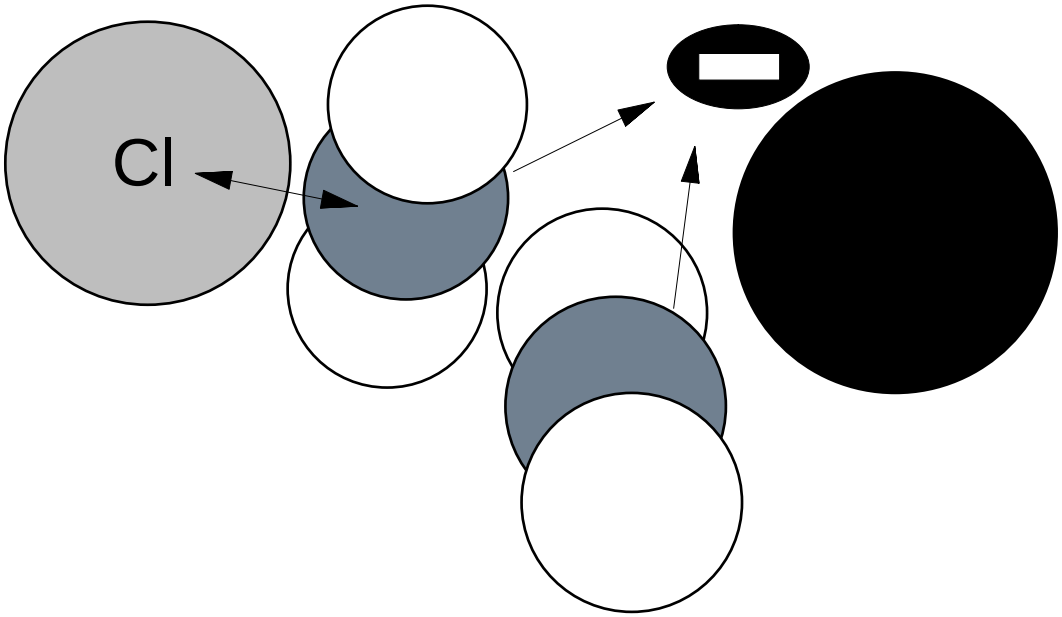

Figure 8.8: Long-range recombination mechanism in $ICl^-(CO_2)_2$. The CO_2 molecules are attracted to the charge that has localized in the I atom. One of the CO_2's is also near the departing Cl atom and pulls it back toward I^-.

5.4 Å. Of the 12 initially uncapped structures 9 dissociate directly producing Cl^- and I^*, while the remaining three eventually recombine by the long-range solvent mechanism described above. Of the 8 initially capped structures, only one dissociates, apparently the result of the solvent separation mechanism discussed below. For $n = 5$, 18 of 20 initial configurations are capped, and all but one of these results in caged $(ICl^-)^*$ fragments at 50 ps. In larger clusters, all of the configurations are capped, and direct dissociation is never observed. The onset of capping at $n = 4$ thus explains the rapid increase in caging that is observed at $n = 4$ and 5.

There are two primary reasons that capping is so effective at caging the dissociating ICl^-. The first is that the match between the Cl and CO_2 masses provides efficient energy transfer during the head-on collisions that occur when a CO_2 occupies the cap position. As we have noted, the Cl atom

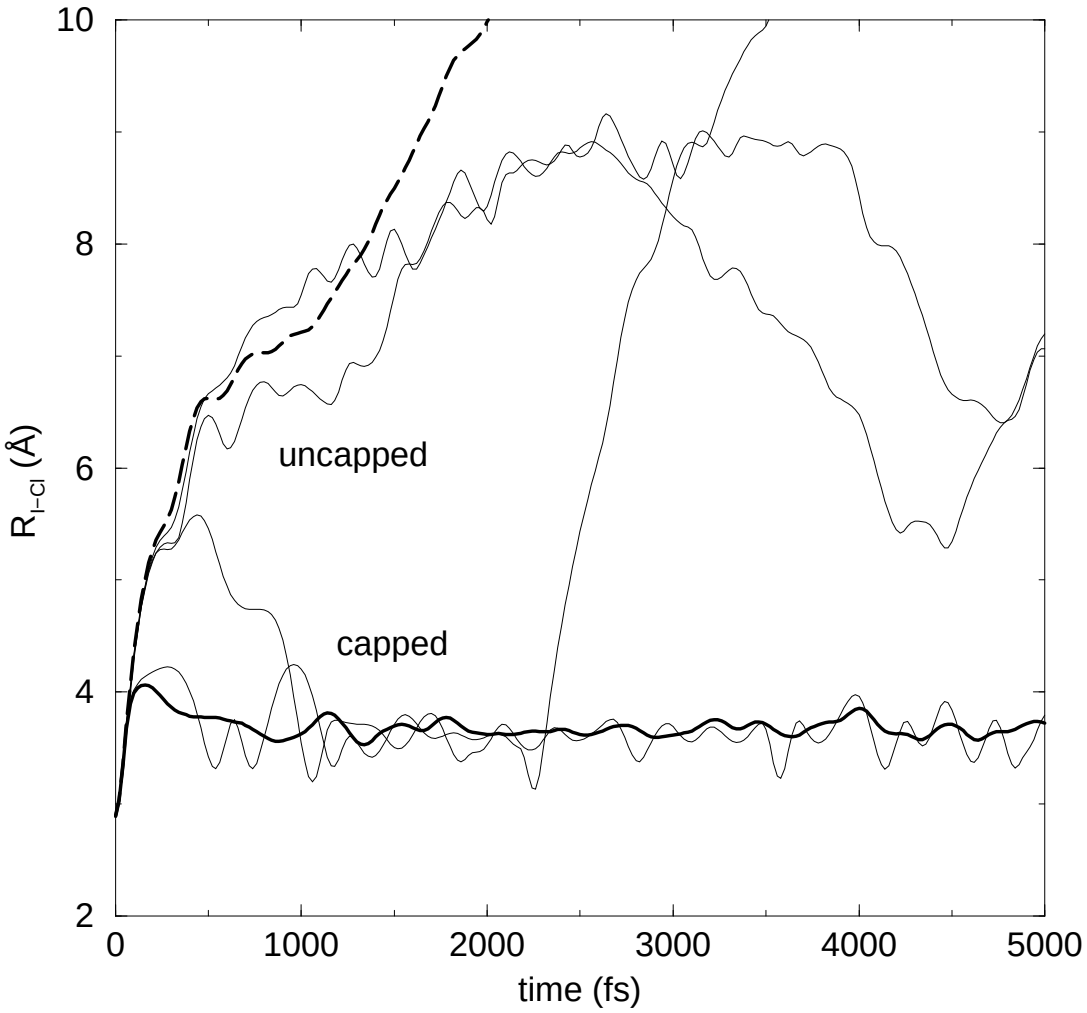

Figure 8.9: I–Cl bond length versus time for simulated photodissociation of $ICl^-(CO_2)_4$. The thick solid line shows the average over all 8 trajectories starting from capped configurations, while the thick dashed line shows the average for the 12 uncapped trajectories. The thin lines show the 3 trajectories where the initially uncapped configurations produced recombined products and the single trajectory where an intially caged configuration dissociated.

gets 75% of the initial kinetic energy released by photoexcitation. But what stops the I atom? The collision with the cap atom occurs at a very short I–Cl bond length, about 3.5 Å, before the I–Cl bond is broken and before charge has localized onto the Cl atom—as it always does for $n \geq 4$. The second reason capping is so effective, then, is that after the collision with the cap molecule stops the Cl atom, there a strong restoring force pulling the partially charged I atom back towards the cluster, and direct dissociation cannot occur.

8.3.2 Production of $Cl^- + I^*$

A surprising result of the simulations is that Cl^--based fragments are always accompanied by production of I^*. Thus Cl^--based products are formed adiabatically, rather than by solvent-induced electronic relaxation as suggested previously [1, 2]. $Cl^- + I^*$ becomes energetically accessible at a small cluster size ($n = 3$ in the simulation) because of the large difference in the solvation energy of I^- and Cl^- (see Tables 8.5 and 8.6). For clusters larger than about $n = 4$, the I^- fragment channel becomes closed, so that only Cl^--based products can be formed by dissociation.

The preference for Cl^- production at $n = 4$, however, is a result of the initial solvent configuration rather than the energetics. At $n = 4$ I^- fragments are lower in energy than the observed Cl^- fragments, but because the initial solvent configuration so heavily favors the Cl end, the charge localizes in the dissociative trajectories very rapidly onto the Cl atom, as shown in Fig. 8.10. Even in the trajectories that recombine, the excited state charge distribution and the solvent configuration continue to favor the Cl end. As discussed below, this is a primary reason that nonadiabatic relaxation to the ground electronic state is not observed in the caged trajectories.

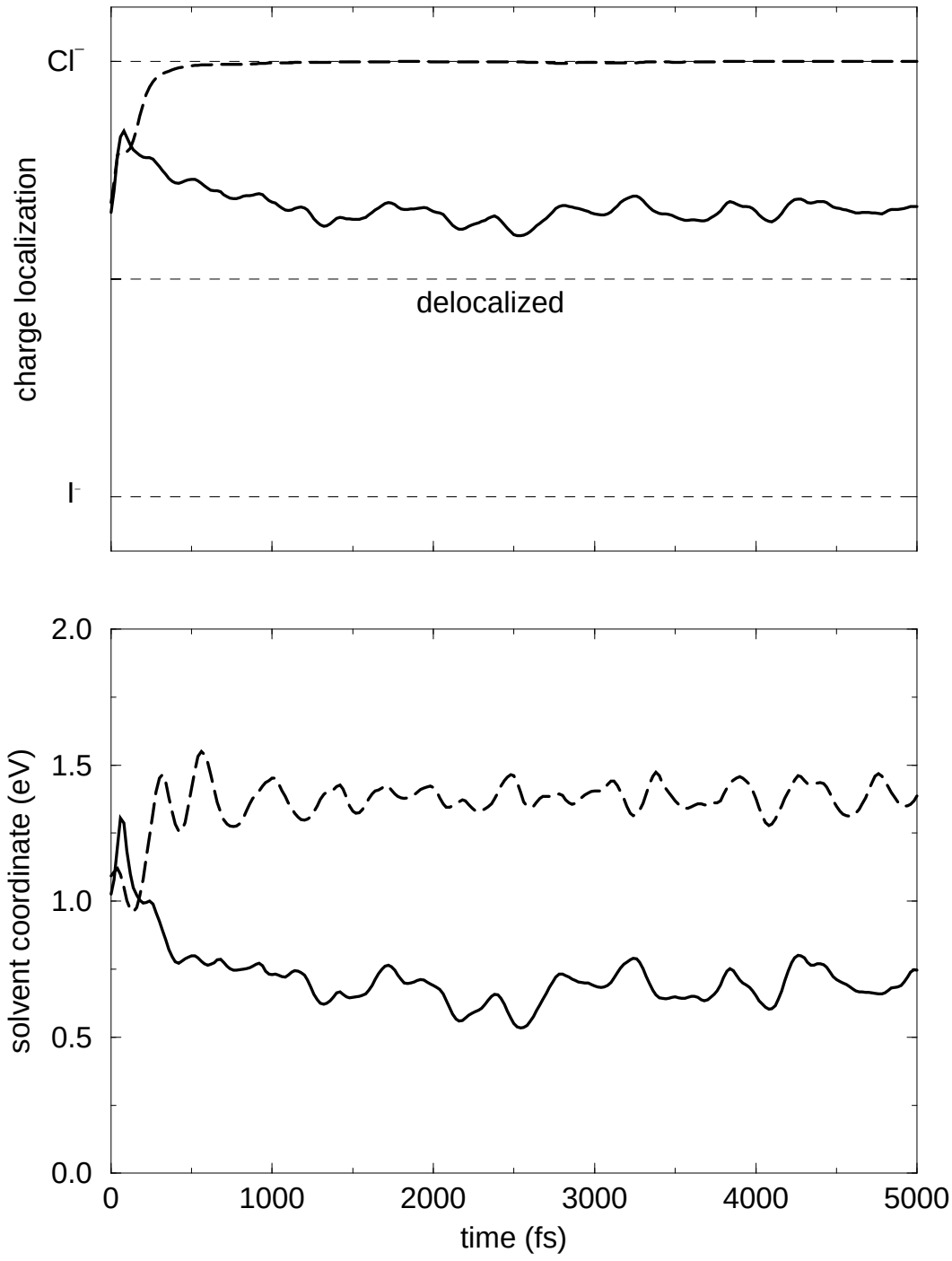

Figure 8.10: Charge localization and solvent coordinate versus time for simulated photodissociation of $ICl^-(CO_2)_4$. The solid line shows averages for the caged trajectories the dashed line shows averages for the 12 uncapped trajectories. Both the charge distribution and the solvent configuration favor the Cl atom.

Nadal et al. [1, 2] have suggested that both the ICl^- and the Cl^- products seen in the experiments are formed following nonadiabatic relaxation to the ground electronic state. As noted above, the large number of monomers lost from the ICl^--based products implies that caged ICl^- relaxes to the ground electronic state by the time the products are detected at several μs after photoexcitation. The number of monomers lost from the Cl^--based fragments is much smaller than the number lost from the ICl^--based fragments, and this difference grows with increasing cluster size. The simulations show that production of the experimentally observed Cl^--based products is energetically allowed when I^* is also produced. To produce the same Cl^- fragments with ground state I atom would require dissipation of a minimum of 700 meV additional energy. At $n = 4$, for example, there are two fragments, one CO_2 and I, available to carry away the excess energy to produce $Cl^-(CO_2)_3$. If Cl^--based products resulted from nonadiabatic relaxation to the ground state, fragments with 2 or 3 additional monomers evaporated would be energetically accessible, but are not observed. It is therefore probable for energetic reasons alone that the Cl^--based product channel involves production of I^* *at all cluster sizes*. Thus, while the caged fragments result from a nonadiabatic process (albeit on an as yet undetermined time scale), the Cl^--based fragments are produced by a purely adiabatic mechanism.

8.3.3 Solvent-induced dissociation

A major finding of this preliminary study is that Cl^--based fragments and I^* can be formed by solvent-induced dissociation of initially caged molecules. This mechanism is observed in isolated cases for $n = 4$ and 5, but dominates the $n = 8$ and 10 trajectories. Once a layer of solvent pushes be-

tween Cl^- and I^*, there is little to hold the I^* to the outside of the cluster—the binding energy with a CO_2 is only about 30 meV. The rate at which solvent-induced dissociation occurs appears to to increase rapidly with cluster size, which may explain why Cl^- formation becomes the dominant channel in the larger clusters. If the rate of nonadiabatic relaxation to the ground state from caged ICl^- in the excited state remains constant or decreases, the probability of solvent-induced dissociation will increase.

8.3.4 Why is nonadiabatic relaxation of $(ICl^-)^*$ not observed in the simulations?

A problematic aspect of the current simulation results is that electronic relaxation of caged $(ICl^-)^*$ is not observed. It is therefore difficult to determine whether a particular trajectory that is caged in the excited state will dissociate adiabatically to form Cl^--based products or relax nonadiabatically to produce ground state ICl^-. Nonadiabatic relaxation takes place only when the excited state comes into resonance with a lower-lying state. Coupling events are occasionally observed on caged trajectories when the solvent reorganizes to favor the I end of the solute. In this solvent configuration, the charge localizes on the I atom, which lowers the energy of the excited state. The two lower lying states, in which the charge favors the Cl atom increase in energy, so that with a large enough solvent asymmetry, they come into resonance with the excited state. The resonance events in the simulations, however, are too short-lived to produce substantial transition probabilities. Also as the cluster size increases, the likelihood of the solvent rearranging to favor the I atom seems to diminish. It is possible that the simulation results are correct, and the rate of nonadiabatic relaxation is just too small to be observed in a 50 ps

simulation. It is also possible, however, that the transition rate is suppressed by one of several factors that should be investigated.

The first is the depth and geometry of the excited state potential well. The caged trajectories rarely make excursions exceeding 4.5 Å in the I–Cl separation, largely because R_e on the scaled potential is 3.7 Å. For the unscaled potential the well depth was 30% smaller and R_e was 4.4 Å. Since the scaling method is arbitrary, this difference reflects the uncertainty in the excited state potential. The bond length and well depth may have a significant effect on the nonadiabatic transition rate because the resonances needed for transitions to occur are easier to produce at larger separations, where the bonding interactions are smaller.

The treatment of the solvent molecules as rigid may also suppress nonadiabatic transitions if coupling to solvent vibrations is an important mechanism for nonadiabatic coupling, as has been observed in other systems. [10]. Both the bend and asymmetric stretch in CO_2 carry strong transition dipole moments and might serve as accepting modes for electronic-vibrational energy transfer.

Finally, the model overestimates the electron affinity difference between I and Cl, which shifts the A' state asymptote up by about 50 meV (see Chapter 3), making it more difficult for the solvent to couple the state with the ones below it. While this is small in energetic terms, reducing the energy gap by 50 meV at certain points along a trajectory could have a large effect on nonadiabatic coupling rates.

8.3.5 Marcus picture of the charge flow and solvation dynamics

Nadal et al. [1, 2] have proposed a simple electron transfer mechanism to explain how ICl^- returns to the ground electronic state in clusters. This mechanism is essentially the same as the one used to explain nonadiabatic relaxation in I_2^- in Chapter 7, but applied to an asymmetric solute molecule. In this picture, photoexcitation causes the charge to localize onto the I atom as the molecule dissociates. This charge localization drives the solvent to rearrange to favor the I end of the molecule. The solvent reorganization lowers the energy of the excited state at the expense of the ground state, which increases in energy. At some time late in the reorganization process, when the solvent substantially favors the I end, the ground and excited states come into resonance, and an electron transfer between I and Cl can occur. The states come into resonance only when the solvent favors the I end instead of at the point of equal solvation, as was the case for I_2^-, because of the difference in the energy of solvating the two ends of the molecule.

As we have seen, however, asymmetric solvation polarizes the charge distribution of the excited state in favor of the Cl end of the anion. At the smallest cluster sizes, the charge can still localize onto the I atom immediately after photoexcitation, which usually produces dissociated I^--based fragments. For clusters as small as $n = 3$, however, the excited state charge distribution begins to favor the Cl atom, primarily because of mixing with the bare ion B state, which dissociates to form $Cl^- + I^*$. Cl^--based products are now formed by direct dissociation because the charge localizes on the Cl atom before the solvent can rearrange to favor the I end. As shown in Fig. 8.12, the polarization of ICl^- in the excited state produces a potential energy well for solvent con-

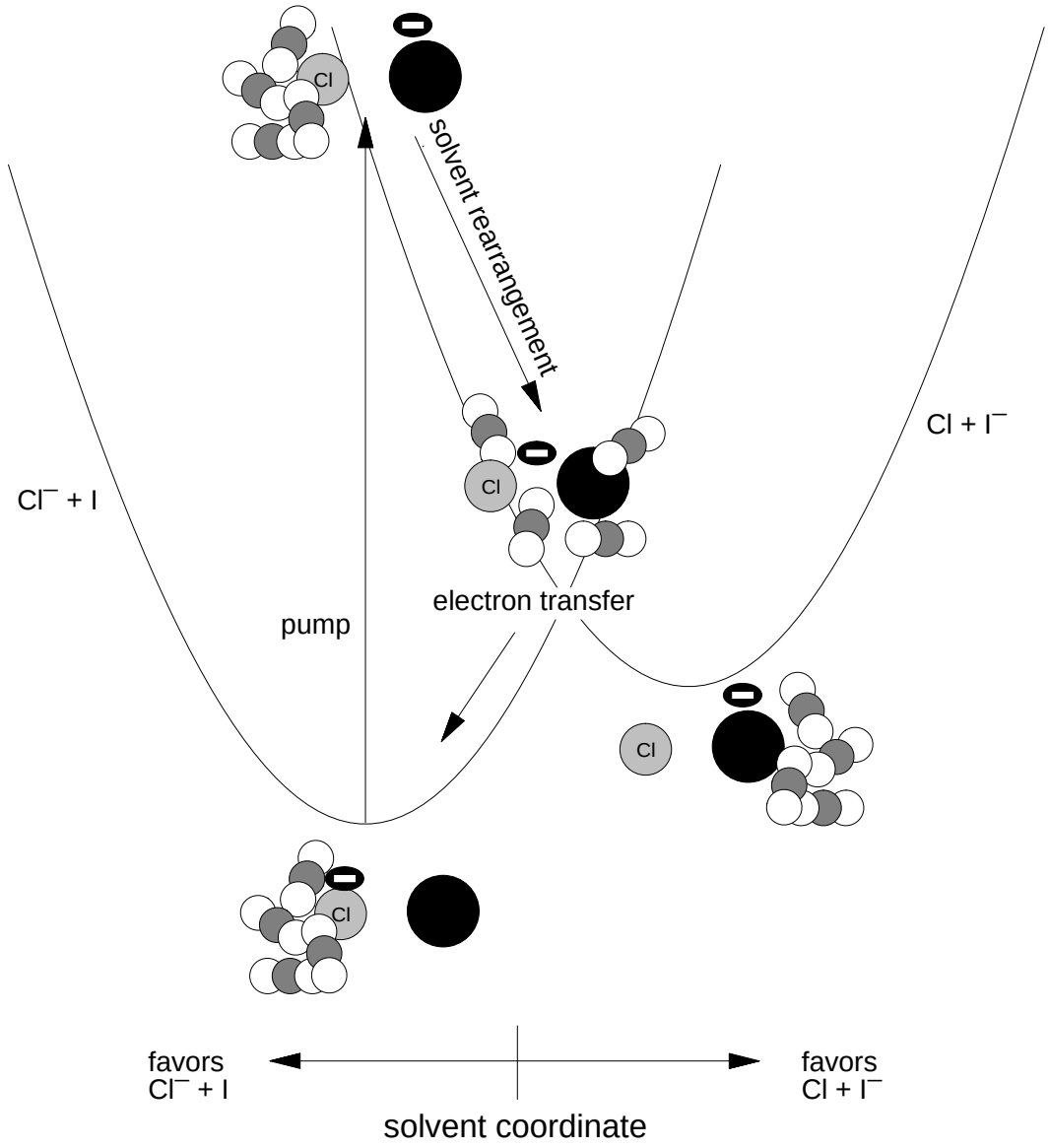

Figure 8.11: Mechanism proposed in Ref. 1 for nonadiabatic relaxation in ICl^- clusters via electron transfer.

figurations favoring the Cl end. The crossing of the $Cl^- + I^*$ and the $Cl + I^-$ curves creates a barrier to adiabatic solvent arrangement in the photoexcited state. Because the solvation energy is greater for the Cl end of the solute than the I end, the energy of the well on the Cl side decreases relative to the well on the I side as cluster size increases. Thus, the barrier to solvent rearrangement may be expected to increase with cluster size.

Figure 8.10 showed that for $n = 4$ the charge distribution in the caged trajectories favors the Cl end of the molecule. This suggests that there is a real barrier to solvent rearrangement about the I end of the solute in the excited state. In the majority of caged trajectories for $n = 4$, the solvent coordinate remains positive throughout the trajectory. Solvent rearrangement to favor I does occur in some trajectories, suggesting that there is sufficient energy to overcome the barrier. The frequency of solvent rearrangement appears to decrease with cluster size which suggests that the barrier to rearrangement increases. In the trajectories where rearrangement is observed, solvation favoring the I atom persists for many picoseconds, making it likely that the solvated I minimum is reached. No crossing with the ground state is observed during the solvent rearrangement, however, which presents the intriguing possibility that the crossing with the ground electronic state occurs in the "Marcus inverted" regime, as shown in Fig. 8.12. Further study is clearly required to support this interpretation.

The barrier to solvent rearrangement in the excited state provides a possible explanation for the disappearance of electronically relaxed ICl^- products in the photofragment distributions at large cluster sizes. We have already seen that the rate of solvent-induced dissociation increases with cluster size, while the barrier to rearrangement seems to slow down the rate of electronic

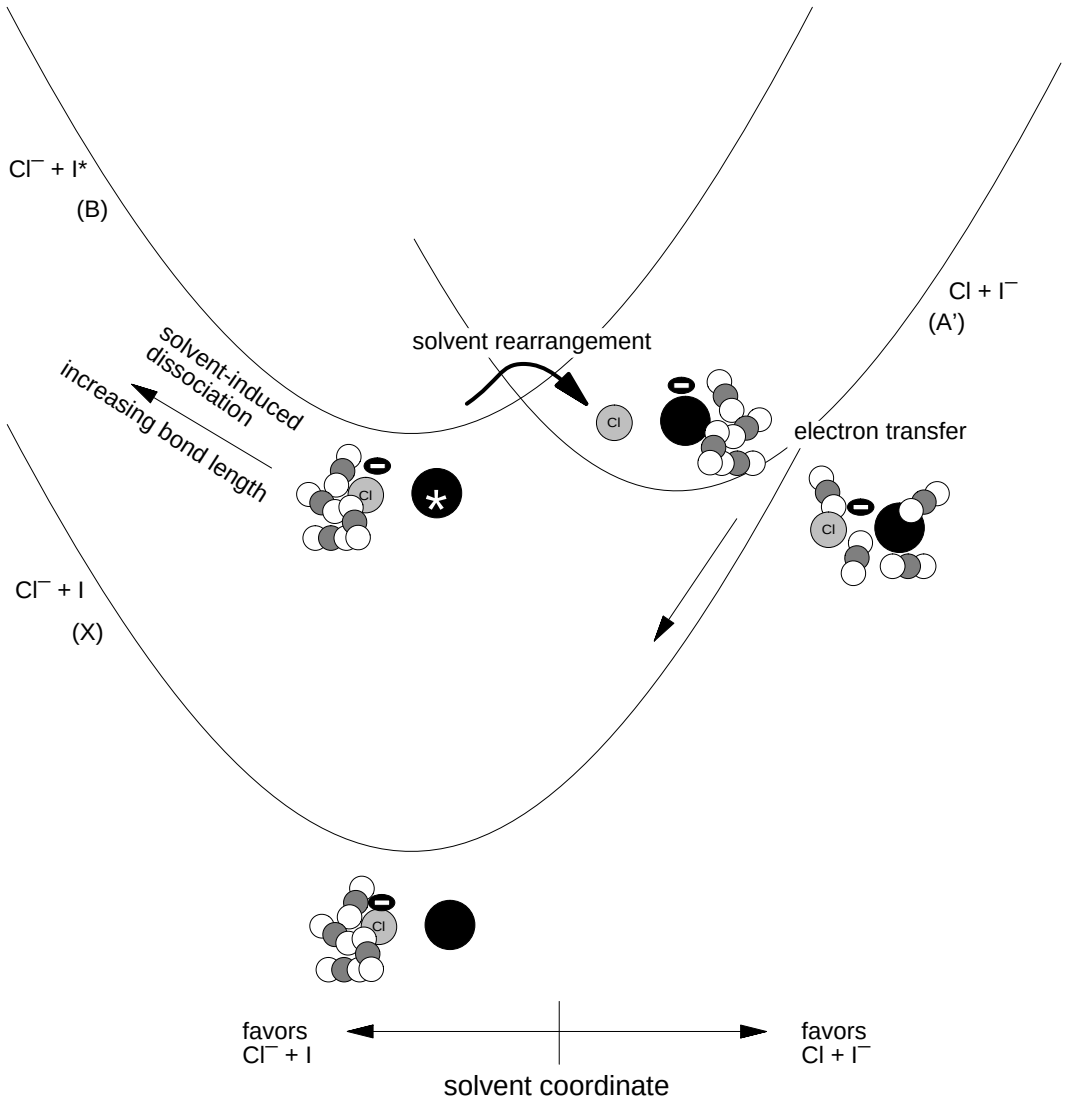

Figure 8.12: Revised mechanism for photodissociation dynamics in ICl^- clusters involving the B state.

relaxation to the ground state. Therefore, as cluster size increases, solvent-induced dissociation becomes the dominant mechanism for product formation. Until nonadiabatic relaxation is directly observed in the simulations, this picture will remain speculative. This explanation is, however, consistent with all of the known facts.

8.4 Conclusions

At the beginning of this chapter, questions were posed about the two unusual features of photodissociation in $ICl^-(CO_2)_n$ clusters: the onset of caging at relatively small cluster sizes, and the disappearance of caging at large cluster sizes.

We have found that caging depends largely on a solvent molecule occupying the cap site on the Cl end of the molecule prior to photoexcitation. The CO_2 molecules strongly prefer to solvate the Cl end of the anion because they can get nearer to the excess charge. As a result, capped configurations dominate the cluster structures starting at about $n = 4$, where caging makes a large jump in both the experiments and the simulations. Caging via long range attractions where the solvent essentially serves as a rope between the dissociating solute atoms is less frequently observed, but does result in some caging at event the smallest cluster size studied, $n = 2$.

A perhaps more important finding is that all of the Cl^--based products in the simulation are accompanied by the formation of spin-orbit excited I^*. Analysis of the fragment internal energies supports the contention that I^* is also formed in the experiments. The production of Cl^--based fragments in ICl^- photodissociation occurs adiabatically and does not indicate electronic

relaxation.

The caged fragments in the simulations do not undergo electronic relaxation to the ground state within the 50 ps spanned by the simulations. Further study is required to determine whether the relaxation is intrinsically long or whether some deficiency in the model is responsible. A time-resolved experimental study of the photodissociation would obviously be of great interest.

At the largest cluster sizes studied, $n = 8$ and 10, solvent-induced dissociation of solute molecules that initially recombine in the excited state becomes the primary mechanism of product formation. Solvent separation in the excited state adiabatically produces Cl^- and I^*, which evaporates relatively quickly from the cluster because of its weak interactions with the solvent molecules.

A simple picture of the charge flow and solvent dynamics based on the Marcus theory of electron transfer [11, 12] illustrates that for all but the smallest cluster sizes there is a barrier to solvent reorganization in the excited state that impedes electronic relaxation of the caged fragments. This barrier appears to increase with cluster size and may, along with the observation of facile solvent-induced dissociation, explain the observation of only uncaged Cl^- fragments for $n > 10$.

References for Chapter 8

[1] M. E. Nadal, P. D. Kleiber, and W. C. Lineberger, J. Chem. Phys. **105**, 504 (1996).

[2] M. Nadal, *The Study of the Photodissociation and Recombination Dynamics of Mass-Selected Cluster Ions: Solvent Effects on the Structure and Dynamics of the Ionic Chromophore*, PhD thesis, University of Colorado, 1996.

[3] J. Papanikolas, J. Gord, N. Levinger, D. Ray, V. Vorsa, and W. Lineberger, J. Phys. Chem. **95**, 8028 (1991).

[4] L. Perera and F. G. Amar, J. Chem. Phys. **90**, 7354 (1989).

[5] R. Compton, P. Reinhardt, and C. Cooper, J. Chem. Phys. **63**, 3821 (1975).

[6] M. DeLuca, B. Niu, and M. Johnson, J. Chem. Phys. **88**, 5857 (1988).

[7] E. J. Heller, J. Chem. Phys. **68**, 2066 (1978).

[8] J. M. Papanikolas, P. E. Maslen, and R. Parson, J. Chem. Phys. **102**, 2452 (1995).

[9] J. M. Papanikolas, *I_2^- Photodissociation and cage recombination dynamics in size-selected $I_2^-(CO_2)_n$ clusters*, PhD thesis, University of Colorado, 1994.

[10] O. V. Prezhdo and P. J. Rossky, J. Phys. Chem. **100**, 17094 (1996).

[11] R. A. Marcus, Ann. Rev. Phys. Chem. **15**, 155 (1964).

[12] M. D. Newton and N. Sutin, Ann. Rev. Phys. Chem. **35**, 437 (1984).

Bibliography

[1] M. Alexander, N. Levinger, M. Johnson, D. Ray, and W. Lineberger, Recombination of Br_2^- photodissociated within mass selected ionic clusters, *J. Chem. Phys.* **88**, 6200, (1988).

[2] M. L. Alexander, M. A. Johnson, N. E. Levinger, and W. C. Lineberger, *Phys. Rev. Lett.* **57**, 976, (1986).

[3] J. Alfano, Y. Kimura, P. Walhout, and P. Barbara, Photodissociation and vibrational relaxation of I_2^- in water, ethanol, and ethanol-d_1, *Chem. Phys.* **175**, 147, (1993).

[4] M. P. Allen and D. J. Tildesley, *Computer Simulation of Liquids*, Claredon Press, Oxford, 1987.

[5] F. G. Amar and L. Perera, Energetics and structure in $I_2^-(CO_2)_n$ clusters, *Z. Phys. D* **20**, 173, (1991).

[6] H. C. Andersen, Rattle: A "velocity" version of the Shake algorithm for molecular dynamics calculations, *J. Comput. Phys.* **52**, 24, (1982).

[7] D. R. T. Appadoo, R. J. Le Roy, P. F. Bernath, S. Gerstenkorn, P. Luc, J. Vergès, J. Sinzelle, J. Chevillard, and Y. D'Aignaux, Comprehensive analysis of the A–X spectrum of I_2: An application of near-dissociation theory, *J. Chem. Phys.* **104**, 903, (1996), and references therein.

[8] D. W. Arnold, S. E. Bradforth, E. H. Kim, and D. M. Neumark, Study of halogen-carbon dioxide clusters and the fluoroformyloxyl radical by photodetachment of $X^-(CO_2)$ (X=I, Cl, Br) and FCO_2^-, *J. Chem. Phys.* **102**, 3493, (1995).

[9] P. W. Atkins, *Molecular Quantum Mechanics*, Oxford, New York, 1983.

[10] D. J. Auerbach, M. M. Hubers, A. P. M. Baede, and J. Los, *Chem. Phys.* **176**, 107, (1973).

[11] R. Azria, R. Abouaf, and D. Teillet-Billy, Negative-ion states of molecular Iodine, *J. Phys. B: At. Mol. Opt. Phys.* **21**, L213, (1988).

[12] L. Bañares and A. G. Ureña, Laser-induced crossed-beam charge transfer: energy threshold of the $Na(3^2P_{3/2}) + I_2 \rightarrow Na^+ + I_2^-$ channel, *Chem. Phys. Lett.* **176**, 178, (1991).

[13] U. Banin, A. Bartana, S. Ruhman, and R. Kosloff, Impulsive excitation of coherent vibrational motion ground surface dynamics induced by intense short pulses, *J. Chem. Phys.* **101**, 8461, (1994).

[14] U. Banin, R. Kosloff, and S. Ruhman, Vibrational relaxation of nascent diiodide ions studied by femtosecond transient resonance impulsive stimulated Raman scattering (TRISRS); experiment and simulation, *Chem. Phys.* **183**, 289, (1994).

[15] U. Banin and S. Ruhman, Ultrafast photodissociation of I_3^-. coherent photochemistry in solution, *J. Chem. Phys.* **98**, 4391, (1993).

[16] U. Banin and S. Ruhman, Ultrafast vibrational dynamics of nascent diiodide fragments studied by femtosecond transient resonance impulsive stimulated Raman scattering, *J. Chem. Phys.* **99**, 9318, (1993).

[17] U. Banin, A. Waldman, and S. Ruhman, Ultrafast photodissociation of I_3^- in solution: Direct observation of coherent product vibrations, *J. Chem. Phys.* **96**, 2416, (1992).

[18] S. Bashkin and J. O. Stoner, Jr, *Atomic Energy-Level and Grotrian Diagrams. Volume I. Hydrogen I – Phosphorous XV*, North-Holland, New York, 1978.

[19] S. Bashkin and J. O. Stoner, Jr, *Atomic Energy-Level and Grotrian Diagrams. Volume II. Sulfur I – Titanium XXII*, North-Holland, New York, 1978.

[20] V. S. Batista and D. F. Coker, Nonadiabatic molecular dynamics simulation of photodissociation and geminate recombination of I_2 liquid xenon, *J. Chem. Phys.* **105**, 4033, (1996).

[21] V. S. Batista and D. F. Coker, Nonadiabatic molecular dynamics simulation of ultrafast pump- probe experiments on I_2 in solid rare gases, *J. Chem. Phys.* **106**, 6923, (1997).

[22] V. S. Batista and D. F. Coker, Nonadiabatic molecular dynamics simulations of the photofragmentation and geminate recombination in size-selected $I_2^- Ar_n$ clusters, *J. Chem. Phys.* **106**, 7102, (1997).

[23] V. S. Batista and W. H. Miller, Semiclassical molecular dynamics simulation of ultrafast photodissociation dynamics associated with the Chappuis band of ozone, *J. Chem. Phys.* **108**, 498, (1998).

[24] I. Benjamin, U. Banin, and S. Ruhman, Ultrafast photodissociation of I_3^- in ethanol: A molecular dynamics study, *J. Chem. Phys.* **98**, 8337, (1993).

[25] I. Benjamin, P. F. Barbara, B. J. Gertner, and J. T. Hynes, Nonequilibrium free energy functions, recombination dynamics, and vibration relaxation of I_2^- in acetonitrile: Molecular dynamics of charge flow in the electronically adiabatic limit, *J. Phys. Chem.* **99**, 7557, (1995).

[26] I. Benjamin and R. M. Whitnell, Vibrational relaxation of I_2^- in water and ethanol: Molecular dynamics simulation, *Chem. Phys. Lett.* **204**, 45, (1993).

[27] R. S. Berry, Structure and dynamics of clusters: An introduction, in *The Chemical Physics of Atomic and Molecular Clusters*, edited by G. Scoles, Proceedings of the International School of Physics "Enrico Fermi", North-Holland, New York, 1990.

[28] R. Bianco and J. T. Hynes, VB resonance theory in solution. I. Multistate formulation, *J. Chem. Phys.* **102**, 7864, (1995).

[29] R. Bianco and J. T. Hynes, VB resonance theory in solution. II. I_2^- to or from $I + I^-$ in acetonitrile, *J. Chem. Phys.* **102**, 7885, (1995).

[30] R. Bianco, J. J. I. Timoneda, and J. T. Hynes, Equilibrium and nonequilibrium solvation and solute electronic structure. 4. quantum theory in a multidiabatic state formulation., *J. Phys. Chem.* **98**, 12103, (1994).

[31] E. Bittner and P. Rossky, Decoherent histories and nonadiabatic quantum molecular dynamics simulations, *J. Chem. Phys.* **107**, 8611, (1997).

[32] E. R. Bittner and P. J. Rossky, Quantum decoherence in mixed quantum-classical systems: Nonadiabatic processes, *J. Chem. Phys.* **103**, 8130, (1995).

[33] D. Booth and R. M. Noyes, *J. Amer. Chem. Soc.* **82**, 1868, (1960).

[34] G. A. Bowmaker, P. Schwerdtfeger, and L. von Szentpaly, Pseudopotential and multiple scattering X alpha calculations of nuclear quadrupole coupling constants and other properties of diatomic halogen molecules and their monoanions and monocations, *J. Mol. Struct. THEOCHEM* **53**, 87, (1989).

[35] A. A. Buchachenko and N. F. Stepanov, Ar-I_2 interactions: the models based on the diatomics- in-molecule approach, *J. Chem. Phys.* **104**, 9913, (1996).

[36] A. D. Buckingham, P. W. Fowler, and A. J. Stone, Electrostatic predictions of shapes and properties of van der Waals molecules, *Internat. Rev. Phys. Chem.* **5**, 107, (1986).

[37] M. L. Burke and W. Klemperer, The one-atom cage effect: Continuum processes in I_2Ar below the B-state dissociation limit, *J. Chem. Phys.* **98**, 1797, (1993).

[38] J. Caesar, *De bello Gallico*, Allyn and Bacon, Boston, 1897, translated by Francis W. Kelsey.

[39] E. C. M. Chen, J. G. Dojahn, and W. E. Wentworth, Characterization of homonuclear diatomic ions by semiempirical Morse potential energy curves. 2. The rare gas positive ions, *J. Phys. Chem. A* **101**, 3088, (1997).

[40] E. C. M. Chen and W. E. Wentworth, Negative ion states of the halogens, *J. Phys. Chem.* **89**, 4099, (1985).

[41] T. Chuang, G. Hoffman, and K. Eisenthal, Picosecond studies of the cage effect and collision induced predissociation of iodine in liquids, *Chem. Phys. Lett.* **25**, 201, (1974).

[42] S. Churassy, F. Martin, R. Bacis, J. Vergès, and R. W. Field, Rotation-vibration analysis of the $B\ 0_u^+$–$a\ 1_g$ and $B\ 0_u^+$–$a'\ 0_g^+$ electronic systems of I_2 by laser-induced-fluorescence Fourier-transform spectroscopy, *J. Chem. Phys.* **75**, 4863, (1981).

[43] G. Ciccotti, M. Ferrario, and J.-P. Ryckaert, Molecular dynamics of rigid systems in cartesian coordinates. A general formulation, *Mol. Phys.* **47**, 1253, (1982).

[44] G. Ciccotti and J.-P. Ryckaert, Molecular dynamics simulation of rigid molecules, *Comput. Phys. Rep.* **4**, 345, (1986).

[45] D. F. Coker, Computer simulation methods for nonadiabatic dynamics in condensed systems, in *Computer Simulation in Chemical Physics*, edited by M. P. Allen and D. J. Tildesley, pp. 315–377, Kluwer, Dordrecht, 1993.

[46] D. F. Coker and L. Xiao, Methods for molecular dynamics with nonadiabatic transitions, *J. Chem. Phys.* **102**, 496, (1995).

[47] R. Compton, P. Reinhardt, and C. Cooper, Collisional ionization of Na, K, and Cs by CO_2, COS and CS_2: Molecular electron affinities, *J. Chem. Phys.* **63**, 3821, (1975).

[48] D. Danovich, J. Hrušák, and S. Shaik, Ab initio calculations for small iodo clusters. Good performance of relativistic effective core potentials, *Chem. Phys. Lett.* **233**, 249, (1995).

[49] N. Delaney, J. Faeder, P. E. Maslen, and R. Parson, Photodissociation, recombination and electron transfer in cluster ions: A nonadiabatic molecular dynamics study of $I_2^-(CO_2)_n$, *J. Phys. Chem. A* **101**, 8147, (1997).

[50] C. J. Delbecq, W. Hayes, and P. H. Yuster, Absorption spectra of F_2^-, Cl_2^-, Br_2^-, and I_2^- in the alkali halides, *Phys. Rev.* **121**, 1043, (1961).

[51] M. DeLuca, B. Niu, and M. Johnson, Photoelectron spectroscopy of $(CO_2)_n^-$ clusters with $2 \leq n \leq 13$: Cluster size dependence of the core molecular ion, *J. Chem. Phys.* **88**, 5857, (1988).

[52] J. G. Dojahn, E. C. M. Chen, and W. E. Wentworth, Characterization of homonuclear diatomic ions by semiempirical Morse potential energy curves. 1. The halogen atoms, *J. Phys. Chem.* **100**, 9649, (1996).

[53] C. E. Dykstra, *Ab Initio calculations of the structures and properties of molecules*, Elsevier, Amsterdam, 1988.

[54] D. J. Evans, On the representation of orientation space, *Mol. Phys.* **34**, 317, (1977).

[55] J. Faeder, N. Delaney, P. Maslen, and R. Parson, Charge flow and solvent dynamics in the photodissociation of cluster ions: A nonadiabatic molecular dynamics study of $I_2^- \cdot Ar_n$, *Chem. Phys. Lett.* **270**, 196, (1997).

[56] J. Faeder and R. Parson, Ultrafast reaction dynamics in cluster ions: Simulation of the transient photoelectron spectrum of $I_2^- Ar_n$ photodissociation, *J. Chem. Phys.*, in press.

[57] J. Franck and E. Rabinowitch, *Trans. Faraday Soc.* **30**, 120, (1934).

[58] A. Gallagher, Collisional depolarization of the Rb 5p and Cs 6p, *Phys. Rev.* **157**, 68, (1967).

[59] M. E. Garcia, G. M. Pastor, and K. H. Bennemann, Delocalization of a hole in van der waals clusters: ionization potential of rare-gas and small Hg_n clusters, *Phys. Rev. B* **48**, 8388, (1993).

[60] J. N. Gehlen, D. Chandler, H. J. Kim, and J. T. Hynes, Free energies of electron transfer, *J. Phys. Chem.* **96**, 1748, (1992).

[61] B. J. Gertner, K. Ando, R. Bianco, and J. T. Hynes, Bihalide ion combination reactions in solution: Electronic structure and solvation aspects, *Chem. Phys.* **183**, 309, (1994).

[62] S. K. Ghosh and B. M. Deb, A density-functional calculation of dynamic dipole polarizabilities of noble gas atoms, *Theor. Chim. Acta* **62**, 209, (1983).

[63] H. Goldstein, *Classical Mechanics*, Addison-Wesley, Reading, MA, 2nd edition, 1980.

[64] C. G. Gray and K. E. Gubbins, *Theory of Molecular Fluids*, volume 1, Clarendon, Oxford, 1984.

[65] B. J. Greenblatt, M. T. Zanni, and D. M. Neumark, Time-resolved studies of dynamics in molecular and cluster anions, *J. Chem. Soc. Faraday Trans.*, submitted.

[66] B. J. Greenblatt, M. T. Zanni, and D. M. Neumark, Photodissociation dynamics of the I_2^- anion using femtosecond photoelectron spectroscopy, *Chem. Phys. Lett.* **258**, 523, (1996).

[67] B. J. Greenblatt, M. T. Zanni, and D. M. Neumark, Time-resolved photodissociation dynamics of $I_2^-Ar_n$ clusters using anion femtosecond photoelectron spectroscopy, *Science* **276**, 1675, (1997).

[68] L. Greengard, *The Rapid Evaluation of Potential Fields in Particle Systems*, MIT Press, Cambridge, MA, 1988.

[69] L. Greengard and V. Rokhlin, A fast algorithm for particle simulations, *J. Comput. Phys.* **73**, 325, (1987).

[70] S. Hammes-Schiffer and J. C. Tully, Proton transer in solution: Molecular dynamics with quantum transitions, *J. Chem. Phys.* **101**, 4657, (1994).

[71] A. L. Harris, J. K. Brown, and C. B. Harris, The nature of simple photodissociation reactions in liquids on ultrafast time scales, *Ann. Rev. Phys. Chem.* **39**, 341, (1988).

[72] E. J. Heller, Quantum corrections to classical photodissociation models, *J. Chem. Phys.* **68**, 2066, (1978).

[73] M. Herman, A semiclassical surface hopping propagator for nonadiabatic problems, *J. Chem. Phys.* **103**, 8081, (1995).

[74] G. Herzberg, *Molecular Spectra and Molecular Structure. I. Spectra of Diatomic Molecules*, Van Nostrand, New York, 2nd edition, 1950.

[75] W. P. Hess, *Laser photodissociation studies of I* quantum yields and dynamics*, PhD thesis, University of Colorado, 1988.

[76] C. A. Hunter, J. K. M. Sanders, and A. J. Stone, Exciton coupling in porphyrin dimers, *Chem. Phys.* **133**, 395, (1989).

[77] A. E. Johnson, N. E. Levinger, and P. F. Barbara, Photodissociation dynamics of I_2^- in water and alcohols, *J. Phys. Chem.* **96**, 7841, (1992).

[78] P. Jungwirth and R. Gerber, Quantum dynamics simulations of nonadiabatic processes in many-atom systems: Photoexcited $Ba(Ar)_{10}$ and $Ba(Ar)_{20}$ clusters, *J. Chem. Phys.* **104**, 5803, (1996).

[79] S. P. Karna, G. B. Talapatra, and P. N. Prasad, Dispersion of linear and nonlinear optical properties of benzene: An ab initio time-dependent coupled-perturbed Hartree-Fock study, *J. Chem. Phys.* **95**, 5873, (1991).

[80] H. J. Kim and J. T. Hynes, Equilibrium and nonequilibrium solvation and solute electronic structure. I. Formulation, *J. Chem. Phys.* **93**, 5194, (1990).

[81] H. J. Kim and J. T. Hynes, Equilibrium and nonequilibrium solvation and solute electronic structure. III. Quantum theory, *J. Chem. Phys.* **96**, 5088, (1992).

[82] W. Klaus, M. E. Garcia, and K. H. Bennemann, Theory for the short-time response of small Hg_n clusters after excitation, *Z. Phys. D* **35**, 43, (1995).

[83] D. A. V. Kliner, J. C. Alfano, and P. F. Barbara, Photodissociation and vibrational relaxation of I_2^- in ethanol, *J. Chem. Phys.* **98**, 5375, (1993).

[84] P. J. Knowles and H.-J. Werner, *Chem. Phys. Lett.* **115**, 259, (1985).

[85] P. J. Knowles and H.-J. Werner, An efficient method for the evaluation of coupling coefficients in configuration interaction calculations, *Chem. Phys. Lett.* **145**, 514, (1988).

[86] A. Krylov and R. Gerber, Photodissociation dynamics of HCl in solid Ar: Cage exit, nonadiabatic transitions, and recombination, *J. Chem. Phys.* **106**, 6574, (1997).

[87] A. I. Krylov, R. B. Gerber, and R. D. Coalson, Nonadiabatic dynamics and electronic energy relaxation of Cl (^2P) atoms in solid Ar, *J. Chem. Phys.* **105**, 4626, (1996).

[88] P. Kuntz, Classical path surface-hopping dynamics. I. General theory and illustrative trajectories, *J. Chem. Phys.* **95**, 141, (1991).

[89] B. M. Ladanyi and R. Parson, Structure and dynamics of molecular ions in clusters: I_2^- in flexible CO_2, *J. Chem. Phys.* **107**, 9326, (1997).

[90] F. W. Lampe and R. M. Noyes, *J. Amer. Chem. Soc.* **76**, 2140, (1954).

[91] I. Last and T. F. George, Interaction of Xe^+ and Cl^- ions and their formed molecules with a Xe solid matrix, *J. Chem. Phys.* **86**, 3787, (1987).

[92] Y. Le Coat, J.-P. Guillotin, and L. Bouby, Sharing between the Cl^- and I^- channels in the dissociative attachment processes in ICl, *J. Phys. B: At. Mol. Opt. Phys.* **24**, 3285, (1991).

[93] H. Lefebvre-Brion and R. W. Field, *Perturbations in the Spectra of Diatomic Molecules*, Academic Press, Boston, 1986.

[94] Z. Li, R. Zadoyan, V. A. Apkarian, and C. C. Martens, Femtosecond many-body dynamics of caging: Experiment and simulation of I_2 photodissociation-recombination in solid Ar, *J. Phys. Chem.* **99**, 7453, (1995).

[95] D. R. Lide, editor, *CRC Handbook of Chemistry and Physics*, Chemical Rubber, Boca Raton, 73rd edition, 1993.

[96] C. Lienau, J. Williamson, and A. Zewail, Femtochemistry at high pressures. The dynamics of an elementary reaction in the gas-liquid transition region, *Chem. Phys. Lett.* **213**, 289, (1993).

[97] C. Lienau and A. Zewail, Femtochemistry at high pressures. Solvent effect in the gas- to-liquid transition region, *Chem. Phys. Lett.* **222**, 224, (1994).

[98] Q. Liu, C. Wan, and A. Zewail, Femtosecond reaction dynamics in the gas-to-liquid transition region: Observation of a three-phase density dependence, *J. Chem. Phys.* **105**, 5294, (1996).

[99] Q. Liu, J.-K. Wang, and A. H. Zewail, Femtosecond dynmaics of dissociation and recombination in solvent cages, *Nature* **364**, 427, (1993).

[100] Q. Liu, J.-K. Wong, and A. H. Zewail, Solvation ultrafast dynamics of reactions. 10. Molecular dynamics studies of dissociation, recombination, and coherence, *J. Phys. Chem.* **99**, 11321, (1995).

[101] D. Lu, M. Zhao, and D. G. Truhlar, Projection operator method for geometry optimization with constraints, *J. Comp. Chem.* **12**, 377, (1991).

[102] G. C. Maitland, M. Rigby, E. B. Smith, and W. A. Wakeham, *Intermolecular Forces, Their Origin and Determination*, Clarendon, Oxford, 1981.

[103] R. A. Marcus, *Ann. Rev. Phys. Chem.* **15**, 155, (1964).

[104] R. A. Marcus, Schrödinger equation for a strongly coupled electron transfer system, *J. Phys. Chem.* **96**, 1753, (1992).

[105] T. Martinez, M. Ben-Nun, and G. Ashkenazi, Classical/quantal method for multistate dynamics: A computational study, *J. Chem. Phys.* **104**, 2847, (1996).

[106] T. J. Martinez, Ab initio molecular dynamics around a conical intersection: Li(2p) + H_2, *Chem. Phys. Lett.* **272**, 139, (1997).

[107] T. J. Martinez, M. Ben-Nun, and R. D. Levine, Multi-electronic-state molecular dynamics: A wave function approach with applications, *J. Phys. Chem.* **100**, 7884, (1996).

[108] T. J. Martinez and R. D. Levine, Nonadiabatic molecular dynamics: Split operator multiple spawning with applications to photodissociation, *J. Chem. Soc. Faraday Trans.* **93**, 940, (1997).

[109] P. E. Maslen, J. Faeder, and R. Parson, An effective Hamiltonian for an electronically excited solute in a polarisable molecular solvent, *Mol. Phys.*, submitted.

[110] P. E. Maslen, J. Faeder, and R. Parson, Ab initio calculations of the ground and excited states of I_2^- and ICl^-, *Chem. Phys. Lett.* **263**, 63, (1996).

[111] P. E. Maslen, J. M. Papanikolas, J. Faeder, R. Parson, and S. V. ONeil, Solvation of electronically excited I_2^-, *J. Chem. Phys.* **101**, 5731, (1994).

[112] L. F. Meadows and R. M. Noyes, *J. Amer. Chem. Soc.* **82**, 1872, (1960).

[113] H. Mei and D. Coker, Quantum molecular dynamics studies of H_2 transport in water, *J. Chem. Phys.* **104**, 4755, (1996).

[114] H. Mei, L. Xiao, and D. Coker, Calculation of the rotational Raman spectrum of H_2 in ice, *J. Chem. Phys.* **105**, 3938, (1996).

[115] T. M. Miller, Electron affinities, In Lide [95].

[116] W. Miller and T. George, Semiclassical theory of electronic transitions in low energy atomic and molecular collisions involving several nuclear degrees of freedom, *J. Chem. Phys.* **56**, 5637, (1972).

[117] MOLPRO, a package of ab initio programs by H.-J. Werner and P. J. Knowles, with contributions from J. Almlöf, R. D. Amos, M. J. O. Deegan, S. T. Elbert, C. Hampel, W. Meyer, K. Peterson, R. Pitzer, A. J. Stone, and P. R. Taylor, version 94.3 (1994).

[118] C. E. Moore, *Atomic Energy Levels*, volume 35 of *National Standards Reference Data Series*, National Bureau of Standards, 2nd edition, 1971.

[119] N. F. Mott, *Proc. Cambridge Philos. Soc.* **27**, 553, (1931).

[120] U. Müller and G. Stock, Surface-hopping modeling of photoinduced relaxation dynamics on coupled potential-energy surfaces, *J. Chem. Phys.* **107**, 6230, (1997).

[121] R. S. Mulliken, Iodine revisited, *J. Chem. Phys.* **55**, 288, (1971).

[122] C. S. Murthy, S. F. O'Shea, and I. R. McDonald, Electrostatic interactions in molecular crystals: Lattice dynamics of solid nitrogen and carbon dioxide, *Mol. Phys.* **50**, 531, (1983).

[123] M. Nadal, *The Study of the Photodissociation and Recombination Dynamics of Mass-Selected Cluster Ions: Solvent Effects on the Structure and Dynamics of the Ionic Chromophore*, PhD thesis, University of Colorado, 1996.

[124] M. E. Nadal, P. D. Kleiber, and W. C. Lineberger, Photofragmentation of mass-selected $ICl^-(CO_2)_n$ cluster ions: Solvation effects on the structure and dynamics of the ionic chromophore, *J. Chem. Phys.* **105**, 504, (1996).

[125] M. E. Nadal, S. Nandi, D. W. Boo, and W. C. Lineberger, Photodissociation and recombination dynamics of I_2^- in N_2O clusters, *J. Chem. Phys.*, submitted.

[126] S. Nandi, A. Sanov, N. Delaney, J. Faeder, R. Parson, and W. C. Lineberger, Photofragmentation and structure of $I_2^-(OCS)_n$ cluster ions, to be submitted.

[127] E. Neria and A. Nitzan, Semiclassical evaluation of nonadiabatic rates in condensed phases, *J. Chem. Phys.* **99**, 1109, (1993).

[128] E. Neria, A. Nitzan, R. N. Barnett, and U. Landman, Quantum dynamical simulations of nonadiabatic processes: Solvation dynamics of the hydrated electron, *Phys. Rev. Lett.* **67**, 1011, (1991).

[129] D. J. Nesbitt and J. T. Hynes, Slow vibrational relxation in picosecond iodine recombination in liquids, *J. Chem. Phys.* **77**, 2130, (1982).

[130] M. D. Newton and N. Sutin, Electron transfer reactions in condensed phases, *Ann. Rev. Phys. Chem.* **35**, 437, (1984).

[131] J. Papanikolas, J. Gord, N. Levinger, D. Ray, V. Vorsa, and W. Lineberger, Photodissociation and geminate recombination dynamics of I_2^- in mass-selected $I_2^-(CO_2)_n$ cluster ions, *J. Phys. Chem.* **95**, 8028, (1991).

[132] J. Papanikolas, V. Vorsa, M. Nadal, P. Campagnola, H. Buchenau, and W. Lineberger, I_2^- photodissociation and recombination dynamics in size-selected $I_2^-(CO_2)_n$ cluster ions, *J. Chem. Phys.* **99**, 8733, (1993).

[133] J. Papanikolas, V. Vorsa, M. Nadal, P. Campagnola, J. Gord, and W. Lineberger, I_2^- photofragmentation/recombination dynamics in size-selected $I_2^-(CO_2)_n$ cluster ions: Observation of coherent I...I^- vibrational motion, *J. Chem. Phys.* **97**, 7002, (1992).

[134] J. M. Papanikolas, *I_2^- Photodissociation and Cage Recombination Dynamics in Size-Selected $I_2^-(CO_2)_n$ Clusters*, PhD thesis, University of Colorado, 1994.

[135] J. M. Papanikolas, P. E. Maslen, and R. Parson, Recombination and relaxation of molecular ions in size-selected clusters: Monte Carlo and molecular dynamics simulations of $I_2^-(CO_2)_n$, *J. Chem. Phys.* **102**, 2452, (1995).

[136] W. Pauli, *General Principles of Quantum Mechanics*, pp. 86–87, Springer-Verlag, New York, 1980, translated by P. Achuthan and K. Venkatesan.

[137] P. Pechukas, Time dependent semiclassical scattering theory. II. Atomic collisions, *Phys. Rev.* **181**, 174, (1969).

[138] L. Perera and F. G. Amar, Charge localization in negative ion dynamics: Effect on caging of Br_2^- in Ar_n and $(CO_2)_n$ clusters, *J. Chem. Phys.* **90**, 7354, (1989).

[139] F. L. Pilar, *Elementary Quantum Chemistry*, McGraw-Hill, New York, 1968.

[140] P. L. A. Popelier and A. J. Stone, Formulae for the first and second derivatives of anisotropic potentials with respect to geometrical parameters, *Mol. Phys.* **82**, 411, (1994).

[141] W. H. Press, S. A. Teukolsky, W. T. Vetterling, and B. P. Flannery, *Numerical Recipes in C: The Art of Scientific Computing*, Cambridge University Press, New York, 2nd edition, 1992.

[142] R. K. Preston and J. C. Tully, Effects of surface crossing in chemical reactions: The H_3^+ system, *J. Chem. Phys.* **54**, 4297, (1971).

[143] O. Prezhdo and P. Rossky, Evaluation of quantum transition rates from quantum- classical molecular dynamics simulations, *J. Chem. Phys.* **107**, 5863, (1997).

[144] O. V. Prezhdo and P. J. Rossky, Solvent mode participation in the nonradiative relaxation of the hydrated electron, *J. Phys. Chem.* **100**, 17094, (1996).

[145] S. L. Price, A. J. Stone, and M. Alderton, Explicit formulae for the electrostatic energy, forces and torques between a pair of molecules of arbitrary symmetry, *Mol. Phys.* **52**, 987, (1984).

[146] D. C. Rappaport, *The Art of Molecular Dynamics Simulation*, Cambridge University Press, New York, 1995.

[147] D. Ray, N. Levinger, J. Papanikolas, and W. Lineberger, Time-resolved measurements of the photodissociation and recombination dynamics of I_2^- in mass selected cluster ions, *J. Chem. Phys.* **91**, 6533, (1989).

[148] E.-A. Reinsch, Calculation of dynamic polarizabilities of He, H_2, Ne, HF, H_2O, NH_3 and CH_4 with MC-SCF wave functions, *J. Chem. Phys.* **83**, 5784, (1985).

[149] P. M. Rodger, A. J. Stone, and D. J. Tildesley, Intermolecular interactions in halogens: bromine and iodine, *Chem. Phys. Lett.* **145**, 365, (1988).

[150] P. M. Rodger, A. J. Stone, and D. J. Tildesley, The intermolecular potential of chlorine. A three phase study, *Mol. Phys.* **63**, 173, (1988).

[151] O. Roncero, N. Halberstadt, and J. A. Beswick, in *Reaction Dynamics in Clusters and Condensed Phases*, edited by J. Jortner, R. D. Levine, and B. Pullman, Kluwer Academic, Dordrecht, 1994.

[152] U. Ross, T. Schulze, and H.-J. Meyer, The electron affinity of ICl from charge-transfer collisions with Ba, *Chem. Phys. Lett.* **121**, 174, (1985).

[153] J.-P. Ryckaert, G. Ciccotti, and H. J. C. Berendsen, Numerical integration of the Cartesian equations of motion of a system with constraints: Molecular dynamics of n-alkanes, *J. Comput. Phys.* **23**, 327, (1977).

[154] A. J. Sadlej, Medium-size polarized basis sets for high-level-correlated calculations of molecular electric properties. II. Second-row atoms: Si through Cl, *Theoretica Chimica Acta* **79**, 123, (1991).

[155] A. J. Sadlej, Medium-size polarized basis sets for high-level-correlated calculations of molecular electric properties. V. Fourth-row atoms: Sn through I, *Theoretica Chimica Acta* **81**, 339, (1992).

[156] K. L. Sanger, G. M. McClelland, and D. R. Herschbach, *J. Phys. Chem.* **85**, 3333, (1981).

[157] A. Sanov, S. Nandi, and W. C. Lineberger, Transient solvent dynamics and incoherent control of photodissociation pathways in I_2^- cluster ions, *J. Chem. Phys.*, in press.

[158] G. C. Schatz and M. A. Ratner, *Quantum Mechanics in Chemistry*, chapter 10, Prentice Hall, Englewood Cliffs, 1993.

[159] J. Schnitker and P. J. Rossky, An electron-water pseudopotential for condensed phase simulation, *J. Chem. Phys.* **86**, 3462, (1987).

[160] B. J. Schwartz, E. R. Bittner, O. V. Prezhdo, and P. J. Rossky, Quantum decoherence and the isotope effect in condensed phase nonadiabatic molecular dynamics simulations, *J. Chem. Phys.* **104**, 5942, (1996).

[161] S. B. Sharp and G. I. Gellene, Ab initio calculations of the ground and excited states of polyiodide atoms, *J. Phys. Chem.* **101**, 2192, (1997).

[162] T. Shida, Y. Takahashi, and H. Hatano, Electronic structures of I_2^- and I_4^- ions in γ-irradiated rigid solutions, *Chem. Phys. Lett.* **33**, 491, (1975).

[163] B. Space and D. Coker, Nonadiabatic dynamics of excited excess electrons in simple fluids, *J. Chem. Phys.* **94**, 1976, (1991).

[164] B. Space and D. Coker, Dynamics of trapping and localization of excess electrons in simple fluids, *J. Chem. Phys.* **96**, 652, (1992).

[165] A. J. Stone, Distributed multipole analysis, or how to describe a molecular charge distribution, *Chem. Phys. Lett.* **83**, 233, (1981).

[166] A. J. Stone, Distributed polarizabilities, *Mol. Phys.* **56**, 1065, (1985).

[167] A. J. Stone, The induction energy of an assembly of polarizable molecules, *Chem. Phys. Lett.* **155**, 102, (1989).

[168] A. J. Stone, *The Theory of Intermolecular Forces*, Oxford, New York, 1996.

[169] A. J. Stone and M. Alderton, Distributed multipole analysis: Methods and applications, *Mol. Phys.* **56**, 1047, (1985).

[170] A. J. Stone and R. J. A. Tough, Spherical tensor theory of long-range intermolecular forces, *Chem. Phys. Lett.* **110**, 123, (1984).

[171] X. Sun and W. Miller, Semiclassical initial value representation for electronically nonadiabatic molecular dynamics, *J. Chem. Phys.* **106**, 6346, (1997).

[172] K. T. Tang and J. P. Toennies, *J. Chem. Phys.* **80**, 3726, (1984).

[173] P. W. Tasker, G. G. Balint-Kurti, and R. N. Dixon, A calculation of the potential curves for the halogen molecule negative ions, *Mol. Phys.* **32**, 1651, (1976).

[174] C. Teichteil and M. Pelissier, Relativistic calculations of the excited states of molecular Iodine, *Chem. Phys.* **180**, 1, (1994).

[175] J. Tellinghuisen, Potentials for weakly bound states in I_2 from diffuse spectra and predissociation data, *J. Chem. Phys.* **82**, 4012, (1985).

[176] B. T. Thole, Molecular polarizabilities calculated with a modified dipole interaction, *Chem. Phys.* **59**, 341, (1981).

[177] B. T. Thole and P. T. van Duijnen, On the quantum mechanical treatment of solvent effects, *Theor. Chim. Acta* **55**, 307, (1980).

[178] D. G. Truhlar, K. Onda, R. A. Eades, and D. A. Dixon, Effective potential approach to electron-molecule scattering theory, *Int. J. Quantum Chem. Symposium* **13**, 601, (1979).

[179] J. C. Tully, Diatomics-in-molecules potential energy surfaces. II. Nonadiabatic and spin-orbit interactions, *J. Chem. Phys.* **59**, 5122, (1973).

[180] J. C. Tully, Nonadiabatic processes in molecular collisions, in *Dynamics of Molecular Collisions*, edited by W. H. Miller, volume Part B, Plenum, New York, 1976.

[181] J. C. Tully, Molecular dynamics with electronic transitions, *J. Chem. Phys.* **93**, 1061, (1990).

[182] J. C. Tully, Nonadiabatic molecular dynamics, *Int. J. Quantum Chem. Quantum Chem. Symposium* **25**, 299, (1991).

[183] J. C. Tully and R. K. Preston, Trajectory surface hopping approach to nonadiabatic molecular collisions: The reaction of H^+ with D_2, *J. Chem. Phys.* **55**, 562, (1971).

[184] J. Valentini and J. Cross, The photodissociation cage effect in van der Waals complexes: Fluorescence spectra of I_2 $B(\,^3\pi_{0_u^+})$ from the hindered photodissociation of I_2Ar at 488 nm, *J. Chem. Phys.* **77**, 572, (1982).

[185] W. F. van Gunsteren and H. J. C. Berendsen, Algorithms for macromolecular dynamics and constraint dynamics, *Mol. Phys.* **34**, 1311, (1977).

[186] L. Verlet, Computer "experiments" on classical fluids. I. Thermodynamical properties of Lennard-Jones molecules, *Phys. Rev.* **159**, 98, (1967).

[187] K. S. Viswanathan and J. Tellinghuisen, The 2880-å emission spectrum of I_2: Ion-pair states near 47000 cm^{-1}, *J. Mol. Spec.* **101**, 285, (1983).

[188] V. Vorsa, *Photodissociation Dynamics of Mass-Selected Anions and Anionic Clusters*, PhD thesis, University of Colorado, 1996.

[189] V. Vorsa, P. J. Campagnola, S. Nandi, M. Larsson, and W. C. Lineberger, Photofragmentation of $I_2^- \cdot Ar_n$ clusters: Observation of metastable isomeric ionic fragments, *J. Chem. Phys.* **105**, 2298, (1996).

[190] V. Vorsa, S. Nandi, P. J. Campagnola, M. Larsson, and W. C. Lineberger, Recombination dynamics of photodissociated I_2^- in size selected Ar and CO_2 clusters, *J. Chem. Phys.* **106**, 1402, (1997).

[191] P. K. Walhout, J. C. Alfano, K. A. M. Thakur, and P. F. Barbara, Ultrafast experiments on the photodissociation, recombination, and vibrational relaxation of I_2^-: Role of solvent-induced solute charge flow, *J. Phys. Chem.* **99**, 7568, (1995).

[192] F. Webster, P. Rossky, and R. Friesner, Nonadiabatic processes in condensed matter: Semiclassical theory and implementation, *Comput. Phys. Comm.* **63**, 494, (1991).

[193] F. Webster, J. Schnitker, M. Friedrichs, R. Friesner, and P. Rossky, Solvation dynamics of the hydrated electron: A nonadiabatic quantum simulation, *Phys. Rev. Lett.* **66**, 3172, (1991).

[194] F. Webster, E. T. Wang, P. J. Rossky, and R. A. Friesner, Stationary phase surface hopping for nonadiabatic dynamics: Two-state systems, *J. Chem. Phys.* **100**, 4835, (1994).

[195] M. J. Weida and D. J. Nesbitt, Geometric isomerism in clusters: High resolution infrared spectroscopy of a noncyclic CO_2 trimer, *J. Chem. Phys.* **105**, 10210, (1996).

[196] H.-J. Werner and P. J. Knowles, *J. Chem. Phys.* **82**, 5053, (1985).

[197] H.-J. Werner and P. J. Knowles, *J. Chem. Phys.* **89**, 5803, (1988).

[198] R. J. Wheatley, Gaussian multipole functions for describing molecular charge distributions, *Mol. Phys.* **79**, 597, (1993).

[199] R. J. Wheatley, First-order Coulomb interaction energies for atoms and diatomic molecules, *Mol. Phys.* **86**, 443, (1995).

[200] R. J. Wheatley and J. B. O. Mitchell, Gaussian multipoles in practice: Electrostatic energies for intermolecular potentials, *J. Comp. Chem.* **15**, 1187, (1994).

[201] C. A. White and M. Head-Gordon, Derivation and efficient implementation of the fast multipole method, *J. Chem. Phys.* **101**, 6593, (1994).

[202] C. A. White, B. G. Johnson, P. M. W. Gill, and M. Head-Gordon, The continuous fast multipole method, *Chem. Phys. Lett.* **230**, 8, (1994).

[203] J.-K. Wong, Q. Liu, and A. H. Zewail, Solvation ultrafast dynamics of reactions. 9. Femtosecond studies of dissociation and recombination of iodine in argon clusters, *J. Phys. Chem.* **99**, 11309, (1995).

[204] L. Xiao and D. Coker, The influence of nonadiabatic rotational transitions on the line shapes of the rotational Raman spectrum of H_2 in liquid argon, *J. Chem. Phys.* **100**, 8646, (1994).

[205] L. Xiao and D. Coker, Nonadiabatic dynamical studies of the rotational Raman spectrum of H_2 in water, *J. Chem. Phys.* **102**, 1107, (1995).

[206] Y. Yan, R. Whitnell, K. Wilson, and A. Zewail, Femtosecond chemical dynamics in solution. Wavepacket evolution and caging of I_2, *Chem. Phys. Lett.* **193**, 402, (1992).

[207] I. Yourshaw, Y. Zhao, and D. M. Neumark, Many-body effects in weakly bound anion and neutral clusters: Zero electron kinetic energy spectroscopy and threshold photodetachment spectroscopy of Ar_nBr^- (n =2–9) and Ar_nI^- (n =2–19), *J. Chem. Phys.* **105**, 351, (1996).

[208] E. A. Yukov, Elementary processes in the active medium of an iodine photodissociation laser, *Sov. J. Quant. Electr.* **3**, 117, (1973).

[209] R. Zadoyan, Z. Li, P. Ashjian, C. Martens, and V. Apkarian, Femtosecond dynamics of coherent photodissociation-recombination of I_2 isolated in matrix Ar, *Chem. Phys. Lett.* **218**, 504, (1994).

[210] R. Zadoyan, Z. Li, C. Martens, and V. Apkarian, The breaking and remaking of a bond: caging of I_2 in solid Kr, *J. Chem. Phys.* **101**, 6648, (1994).

[211] M. T. Zanni, T. R. Taylor, B. J. Greenblatt, B. Soep, and D. M. Neumark, Characterization of the I_2^- anion ground state using conventional and femtosecond photoelectron spectroscopy, *J. Chem. Phys.* **107**, 7613, (1997).

[212] Y. Zhao, C. C. Arnold, and D. M. Neumark, Study of the $I{\cdot}CO_2$ van der Waals complex by threshold photodetachment spectroscopy of I^-CO_2, *J. Chem. Soc. Faraday Trans.* **89**, 1449, (1993).

[213] Y. Zhao, I. Yourshaw, G. Reiser, C. C. Arnold, and D. M. Neumark, Study of the $ArBr^-$, ArI^-, and KrI^- anions and the corresponding neutral van der Waals complexes by anion zero electron kinetic energy spectroscopy, *J. Chem. Phys.* **101**, 6538, (1994).

[214] J. Zimmerman and R. M. Noyes, *J. Chem. Phys.* **21**, 2086, (1950).